Numerical Analysis of Reflux Condensation

by

Foad Hassaninejadfarahani

A Thesis submitted to the Faculty of Graduate Studies of
The University of Manitoba
in partial fulfilment of the requirements for the degree of

Doctor of Philosophy

Department of Mechanical Engineering
University of Manitoba
Winnipeg, Manitoba, Canada

Abstract

Reflux condensation occurs in a vertical tube when there is an upward core flow of vapour (or gas-vapour mixture) and a downward flow of the liquid film. The understanding of this condensation configuration is crucial in the design of reflux condensers and in loss-of-coolant safety analyses in nuclear power plant steam generators.

A range of modelling approaches exists for co-current film condensation from gas-vapour mixtures in parallel-plate channels and tubes. These methods are based on marching from the inlet down the tube and do not apply to the reflux condensation. In this research, however, a two-dimensional two-phase model was developed that solves the steady, full elliptic governing equations in both the film and the gas-vapour core flow on a non-orthogonal mesh that dynamically adapts to the phase interface. Gas-vapour shear and heat and mass transfer at the interface were accounted for fundamentally. This modelling is a big step ahead of current capabilities by removing the limitations of previous reflux condensation models which inherently cannot account for the detailed local balances of shear, mass, and heat transfer at the phase interface.

The model was developed and applied for co-current and counter-current flows in vertical parallel-plate channels, followed by vertical tubes. In each stage, the model results were compared against the available experimental and numerical data for validation purposes. A wide range of boundary conditions and geometries have been studied to examine the details of co-current and counter-current condensation phenomena. Velocity, temperature, pressure, and gas mass fraction profiles along with the axial variation of various parameters such as local Nusselt number, film thickness, interface and centre-line temperature and gas mass fraction are presented in parametric studies.

Acknowledgements

"As we express our gratitude, we must never forget that the highest appreciation is not to utter words, but to live by them." John F. Kennedy

First and foremost, I would like to express my sincere gratitude to my advisor, Dr. Scott Ormiston, for the continuous support of my Ph.D. study and related research, for his patience, motivation, and immense knowledge. Furthermore, I would like to thank the rest of my thesis committee: Dr. Birouk, Dr. Clark, and Dr. Daun, for their insightful comments and encouragements, and also for the hard questions which incented me to widen my research from various perspectives.

I am particularly grateful to Dr. Karen Vierow. She generously provided detailed experimental data for the validation phase of this research.

My sincere thanks also go to Dr. Hossein Pourreza and Dr. Grigory Shamov, who provided me with invaluable assist in the application of HPC[1] resources.

I recognize that this research would not have been possible without the financial assistance of the University of Manitoba Graduate Studies Fellowship, Graduate Enhancement of Tri-Council Stipends, and NSERC. I am deeply grateful to them.

I would like to thank administrative staff members of the Department of Mechanical Engineering at the University of Manitoba who have been kind enough to advise and help in their respective roles.

I thank my fellow labmate, Esam Saleh, for the stimulating discussions, for the sleepless nights we were working together before deadlines, and for all the fun we have had in the last five years.

[1] High Performance Computing

Words cannot express how grateful I am to my mother and father, Maryam and Ali, for all of the sacrifices that they have made on my behalf. Special thanks to my lovely wife, Faezeh. Without her support and encouragement, quiet patience, and unwavering love; I could not have finished this work. I would like to express my gratitude to my kind brother-in-law, Farid, for all his support and help.

Last but not definitely least, I would like to show my greatest appreciation to my incredible and invaluable friends: Aman, Bahareh, Ehsan, Elham, Forough, Niloufar, Nozhan, Pedram, Saman, and Shekoofeh; for tolerating my occasional vulgar moods and idiosyncrasies, and for their unconditional devoted support.

To my sweet and loving Father & Mother,

Ali & Maryam

And my incredible wife and best friend.

Faezeh

Contents

List of Tables

List of Figures

Nomenclature

A	area, [m^2]
A_{r1}, A_{r2}, A_{r3}, A_{r4}	geometrical parameters Eq. (4.99)
A_{z1}, A_{z2}, A_{z3}, A_{z4}	geometrical parameters Eq. (4.98)
b	source term in algebraic equations
$\tilde{b}$	source terms in PWIM equations, Eqs. (4.9) and (4.10)
B_{r1}, B_{r2}, B_{r3}, B_{r4}	geometrical parameters Eq. (4.101)
B_{z1}, B_{z2}, B_{z3}, B_{z4}	geometrical parameters Eq. (4.100)
C	coefficients for the interpolations of the corner values
C_p	specific heat, [$J/kg \cdot K$]
D	diffusion coefficient of a transport equation
D^{12}	binary diffusion coefficient, [m^2/s]
$\tilde{D}$	extra terms of the energy equation for mixture
$\hat{d}$	weight function for PWIM, Eq. (4.11)
ds	distance along $\hat{s}$ vector for a single control volume, [m]
dt	distance along $\hat{t}$ vector for a single control volume, [m]
E	E-factor
F	degradation factor
g	acceleration due to gravity, [m/s^2]
G	interface temperature function
H	domain half height, [m]
h	heat transfer coefficient, [$W/m^2 \cdot K$]
h_{fg}	latent heat of vapourisation, [J/kg]
i	index in the x or z direction
$\hat{\imath}$	normal unit vector in the x or z direction
$i_{\mathrm{B}}, i_{\mathrm{E}}$	first, last control volume indices in the x or z directions
j	index in the y or r directions
$\hat{\jmath}$	normal unit vector in the y or r direction

Ja	Jakob number: $C_{p,L}\frac{(T_{\text{sat}}-T_{\text{wall}})}{h_{fg}}$
$j_{\text{B}}, j_{\text{E}}$	first, last control volume indices in the y or r directions
$j_{\text{B}L}, j_{\text{E}L}$	first, last control volume indices in liquid in the y or r directions
$j_{\text{B}M}, j_{\text{E}M}$	first, last control volume indices in mixture in the y or r directions
k	thermal conductivity, [W/m · K]
K	curvature of the interface, [m^{-1}]
L	length, [m]
M	molecular weight, [kg/kmol]
$\dot{m}$	mass flow rate, [kg/s]
N	number of nodes
n	normal direction
$\hat{n}$	normal unit vector: $n_x\,\hat{\imath} + n_y\,\hat{\jmath}$ or $n_z\,\hat{\imath} + n_r\,\hat{\jmath}$
Nu	Nusselt number
P	pressure, [N/m^2]
P^*	dimensionless pressure: $(P - P_{\text{in}})/(0.5\rho_{\text{in}}U_{\text{in}}^2)$
P_{ref}	reference absolute pressure: 1 bar
q''	heat flux, [W/m^2]
R	tube radius, [m]
$\mathcal{R}$	geometric parameter for the calculation of gradient: Eqs. (4.43) and (4.44)
r	cylindrical coordinate direction, [m]
r_1	interface location in cylindrical coordinates: $R - \delta$, [m]
r_b	break-point location, [m]
Re_{in}	Reynolds number: $(\rho_{M,\text{in}}U_{M,\text{in}}H)/\mu_{M,\text{in}}$ in Chapter 5, $(\rho_{M,\text{in}}\lvert\,\overline{U}_{M,\text{in}}\,\rvert H)/\mu_{M,\text{in}}$ in Chapter 6
Re_{in}	Reynolds number: $(2\rho_{M,\text{in}}U_{M,\text{in}}R)/\mu_{M,\text{in}}$ in Chapter 7, $(2\rho_{M,\text{in}}\lvert\,\overline{U}_{M,\text{in}}\,\rvert R)/\mu_{M,\text{in}}$ in Chapter 8

Re_L	liquid Reynolds number: $(4\dot{m}_L)/\mu_L$ in Chapter 5, $(4\dot{m}_L)/(2\pi R\mu_L)$ in Chapter 8
S	grid geometric expansion factor
s	west to east node-to-node and node-to-face directions
$\hat{s}$	west to east geometric unit vector: $s_x\,\hat{\imath} + s_y\,\hat{\jmath}$ or $s_z\,\hat{\imath} + s_r\,\hat{\jmath}$
T	temperature, [K]
$T^\star$	dimensionless temperature: $(T - T_{\text{wall}})/(T_{\text{in}} - T_{\text{wall}})$
t	time, [s]
t	south to north node-to-node and node-to-face directions
$\hat{t}$	south to north geometric grid unit vector: $t_x\,\hat{\imath} + t_y\,\hat{\jmath}$ or $t_z\,\hat{\imath} + t_r\,\hat{\jmath}$
U	velocity in the x or z directions, [m/s]
$\overline{U}_{M,\text{in}}$	average mixture inlet velocity, $(\dot{m}_{M,\text{in}})_{\text{net}}/(\rho_{M,\text{in}}A_{\text{in}})$, [m/s]
$U^\star$	dimensionless U velocity: $U/\mid \overline{U}_{M,\text{in}} \mid$
V	velocity in the x or z directions, [m/s]
$V^\star$	dimensionless V velocity: $V/\mid \overline{U}_{M,\text{in}} \mid$
$\vec{V}$	velocity vector, [m/s]: $U\,\hat{\imath} + V\,\hat{\jmath}$
$\forall$	volume of a control volume, [m^3]
W	gas mass fraction: $\dot{m}_g/\dot{m}_{\text{tot}}$
$\mathcal{W}$	geometric linear interpolation factor
x	Cartesian coordinate direction, [m]
$x^\star$	dimensionless length: x/H
y	Cartesian coordinate direction, [m]
$\mathcal{Z}$	geometric parameter for the calculation of gradient: Eqs. (4.41) and (4.42)
z	cylindrical coordinate direction, [m]
$z^\star$	dimensionless length: z/D in Chapter 7 and Eq. (8.2) in Chapter 8
ΔP	pressure difference: $P_{M,\text{in}} - P_{M,\text{out}}$, [Pa]

Δr	control volume size in liquid in r direction: $\dfrac{\delta}{\mathtt{N}_{r,L}}$, [m]
ΔT	inlet-to-wall temperature difference: $T_{\text{in}} - T_{\text{wall}}$, [K]

Greek Letters

α	convective weighting coefficient
β	diffusive weighting coefficient
Γ	gradient value at the boundary
γ	geometric parameter, Eq. (4.75)
δ	liquid film thickness, [m]
δ^*	dimensionless liquid film thickness: δ/H
Δ^ϕ	steady-state convergence criterion
η	dimensionless coordinate, Eqs. (5.4) and (7.4)
μ	dynamic viscosity, $[\text{N} \cdot \text{s/m}^2]$
ρ	density, $[\text{kg/m}^3]$
σ	surface tension, [N/m]
$\boldsymbol{\tau}$	stress tensor, $[\text{N/m}^2]$
Φ	general variable (referring to U, V, P, T, or W)
ϕ	relative humidity
Ψ_1, Ψ_2	geometrical parameters, Eq. (4.102)

Subscripts

a	referring to the air
bc	referring to boundary conditions
c	referring to the cooled section

cl	referring to the centre-line
cond	referring to condensation
e, w, s, n	referring to the quantities at the east, west, south, and north face of a control volume
E, W, S, N	referring to the nodal quantities to the east, west, south, and north of a control volume
exp	referring to the experiment
f	referring to the liquid film
f	referring to the quantities at faces of a control volume
F	referring to the adjacent node
g	referring to the gas
i	west to east control volume index
iL	referring to the quantities at the liquid side of the interface
iM	referring to the quantities at the mixture side of the interface
in	referring to the inlet
int	referring to the interface
j	south to north control volume index
L	referring to liquid
M	referring to mixture
NB	referring to the neighbour nodes
NB4	referring to E, W, N, S
NB8	referring to NB4 and NE, NW, SE, SW
ne, nw, se, sw	referring to the quantities at the north east, north west, south east, and south west of a control volume
net	referring to the net value
NE, NW, SE, SW	referring to the nodal quantities to the north east, north west, south east, and south west of a control volume

P	referring to the typical control volume
p	referring to the node
out	referring to the outlet
r	referring to the r direction
re	referring to the r component of a vector on the east face
rn	referring to the r component of a vector on the north face
rp	referring to the r component of a vector on the node
s	referring to steam
sat	referring to saturation conditions
spec	referring to a specified value
t	referring to the tangential direction
tot	referring to the total amount
v	referring to vapour
wall	referring to the wall
we	referring to a calculation from west to east
x	referring to the x direction
y	referring to the y direction
z	referring to the z direction
ze	referring to the z component of a vector on the east face
zn	referring to the z component of a vector on the north face
zp	referring to the z component of a vector on the node

Superscripts

e	referring to a transport equation
c, u, v, t, w	referring to continuity, U, V, energy, and gas mass fraction equations

ϕ	referring to a general transport parameter
$\star$	referring to a dimensionless parameter
$\oplus$	referring to the modifications
o	referring to the previous time step
$''$	per unit area

Miscellaneous

CV	Control Volume
G1, G2, G3	three geometries for the reflux case studies
HPC	High Performance Computing
ILMB	Integral Liquid Mass Balance
ip	integration point
L_1, L_2, L_3	lengths of top, middle and bottom sections
PETSc	The Portable, Extensible Toolkit for Scientific Computation
PWIM	Pressure-Weighted Interpolation Method

Chapter 1

Introduction

1.1 Overview

Condensation is the process by which a vapour is changed to a liquid state. Due to the large difference between the liquid and vapour internal energies, there is a significant amount of energy released during the condensation process, even for a small temperature difference. Therefore, condensation heat transfer is an important process in many industrial applications and thermal systems.

Condensation occurs when the vapour temperature is reduced below its saturation temperature. Four common modes of condensation are: filmwise, dropwise, homogeneous and direct contact. Condensation heat transfer is mostly investigated under one of the following categories: condensation of pure vapour, mixtures of vapours or vapour-non-condensing gas mixtures. In addition, the flow phenomena can be classified as external or internal flow, laminar or turbulent flow, and co-current or counter-current flow.

1.2 Film Condensation

The dominant form of condensation is filmwise, which occurs when the condensate wets the surface and forms a liquid film. This phenomenon is the result of a temperature difference between the entering vapour or vapour-gas mixture and the wall of the tube or channel. As the liquid film builds up, it starts to move in a specific direction which is determined by the liquid-vapour/mixture interface shear stresses, wall shear stresses and the gravity force. Generally, film condensation takes place in the presence of a cold, clean, uncontaminated surface [1]. The entering main flow could be pure vapour or a mixture of vapour and gas.

For the mixtures, the gas may be lighter or heavier than the vapour. The focus of the following discussion is on film condensation of gas-vapour mixtures. However, pure vapour film condensation is simply a gas-vapour mixture condensation with the gas mass fraction of zero.

Co-current condensation, as shown in Fig. 1.1a, occurs in a horizontal or vertical duct when the core flow of gas-vapour mixture and the liquid film are flowing in the same direction. Counter-current condensation as shown in Fig. 1.1b, however, happens when the core flow of the gas-vapour mixture and the liquid film are flowing in opposite directions.

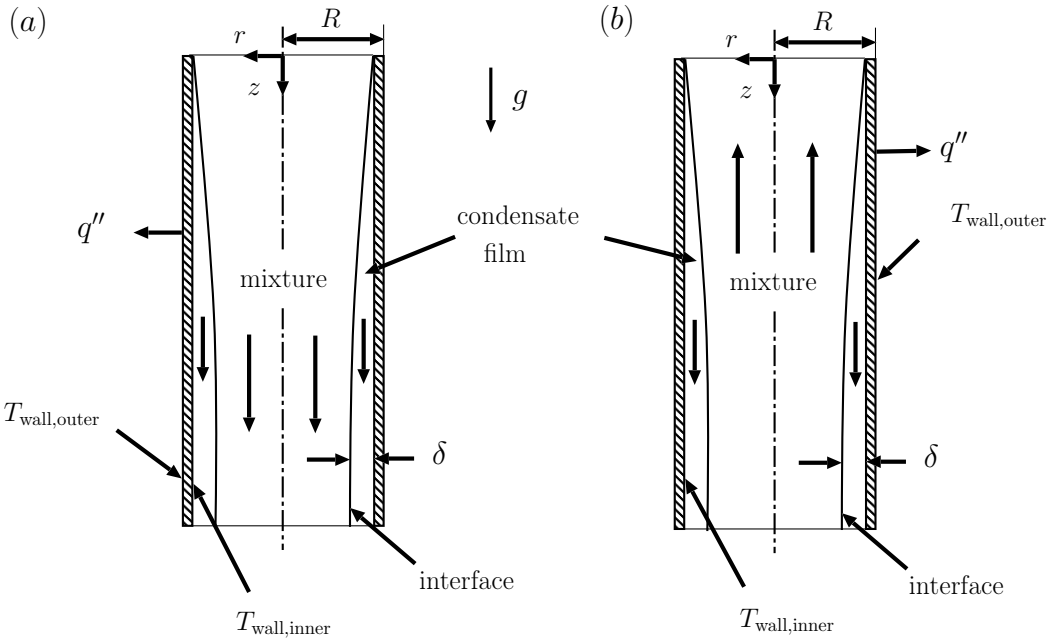

Figure 1.1: Condensation (a)co-current flow (b)counter-current flow

Non-condensing gases reduce condensation heat transfer by accumulating along the liquid-mixture interface, thus preventing vapour from reaching the heat transfer surface. The presence of the gas also reduces the interface temperature because of the reduction of the partial pressure of the vapour where gas builds up. In the presence of a non-condensable gas, vapour must diffuse through the gas layer to reach the liquid region. Vapour partial

pressure at the interface will be significantly lower than the vapour partial pressure in the bulk of the mixture and most of the vapour may pass through the tube or channel without condensing. For the mixtures with gas lighter than vapour, (*e.g.*, Helium and steam), as the vapour condenses in the duct, the mixture becomes lighter and lighter. For downward co-current condensation in vertical ducts, reduction of mixture weight due to the condensation continues to the point that buoyancy force would be higher than the gravitational force. In this instance, flow reversal may occur and the mixture would start to move upwards.

Counter-current condensation has completely different characteristics compared to co-current condensation. In the presence of a non-condensable gas, the gas concentration increases along the gas flow direction for both cases while the condensate film thickness increases under co-current conditions but decreases under counter-current conditions. This difference in film thickness causes different local heat transfer resistance of the condensate film in the two cases. Mainly, for a laminar liquid film, the shear stresses retard film flow and thicken the film for the counter-current condensation while they accelerate film flow and thin the film in the case of co-current condensation.

Counter-current condensation is an important phenomenon in many industrial applications such as compact heat exchangers, thermosyphons, and steam generators of nuclear power plants. The focus of this research is on the counter-current condensation in vertical tubes or channels. Because of the non-negligible presence of gravity in vertical cases of counter-current condensation, these problems are investigated under the category of Reflux Condensation.

1.3 Reflux Condensation

Reflux condensation can occur in vertical or inclined tubes or channels. The unique feature of reflux condensation is the upward flow of the gas-vapour mixture (or pure vapour) that

retards the liquid flow via shear at the liquid-mixture (or liquid-vapour) interface. With sufficiently high vapour velocity and small tube diameter, the liquid can be held up by the mixture and completely close off the tube to vapour flow; this phenomenon is called flooding or inverted-slug flow. It represents a serious limitation to the operation of reflux condensers and much attention has been placed on determining the onset of flooding [2]. The motion of the liquid film is governed by the gravitational driving force and retarding force from the interfacial shear. At a particular mixture mass flow rate, the film velocity at the interface becomes zero. In this situation, the interfacial shear and gravitational force are equal. For higher gas phase mass flow rates, flow reversal occurs in the liquid film. Finally, the interfacial shear becomes dominant and the system reaches the total flooding limit.

Reflux condensation is one of the major heat removal mechanisms in loss of coolant safety analyses in nuclear power plant steam generators. Figure 1.2 shows schematically a portion of a pressurized water reactor and a steam generator of a nuclear power plant. In this system, reflux condensation is expected to occur in the hot leg or U-tube during accidents caused by loss of coolant or by loss of heat removal in the mid-loop operation [3]. These accident scenarios occurred in pressurized water reactor plants in the USA in 1987 and 1990 [4].

Reflux condensation also can be observed in thermosyphons and heat pipes. Figure 1.3 shows a simple thermosyphon system. Thermosyphons transfer heat in the same way as heat pipes by the use of evaporation and condensation phenomena. In thermosyphons, there is no external equipment for the liquid transport from the condenser back to the evaporator and thus the evaporator must be located vertically below the condenser. Gravity is responsible to return the condensate to the evaporator. Sometimes, thermosyphons are called gravity-assisted heat pipes.

Finally, an understanding of reflux condensation is crucial in the design of reflux condensers and distillation columns. In distillation columns, for example, counter-current flow is used to separate components in mixtures of vapours that condense at different temperatures.

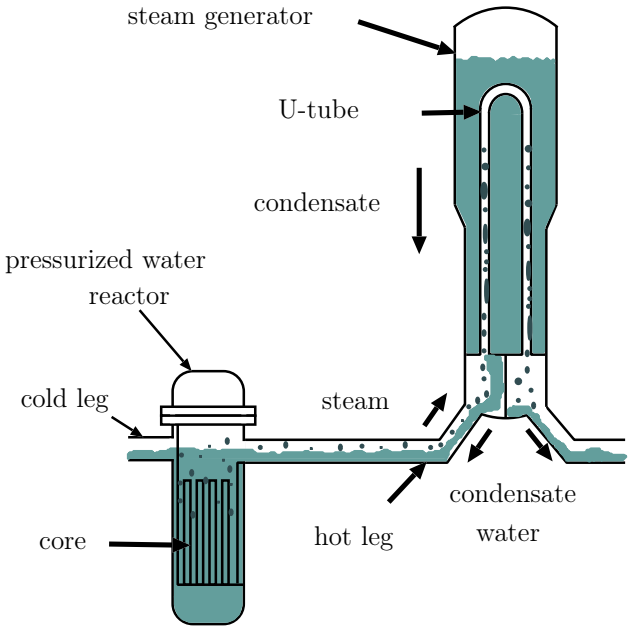

Figure 1.2: Reflux condensation in pressurized water reactor and steam generator of the nuclear power plant

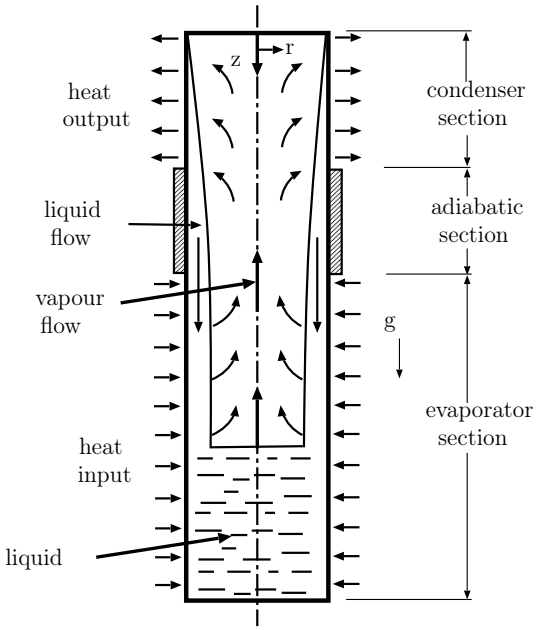

Figure 1.3: Closed thermosyphon

1.4 Problem Statement

The main objective of this research is to develop a detailed numerical model for reflux condensation in a vertical tube. The fundamental setup of condensation in vertical tube has a cooled section where the wall temperature (T_{wall}) is below the saturation temperature of the vapour. Due to the temperature difference between the mixture and wall, the vapour starts condensing on the tube wall and forms a thin film of condensate with the thickness of δ. The film thickness increases along the tube and the condensate flows downward as long as the summation of shear stress at the wall and at the interface is smaller than the gravitational force. As the mixture flows upward, the condensation rate decreases due to the interface temperature decrease and gas mass fraction increase. Finally, the condensation will stop and single phase mixture will exit the tube.

In Fig. 1.4, the cooled section is the section with length of L_2. The wall temperature could be constant or vary axially to emulate a flow of cooling water in an annulus around the tube. Above and below the cooling section, boundary conditions must be specified for the mixture flow. The conditions of the mixture flow entering the tube from below are dependent on the geometry and thermal conditions in the piping that supplies the mixture. Taking this into account would extend the solution domain to include a three-dimensional region that is application-specific. Because developing a two-phase counter-current flow model will be a challenge itself, a two-dimensional axisymmetric model is considered an excellent starting point. Therefore, in order to keep the model domain two-dimensional and reasonable in size, an inlet section with an adiabatic wall with length of L_3 is added at the mixture inlet side of the cooled section. This additional length permits the development of the mixture flow before the cooled section and section of film flow with no mass flow change. Likewise, a pipe section with an adiabatic wall of length L_1 is added at the mixture outlet side of the cooled section. This additional section permits the application of an appropriate outflow condition on the mixture as it flows without mass removal.

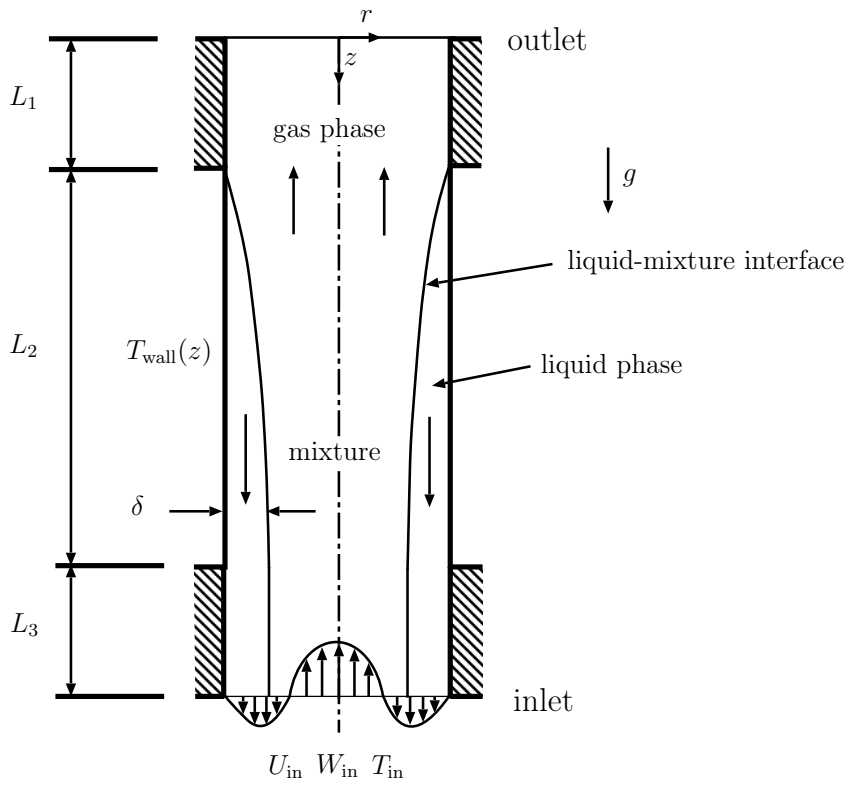

Figure 1.4: Reflux condensation in vertical tube

1.5 Literature Review

The main literature survey is organized into three sections. Since there are common approaches that have been used for both the co-current and counter-current condensation problems, the first section covers previous research on co-current condensation. Following that, a survey of previous work on reflux condensation is presented in the two categories of experimental and theoretical studies.

When film condensation in a duct is analysed using a parabolic solution approach, the film thickness is determined at the convergence of the calculations at each axial station. When an elliptic approach is used, however, the film thickness must be computed for the entire domain at each time step taken toward a steady-state solution. If one views the film thickness as the location of the boundary between the two phases, then the elliptic approach

involves a moving boundary problem; this could also be called an interface capturing or tracking problem. Due to the importance of interface moving strategy in the numerical simulation of condensation using an elliptic approach, the last section gives a brief review about interface moving algorithms.

1.5.1 Previous Work on Co-Current Condensation

The first notable analysis of film condensation was done by Nusselt in 1916 for laminar falling-film condensation on a vertical wall [1]. Nusselt assumed laminar flow, pure vapour and constant properties. He also assumed that subcooling of liquid is negligible in the energy balance, that the inertia effects are negligible in the momentum balance, that the vapour is stationary, that there is no interface shear, that the interface between the liquid and vapour is smooth, and that the heat transfer across the film is only by conduction. The Nusselt analysis provided a solution for the film thickness as a function of distance from the top of the plate and for the local heat transfer coefficient [1]. Since 1916 researchers have worked on improving film condensation modelling by removing various restrictions used in the Nusselt analysis.

Internal convective condensation is important in the design of many power and refrigeration systems. Thus, many researchers focused on the different aspects of condensation heat transfer in channels and tubes for laminar and turbulent flows. For instance, Dobran and Thorsen [5] studied the laminar pure vapour condensation in a vertical tube. They modelled laminar flow in both the film and the vapour. Starting from the full governing equations, they obtained a set of ordinary differential equations by using an integral analysis and profile assumptions for the velocity in the liquid and in the vapour. They also used a fully-developed inlet velocity profile and studied the effect of selected dimensionless groups.

The detailed numerical simulation of the co-current laminar film condensation from a gas-vapour mixture in vertical parallel-plate channels has been made by Siow *et al.* [6] and

Dharma Rao *et al.* [7].

Siow *et al.* [6] modelled steady film condensation from an air-water mixture and used a fully coupled implicit numerical approach in order to solve problems with a wide range of inlet gas mass fractions. They developed a two-dimensional, two-phase, boundary-layer equation model for laminar film condensation using a transformation of coordinates. By applying a fully coupled approach and with the help of marching scheme on a structured grid, the whole system of non-linear parabolic governing equations was solved simultaneously at each axial location. The interface height was calculated based on energy conservation at the interface coupled with mass, momentum and energy conservation equations. In addition, constant pressure in the y direction was assumed and the y-momentum equation was not solved. Siow *et al.* presented their results on the effect of changing the four key parameters of the problem: U_{in}, P_{in}, W_{in}, $(T_{\text{in}} - T_{\text{wall}})$. They developed an in-house code that works for a variety of problems [8].

Dharma Rao *et al.* [7] also developed a model for laminar convective condensation of steam in vertical parallel plate channels in the presence of air. The focus of their research was on cases with high air concentration. They used the parabolic forms of the momentum, energy, and diffusion equations and used an implicit finite difference method to solve the equations with a marching scheme along the channel. The Nusselt solution was applied for the film and the interface temperature was calculated iteratively based on an energy balance equation. The vapour density was used instead of gas mass fraction in their equations because in condensation with high gas mass concentration the controlling parameter is the relative humidity. Dharma Rao *et al.* presented the results for the relative humidity of 80% and 100% at the inlet with room temperature and Reynolds numbers of 1000 and 2000.

For laminar film condensation from a gas-vapour mixture in a vertical tube for co-current flows, Hassaninejadfarahani *et al.* [9], Groff *et al.* [10], Dharma Rao *et al.* [11], and El-Hammami *et al.* [12] modelled steady axisymmetric film condensation from an air-water-

vapour mixture.

Groff *et al.* [10] solved implicitly the complete parabolic set of governing equations for laminar film and vapour flow. A marching procedure was used to obtain the solution field results along the tube. They presented results on the effects of changing the inlet Reynolds number, the inlet-to-wall temperature difference, the inlet pressure, and the inlet air mass fraction. Inlet air mass fraction values were limited to 0.80 or less.

El-Hammami *et al.* [12] modelled film condensation from a steam-air mixture with small concentrations of vapour (*i.e.*, high air mass fraction) in a vertical tube. They solved parabolic governing equations in both phases and neglected advection terms in the liquid axial momentum and energy equations. They used a finite difference discretisation approach and a marching procedure to determine the velocities, temperature, vapour mass fraction, and film thickness along the tube. In their solution scheme, the values of the pressure gradient and the film thickness were first guessed and then corrections were applied to them and the axial velocity, based on imbalances in mass conservation.

Hassaninejadfarahani *et al.* [9] extended the approach used by Groff *et al.* to examine co-current steam-air flows with very high inlet gas mass fraction (greater than 0.80). They varied the inlet relative humidity from 30% to 100% and the inlet temperature from 25°C to 90°C. These conditions covered the range of inlet air mass fraction approximately from 0.865 to 0.995 for an inlet pressure of 1 bar. In addition, they examined the effects of varying the inlet Reynolds number (500 to 2000), the wall temperature (5°C and 15°C), and the tube radius (2.5 mm to 10.0 mm). They found that decreasing the inlet relative humidity reduced the heat transfer rate and that the condensate film thickness increased with an increase in the inlet Reynolds number, inlet-to-wall temperature difference, and inlet relative humidity. They also reported that due to high air mass fraction, in some cases only 40% or less of the total heat transfer to the tube wall was due to condensation. Moreover, they observed that for a fixed Reynolds number, decreasing the tube radius increased the condensation rate.

Many models have been developed for the case of film condensation with a turbulent flow of a gas-vapour mixture. Some of those are simplified theoretical models (*e.g.*, [13–19]) and others are detailed models based on the governing differential equations (*e.g.*, [20, 21]). Among the examples listed, some considered a laminar film and a turbulent mixture flow.

While some of the governing equations (for example, those in the liquid region) used in the co-current analyses may be applicable for reflux condensation, the marching solution scheme is not.

1.5.2 Previous Work on Reflux Condensation

There are numerous theoretical and experimental investigations in the field of reflux condensation analyses which are mostly focused on flooding phenomenon and its limits (*e.g.*, [22–27]). Very few of them considered condensation heat transfer. The reviews of experimental and theoretical works on reflux condensation heat transfer now follow.

Experimental Works

Condensation heat transfer key parameters for pure vapour or gas-vapour mixtures were measured in many experiments. However, very few of those experiments focused on counter-current flow and reflux condensation heat transfer.

Chen *et al.* [28] wanted to describe local behaviours of the turbulent flows in both phases. Beside their theoretical study (which will be discussed shortly), they conducted experiments for a closed thermosyphon such as the one shown in Fig. 1.3. A tube with a diameter of 14.2 mm and length of 2.2 m was used as the main core of the apparatus. Chen *et al.* used methanol and water and measured the temperature at different locations and calculated the Nusselt number.

Girard and Chang [29] studied the turbulent reflux condensation of pure steam and specifically the flooding experimentally. Their experimental apparatus consisted of a series

of eight vertical double pipe heat exchangers made of Pyrex glass. Using the glass helped them to observe the flow patterns before and after flooding. They observed new phenomena after flooding: when the flooding point was reached, the condensate accumulated in the form of a water column instead of being ejected from the tube. Girard and Chang called this a quasi-static situation that could be held indefinitely.

Moon *et al.* [30] measured the local heat transfer coefficient for the reflux condensation in counter-current turbulent flows between steam-air mixture and the condensate. They placed a single vertical tube with the inner diameter of 19.05 mm and length of 2.4 m as the main test section. Moon *et al.* measured temperature at 11 locations in the vertical direction. Each location had three measurement points in the radial direction: tube centre, outer wall, coolant side. The experiment ranges were:

$1.0 \text{ bar} \leq P \leq 2.5 \text{ bar}$

$1.348 \text{ kg/h} \leq \dot{m}_{v,\text{in}} \leq 3.282 \text{ kg/h}$

$11.8\% \leq W \leq 55\%$

where, P, $\dot{m}_{v,\text{in}}$ and W are the pressure, inlet vapour mass flow rate and the gas mass fraction, respectively. They calculated the heat flux based on the coolant temperature increase. Also, the tube inner wall temperature was calculated based on the conductivity of the tube wall and the measured outer wall temperature. Due to the use of steel tube, the flooding could not be captured visually. The tube centre-line temperature oscillation was used to discern the occurrence of flooding. Their parametric study showed that a modified Nusselt solution could be used to calculate the heat transfer coefficient. The modification factor was named as a degradation factor. Moon *et al.* correlated this factor to the mixture Reynolds number (Re_g), film Reynolds number (Re_f), Jakob number (Ja) and local gas mass fraction (W). The factor was given as:

$$F = \frac{h_{\text{exp}}}{h_\text{f}} = 2.58 \times 10^{-4} \text{Re}_g{}^{0.2} \text{Re}_\text{f}{}^{0.502} \text{Ja}^{-0.642} W^{-0.244} \tag{1.1}$$

The application ranges of Eq. (1.1) are:

$6119 \leq \mathrm{Re}_g \leq 66586$

$0.14 \leq W \leq 0.972$

$0.03 \leq \mathrm{Ja} \leq 0.125$

$1.2 \leq \mathrm{Re}_\mathrm{f} \leq 166.6$

where,

$$\mathrm{Re}_g = \frac{4\dot{m}_g}{\pi D \mu_g} \quad , \quad \mathrm{Re}_\mathrm{f} = \frac{4\dot{m}_\mathrm{f}}{\pi D \mu_\mathrm{f}} \quad , \quad \mathrm{Ja} = \frac{C_{p,\mathrm{f}}(T_b - T_\mathrm{wall})}{h_{fg}}$$

and h_f was defined as:

$$h_\mathrm{f} = \frac{k_\mathrm{f}}{\delta} \quad \text{where,} \quad \delta = \left[\frac{3\mu_\mathrm{f}^2 \mathrm{Re}_\mathrm{f}}{4\rho_\mathrm{f}\left(\rho_\mathrm{f} - \rho_g\right) g}\right]^{1/3} \tag{1.2}$$

As expected, it was concluded that the presence of non-condensable gas causes a remarkable decrease of the heat transfer coefficient compared to the same flow rate of pure vapour. It was shown that the increase of inlet steam mass flow results in the increase of the heat transfer coefficient. Furthermore, they showed that the pressure increase leads to an increase of heat transfer coefficient near the tube inlet and a decrease away from the inlet.

Vierow *et al.* [31] established a facility including water heater, non-condensable gas supply, coolant water supply, test section (vertical tube with the diameter of 19.3 mm and length of 1.78 m), condensate collection system, associated piping and water storage tanks, and instrumentation and data acquisition system to perform a variety of repeatable steady-state experiments about reflux condensation and flooding phenomena. The tests were run for the ranges of:

0.1 MPa $\leq P \leq$0.4 MPa

1.0 g/s $\leq \dot{m}_{v,\mathrm{in}} \leq$ 3.0 g/s

0.0 g/s $\leq \dot{m}_{a,\mathrm{in}} \leq$ 0.18 g/s

Vierow *et al.* checked energy balances for each test and mentioned that the calculated amount of heat removed by the coolant agreed within 5% with the calculated amount of steam condensed for low pressure tests (0.1 MPa and 0.2 MPa). The outcome of their study was a correlation for condensation heat transfer coefficient and Nusselt number for the conditions when the gas and the condensate film are both laminar.

$$h_z = 0.15\frac{P_{\mathrm{s}}}{P_a} \tag{1.3}$$

$$\mathrm{Nu}_z = 120(\frac{P_{\mathrm{s}}}{P_a})^{0.75} \qquad , \qquad \mathrm{Nu}_z < 1000 \tag{1.4}$$

where, P_{s} and P_a are the steam and air pressures, respectively.

They mentioned that the correlation is applicable for condensation heat transfer coefficients under 1 kW/m^{2}K. Vierow *et al.* were not able to conduct steady-state tests for pure steam reflux condensation because the entire facility headed toward vacuum conditions for that situation.

Fiedler and Auracher [32] carried out experiments with refrigerant R134a in an inclined small diameter tube. They investigated the flooding point and showed that the inclination has a significant effect on the flooding point, as well as the heat transfer coefficient during reflux condensation. Based on their studies, the optimum inclination angle for the heat transfer was close to 40° while the optimum inclination angle at which the highest flooding vapour velocity occurs was found between 45° and 60°.

Nagae *et al.* [33] evaluated reflux condensation heat transfer characteristics in steam generator U-tubes in the presence of air. They conducted experiments for a vertical tube with an inside diameter of 19.3 mm and used the same facility as Vierow *et al.* [31]. Figure 1.5 is a schematic representation of the measurement section of the experimental facility. The experimental setup had a main section with a vertical double-pipe cylinder made of stainless steel. Mixture of steam and air flowed into the tube from bottom inlet while the coolant water flowed upward along the outer surface of the tube. Nagae *et al.* ran steady-state tests

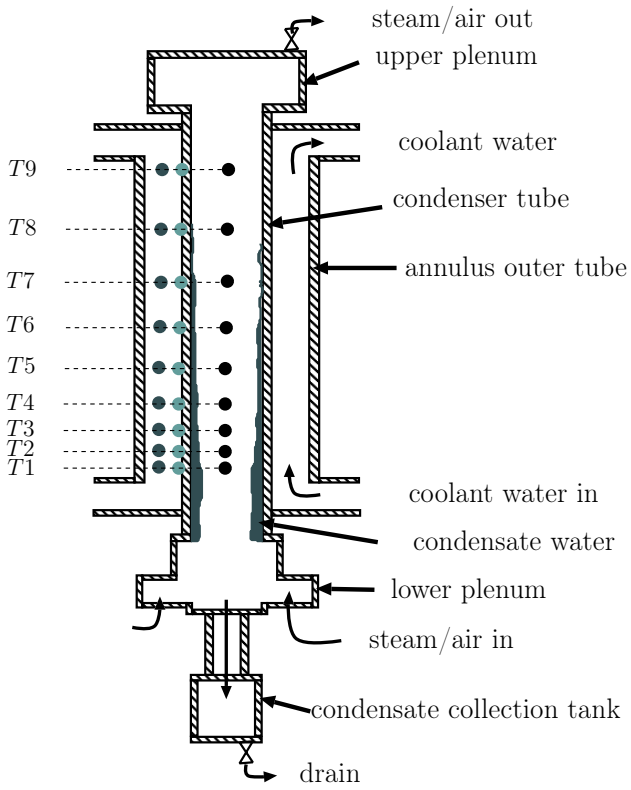

Figure 1.5: Core of the experimental setup used by Nagae *et al.* [33]

and measured the steam-air mixture temperature, tube outer wall temperature and coolant water temperature at nine locations distributed along the tube. The test conditions were:

0.1 MPa $\leq P \leq$0.4 MPa

0.5 g/s $\leq \dot{m}_{v,\text{in}} \leq$ 1.9 g/s

0.03 g/s $\leq \dot{m}_{a,\text{in}} \leq$ 0.18 g/s

Their study focused on condensation heat transfer under laminar flow conditions and, as a result, an empirical correlation was obtained for the condensation heat transfer coefficient. Heat fluxes were calculated from the temperature variation of the coolant in the upstream. In the areas other than upstream, the heat fluxes were calculated from the mixture temperature variation. Nagae *et al.* assumed that the condensation heat transfer coefficient can be

expressed by:

$$\frac{1}{h_{\text{cond}}} = \frac{1}{h_{\text{f}}} + \frac{1}{h_{\text{int}}} \tag{1.5}$$

where, h_{f} is the heat transfer coefficient of the liquid film and h_{int} is the heat transfer coefficient at the gas-liquid interface. They used a correlation for the film heat transfer coefficient based on the Nusselt model of a falling film on a flat plate multiplied by a compensation factor and were therefore able to determine h_{int}.

Based on the mentioned ranges of experiments, the collected data for turbulent flow were not sufficient to provide a robust correlation. Therefore, Nagae *et al.* conducted a new set of experiments based on a new test matrix for turbulent flow [34]. The setup was the same as their previous work. The pressure range for the tests was from 0.2 MPa to 0.4 MPa and the air mass flow rate was increased to produce turbulent flow conditions. They validated part of their test using the previous work by Moon *et al.* [3]. Nagae *et al.* presented a new correlation for the reflux condensation heat transfer coefficient under turbulent conditions.

The main intention of experimental work by Vierow *et al.* and Nagae *et al.* was to model the mid-loop operation of the pressurized water reactor plant. They used single vertical tube surrounded by a concentric coolant jacket in which the flow regime was forced convection. However, during the mid-loop operation, the heat transfer condition at the secondary side of the steam generator U-tubes was a natural convection or pool boiling.

Lee *et al.* [35] conducted steady state experiments for reflux condensation with pure steam and steam-air mixtures in vertical tubes. The main difference of their work with Vierow *et al.* and Nagae *et al.* was considering the effects of steam generator secondary side pool temperature. For pure steam, experimental results were close to the Nusselt theory. For high Reynolds number, however, their results were slightly higher than the Nusselt solution. To consider the effect of non-condensable gas, they developed a correlation for the heat transfer coefficient based on a degradation factor. This degradation factor was correlated in terms of the condensate Reynolds number, the air mass fraction, and the Jakob number as

follows:

$$F = \frac{h_{\text{exp}}}{h_{\text{f}}} = 4.88 \times 10^{-4} \text{Re}_{\text{f}}^{\ 0.59} W^{-0.29} \text{Ja}^{-0.89} \tag{1.6}$$

The applicable ranges of Eq. (1.6) are:

$1.5 < \text{Re}_{\text{f}} < 246$

$0.02 < W < 0.96$

$0.014 < \text{Ja} < 0.123$

where,

$$\text{Re}_{\text{f}} = \frac{4\dot{m}_{\text{f}}}{\pi D \mu_{\text{f}}} \quad , \quad \text{Ja} = \frac{C_{p,\text{f}}(T_b - T_{\text{wall}})}{h_{fg}} \quad , \quad W = \frac{\dot{m}_a}{\dot{m}_a + \dot{m}_s}$$

and the definition of h_{f} is the same as Eq. (1.2).

Klahm *et al.* [36] performed tests for the turbulent reflux condensation of the mixture of R134a and R123 in a narrow tube and rectangular channel with the same hydraulic diameter of 7 mm. They kept the pressure constant at 0.44 MPa and varied the vapour mass flow rate from 0.5 g/s to 1.1 g/s. The focus of their research was on the effect of inclination on the heat transfer coefficient and also they compared the heat transfer coefficients between a tube and a rectangular channel. Like the previous works, Klahm *et al.* found the positive effect of the inclination on the condensation rate. In addition, it was revealed that rectangular geometry with the same hydraulic diameter as a corresponding tube largely reduces heat transfer coefficient at a given mass flow rate.

Another example of experimental works that used gas other than air in the mixture is that of Noel and Deruaz [37]. They used nitrogen as a gas in the experimental investigation of a reflux condenser. The focus of their work was on the problem of heat losses in the pressurized reactor which may cause undesirable distortions in the pipes. The flow was turbulent in their studies.

Table 1.1 presents a summary of the review of previous experimental works on reflux condensation.

Table 1.1: Review of experimental works on reflux condensation in tubes

	Reference	**P/M**[a]	**L/T**[b]	**V/I**[c]
1	Chen *et al.* [28]	P	T	V
2	Girard and Chang [29]	P	T	V
3	Moon *et al.* [30]	M	T	V
4	Vierow *et al.* [31]	M	L	V
5	Fiedler and Auracher [32][d]	P	T	I
6	Nagae *et al.* [33]	M	L	V
7	Nagae *et al.* [34]	M	T	V
8	Lee *et al.* [35]	M	T	V
9	Klahm *et al.* [36][e]	M	T	I
10	Noel and Deruaz [37][f]	M	T	V

[a] P: Pure Vapour, M: Gas-Vapour Mixture
[b] L: Laminar, T: Turbulent
[c] V: Vertical, I: Inclined
[d] used R134a
[e] used a mixture of R134a and R123
[f] used Nitrogen as non-condensing gas

As shown, Nagae *et al.* [33] and Vierow *et al.* [31] are the only works that focused on laminar reflux condensation. Although the inlet conditions that they reported correspond to turbulent flow, the flow in the measurement section was laminar during their experiments. The detailed information and results provided by Nagae *et al.* and Vierow *et al.* were not sufficient for the purpose of comparison and validation. It was possible, however, to obtain from Dr. Vierow [38] two detailed unpublished technical reports of experiments using the same apparatus as Nagae *et al.* which include the necessary information and results. The case that was used for the comparison was defined based on the information in those reports.

Theoretical Works

The majority of previous modelling approaches for reflux condensation have been based on similar approximate governing equations and correlations at the interface. Most of them

solved the equations for the liquid region and used correlations or simplified equations for the interface and mixture region. In addition, many of them did not consider gas in the mixture region and assumed pure vapour.

Seban and Hodgson [39] developed a theoretical model for the condensation of pure saturated vapour flowing upward in a vertical tube. The model was based on constant liquid and vapour properties, and for the conditions given the liquid flow remained laminar while the gas is tubulent. They neglected the curvature of the film layer and convective terms in the energy equation. In addition, zero inertial terms in the momentum equations were assumed. They solved the simplified form of the boundary layer equations just for the liquid region with the assumption of linear temperature profile in the liquid. No detailed consideration was made of the velocity distribution in the vapour and they assumed uniform average velocity based on the mass flow rate of steam. Also, modified correlations for the friction factor at the interface were used. They claimed that since the friction factor generally is defined for the conditions of zero normal velocity, it needs to be modified if there is condensation. They used the vapour-liquid relative velocity and condensation mass flow to modify the interfacial stress. Seban and Hodgson neglected the pressure gradient and used an iterative scheme to adjust the film thickness based on the mass balance and interfacial shear at each iteration until convergence. Their simple model is one of the basic models that was modified and expanded later by other researchers.

Chen *et al.* [28] studied reflux condensation flow in a two-phase closed thermosyphon such as the one shown in Fig. 1.3. They considered a heat pipe which had three sections: evaporator, adiabatic, and condenser. Boundary layer equations for vertical plate were used for the liquid phase. The fluid inertia and energy convection were neglected and equal pressure gradient in both phases was assumed. The pressure gradient was calculated based on a force balance for both phases. Chen *et al.* assumed uniform one-dimensional turbulent pure vapour flow at saturated temperature and used a correlation to obtain the interfacial shear stress. Finally, an iterative finite difference method was applied to solve the one-dimensional

set of equations in the liquid region. The solution was started by assuming interfacial shear and then calculation of the film thickness, interfacial velocity and vapour velocity for the whole domain. Based on an updated solution, the interfacial shear was modified and the steps were repeated until convergence. They compared the theoretical solution with the Nusselt solution and their own experimental data for steady-state conditions. It was concluded that the Nusselt solution without any improvements could not predict satisfactorily the film flow.

Girard and Chang [29] followed the Nusselt approach to solve the reflux condensation of turbulent pure steam in a vertical tube. Their assumptions were the same as Seban and Hodgson, except they solved the energy equation for the liquid region and assumed same pressure in both phases that was only a function of axial position. In addition, constant physical properties and constant heat flux at the wall were assumed. Also, the interfacial friction factor was calculated from the Baharathan-Wallis correlation [40]. Girard and Chang performed a linearised stability analysis of film-wise condensation to compute the steam mass flow rate that causes flooding and compared global parameters from their numerical results with experimental data.

Chou and Chen [41] studied turbulent pure vapour reflux condensation in a single vertical tube with both constant heat flux and constant temperature boundary conditions at the inner wall of the tube. They developed an analytical model using the simple laminar form of the boundary layer equations in the liquid region and correlations for the interfacial friction factor. However, they did not clearly state the correlations used for the friction factor and also the relation between the liquid pressure and that factor. They used the velocity profile obtained from the momentum equations to determine the temperature profile. A combination of the heat and mass interfacial jump conditions provided them with a differential equation for the film thickness. This equation could not be integrated analytically. Thus, a fourth-order Runge-Kutta scheme was used to do the integration numerically. They concluded that the interfacial shear stress retards the liquid flow and thickens the film layer and decreases the condensation heat transfer coefficient.

Chou and Chen [42] extended their own work to a general case for convective heat transfer from external tube surface to an isothermal fluid environment with a uniform heat transfer coefficient and constant temperature. Compared to their previous work, there was just a change in the boundary conditions at the inner wall.

Pan [43] focused on the influence of interfacial shear on pure vapour condensation in vertical tubes for turbulent flows. Pan investigated both the co-current and counter-current condensation. He used these simplifications: negligible curvature effect, governing equations of boundary layer type for a vertical plate, laminar liquid film, negligible inertia terms in the momentum equations, linear temperature in the film and constant properties. In addition, uniform constant temperature equal to the saturation temperature was assumed for the vapour region, it was assumed that all the vapour condenses at the end of the domain, and constant uniform velocity was calculated for the vapour based on the inlet mass flow rate. Pan applied available correlations for the shear stress at the interface and presented the axial variation of the Nusselt number for water and methanol. The proposed analytical model suggested that the effect of interfacial shear depends on the mass transfer and vapour velocity.

Fiedler and Auracher [32] worked on the effect of inclination angle on the flooding point, as well as on the heat transfer coefficient during reflux condensation of turbulent pure vapour R134-a in tubes. They tried to find the optimum angle at which the highest flooding vapour velocity occurs. To develop a model, they simplified the equations using the following assumptions: pure saturated vapour, smooth laminar condensate film, constant saturation temperature on the interface (neglecting the pressure drop in the vapour), constant temperature at the inner wall of the tube, and constant physical properties. In addition, the curvature of the tube wall and convective heat transfer in the condensate were neglected. They obtained the velocity profile of the condensate by solving the momentum equations considering the tube inclination angle. Using the velocity profiles, the mass flow rate was calculated and with the help of the assumption of only heat conduction across the conden-

sate, the governing equation for the film thickness was obtained. Flooding data and Nusselt number, as well as the film thickness for different inclination angles were presented.

Liao *et al.* [44] developed a heat and mass transfer analogy model for local heat transfer in reflux condensation of flowing vapour and non-condensable gases and compared the theoretical heat transfer with experiments. In their work, a liquid film model was derived from the two-phase integral momentum equation under counter-current flow conditions. However, the inertial force terms in the momentum equation were neglected. In addition, it was assumed that the temperature profile was linear in the liquid region and longitudinal pressure gradient was equal in the gas and liquid regions. They calculated δ based on Reynolds of the film and parabolic liquid velocity profile that was obtained from the solution of the momentum equation in the liquid region. For the gas phase, they used the heat and mass transfer analogy approach employing a diffusion layer model for turbulent flows by Liao and Vierow [45] and applied a correlation to evaluate the friction factor at the interface for counter-current flow. An iterative marching scheme was used based on the assumption of an initial value for outlet vapour mass flow rate and interface temperature. Liao *et al.* predicted the heat transfer coefficients along the tube for a wide variety of turbulent reflux condensation conditions. Furthermore, they compared co-current and counter-current condensation and showed that the local condensate film behaviour should be treated differently between these two cases. They proposed that the condensate hydrodynamics are coupled to the gas motion and vapour condensation.

Lakehal *et al.* [46] developed a numerical model for horizontal condensing counter-current stratified turbulent flows. The main intention of their study was to achieve better understanding of turbulent transport at sheared deformable interfaces in the presence of condensation. They assumed a two phase flow of steam and water liquid in a channel which was inclined by one degree from the horizontal position. The pressure gradients were kept constant, and to satisfy an overall mass balance, free slip boundary conditions were assumed for the top and bottom boundaries of the channel. Therefore, the condensing mass flux at

the interface was re-injected at the top of the vapour domain and removed from the bottom of the liquid domain. In other words, the numerical domain had no walls. Lakehal *et al.* applied DNS and solved the full set of mass, momentum and energy conservation equations separately in each phase and then coupled the solutions at the interface by using the force, mass and energy balances on the interface. The interface was captured using a boundary fitting method. They studied the effects of interfacial stresses and deformation, as well as condensation on the heat transfer coefficients in both phases.

Utanohara and Murase [4] used the commercial CFD code Fluent to analyse the behaviour of the turbulent non-condensable gases in the pressurizer of a water reactor in a nuclear power plant after the initiation of reflux cooling. They investigated the possibility of migration of non-condensable gases through the surge line to the hot leg. They modelled the pressurizer and simplified forms of the surge line and hot leg to determine if air flowed from the pressurizer through the surge line to the hot leg. Later, Utanohara *et al.* [47] simulated the turbulent counter-current gas-liquid flows in a pressurized water reactor hot leg, again using Fluent. They compared the results with the data obtained from the 1/15 scale circular channel test. In the Fluent model, a first order upwind scheme, structured mesh, and the SIMPLE algorithm were used. Utanohara *et al.* did the 3D transient simulation under turbulent mixture flow conditions with the application of interfacial drag correlations and presented the flow patterns for different conditions inside the hot leg. Energy conservation equation was not considered in their research and they used the condensate mass flow rate given in experimental data.

A summary of the review of previous theoretical works on reflux condensation is given in Table 1.2.

Table 1.2: Review of theoretical works on reflux condensation in vertical tube

	Reference	P-M[a]	2D-3D	Liquid Eqs.[b]	Mixture Eqs.[b]	Interfacial Shear[c]	Interface Location[d]
1	Seban and Hodgson [39]	P	2D	BL	—	C	DE
2	Chen *et al.* [28]	P	2D	BL	—	C	DE
3	Girard and Chang [29]	P	2D	BL	—	C	DE
4	Chou and Chen [41]	P	2D	BL	—	C	DE
5	Pan [43]	P	2D	BL	—	C	DE
6	Fiedler and Auracher [32]	P	2D	BL	—	C	DE
7	Lakehal *et al.* [46][e]	P	3D	CM	CM	B	BF
8	Liao *et al.* [44]	M	2D	BL	—	C	DE
9	Utanohara *et al.* [47][f]	M[g]	3D	CM	CM	C	VOF

[a]P: Pure Vapour, M: Gas-Vapour Mixture
[b]BL: Boundary Layer Eqs., CM: Continuity and Momentum Eqs.
[c]C: Correlation, B: Balance Eqs.
[d]DE: Differential Eq., BF: Boundary Fitted technique, VOF: Volume of Fluid technique
[e]Lakehal *et al.* studied the condensation in a horizontal channel
[f]Utanohara-Y *et al.* modelled the counter-current gas-liquid flow without condensation
[g]Considered mixture was air without steam

1.5.3 Interface Moving Strategy

The Interface

The interface is a surface that separates two immiscible fluids or two fluid phases. At the interface, flow fields have to be coupled appropriately by applying certain conditions that relate the variables in each side of the interface.

In gas-liquid fluid flows that involve moving boundaries such as stratified or condensing flows, the location of the interface that separates two phases must be part of the solution. The calculations can be performed on either fixed or moving meshes. For the moving mesh, interface could be moved as part of the solution, or it could be moved after a computation on a fixed mesh.

When using the parabolic set of equations, it is possible to march through the domain and obtain the interface location at each station along the axial direction. Applying elliptic set of equations couples the interface position to all other unknowns and makes the numerical simulation more challenging. Reflux condensation cannot be modelled by the parabolic set of equations and marching scheme. Therefore, a new approach is needed to track the interface.

Interface modelling techniques can be viewed as either a capturing technique or a tracking technique. Capturing techniques usually use an artificial scalar field for an implicit description of the interface location. A well-known approach from this group is the volume of fluid (VOF) method. Tracking techniques locate the interface explicitly by the computational mesh. Therefore, the movement of the interface is considered by adjusting the position of the nodes on the interface. The movement of the interface nodes could be prescribed by one of the physical equations or the velocity field. The tracking methods have good accuracy while they are not applicable to problems with severe interface motion.

Existing Interface Numerical Modelling Approaches

In general, the existing algorithms can be divided into the following categories [48]: Eulerian methods, Lagrangian methods, Mixed Eulerian-Lagrangian methods

For the Eulerian methods, the coordinate system is stationary or moving with a specific velocity which necessarily does not have any relation with the fluid velocity. Most Eulerian methods use fixed grids. Thus, they are not able to track the interface. MAC methods [49], and VOF methods [50] are two well-known methods in this category. Although Eulerian methods, generally are capturing (not tracking) methods, there are some adaptive (moving) grid methods which alter the computational grid so that the interface always coincides with one of the grid lines [51]. These methods are not applicable to the problems with large domain deformation.

For the Lagrangian methods, the coordinate system moves with the same velocity as the fluid. Therefore, each computational cell always contains the same fluid elements. The main

issue with these methods is mesh folding. Also, numerical inaccuracy may happen due to irregular meshes that can appear during the solution process. There have been many attempts to avoid the mentioned drawbacks, such as remeshing and rezoning. The Lagrangian methods that use rezoning are called Arbitrary-Lagrangian-Eulerian (ALE) methods [52].

Mixed Eulerian-Lagrangian methods are suitable for the class of problems that some part of the domain should be seen in a Lagrangian way, while the other parts are better suited for Eulerian calculations. There are some authors that put ALE methods under this category. The mixed techniques usually are able to combine the advantages of both Eulerian and Lagrangian methods. To track the interface sharply, adaptive Eulerian-Lagrangian or mixed methods have reasonable performance [53].

1.6 Contributions of the Present Work

1.6.1 Co-Current Condensation

As discussed in section 1.5.1, all the numerical works used the parabolic set of equations and marching scheme to solve the problem. Also, they all have assumptions for the approximation of the pressure gradient. These approaches are not able to handle problems with high condensation rate that have reverse flow in the mixture.

The present work solves the fully-coupled, elliptic two-dimensional set of equations on a structured non-orthogonal grid including calculation of the entire pressure field. Solving the whole domain provides the capability of capturing reverse flow for the cases with high condensation rate. This will be discussed later in section 5.

1.6.2 Reflux Condensation

To the best of the author's knowledge, no correlation or theoretical model has been able to consistently predict available experimental data for reflux condensation in a vertical tube. As mentioned earlier, researchers compared their models and correlations with very limited ranges of experimental conditions.

Although a few of the previous theoretical works used numerical methods to solve the equations, all but two of them did not solve the full set of equations for both phases. The two exceptions are an in-house code for horizontal stratified flow [46] and applying a commercial software for the simulation of a hot leg in a nuclear power plant steam generator [47]. Therefore, the theoretical works could be categorized as:

- General models [28, 29, 32, 39, 41, 43, 44]
- Detailed models [46, 47]

As seen in Table 1.2, most of the theoretical works modelled only pure vapour and did not consider gas. Liao *et al.* [44] considered a steam-air mixture, but they did not solve the governing equations in the gas phase. Utanohara *et al.* [47] also studied the gas effect, but they did not consider condensation, conservation of energy, and gas mass fraction.

In addition, beside Lakehal *et al.* [46], none of the mentioned references applied precise normal and tangential force balances on the interface and they used a variety of correlations to approximate the interfacial shear stress. Furthermore, the work of Lakehal *et al.* was applied to a horizontal counter-current flow without considering non-condensable gas and also they used a periodic boundary conditions at the outer boundaries of the domain.

Regarding the interface shape and location, among the detailed models, Lakehal *et al.* [46] and Utanohara *et al.* [47] applied a boundary-fitted method and a volume of fluid (VOF) method, respectively. These are interface capturing techniques and they do not track the interface sharply.

Moreover, all the previous theoretical works applied constant thermophysical properties for both phases.

The present work develops and applies a detailed numerical model of two-phase filmwise laminar reflux condensation of gas-vapour mixture in a vertical tube. A model solves numerically a fully coupled elliptic set of governing partial differential equations for both phases including fundamental force, mass and energy balances equations at the phase interface. An Eulerian approach is used for the solution of the field variables, followed by a mesh movement that tracks the interface exactly. The effect of non-condensable gas and interfacial shear is included fundamentally. In addition, the physical properties are calculated based on temperature, pressure and gas mass fraction for the whole domain.

This new, detailed model has the following advantages over the existing models:

- solution of the governing equations in both phases (liquid and gas)
- consideration of the gas-vapour mixture (as the gas phase)
- application of the variable thermophysical properties of the fluids
- application of the appropriate tangential force, normal force, mass, and energy balances on the interface
- sharp tracking of the interface location
- coupled solution of all the governing equations

1.7 Layout of the Thesis

Because the main focus of this work is on reflux condensation in tubes, the main body presentation of the modelling uses cylindrical coordinates. Studies were also performed on

parallel plate geometries, so, for completeness, Cartesian coordinate details are provided in an Appendix. The remainder of the thesis is arranged as follows:

Chapter 2 presents the mathematical model including the governing equations in both gas and liquid phases along with all the equations at the interface. The interface moving strategy is explained. The boundary conditions are described in detail in this chapter.

Chapter 3 presents the discretisation of the domain and grid generation. The basic nomenclature of the grid system is also illustrated.

Chapter 4 presents the numerical solution method. In this chapter, discretisation of the governing equations is described. There is a detailed discussion of the each term in the set of equations, as well as the boundary conditions implementation.

Chapter 5 presents the results for the laminar co-current film condensation in parallel-plate channels. This chapter includes the validation results and also new results for the cases that previous numerical approaches are not able to solve.

Chapter 6 presents detailed results for the laminar reflux condensation from steam-air mixtures flowing in vertical parallel-plate channels. The results include velocity and gas mass fraction profiles, as well as axial variation of film thickness.

Chapter 7 presents the results for the co-current condensation in tubes. This chapter includes the validation results and also new results for the cases with diferent Reynolds numbers, inlet-to-wall temperature differences, and inlet gas mass fractions.

Chapter 8 presents the results for the laminar reflux condensation from steam-air mixtures flowing in vertical tubes. This chapter includes the validation results, as well as the paramteric study.

Chapter 9 provides a summary of the main results in this work and presents the significant conclusions.

Chapter 2

Mathematical Model

2.1 Governing Equations

The governing equations are written for conservation of mass, momentum, and energy of two-dimensional Newtonian fluid flow. It has been assumed that the flow is laminar and incompressible with negligible viscous dissipation and pressure work source terms in the energy equation. Radiation heat transfer is also neglected. The equations for conservation of mass, momentum, and energy are written for each phase separately and are connected using the liquid-mixture interface jump conditions. The governing equations are presented here in cylindrical coordinates. The U and V velocities are in the z and r directions, respectively (see Fig. 1.4). For the numerical analysis of flow in parallel-plate channels the Cartesian form of the equations is used as given in Appendix A.

2.1.1 Liquid Region

- Liquid continuity equation

$$\frac{\partial \rho_L}{\partial t} + \frac{\partial}{\partial z}\left(\rho_L U_L\right) + \frac{1}{r}\frac{\partial}{\partial r}\left(r\rho_L V_L\right) = 0 \tag{2.1}$$

- Liquid momentum equation in the z direction

$$\frac{\partial}{\partial t}\left(\rho_L U_L\right) + \frac{\partial}{\partial z}\left(\rho_L U_L U_L\right) + \frac{1}{r}\frac{\partial}{\partial r}\left(r\rho_L U_L V_L\right) = -\frac{\partial P_L}{\partial z} + \frac{1}{r}\frac{\partial}{\partial r}\left(\mu_L r\frac{\partial U_L}{\partial r}\right) + \frac{\partial}{\partial z}\left(\mu_L \frac{\partial U_L}{\partial z}\right) + \rho_L g \tag{2.2}$$

- Liquid momentum equation in the r direction

$$\frac{\partial}{\partial t}\left(\rho_L V_L\right) + \frac{\partial}{\partial z}\left(\rho_L U_L V_L\right) + \frac{1}{r}\frac{\partial}{\partial r}\left(r\rho_L V_L V_L\right) = -\frac{\partial P_L}{\partial r} + \frac{\partial}{\partial r}\left(\frac{\mu_L}{r}\frac{\partial}{\partial r}\left(rV_L\right)\right) + \frac{\partial}{\partial z}\left(\mu_L \frac{\partial V_L}{\partial z}\right) \tag{2.3}$$

- Liquid energy equation

$$\frac{\partial}{\partial t}\left(\rho_L C_{p,L} T_L\right)+\frac{\partial}{\partial z}\left(\rho_L U_L C_{p,L} T_L\right)+\frac{1}{r}\frac{\partial}{\partial r}\left(r\rho_L V_L C_{p,L} T_L\right)=\frac{1}{r}\frac{\partial}{\partial r}\left(rk_L\frac{\partial T_L}{\partial r}\right)+\frac{\partial}{\partial z}\left(k_L\frac{\partial T_L}{\partial z}\right) \tag{2.4}$$

2.1.2 Mixture Region

- Mixture continuity equation

$$\frac{\partial \rho_M}{\partial t}+\frac{\partial}{\partial z}\left(\rho_M U_M\right)+\frac{1}{r}\frac{\partial}{\partial r}\left(r\rho_M V_M\right)=0 \tag{2.5}$$

- Mixture momentum equation in the z direction

$$\frac{\partial}{\partial t}\left(\rho_M U_M\right)+\frac{\partial}{\partial z}\left(\rho_M U_M U_M\right)+\frac{1}{r}\frac{\partial}{\partial r}\left(r\rho_M U_M V_M\right)=-\frac{\partial P_M}{\partial z}+\frac{1}{r}\frac{\partial}{\partial r}\left(\mu_M r\frac{\partial U_M}{\partial r}\right)+\frac{\partial}{\partial z}\left(\mu_M\frac{\partial U_M}{\partial z}\right)+\rho_M g \tag{2.6}$$

- Mixture momentum equation in the r direction

$$\frac{\partial}{\partial t}\left(\rho_M V_M\right)+\frac{\partial}{\partial z}\left(\rho_M U_M V_M\right)+\frac{1}{r}\frac{\partial}{\partial r}\left(r\rho V_M V_M\right)=-\frac{\partial P_M}{\partial r}+\frac{\partial}{\partial r}\left(\frac{\mu_M}{r}\frac{\partial}{\partial r}\left(rV_M\right)\right)+\frac{\partial}{\partial z}\left(\mu_M\frac{\partial V_M}{\partial z}\right) \tag{2.7}$$

- Mixture energy equation

$$\frac{\partial}{\partial t}\left(\rho_M C_{p,M} T_M\right)+\frac{\partial}{\partial z}\left(\rho_M U_M C_{p,M} T_M\right)+\frac{1}{r}\frac{\partial}{\partial r}\left(r\rho_M V_M C_{p,M} T_M\right)=\frac{1}{r}\frac{\partial}{\partial r}\left(rk_M\frac{\partial T_M}{\partial r}\right)+\frac{\partial}{\partial z}\left(k_M\frac{\partial T_M}{\partial z}\right)+\frac{1}{r}\frac{\partial}{\partial r}\left(r\rho_M D^{12}(C_{p,g}-C_{p,v})\frac{\partial W}{\partial r}T_M\right)+\frac{\partial}{\partial z}\left(\rho_M D^{12}(C_{p,g}-C_{p,v})\frac{\partial W}{\partial z}T_M\right) \tag{2.8}$$

- Mass conservation equation for the gas

$$\frac{\partial}{\partial t}\left(\rho_M W\right)+\frac{\partial}{\partial z}\left(\rho_M U_M W\right)+\frac{1}{r}\frac{\partial}{\partial r}\left(r\rho_M V_M W\right)=\frac{1}{r}\frac{\partial}{\partial r}\left(r\rho_M D^{12}\frac{\partial W}{\partial r}\right)+\frac{\partial}{\partial z}\left(\rho_M D^{12}\frac{\partial W}{\partial z}\right) \tag{2.9}$$

2.2 Interface Conditions

The conditions used to connect the two phases are referred to as the jump conditions. The aim of these conditions is to ensure force and mass balances across the interface. In the present work, for the energy balance and gas impermeability, extra conditions are needed to close the problem.

The interface conditions are:

- Normal force balance

$$\left[(\hat{n}\cdot\boldsymbol{\tau})\cdot\hat{n}\right]_{iL} + \sigma K = -\left[(\hat{n}\cdot\boldsymbol{\tau})\cdot\hat{n}\right]_{iM} \tag{2.10}$$

- Tangential force balance

$$\left[(\hat{n}\cdot\boldsymbol{\tau})\cdot\hat{s}\right]_{iL} - \frac{\partial\sigma}{\partial s} = \left[(\hat{n}\cdot\boldsymbol{\tau})\cdot\hat{s}\right]_{iM} \tag{2.11}$$

  where, $\boldsymbol{\tau}$ is the stress tensor, $\hat{n}$ is the local normal unit vector to the interface, σ is the surface tension and K is the curvature of the interface. In addition, $\hat{s}$ is the local tangential unit vector to the interface and the stress tensor components are:

$$\begin{aligned}
\tau_{zz} &= -P + 2\mu\frac{\partial U}{\partial z} \\
\tau_{zr} &= \mu\left(\frac{\partial U}{\partial r} + \frac{\partial V}{\partial z}\right) \\
\tau_{rr} &= -P + 2\mu\frac{\partial V}{\partial r}
\end{aligned} \tag{2.12}$$

- Mass balance across the interface-1

$$\dot{m}_{iL} = \dot{m}_{iM} \tag{2.13}$$

- Mass balance across the interface-2

$$\dot{m}_{iL} = \dot{m}_{\text{cond}} \tag{2.14}$$

where

$$\dot{m}_{\text{cond}} = \frac{A_{iL}}{h_{fg}} \left(-k_{iL} \frac{\partial T_L}{\partial n}\bigg|_{iL} + k_{iM} \frac{\partial T_M}{\partial n}\bigg|_{iM} \right) \tag{2.15}$$

- Continuity of tangential velocity

$$\overrightarrow{(V_t)}_{iL} = \overrightarrow{(V_t)}_{iM} \tag{2.16}$$

The notation of 'iL' and 'iM' refer to interface values in the liquid and the mixture, respectively.

- Prevailing saturation condition

$$T_{iL} = T_{iM} = T_{\text{sat}} \tag{2.17}$$

where, T_{sat} is a vapour-specific function of the partial pressure of the vapour ($P_{v,iM}$).

The partial pressure of the vapour at the interface depends on the gas mass fraction at the interface and the mixture pressure. The relation is given in Eq. (2.18).

$$P_{v,iM} = P_{iM} \left[\frac{(1 - W_{iM})\, M_g}{M_g + W_{iM}\,(M_v - M_g)} \right] \tag{2.18}$$

- Impermeability to gas at the interface

$$\dot{m}_{iM} W_{iM} - (\rho D^{12})_{iM} A_{iM} \frac{\partial W}{\partial n}\bigg|_{iM} = 0 \tag{2.19}$$

where, A_{iM} is the local interfacial area.

- A final closure condition for pressure in the mixture at the interface

$$\frac{\partial P}{\partial n}\bigg|_{iM} = 0 \tag{2.20}$$

An explanation of the necessity of using Eq. (2.20) will be discussed later with respect to the algebraic equations at the interface as part of the numerical solution method discussion.

2.3 Domain and Boundary Condition Definitions

Definition of the appropriate boundary conditions for detailed numerical simulation of reflux condensation in a vertical tube is a challenging process. These conditions should be prescribed to be able to model realistic applications. However, due to the complexity of imposing actual boundary conditions for reflux condensation, the model should be developed based on physical boundary conditions that are feasible and can emulate the experimental conditions. For instance, as mentioned before, Lakehal *et al.* applied a constant pressure gradient and periodic boundary conditions at the outer boundaries in order to conserve the global mass.

As discussed in Section 1.4, the domain has three sections. The middle section is the main reflux condensation section. The top and bottom sections are added to ensure the correct application of inlet and outlet boundary conditions. Figure 2.1 shows the domain and boundary conditions.

Fully developed flow conditions, as shown in Eqs. (2.21) and (2.22), are applied to the liquid and mixture outflow velocities.

$$\frac{\partial U_{_M}}{\partial z} = \frac{\partial V_{_M}}{\partial z} = \frac{\partial T_{_M}}{\partial z} = \frac{\partial W}{\partial z} = 0 \tag{2.21}$$

$$\frac{\partial U_{_L}}{\partial z} = \frac{\partial V_{_L}}{\partial z} = \frac{\partial T_{_L}}{\partial z} = 0 \tag{2.22}$$

Application of the fully developed boundary conditions at the outlet (top) could allow flow out of the domain or into the domain if insufficient mass is supplied at the inlet (bottom) compared to the condensation rate. Symmetry boundary conditions are applied at the centre-line of the tube. No slip boundary conditions are prescribed at the wall. The wall temperature could be defined as a function of z in the cooled section (L_2). Adiabatic conditions are applied at the wall in sections L_1 and L_3.

As shown in Fig. 2.1, at the tube inlet, part of the mixture flows out (downward) while the other part flows in (upward). This means that the mixture flow is divided in two regions

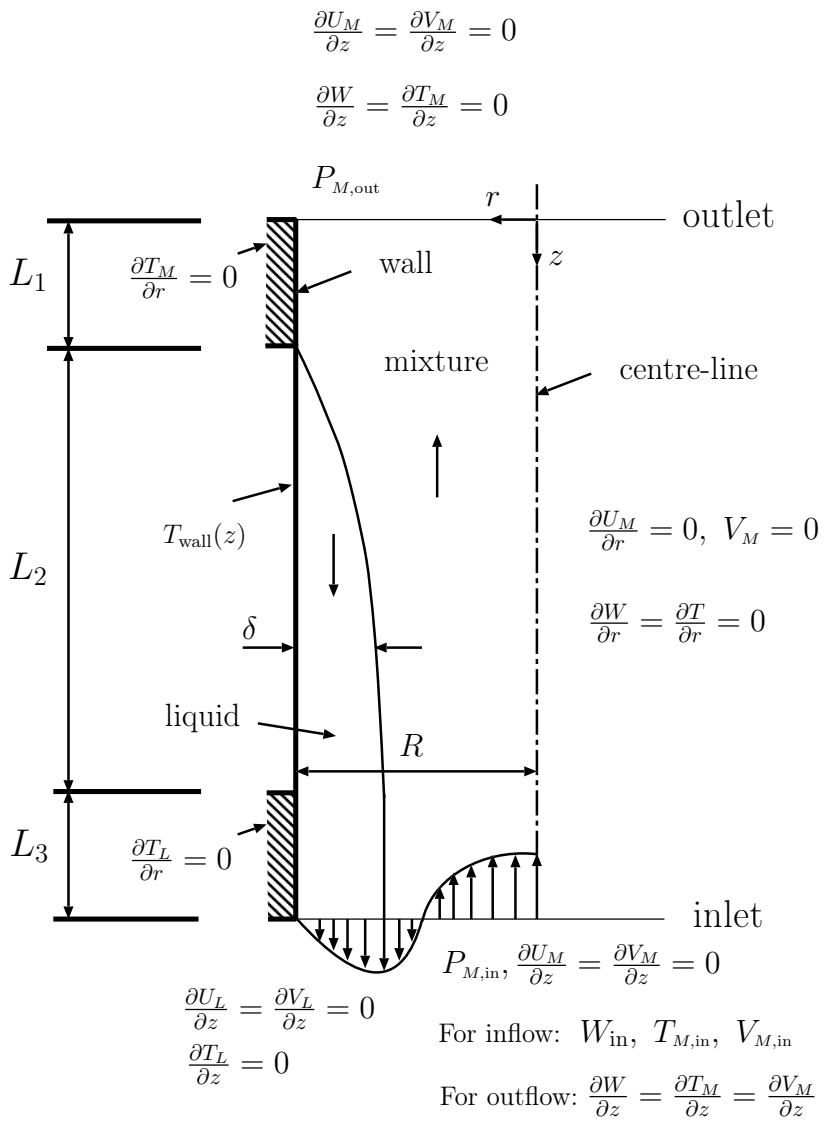

Figure 2.1: Boundary conditions for the simulation of reflux condensation in a vertical tube

by the point at where the mixture velocity is zero: an outflow region and an inflow region. Note that the location of zero velocity (referred to hereafter as the "break-point") is part of the solution and is not known from the beginning. Therefore, dynamic boundary conditions should be applied for the mixture region at the inlet of the tube. This makes the numerical solution more complicated because the boundary conditions can change in each iteration, depending on the flow direction resulting from the solution of the governing equations.

As mentioned before, for the outflow region, fully developed boundary conditions are applied. For the inflow region in the mixture, Dirichlet boundary conditions are imposed for gas mass fraction and temperature and their values are specified. For this region, the velocity profiles are part of the solution and can not be used as boundary conditions. The main intention of adding the bottom section to the cooled section was to overcome this complication. Fully developed boundary conditions are used for the inlet velocities and pressure is defined as a controlling parameter of the inlet mass flow rate.

2.4 Problem Parameters

The problem being modelled is prescribed by specifying the model independent parameters. Those independent parameters define the geometry, the boundary conditions, and the auxiliary relations needed to calculate the thermophysical and transport properties of the two-phases. Once the problem is specified, the solution of the mathematical model will produce the dependent variables: the fields of U, V, P, T, and W, and the location of the phase interface.

Once the geometry, the properties, and the outlet boundary conditions are prescribed, the present model for reflux condensation in a vertical tube is completed by specifying a further five independent parameters: (1) the inlet V velocity profile, (2) the inlet gas mass fraction W_{in} (3), the reference absolute pressure, P_{ref}, (4) the inlet-to-wall temperature difference, ΔT, and (5) the inlet relative pressure, P_{in}. The inlet U profile is part of the solution.

Assuming saturation conditions, the inlet temperature is determined from the inlet partial pressure of the vapour, which is determined from the inlet pressure and the inlet gas mass fraction. The wall temperature is then found from ΔT.

For a given set of the five independent parameters listed above, there is no guarantee that a viable solution may be obtained. In this work, an acceptable solution must have an

inlet Reynolds number in the laminar regime (less than or equal to 2300), a flow of mixture exiting at the top of the tube, and a non-oscillatory steady-state solution. The next section describes how the inlet relative pressure specification is related to these problem constraints.

2.5 Role of the Inlet Relative Pressure

The overall pressure difference should be specified very carefully. Here are the important considerations related to the process of assigning the inlet relative pressure value:

- **Inlet Reynolds number**: The inlet relative pressure should be defined in a way that keeps the inlet flow in the laminar regime. The inlet relative pressure should be specified high enough to drive sufficient flow but not so high that the inlet Reynolds number exceeds 2300.
- **Downward flow at the outlet**: The inlet relative pressure should be high enough so that there is sufficient mass at the inlet to supply the condensation rate and to have flow out (upward) at the outlet. The condensation rate is a function of inlet-to-wall temperature difference, inlet gas mass fraction and inlet mass flow rate. For the cases with high condensation rates (*e.g.*, low inlet gas mass fraction and/or high inlet-to-wall temperature difference), specifying an inlet relative pressure that is too low results in bringing mass from the outlet.
- **Liquid hold-up and instabilities**: High inlet Reynolds number of the mixture in conjunction with high gas mass fraction and/or low inlet-to-wall temperature difference can lead to liquid hold-up or instabilities in the liquid region. This happens due to the existence of an extremely thin film and/or high mixture velocity at the interface.

Considering all these crucial factors would help to prescribe a proper inlet relative pressure. However, what value to specify is not clear from the beginning. The solution is an

iterative process during which the break point and interface location as well as the variable fields change. The interface velocity, inlet Reynolds number and outlet velocity should be monitored during the iterative solution and the inlet relative pressure value must be altered according to the behaviour of these parameters. There can easily be a combination of problem parameters that will not yield a solution because the inlet Reynolds number is to high or there is liquid film instability.

2.6 Interface Moving Strategy

Reflux condensation is a moving boundary problem and the location of the interface that is separating two phases must be part of a detailed solution. Often in these simulations, the calculations are performed on fixed meshes. At the end of each time step, the location of the interface should be corrected. The approach that is implemented to modify the interface location is called ILMB method and is described here.

2.6.1 Integral Liquid Mass Balance (ILMB)

This method is based on the mass balance at each column of the liquid region. The interface location is calculated by imposing the mass balance at the end of each time step and for all columns of liquid such as the typical one shown in Fig. 2.2.

The mass balance equation in the cylindrical coordinate is written as:

$$\int_{\delta_e}^{R} \rho_L U_e \, r \, dr = \int_{\delta_w}^{R} \rho_L U_w \, r \, dr + \frac{\dot{m}_{\text{cond}}}{2\pi} \tag{2.23}$$

where δ_w and δ_e are the film thickness on the west and east sides of a particular column of control volumes in the liquid phase. Equation (2.23) states that the total mass flow rate that crosses the control volumes through the west faces and the condensate mass flow rate crossing the interface must be equal to the total mass flow rate that leaves the column from

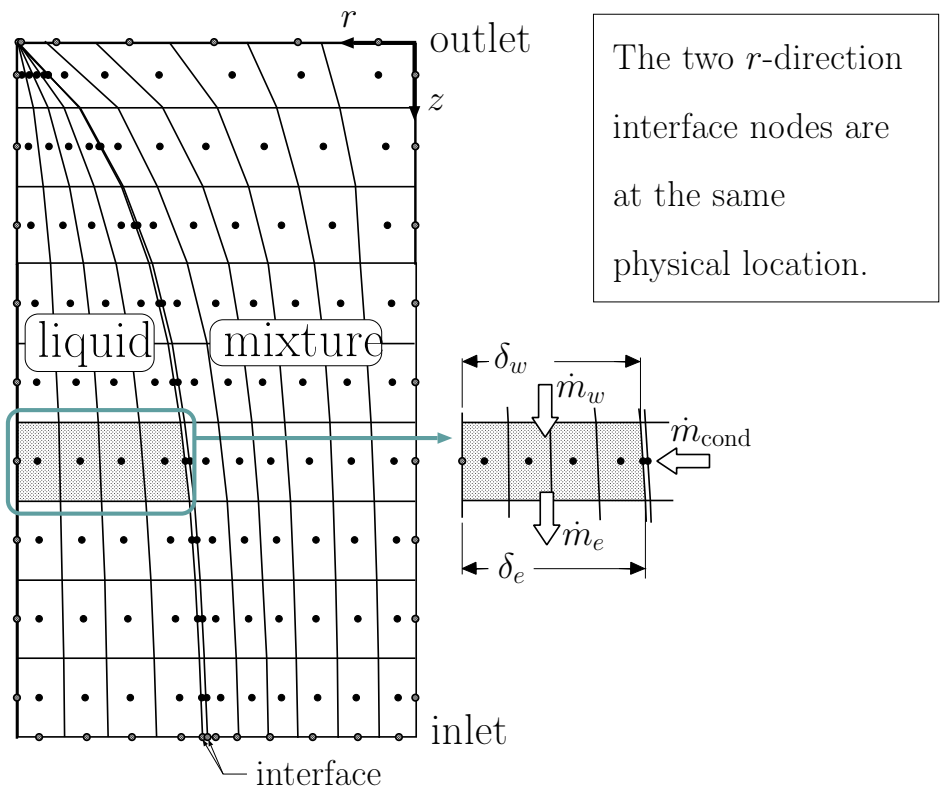

Figure 2.2: Grid formation and liquid region used in the ILMB method; the spacing between the nodes at the interface is exaggerated for illustration purposes.

the east faces. Equation (2.23) therefore leads to a connection between δ_w and δ_e and can be applied, starting at the inlet, to determine the film thickness all along the domain. For the cases that do not have liquid film at the beginning of the numerical simulation, δ_{in} is set in the range of 1×10^{-9} m to 1×10^{-7} m. For the problems without mass crossing the interface, $\dot{m}_{\text{cond}}$ should be set to zero. The details of the grid are described in Section 3 and further details about discretised form of the ILMB equation are presented in Section 4.6.

Chapter 3

Discretisation of the Domain

3.1 Introduction

A structured, non-orthogonal grid is used to discretise the domain. The grid generation uses transfinite interpolation and permits splitting the domain into different panels in the coordinate directions, as described in [54]. In this work, the computational domain has two separate regions: liquid and mixture. These regions are separated by a smooth interface. For the grid generation, each region is an independent panel. On the interface, there are two rows of nodes which form zero-width control volumes. In these two rows of interface nodes, the upper row represents the mixture side of the interface while the lower one represents the liquid side. As shown in Figure 3.1, $j_{\mathrm{B}L}$ to $j_{\mathrm{E}L}+1$ and $j_{\mathrm{B}M}-1$ to $j_{\mathrm{B}M}+1$ belongs to the liquid region and mixture region, respectively. The i and j indices reference each control volume in an organized fashion. The i index proceeds from i_{B} for the first interior control volume on the west side of the domain to i_{E} for the last interior control volume on the east, where $\mathtt{N}_z$ is the number of control volumes along the i index. Each control volume is made up of four quadrants, each referred to by geographical directions, northeast (NE), southeast (SE), northwest (NW), and southwest (SW). Along the j index, the liquid region has $\mathtt{N}_{r,L}$ interior control volumes and the mixture has $\mathtt{N}_{r,M}$ interior control volumes.

There are nodes in zero-width control volumes on the boundaries of the domain to implement the boundary conditions. These nodes are referenced by $i_{\mathrm{B}}-1$ on the west, $i_{\mathrm{E}}+1$ on the east, $j_{\mathrm{B}}-1$ on the south, and $j_{\mathrm{E}}+1$ on the north.

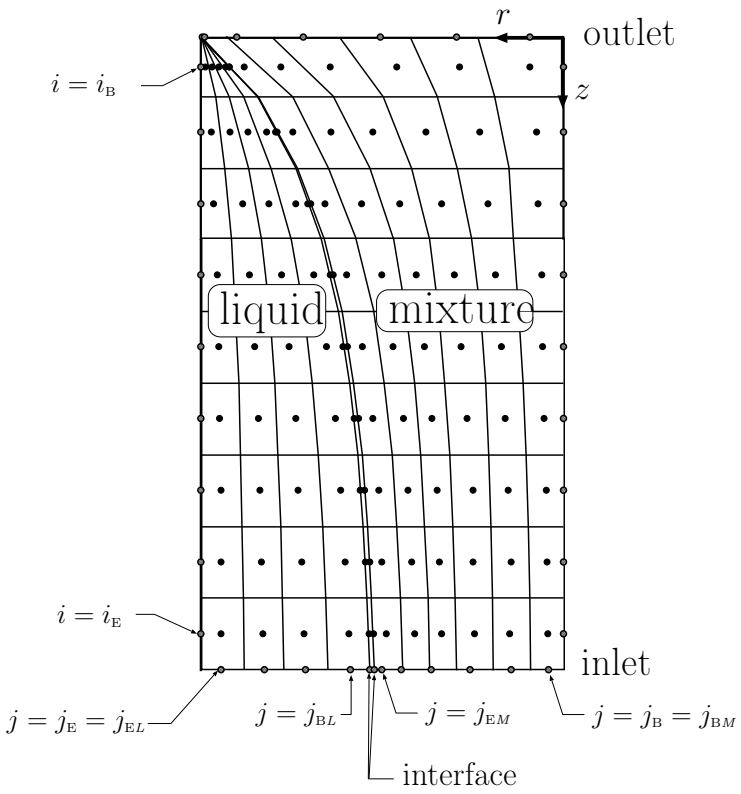

Figure 3.1: Grid formation in the liquid and mixture regions; the spacing between the nodes at the interface is exaggerated for illustration purposes.

3.2 Grid Nomenclature

The typical control volume and its eight neighbours on a structured grid are shown in Fig. 3.2. The quadrant notation used in a each control volume is shown in Fig. 3.3.

The locations of points where z and r coordinate values are stored are labeled in Fig. 3.4. The centre node, "P", is referenced as "southwest" and the top right corner as "northeast". The south points are referenced as the north points of the control volume to the south, for example $(\mathrm{ZNW}_{(i,j-1)}, \mathrm{RNW}_{(i,j-1)})$. The west points are referenced as the east points of the control volume to the west. The southwest corner is referenced as $(\mathrm{ZNE}_{(i-1,j-1)}, \mathrm{RNE}_{(i-1,j-1)})$.

The nomenclature for control volume distances, areas, and volumes is shown in Fig. 3.5.

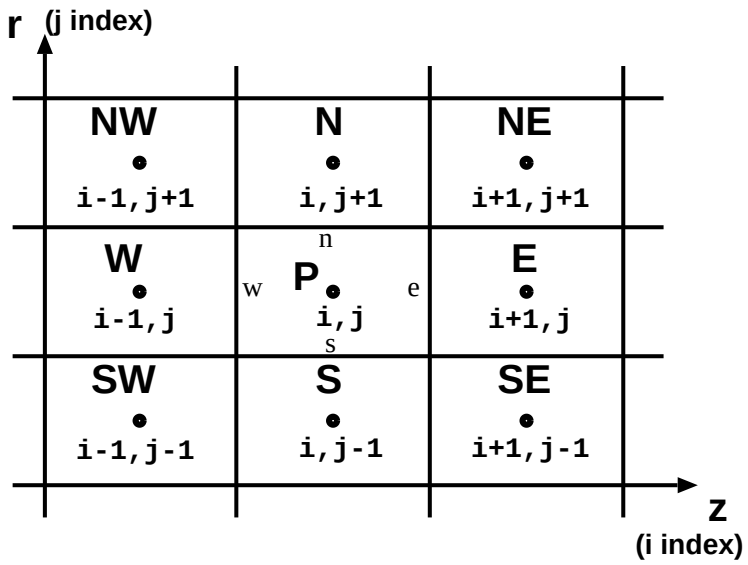

Figure 3.2: Indexing notation for neighbouring control volumes

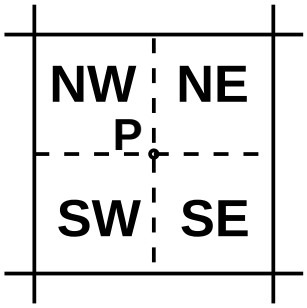

Figure 3.3: Quadrant notation for a control volume

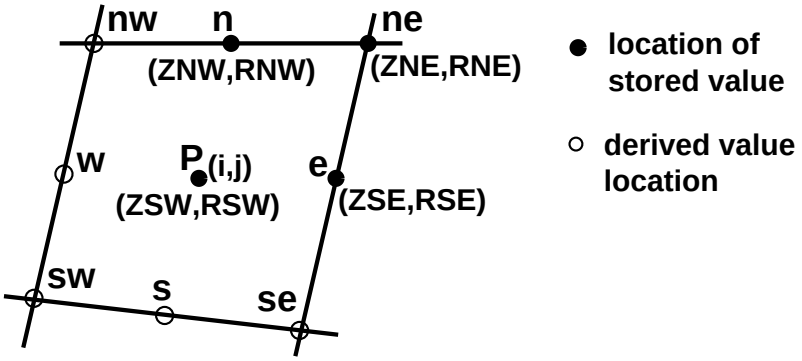

Figure 3.4: Locations of control volume points

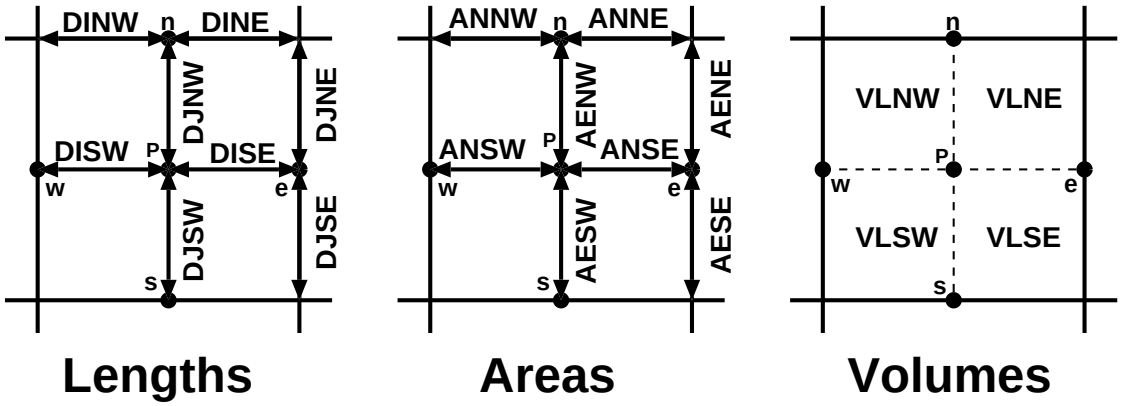

Figure 3.5: Nomenclature for lengths, areas, and volumes of a control volume

The distances are the length between points in the quadrilateral control volume. The quadrants are split into two triangles each. The volume of each triangle is calculated and then the two are added together to get the correct volume for each quadrant. A unit depth is used to compute areas and volumes.

The non-orthogonal grid needs some direction unit vectors and distances defined because the grid will not necessarily be aligned with the cylindrical coordinate directions. As shown in Fig. 3.6, there are separate direction vectors for each face and the central node of the main control volume. The $\hat{s}$ vectors point from west to east and the $\hat{t}$ vectors point from south to north. The vectors on the east face of the present node have subscript "e", and on the north face they have subscript"n". At an east face, the $\hat{t}$ vector is along the face. Likewise, on a north face, the $\hat{s}$ vector is along the face. The vectors on the west and south of the typical node are referenced by $i-1$ and $j-1$, respectively.

Since the grid is non-orthogonal, variables have been designated to illustrate the distance between locations. The location of the distance variables is shown in Fig. 3.7 for the non-orthogonal grid.

Equation (3.1) calculates the distance between a node and its neighbor to the east, along

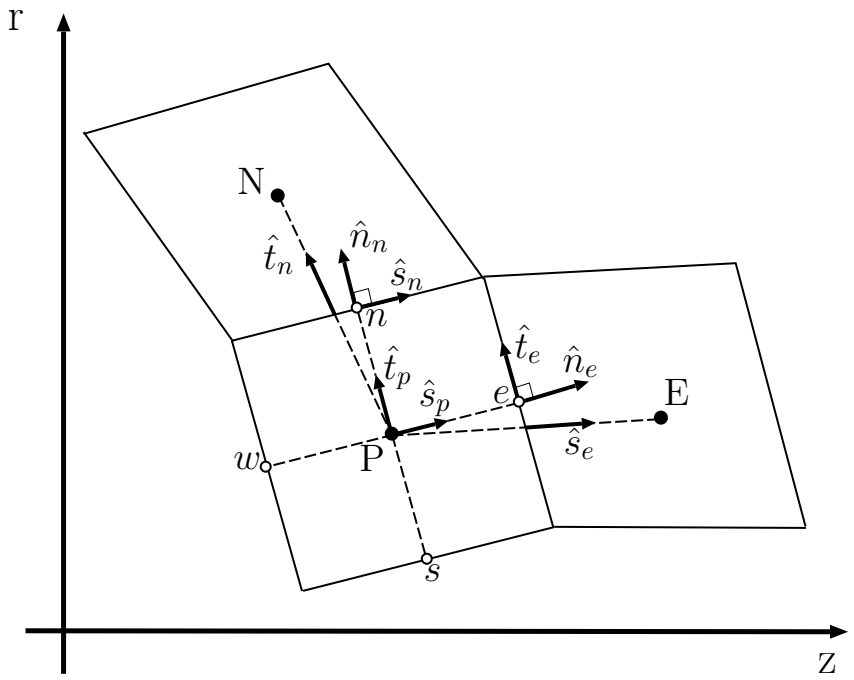

Figure 3.6: Grid direction vectors

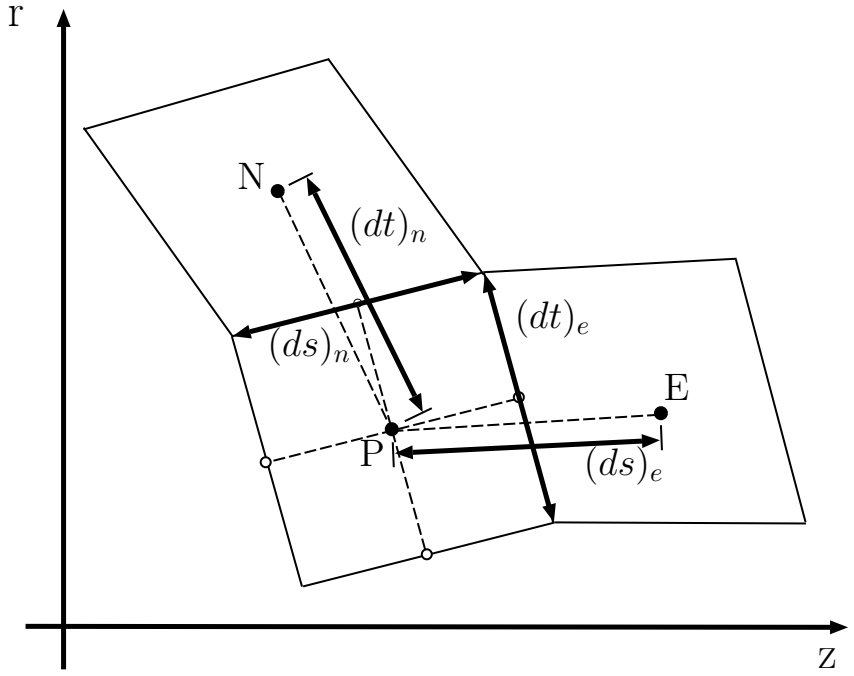

Figure 3.7: Locations of distance variables

the $\hat{s}_e$ vector.

$$(ds)_{e_{(i,j)}} = \sqrt{\left(\mathrm{ZSW}_{(i+1,j)} - \mathrm{ZSW}_{(i,j)}\right)^2 + \left(\mathrm{RSW}_{(i+1,j)} - \mathrm{RSW}_{(i,j)}\right)^2} \tag{3.1}$$

Similarly, the distance between a node and its neighbor to the north, along the $\hat{t}_n$ vector, can be calculated using:

$$(dt)_{n_{(i,j)}} = \sqrt{\left(\mathrm{ZSW}_{(i,j+1)} - \mathrm{ZSW}_{(i,j)}\right)^2 + \left(\mathrm{RSW}_{(i,j+1)} - \mathrm{RSW}_{(i,j)}\right)^2} \tag{3.2}$$

The distances $(ds)_n$ and $(dt)_e$ are defined as:

$$(ds)_{n_{(i,j)}} = \mathrm{DINW}_{(i,j)} + \mathrm{DINE}_{(i,j)} \tag{3.3}$$

and,

$$(dt)_{e_{(i,j)}} = \mathrm{DJSE}_{(i,j)} + \mathrm{DJNE}_{(i,j)} \tag{3.4}$$

The distances are always equal to the sum of grid quadrant distance variables even in the case of skewed grid.

The distances (ds) and (dt) are calculated for the nodal location $(ds)_p$ and $(dt)_p$. Also, equivalent equations to Eqs. (3.3) and (3.4) are used to evaluate the west face $(dt)_w$ and the south face $(ds)_s$. Comparably, Eqs. (3.1) and (3.2) are deployed in a similar manner to determine $(ds)_w$ and $(dt)_s$, respectively. West face and south face distances are not shown in Fig. 3.7.

The north normal unit vector, $\hat{n}_n$, and its equivalent with regard to arc lengths are determined using Eqs. (3.5) and (3.6), accordingly. Vector $\hat{n}_n$ is defined outward normal to the north face of a control volume.

$$\hat{n}_{n(i,j)} = \frac{-\left(\mathrm{RNE}_{(i,j)} - \mathrm{RNE}_{(i-1,j)}\right)}{\sqrt{\left(\mathrm{ZNE}_{(i,j)} - \mathrm{ZNE}_{(i-1,j)}\right)^2 + \left(\mathrm{RNE}_{(i,j)} - \mathrm{RNE}_{(i-1,j)}\right)^2}}\,\hat{\imath} + \frac{\left(\mathrm{ZNE}_{(i,j)} - \mathrm{ZNE}_{(i-1,j)}\right)}{\sqrt{\left(\mathrm{ZNE}_{(i,j)} - \mathrm{ZNE}_{(i-1,j)}\right)^2 + \left(\mathrm{RNE}_{(i,j)} - \mathrm{RNE}_{(i-1,j)}\right)^2}}\,\hat{\jmath} \tag{3.5}$$

$$\hat{n}_{n(i,j)} = \frac{-\left(\mathrm{RNE}_{(i,j)} - \mathrm{RNE}_{(i-1,j)}\right)}{(ds)_n}\,\hat{\imath} + \frac{\left(\mathrm{ZNE}_{(i,j)} - \mathrm{ZNE}_{(i-1,j)}\right)}{(ds)_n}\,\hat{\jmath} \tag{3.6}$$

The gradients are defined and evaluated at the north face and converted to normal unit vector notation as follows:

$$\hat{n}_{n(i,j)} = \left.\frac{\partial z}{\partial n}\right|_n \hat{\imath} + \left.\frac{\partial r}{\partial n}\right|_n \hat{\jmath} = n_{zn}\,\hat{\imath} + n_{rn}\,\hat{\jmath} \tag{3.7}$$

The same steps are repeated to define east normal unit vector,$\hat{n}_e$, its equivalent in terms of arc length, and its gradients which are evaluated at the east face and converted to normal unit vector notation. The equations are shown below. Same as the north normal unit vector, the east normal unit vector is specified to be outward normal to the east face of a control volume.

$$\hat{n}_{e(i,j)} = \frac{\left(\mathrm{RNE}_{(i,j)} - \mathrm{RNE}_{(i,j-1)}\right)}{\sqrt{\left(\mathrm{ZNE}_{(i,j)} - \mathrm{ZNE}_{(i,j-1)}\right)^2 + \left(\mathrm{RNE}_{(i,j)} - \mathrm{RNE}_{(i,j-1)}\right)^2}}\,\hat{\imath} + \frac{-\left(\mathrm{ZNE}_{(i,j)} - \mathrm{ZNE}_{(i,j-1)}\right)}{\sqrt{\left(\mathrm{ZNE}_{(i,j)} - \mathrm{ZNE}_{(i,j-1)}\right)^2 + \left(\mathrm{RNE}_{(i,j)} - \mathrm{RNE}_{(i,j-1)}\right)^2}}\,\hat{\jmath} \tag{3.8}$$

$$\hat{n}_{e(i,j)} = \frac{\left(\mathrm{RNE}_{(i,j)} - \mathrm{RNE}_{(i,j-1)}\right)}{(dt)_e}\,\hat{\imath} + \frac{-\left(\mathrm{ZNE}_{(i,j)} - \mathrm{ZNE}_{(i,j-1)}\right)}{(dt)_e}\,\hat{\jmath} \tag{3.9}$$

$$\hat{n}_{e(i,j)} = \left.\frac{\partial z}{\partial n}\right|_e \hat{\imath} + \left.\frac{\partial r}{\partial n}\right|_e \hat{\jmath} = n_{ze}\,\hat{\imath} + n_{re}\,\hat{\jmath} \tag{3.10}$$

The west to east geometric grid unit vector for the north face of a control volume, $\hat{s}_n$, and its equivalent with regard to arc lengths are determined as in Eqs. (3.11) and (3.12), respectively. The $\hat{s}_n$ vector is defined along the line between the northwest and northeast corners of a control volume.

$$\hat{s}_{n(i,j)} = \frac{\left(\mathrm{ZNE}_{(i,j)} - \mathrm{ZNE}_{(i-1,j)}\right)}{\sqrt{\left(\mathrm{ZNE}_{(i,j)} - \mathrm{ZNE}_{(i-1,j)}\right)^2 + \left(\mathrm{RNE}_{(i,j)} - \mathrm{RNE}_{(i-1,j)}\right)^2}}\,\hat{\imath} + \frac{\left(\mathrm{RNE}_{(i,j)} - \mathrm{RNE}_{(i-1,j)}\right)}{\sqrt{\left(\mathrm{ZNE}_{(i,j)} - \mathrm{ZNE}_{(i-1,j)}\right)^2 + \left(\mathrm{RNE}_{(i,j)} - \mathrm{RNE}_{(i-1,j)}\right)^2}}\,\hat{\jmath} \tag{3.11}$$

$$\hat{s}_{n(i,j)} = \frac{\left(\mathrm{ZNE}_{(i,j)} - \mathrm{ZNE}_{(i-1,j)}\right)}{(ds)_n}\,\hat{\imath} + \frac{\left(\mathrm{RNE}_{(i,j)} - \mathrm{RNE}_{(i-1,j)}\right)}{(ds)_n}\,\hat{\imath} \tag{3.12}$$

The gradients are defined and evaluated at the north face and converted to a west to east geometric grid unit vector notation as follows:

$$\hat{s}_{n(i,j)} = \left.\frac{\partial z}{\partial s}\right|_n \hat{\imath} + \left.\frac{\partial r}{\partial s}\right|_n \hat{\jmath} = s_{zn}\,\hat{\imath} + s_{rn}\,\hat{\jmath} \tag{3.13}$$

Equation (3.14) illustrates the west to east geometric grid unit vector calculation method for the east face of a control volume, $\hat{s}_e$. The vector is defined along the line between the present node and east node.

$$\hat{s}_{e(i,j)} = \frac{\left(\mathrm{ZSW}_{(i+1,j)} - \mathrm{ZSW}_{(i,j)}\right)}{(ds)_{e_{(i,j)}}}\,\hat{\imath} + \frac{\left(\mathrm{RSW}_{(i+1,j)} - \mathrm{RSW}_{(i,j)}\right)}{(ds)_{e_{(i,j)}}}\,\hat{\jmath} \tag{3.14}$$

The gradients are defined and evaluated at the east face and converted to a west to east geometric grid unit vector notation as follows:

$$\hat{s}_{e(i,j)} = \left.\frac{\partial z}{\partial s}\right|_e \hat{\imath} + \left.\frac{\partial r}{\partial s}\right|_e \hat{\jmath} = s_{ze}\,\hat{\imath} + s_{re}\,\hat{\jmath} \tag{3.15}$$

The west to east geometric grid unit vector for the centre of a control volume, $\hat{s}_p$, and its equivalent with regard to arc lengths are calculated using Eqs. (3.16) and (3.17), accordingly. The $\hat{s}_p$ vector is defined along a line between the centre of the west face and centre of the east face.

$$\hat{s}_{p(i,j)} = \frac{\left(\mathrm{ZSE}_{(i,j)} - \mathrm{ZSE}_{(i-1,j)}\right)}{\sqrt{\left(\mathrm{ZSE}_{(i,j)} - \mathrm{ZSE}_{(i-1,j)}\right)^2 + \left(\mathrm{RSE}_{(i,j)} - \mathrm{RSE}_{(i-1,j)}\right)^2}}\,\hat{\imath} + \frac{\left(\mathrm{RSE}_{(i,j)} - \mathrm{RSE}_{(i-1,j)}\right)}{\sqrt{\left(\mathrm{ZSE}_{(i,j)} - \mathrm{ZSE}_{(i-1,j)}\right)^2 + \left(\mathrm{RSE}_{(i,j)} - \mathrm{RSE}_{(i-1,j)}\right)^2}}\,\hat{\jmath} \tag{3.16}$$

$$\hat{s}_{p(i,j)} = \frac{\left(\mathrm{ZSE}_{(i,j)} - \mathrm{ZSE}_{(i-1,j)}\right)}{(ds)_p}\,\hat{\imath} + \frac{\left(\mathrm{RSE}_{(i,j)} - \mathrm{RSE}_{(i-1,j)}\right)}{(ds)_p}\,\hat{\imath} \tag{3.17}$$

The gradients are defined and evaluated at the centre of a control volume and converted to a west to east geometric grid unit vector notation as follows:

$$\hat{s}_{p(i,j)} = \left.\frac{\partial z}{\partial s}\right|_p \hat{\imath} + \left.\frac{\partial r}{\partial s}\right|_p \hat{\jmath} = s_{zp}\,\hat{\imath} + s_{rp}\,\hat{\jmath} \tag{3.18}$$

Equation (3.19) demonstrates how to calculate the south to north geometric grid unit vector for the north face of a control volume, $\hat{t}_n$. The $\hat{t}_n$ vector is defined along the line between the present node and north node.

$$\hat{t}_{n(i,j)} = \frac{\left(\mathrm{ZSW}_{(i,j+1)} - \mathrm{ZSW}_{(i,j)}\right)}{(dt)_{n_{(i,j)}}}\,\hat{\imath} + \frac{\left(\mathrm{RSW}_{(i,j+1)} - \mathrm{RSW}_{(i,j)}\right)}{(dt)_{n_{(i,j)}}}\,\hat{\jmath} \tag{3.19}$$

The gradients are defined and evaluated at the north face and converted to a south to north geometric grid unit vector notation as follows:

$$\hat{t}_{n(i,j)} = \left.\frac{\partial z}{\partial t}\right|_n \hat{\imath} + \left.\frac{\partial r}{\partial t}\right|_n \hat{\jmath} = t_{zn}\,\hat{\imath} + t_{rn}\,\hat{\jmath} \tag{3.20}$$

The south to north geometric grid unit vector for the east face of a control volume, $\hat{t}_e$, and its equivalent with regard to arc lengths are evaluated using Eqs. (3.21) and (3.22), respectively. The vector $\hat{t}_e$ is defined along the line between the southeast and northeast corners of a control volume.

$$\begin{aligned}\hat{t}_{e(i,j)} = {} & \frac{\left(\mathrm{ZNE}_{(i,j)} - \mathrm{ZNE}_{(i,j-1)}\right)}{\sqrt{\left(\mathrm{ZNE}_{(i,j)} - \mathrm{ZNE}_{(i,j-1)}\right)^2 + \left(\mathrm{RNE}_{(i,j)} - \mathrm{RNE}_{(i,j-1)}\right)^2}}\,\hat{\imath} \\ & + \frac{\left(\mathrm{RNE}_{(i,j)} - \mathrm{RNE}_{(i,j-1)}\right)}{\sqrt{\left(\mathrm{ZNE}_{(i,j)} - \mathrm{ZNE}_{(i,j-1)}\right)^2 + \left(\mathrm{RNE}_{(i,j)} - \mathrm{RNE}_{(i,j-1)}\right)^2}}\,\hat{\jmath}\end{aligned} \tag{3.21}$$

$$\hat{t}_{e(i,j)} = \frac{\left(\mathrm{ZNE}_{(i,j)} - \mathrm{ZNE}_{(i,j-1)}\right)}{(dt)_e}\,\hat{\imath} + \frac{\left(\mathrm{RNE}_{(i,j)} - \mathrm{RNE}_{(i,j-1)}\right)}{(dt)_e}\,\hat{\imath} \tag{3.22}$$

The gradients are interpreted and assessed at the east face and converted to a south to north geometric grid unit vector notation as follows:

$$\hat{t}_{e(i,j)} = \left.\frac{\partial z}{\partial t}\right|_e \hat{\imath} + \left.\frac{\partial r}{\partial t}\right|_e \hat{\jmath} = t_{ze}\,\hat{\imath} + t_{re}\,\hat{\jmath} \tag{3.23}$$

The south to north geometric grid unit vector for the centre of a control volume, $\hat{t}_p$, and its equivalent in terms of arc lengths are expressed through Eqs. (3.24) and (3.25), accordingly. The $\hat{t}_p$ vector is defined along a line between the centre of the south face and the centre of the north face.

$$\hat{t}_{p(i,j)} = \frac{\left(\mathrm{ZNW}_{(i,j)} - \mathrm{ZNW}_{(i,j-1)}\right)}{\sqrt{\left(\mathrm{ZNW}_{(i,j)} - \mathrm{ZNW}_{(i,j-1)}\right)^2 + \left(\mathrm{RNW}_{(i,j)} - \mathrm{RNW}_{(i,j-1)}\right)^2}}\,\hat{\imath} + \frac{\left(\mathrm{RNW}_{(i,j)} - \mathrm{RNW}_{(i,j-1)}\right)}{\sqrt{\left(\mathrm{ZNW}_{(i,j)} - \mathrm{ZNW}_{(i,j-1)}\right)^2 + \left(\mathrm{RNW}_{(i,j)} - \mathrm{RNW}_{(i,j-1)}\right)^2}}\,\hat{\jmath} \quad (3.24)$$

$$\hat{t}_{p(i,j)} = \frac{\left(\mathrm{ZNW}_{(i,j)} - \mathrm{ZNW}_{(i,j-1)}\right)}{(dt)_p}\,\hat{\imath} + \frac{\left(\mathrm{RNW}_{(i,j)} - \mathrm{RNW}_{(i,j-1)}\right)}{(dt)_p}\,\hat{\imath} \quad (3.25)$$

The gradients are defined and evaluated at the centre of a control volume and converted to a south to north geometric grid unit vector notation as follows:

$$\hat{t}_{p(i,j)} = \left.\frac{\partial z}{\partial t}\right|_p \hat{\imath} + \left.\frac{\partial r}{\partial t}\right|_p \hat{\jmath} = t_{zp}\,\hat{\imath} + t_{rp}\,\hat{\jmath} \quad (3.26)$$

3.3 Grid Expansion Factor

The control volumes do not need to be uniformly spaced between vertices of the grid. An expansion factor is defined such that the ratio of the lengths of neighbouring control volume edges along a grid boundary is fixed. This geometric expansion is carried out on all four boundaries separately. As an example, the equation

$$ds(i+1, j_{\mathrm{B}} - 1) = ds(i, j_{\mathrm{B}} - 1)\; S \quad (3.27)$$

shows that the expansion factor (S) for the south boundary of a grid multiplies the present control volume south-face length to find the length of the adjacent control volume south face.

The expansion factor is applied to each panel separately, so different panels can have control volumes that expand or contract at different rates and the way of controlling the

change in control volume size between panels becomes somewhat complicated. From a previous panel, the last control volume width is known. To achieve a smooth transition between panels, the ratio of the width of the last control volume in the first panel to the first control volume in the next panel is specified. In addition, overall width and the number of control volumes are known, but the expansion factor is not known. A Newton-Raphson root search is used to solve an algebraic equation for the sum of the expansion factor geometric progression for the present panel [55]. The panel method is a very powerful development tool to produce grids that match the shape of a complicated solution domain.

Chapter 4

Numerical Solution Method

To develop the numerical model, the partial differential governing equations in each phase, interface conditions, and boundary conditions are discretised to obtain a set of algebraic equations for the solution variables. Solving the full set of algebraic equations for the whole physical domain gives the solution fields (U, V, P, T and W) at all nodal locations in the computational mesh.

The equations listed in Chapter 2 are written in the cylindrical coordinate system as the basis for the numerical model for flow in tubes. Details of the cylindrical discretisation is given in this chapter. The same approach was applied for the Cartesian form of the equations but is not presented in this thesis for brevity.

4.1 Discretisation of the Governing Equations

In the present work, a finite volume method [56] is used to discretise the governing differential equations. All the equations are integrated over a typical non-orthogonal control volume centred at P as shown in Fig. 4.1. For each face of the typical control volume, the mass flow rate is determined using the face velocities, which are determined at the integration point (ip) at the centre of the face (denoted by e, w, n, and s in Fig. 4.1). Other fluxes are determined using the face value and gradient of the dependent variables evaluated at the integration points. All fluxes computed at an ip are assumed constant along the face. A co-located variable storage scheme is applied in this work which means all unknowns are located at cell centres and the values at ne, nw, se, and sw corners in Fig. 4.1 are estimated by linear interpolation. Also shown in Fig. 4.1 are unit vectors that are used at each ip. The pressure-velocity coupling is treated by using an approach based on the work of Rhie

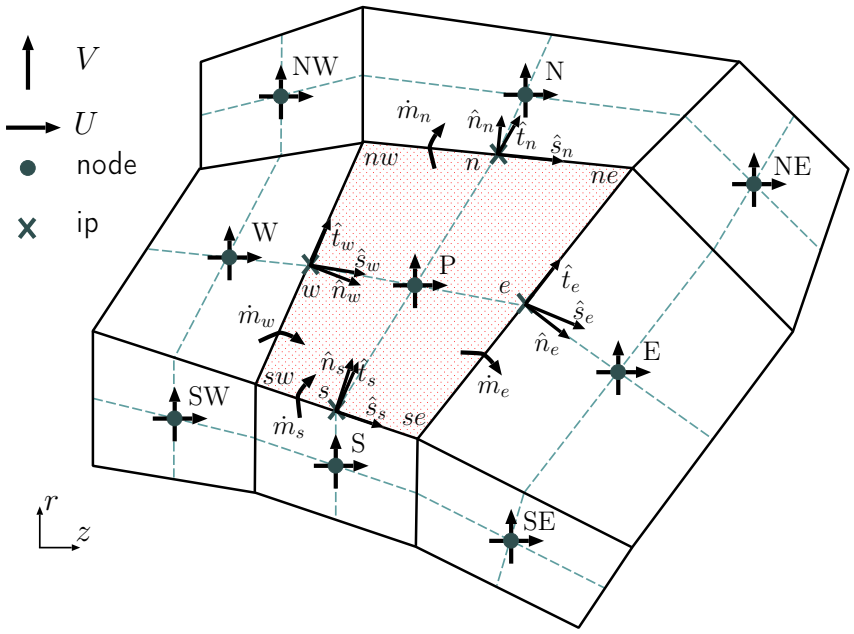

Figure 4.1: Control volume nomenclature

and Chow [57]. It is similar to the approach described by Yu *et al.* [58] and Vakilipour and Ormiston [59].

All the discretisation procedures in the this chapter are applicable to both phases (liquid and gas). The gas phase is chosen for the detailed explanations in the following sections. For ease of presentation, the subscript M is omitted. The level 1 discretisation of Eqs. (2.5) to (2.9) yields the following algebraic equations for conservation of mass, momentum, energy, and gas mass fraction, respectively.

$$\dot{m}_e \; - \; \dot{m}_w \; + \; \dot{m}_n \; - \; \dot{m}_s \; = \; 0 \tag{4.1}$$

$$\begin{aligned} \frac{(\rho_{\mathrm{P}} \forbidden{\mathcal{V}_{\mathrm{P}}})}{\Delta t} \left(U_{\mathrm{P}} - U_{\mathrm{P}}{}^{o}\right) + \dot{m}_e U_e \; - \; \dot{m}_w U_w + \dot{m}_n U_n \; - \; \dot{m}_s U_s = \\ - \left.\frac{\partial P}{\partial z}\right|_{\mathrm{P}} \forbidden{\mathcal{V}_{\mathrm{P}}} + \rho_{\mathrm{P}} g \forbidden{\mathcal{V}_{\mathrm{P}}} + D_e^u \left.\frac{\partial U}{\partial n}\right|_e - D_w^u \left.\frac{\partial U}{\partial n}\right|_w + D_n^u \left.\frac{\partial U}{\partial n}\right|_n - D_s^u \left.\frac{\partial U}{\partial n}\right|_s \end{aligned} \tag{4.2}$$

$$\frac{(\rho_{\mathrm{P}} \forbidden{\mathcal{V}_{\mathrm{P}}})}{\Delta t}(V_{\mathrm{P}} - V_{\mathrm{P}}{}^{o}) + \dot{m}_e V_e \; - \; \dot{m}_w V_w + \dot{m}_n V_n \; - \; \dot{m}_s V_s = \\ - \left.\frac{\partial P}{\partial r}\right|_{\mathrm{P}} \forbidden{\mathcal{V}_{\mathrm{P}}} + D_e^v \left.\frac{\partial V}{\partial n}\right|_e - D_w^v \left.\frac{\partial V}{\partial n}\right|_w + D_n^v \left.\frac{\partial V}{\partial n}\right|_n - D_s^v \left.\frac{\partial V}{\partial n}\right|_s \quad (4.3)$$

$$\frac{(\rho_{\mathrm{P}} \forbidden{\mathcal{V}_{\mathrm{P}}})}{\Delta t}(T_{\mathrm{P}} - T_{\mathrm{P}}{}^{o}) + \dot{m}_e T_e \; - \; \dot{m}_w T_w + \dot{m}_n T_n \; - \; \dot{m}_s T_s = \\ D_e^t \left.\frac{\partial T}{\partial n}\right|_e - D_w^t \left.\frac{\partial T}{\partial n}\right|_w + D_n^t \left.\frac{\partial T}{\partial n}\right|_n - D_s^t \left.\frac{\partial T}{\partial n}\right|_s + \tilde{D}_e^t T_e - \tilde{D}_w^t T_w + \tilde{D}_n^t T_n - \tilde{D}_s^t T_s \quad (4.4)$$

$$\frac{(\rho_{\mathrm{P}} \forbidden{\mathcal{V}_{\mathrm{P}}})}{\Delta t}(W_{\mathrm{P}} - W_{\mathrm{P}}{}^{o}) + \dot{m}_e W_e \; - \; \dot{m}_w W_w + \dot{m}_n W_n \; - \; \dot{m}_s W_s = \\ D_e^w \left.\frac{\partial W}{\partial n}\right|_e - D_w^w \left.\frac{\partial W}{\partial n}\right|_w + D_n^w \left.\frac{\partial W}{\partial n}\right|_n - D_s^w \left.\frac{\partial W}{\partial n}\right|_s \quad (4.5)$$

In the development of the coupled algebraic equations, unsuperscripted dependent variables indicate values at the new time step level.

In level 2 of the discretisation, the mass flow rates, the face values in the advection terms, and the derivatives must be approximated appropriately.

The mass flow rate at a face is calculated as:

$$\dot{m}_f = \rho A_f \left(\vec{\mathbf{V}}_f \cdot \hat{n}_f\right) = \rho A_f \left(U_f \, n_{f,z} + V_f \, n_{f,r}\right) \quad (4.6)$$

where the face velocity components are U_f and V_f and $n_{f,z}$ $n_{f,r}$ are the components of the normal unit vector on the face. The normal unit vectors at faces are shown in Fig. 4.1. Note that the normal unit vector is outward on the n and e faces and inward on the w and s faces.

A momentum interpolation scheme referred to here as the Pressure-Weighted Interpolation Method (PWIM) is used to estimate the face velocities in Eq. (4.6). The PWIM used in this work is based on the work of Rhie and Chow [57] and is similar to the approach described by Yu *et al.* [58]. It is formulated so that the converged solution is independent of the time step size. The PWIM estimations of the face velocity components are:

$$U_f = \mathcal{W}_f \, U_{\mathrm{P}} + (1 - \mathcal{W}_f) \, U_{\mathrm{F}} - \hat{d}_f^u \left.\frac{\partial P}{\partial z}\right|_f + \tilde{b}_f^u \quad (4.7)$$

$$V_f = \mathcal{W}_f\, V_{\mathrm{P}} + (1-\mathcal{W}_f)\, V_{\mathrm{F}} - \hat{d}_f^v \left.\frac{\partial P}{\partial r}\right|_f + \tilde{b}_f^v \tag{4.8}$$

where,

$$\tilde{b}_f^u = \hat{d}_f^u \left\{ \mathcal{W}_f \left.\frac{\partial P}{\partial z}\right|_{\mathrm{P}}^{o} + (1-\mathcal{W}_f) \left.\frac{\partial P}{\partial z}\right|_{\mathrm{F}}^{o} \right\} + \frac{\rho}{\Delta t}\hat{d}_f^u \left\{ \widehat{U}_f^o - \left[\mathcal{W}_f U_{\mathrm{P}}^o + (1-\mathcal{W}_f)\, U_{\mathrm{F}}^o \right] \right\} \tag{4.9}$$

$$\tilde{b}_f^v = \hat{d}_f^v \left\{ \mathcal{W}_f \left.\frac{\partial P}{\partial r}\right|_{\mathrm{P}}^{o} + (1-\mathcal{W}_f) \left.\frac{\partial P}{\partial r}\right|_{\mathrm{F}}^{o} \right\} + \frac{\rho}{\Delta t}\hat{d}_f^v \left\{ \widehat{V}_f^o - \left[\mathcal{W}_f V_{\mathrm{P}}^o + (1-\mathcal{W}_f)\, V_{\mathrm{F}}^o \right] \right\} \tag{4.10}$$

$$\hat{d}_f^\phi = \forbar{V}_f \left\{ \frac{\mathcal{W}_f}{\left(a_{\mathrm{P}}^{\phi,\phi}\right)_{\mathrm{P}}} + \frac{(1-\mathcal{W}_f)}{\left(a_{\mathrm{P}}^{\phi,\phi}\right)_{\mathrm{F}}} \right\} \tag{4.11}$$

In Eqs. (4.7) to (4.11), F = {E,W,N,S} corresponding to f = {e,w,n,s}, and $\mathcal{W}_f$ is a geometric linear interpolation factor at the face separating two adjacent nodes at P and F. The factor $\mathcal{W}_f$ is computed using the distances from the integration point to the centres of the two adjacent nodal points; it is equal to 0.5 for a uniformly spaced mesh. The grid weights are given in Section 4.1.1.

In order to compute $\forbar{V}_f$ in Eq. (4.11), each control volume is divided into quadrants by lines connecting the integration points e to w and n to s as shown in Fig. 4.1. The volume at an integration point, $\forbar{V}_f$, is the summation of the volumes of the quadrants in control volumes for nodes P and F which are adjacent to the face f.

Equations (4.7) and (4.8) have been written to contrast the active nodal velocity and face pressure gradient terms that lead to the coupled algebraic equations versus the lagged terms which are given in Eqs. (4.9) and (4.10). The pressure gradients at faces in Eqs. (4.7) and (4.8) are evaluated using the appropriate combination of co-ordinate derivatives ($\frac{\partial z}{\partial s}$,$\frac{\partial z}{\partial t}$,$\frac{\partial r}{\partial s}$,$\frac{\partial r}{\partial t}$) and derivatives of pressure in the $\hat{s}$ and $\hat{t}$ directions (shown in Fig. 4.1). The derivatives in the $\hat{s}$ and $\hat{t}$ directions create connections to the six nodal pressures surrounding each face f. Therefore, the discretisation of Eq. (4.1) produces implicit connections to five U nodes, five V nodes, and nine P nodes. The pressure gradients at control volume centres in Eqs. (4.2),

(4.3), (4.9), and (4.10), on the other hand, are determined from face pressures which are computed by geometric interpolation using surrounding nodal values.

The advection terms in Eqs. (4.2) and (4.3) are made linear using mass flow rates from the previous time step:

$$\dot{m}_f U_f = \dot{m}_f^o U_f \tag{4.12}$$

$$\dot{m}_f V_f = \dot{m}_f^o V_f \tag{4.13}$$

$$\dot{m}_f T_f = \dot{m}_f^o T_f \tag{4.14}$$

$$\dot{m}_f W_f = \dot{m}_f^o W_f \tag{4.15}$$

The face values of the dependent variable (Φ_f) and its derivative in the diffusion terms ($\frac{\partial \Phi}{\partial n}\big|_f$) are approximated in terms of nodal values. The advected scalars at the faces are estimated using an approximation to the exponential differencing scheme as proposed by Raithby [60]. Gradients at faces are calculated by linear interpolation and have a diffusion weighting coefficient applied to them as in [60]. The details are given below.

$$\Phi_e = (0.5 + \alpha_e)\,\Phi_{\mathrm{P}} + (0.5 - \alpha_e)\,\Phi_{\mathrm{E}} \tag{4.16}$$

$$\Phi_w = (0.5 + \alpha_w)\,\Phi_{\mathrm{W}} + (0.5 - \alpha_w)\,\Phi_{\mathrm{P}} \tag{4.17}$$

$$\Phi_n = (0.5 + \alpha_n)\,\Phi_{\mathrm{P}} + (0.5 - \alpha_n)\,\Phi_{\mathrm{N}} \tag{4.18}$$

$$\Phi_s = (0.5 + \alpha_s)\,\Phi_{\mathrm{S}} + (0.5 - \alpha_s)\,\Phi_{\mathrm{P}} \tag{4.19}$$

The convective weight coefficients at each face, α_f, are computed as a function of the local ratio of advective to diffusive transport rates, using the approximation to the exponential differencing scheme proposed by Raithby in [60].

$$\alpha_f = \frac{1}{2}\left(\frac{\left(\frac{\dot{m}_f}{D_f^\phi}\right)^2}{5 + \left(\frac{\dot{m}_f}{D_f^\phi}\right)^2}\right) \tag{4.20}$$

To get the correct sign on α_f (it should carry the sign of the mass flow), α_f is further calculated using:

$$\alpha_f = \alpha_f \frac{|\dot{m}|}{\dot{m}} \tag{4.21}$$

Gradients at faces are calculated by linear interpolation. For example, at the east face:

$$\left.\frac{\partial \phi}{\partial s}\right|_e = \beta_e \frac{(\phi_{\mathrm{E}} - \phi_{\mathrm{P}})}{(\delta s)_e} \tag{4.22}$$

More details of gradient calculations are given in Section 4.1.3.

The diffusion weighting factor, β_f, applied as in [60]:

$$\beta_f = \frac{1 + 0.005 \left(\frac{\dot{m}_f}{D_f^{\phi}}\right)^2}{1 + 0.05 \left(\frac{\dot{m}_f}{D_f^{\phi}}\right)^2} \tag{4.23}$$

Following the discretisation procedure described above, the final form of the linearised set of coupled algebraic equations for conservation of mass, momentum, energy, and gas mass fraction can be written as:

$$a_{\mathrm{P}}^{c,p} P_{\mathrm{P}} + \sum a_{\mathrm{NB8}}^{c,p} P_{\mathrm{NB8}} + a_{\mathrm{P}}^{c,u} U_{\mathrm{P}} + \sum a_{\mathrm{NB4}}^{c,u} U_{\mathrm{NB4}} + a_{\mathrm{P}}^{c,v} V_{\mathrm{P}} + \sum a_{\mathrm{NB4}}^{c,v} V_{\mathrm{NB4}} = b_{\mathrm{P}}^{c} \tag{4.24}$$

$$a_{\mathrm{P}}^{u,u} U_{\mathrm{P}} + \sum a_{\mathrm{NB8}}^{u,u} U_{\mathrm{NB8}} + a_{\mathrm{P}}^{u,p} P_{\mathrm{P}} + \sum a_{\mathrm{NB4}}^{u,p} P_{\mathrm{NB4}} = b_{\mathrm{P}}^{u} \tag{4.25}$$

$$a_{\mathrm{P}}^{v,v} V_{\mathrm{P}} + \sum a_{\mathrm{NB8}}^{v,v} V_{\mathrm{NB8}} + a_{\mathrm{P}}^{v,p} P_{\mathrm{P}} + \sum a_{\mathrm{NB4}}^{v,p} P_{\mathrm{NB4}} = b_{\mathrm{P}}^{v} \tag{4.26}$$

$$a_{\mathrm{P}}^{t,t} T_{\mathrm{P}} + \sum a_{\mathrm{NB8}}^{t,t} T_{\mathrm{NB8}} = b_{\mathrm{P}}^{t} \tag{4.27}$$

$$a_{\mathrm{P}}^{w,w} W_{\mathrm{P}} + \sum a_{\mathrm{NB8}}^{w,w} W_{\mathrm{NB8}} = b_{\mathrm{P}}^{w} \tag{4.28}$$

The first and second superscripts of the a coefficients refer to the equation label and the multiplied variable, respectively. In summations, NB4={E,W,N,S} and NB8={NB4,NE, NW, SE,SW}. The details of the summations are:

$$\sum a_{\mathrm{NB4}}^{e,\phi} \Phi_{\mathrm{NB4}} = a_{\mathrm{E}}^{e,\phi} \Phi_{\mathrm{E}} + a_{\mathrm{W}}^{e,\phi} \Phi_{\mathrm{W}} + a_{\mathrm{N}}^{e,\phi} \Phi_{\mathrm{N}} + a_{\mathrm{S}}^{e,\phi} \Phi_{\mathrm{S}} \tag{4.29}$$

and,

$$\sum a^{e,\phi}_{\mathrm{NB8}}\Phi_{\mathrm{NB8}} = \sum a^{e,\phi}_{\mathrm{NB4}}\Phi_{\mathrm{NB4}} + a^{e,\phi}_{\mathrm{NE}}\Phi_{\mathrm{NE}} + a^{e,\phi}_{\mathrm{NW}}\Phi_{\mathrm{NW}} + a^{e,\phi}_{\mathrm{SE}}\Phi_{\mathrm{SE}} + a^{e,\phi}_{\mathrm{SW}}\Phi_{\mathrm{SW}} \tag{4.30}$$

The details of grid weights and gradient calculations will now be presented, followed by the details of the algebraic equation coefficients in which those calculations are used.

4.1.1 Grid Weights

The grid weights used in Eqs. (4.7) to (4.11) are computed using the grid distances shown in Fig. 3.5. The four face grid weights are computed as follows:

$$\mathcal{W}_{e_{(i,j)}} = \frac{\mathrm{DISW}_{(i+1,j)}}{\mathrm{DISE}_{(i,j)} + \mathrm{DISW}_{(i+1,j)}} \tag{4.31}$$

$$\mathcal{W}_{n_{(i,j)}} = \frac{\mathrm{DJSW}_{(i+1,j)}}{\mathrm{DJNW}_{(i,j)} + \mathrm{DJSW}_{(i+1,j)}} \tag{4.32}$$

$$\mathcal{W}_{w_{(i,j)}} = \mathcal{W}_{e_{(i-1,j)}} \tag{4.33}$$

$$\mathcal{W}_{s_{(i,j)}} = \mathcal{W}_{n_{(i,j-1)}} \tag{4.34}$$

4.1.2 Corner Interpolations

In order to use nine-point solution method, the values at corners are incorporated to estimate derivatives on the faces. The corner vertices are indicated as ne, nw, se, and sw in Fig. 4.1. Geometric interpolations are used to approximate scalar values at corners in a non-uniform grid.

$$\phi_{ne} = C_{ne1}\Phi_{\mathrm{P}} + C_{ne2}\Phi_{\mathrm{E}} + C_{ne3}\Phi_{\mathrm{NE}} + C_{ne4}\Phi_{\mathrm{N}} \tag{4.35}$$

$$\phi_{nw} = C_{nw1}\Phi_{\mathrm{W}} + C_{nw2}\Phi_{\mathrm{P}} + C_{nw3}\Phi_{\mathrm{N}} + C_{nw4}\Phi_{\mathrm{NW}} \tag{4.36}$$

$$\phi_{se} = C_{se1}\Phi_{\mathrm{S}} + C_{se2}\Phi_{\mathrm{SE}} + C_{se3}\Phi_{\mathrm{E}} + C_{se4}\Phi_{\mathrm{P}} \tag{4.37}$$

$$\phi_{sw} = C_{sw1}\Phi_{\mathrm{SW}} + C_{sw2}\Phi_{\mathrm{S}} + C_{sw3}\Phi_{\mathrm{P}} + C_{sw4}\Phi_{\mathrm{W}} \tag{4.38}$$

where the numbering order of C coefficients starts from 1 for the left bottom corner node and goes counter-clockwise around the control volume.

4.1.3 Gradient Calculations

On a non-orthogonal grid, the face derivatives in cylindrical z and r directions must be defined in terms of the gradients along the unit vector directions, $\hat{s}$ and $\hat{t}$ as shown in Fig. 3.6. Using the chain rule and Cramer's rule, the derivatives in cylindrical z and r directions on face f are equal to:

$$\left.\frac{\partial\Phi}{\partial z}\right|_f = \mathcal{R}_{t,f}\left.\frac{\partial\Phi}{\partial s}\right|_f - \mathcal{R}_{s,f}\left.\frac{\partial\Phi}{\partial t}\right|_f \tag{4.39}$$

$$\left.\frac{\partial\Phi}{\partial r}\right|_f = \mathcal{Z}_{s,f}\left.\frac{\partial\Phi}{\partial t}\right|_f - \mathcal{Z}_{t,f}\left.\frac{\partial\Phi}{\partial s}\right|_f \tag{4.40}$$

where,

$$\mathcal{Z}_{s,f} = \frac{\left.\frac{\partial z}{\partial s}\right|_f}{\left(\left.\frac{\partial z}{\partial s}\right|_f \left.\frac{\partial r}{\partial t}\right|_f - \left.\frac{\partial z}{\partial t}\right|_f \left.\frac{\partial r}{\partial s}\right|_f\right)} \tag{4.41}$$

$$\mathcal{Z}_{t,f} = \frac{\left.\frac{\partial z}{\partial t}\right|_f}{\left(\left.\frac{\partial z}{\partial s}\right|_f \left.\frac{\partial r}{\partial t}\right|_f - \left.\frac{\partial z}{\partial t}\right|_f \left.\frac{\partial r}{\partial s}\right|_f\right)} \tag{4.42}$$

$$\mathcal{R}_{s,f} = \frac{\left.\frac{\partial r}{\partial s}\right|_f}{\left(\left.\frac{\partial z}{\partial s}\right|_f \left.\frac{\partial r}{\partial t}\right|_f - \left.\frac{\partial z}{\partial t}\right|_f \left.\frac{\partial r}{\partial s}\right|_f\right)} \tag{4.43}$$

$$\mathcal{R}_{t,f} = \frac{\left.\frac{\partial r}{\partial t}\right|_f}{\left(\left.\frac{\partial z}{\partial s}\right|_f \left.\frac{\partial r}{\partial t}\right|_f - \left.\frac{\partial z}{\partial t}\right|_f \left.\frac{\partial r}{\partial s}\right|_f\right)} \tag{4.44}$$

As shown in Fig. 3.6, there are separate direction vectors $\hat{s}$ and $\hat{t}$ for each face (i.e. e, w, n, and s) and central node for the main control volume. Thus, the derivatives in Cylindrical directions (Eqs. (4.39) and (4.40)) should be approximated for each face using nodal and corner values.

$$\left.\frac{\partial \Phi}{\partial z}\right|_e = \frac{\mathcal{R}_{t,e}}{(ds)_e}(\Phi_{\mathrm{P}} - \Phi_{\mathrm{E}}) - \frac{\mathcal{R}_{s,e}}{(dt)_e}(\Phi_{ne} - \Phi_{se}) \tag{4.45}$$

$$\left.\frac{\partial \Phi}{\partial r}\right|_e = \frac{\mathcal{Z}_{t,e}}{(ds)_e}(\Phi_{\mathrm{E}} - \Phi_{\mathrm{P}}) + \frac{\mathcal{Z}_{s,e}}{(dt)_e}(\Phi_{ne} - \Phi_{se}) \tag{4.46}$$

$$\left.\frac{\partial \Phi}{\partial z}\right|_w = \frac{\mathcal{R}_{t,w}}{(ds)_w}(\Phi_{\mathrm{W}} - \Phi_{\mathrm{P}}) - \frac{\mathcal{R}_{s,w}}{(dt)_w}(\Phi_{nw} - \Phi_{sw}) \tag{4.47}$$

$$\left.\frac{\partial \Phi}{\partial r}\right|_w = \frac{\mathcal{Z}_{t,w}}{(dt)_w}(\Phi_{\mathrm{P}} - \Phi_{\mathrm{W}}) + \frac{\mathcal{Z}_{s,w}}{(ds)_w}(\Phi_{nw} - \Phi_{sw}) \tag{4.48}$$

$$\left.\frac{\partial \Phi}{\partial z}\right|_n = \frac{\mathcal{R}_{s,n}}{(ds)_n}(\Phi_{\mathrm{N}} - \Phi_{\mathrm{P}}) + \frac{\mathcal{R}_{t,n}}{(dt)_n}(\Phi_{ne} - \Phi_{nw}) \tag{4.49}$$

$$\left.\frac{\partial \Phi}{\partial r}\right|_n = \frac{\mathcal{Z}_{s,n}}{(dt)_n}(\Phi_{\mathrm{P}} - \Phi_{\mathrm{N}}) - \frac{\mathcal{Z}_{t,n}}{(ds)_n}(\Phi_{ne} - \Phi_{nw}) \tag{4.50}$$

$$\left.\frac{\partial \Phi}{\partial z}\right|_s = \frac{\mathcal{R}_{s,s}}{(ds)_s}(\Phi_{\mathrm{P}} - \Phi_{\mathrm{S}}) + \frac{\mathcal{R}_{t,s}}{(dt)_s}(\Phi_{se} - \Phi_{sw}) \tag{4.51}$$

$$\left.\frac{\partial \Phi}{\partial r}\right|_s = \frac{\mathcal{Z}_{s,s}}{(dt)_s}(\Phi_{\mathrm{S}} - \Phi_{\mathrm{P}}) - \frac{\mathcal{Z}_{t,s}}{(ds)_s}(\Phi_{se} - \Phi_{sw}) \tag{4.52}$$

4.2 Coefficients of the Coupled Algebraic Equations

4.2.1 Continuity

Substituting Eqs. (4.35) to (4.38) into Eqs. (4.45) to (4.52) for the pressure variable ($\Phi = P$), the pressure gradients on the faces in Eqs. (4.7) and (4.8) are approximated in terms of nodal values. Now, the coefficients of continuity equation (Eq. (4.24)) are:

$$a_{\mathrm{P}}^{c,u} = a_{\mathrm{P}}^{c,v} = \sum (\rho_f A_f \mathcal{W}_f) = \rho_e A_e \mathcal{W}_e + \rho_w A_w \mathcal{W}_w + \rho_n A_n \mathcal{W}_n + \rho_s A_s \mathcal{W}_s \tag{4.53}$$

$$a_{\mathrm{F}}^{c,u} = a_{\mathrm{F}}^{c,v} = \rho_f A_f \left(1 - \mathcal{W}_f\right) \tag{4.54}$$

$$\begin{aligned} a_{\mathrm{P}}^{c,p} = &-\rho_e A_e \hat{d}_e^u \left[\frac{\mathcal{R}_{t,e}}{(ds)_e} + \frac{\mathcal{R}_{s,e}}{(dt)_e}\left(C_{ne1} - C_{se4}\right)\right] + \rho_w A_w \hat{d}_w^u \left[\frac{\mathcal{R}_{t,w}}{(ds)_w} - \frac{\mathcal{R}_{s,w}}{(dt)_w}\left(C_{nw2} - C_{sw3}\right)\right] \\ &+\rho_n A_n \hat{d}_n^u \left[\frac{\mathcal{R}_{s,n}}{(dt)_n} + \frac{\mathcal{R}_{t,n}}{(ds)_n}\left(C_{ne1} - C_{nw2}\right)\right] - \rho_s A_s \hat{d}_s^u \left[\frac{\mathcal{R}_{s,s}}{(dt)_s} - \frac{\mathcal{R}_{t,s}}{(ds)_s}\left(C_{se4} - C_{sw3}\right)\right] \\ &+\rho_e A_e \hat{d}_e^v \left[\frac{\mathcal{Z}_{t,e}}{(ds)_e} + \frac{\mathcal{Z}_{s,e}}{(dt)_e}\left(C_{ne1} - C_{se4}\right)\right] - \rho_w A_w \hat{d}_w^v \left[\frac{\mathcal{Z}_{t,w}}{(ds)_w} - \frac{\mathcal{Z}_{s,w}}{(dt)_w}\left(C_{nw2} - C_{sw3}\right)\right] \\ &-\rho_n A_n \hat{d}_n^v \left[\frac{\mathcal{Z}_{s,n}}{(dt)_n} + \frac{\mathcal{Z}_{t,n}}{(ds)_n}\left(C_{ne1} - C_{nw2}\right)\right] + \rho_s A_s \hat{d}_s^v \left[\frac{\mathcal{Z}_{s,s}}{(dt)_s} - \frac{\mathcal{Z}_{t,s}}{(ds)_s}\left(C_{se4} - C_{sw3}\right)\right] \end{aligned} \tag{4.55}$$

$$\begin{aligned} a_{\mathrm{E}}^{c,p} = &\rho_e A_e \left(\hat{d}_e^u \frac{\mathcal{R}_{t,e}}{(ds)_e} - \hat{d}_e^v \frac{\mathcal{Z}_{t,e}}{(ds)_e}\right) + \rho_n A_n \left(\hat{d}_n^u \frac{\mathcal{R}_{t,n}}{(ds)_n} - \hat{d}_n^v \frac{\mathcal{Z}_{t,n}}{(ds)_n}\right) C_{ne2} \\ &+ \rho_s A_s \left(\hat{d}_s^u \frac{\mathcal{R}_{t,s}}{(ds)_s} - \hat{d}_s^v \frac{\mathcal{Z}_{t,s}}{(ds)_s}\right) C_{se3} - \rho_e A_e \left(\hat{d}_e^u \frac{\mathcal{R}_{s,e}}{(dt)_e} - \hat{d}_e^v \frac{\mathcal{Z}_{s,e}}{(dt)_e}\right)\left(C_{ne2} - C_{se3}\right) \end{aligned} \tag{4.56}$$

$$\begin{aligned} a_{\mathrm{W}}^{c,p} = &-\rho_w A_w \left(\hat{d}_w^u \frac{\mathcal{R}_{t,w}}{(ds)_w} - \hat{d}_w^v \frac{\mathcal{Z}_{t,w}}{(ds)_w}\right) + \rho_n A_n \left(\hat{d}_n^u \frac{\mathcal{R}_{t,n}}{(ds)_n} + \hat{d}_n^v \frac{\mathcal{Z}_{t,n}}{(ds)_n}\right) C_{nw1} \\ &- \rho_s A_s \left(\hat{d}_s^u \frac{\mathcal{R}_{t,s}}{(ds)_s} - \hat{d}_s^v \frac{\mathcal{Z}_{t,s}}{(ds)_s}\right) C_{sw4} + \rho_w A_w \left(\hat{d}_w^u \frac{\mathcal{R}_{s,w}}{(dt)_w} - \hat{d}_w^v \frac{\mathcal{Z}_{s,w}}{(dt)_w}\right)\left(C_{sw4} - C_{nw1}\right) \end{aligned} \tag{4.57}$$

$$\begin{aligned} a_{\mathrm{N}}^{c,p} = &-\rho_n A_n \left(\hat{d}_n^u \frac{\mathcal{R}_{s,n}}{(dt)_n} + \hat{d}_n^v \frac{\mathcal{Z}_{s,n}}{(dt)_n}\right) - \rho_e A_e \left(\hat{d}_e^u \frac{\mathcal{R}_{s,e}}{(dt)_e} - \hat{d}_e^v \frac{\mathcal{Z}_{s,e}}{(dt)_e}\right) C_{ne4} \\ &- \rho_w A_w \left(\hat{d}_w^u \frac{\mathcal{R}_{s,w}}{(dt)_w} - \hat{d}_w^v \frac{\mathcal{Z}_{s,w}}{(dt)_w}\right) C_{nw3} + \rho_n A_n \left(\hat{d}_n^u \frac{\mathcal{R}_{t,n}}{(ds)_e} - \hat{d}_n^v \frac{\mathcal{Z}_{t,n}}{(ds)_e}\right)\left(C_{ne4} - C_{nw3}\right) \end{aligned} \tag{4.58}$$

$$\begin{aligned} a_{\mathrm{S}}^{c,p} = &\rho_s A_s \left(\hat{d}_s^u \frac{\mathcal{R}_{s,s}}{(dt)_s} - \hat{d}_s^v \frac{\mathcal{Z}_{s,s}}{(dt)_s}\right) + \rho_e A_e \left(\hat{d}_e^u \frac{\mathcal{R}_{s,e}}{(dt)_e} - \hat{d}_e^v \frac{\mathcal{Z}_{s,e}}{(dt)_e}\right) C_{se1} \\ &+ \rho_w A_w \left(\hat{d}_w^u \frac{\mathcal{R}_{s,w}}{(dt)_w} - \hat{d}_w^v \frac{\mathcal{Z}_{s,w}}{(dt)_w}\right) C_{sw2} + \rho_s A_s \left(\hat{d}_s^u \frac{\mathcal{R}_{t,s}}{(ds)_s} - \hat{d}_s^v \frac{\mathcal{Z}_{t,s}}{(ds)_s}\right)\left(C_{se1} - C_{sw2}\right) \end{aligned} \tag{4.59}$$

$$a_{\mathrm{NE}}^{c,p} = -\left(\rho_e A_e \hat{d}_e^u \frac{\mathcal{R}_{s,e}}{(dt)_e} - \rho_e A_e \hat{d}_e^v \frac{\mathcal{Z}_{s,e}}{(dt)_e} - \rho_n A_n \hat{d}_n^u \frac{\mathcal{R}_{t,n}}{(ds)_n} + \rho_n A_n \hat{d}_n^v \frac{\mathcal{Z}_{t,n}}{(ds)_n}\right) C_{ne3} \tag{4.60}$$

$$a_{\mathrm{NW}}^{c,p} = -\left(\rho_w A_w \hat{d}_w^u \frac{\mathcal{R}_{s,w}}{(dt)_w} - \rho_w A_w \hat{d}_w^v \frac{\mathcal{Z}_{s,w}}{(dt)_w} + \rho_n A_n \hat{d}_n^u \frac{\mathcal{R}_{t,n}}{(ds)_n} - \rho_n A_n \hat{d}_n^v \frac{\mathcal{Z}_{t,n}}{(ds)_n}\right) C_{nw4} \tag{4.61}$$

$$a_{\mathrm{SE}}^{c,p} = \left(\rho_e A_e \hat{d}_e^u \frac{\mathcal{R}_{s,e}}{(dt)_e} - \rho_e A_e \hat{d}_e^v \frac{\mathcal{Z}_{s,e}}{(dt)_e} + \rho_s A_s \hat{d}_s^u \frac{\mathcal{R}_{t,s}}{(ds)_s} - \rho_s A_s \hat{d}_s^v \frac{\mathcal{Z}_{t,s}}{(ds)_s} \right) C_{se2} \tag{4.62}$$

$$a_{\mathrm{SW}}^{c,p} = \left(\rho_w A_w \hat{d}_w^u \frac{\mathcal{R}_{s,w}}{(dt)_w} - \rho_w A_w \hat{d}_w^v \frac{\mathcal{Z}_{s,w}}{(dt)_w} - \rho_s A_s \hat{d}_s^u \frac{\mathcal{R}_{t,s}}{(ds)_s} + \rho_s A_s \hat{d}_s^v \frac{\mathcal{Z}_{t,s}}{(ds)_s} \right) C_{sw1} \tag{4.63}$$

$$b_{\mathrm{P}}^c = \sum \rho_f A_f \left(\tilde{b}_f^u + \tilde{b}_f^v \right) \tag{4.64}$$

4.2.2 Z-Momentum

Using geometric directions for each face of the typical control volume, the diffusion terms in z-momentum equation are approximated in terms of nodal values. In Eq. (4.25), the U velocity coefficients of main node ($a_{\mathrm{P}}^{u,u}$) and its eight neighbour nodes ($a_{\mathrm{NB8}}^{u,u}$) are as follows:

$$\begin{aligned} a_{\mathrm{P}}^{u,u} = & \left(\frac{\rho_{\mathrm{P}} \forall_{\mathrm{P}}}{\Delta t} \right) - (0.5 - \alpha_e)\, \dot{m}_e + (0.5 + \alpha_w)\, \dot{m}_w - (0.5 - \alpha_n)\, \dot{m}_n + (0.5 + \alpha_s)\, \dot{m}_s \\ & + \frac{D_e^u \beta_e}{\hat{n}_e \cdot \hat{s}_e} + \frac{D_w^u \beta_w}{\hat{n}_w \cdot \hat{s}_w} + \frac{D_n^u \beta_n}{\hat{n}_n \cdot \hat{s}_n} + \frac{D_s^u \beta_s}{\hat{n}_s \cdot \hat{s}_s} + D_e^u \beta_e \gamma_{z,e} \left(C_{ne1} - C_{se4} \right) \\ & - D_w^u \beta_w \gamma_{z,w} \left(C_{nw2} - C_{sw3} \right) + D_n^u \beta_n \gamma_{r,n} \left(C_{ne1} - C_{nw2} \right) - D_s^u \beta_s \gamma_{r,s} \left(C_{se4} - C_{sw3} \right) \end{aligned} \tag{4.65}$$

$$\begin{aligned} a_{\mathrm{E}}^{u,u} = & (0.5 - \alpha_e)\, \dot{m}_e - \frac{D_e^u \beta_e}{\hat{n}_e \cdot \hat{s}_e} + D_n^u \beta_n \gamma_{r,n} C_{ne2} - D_s^u \beta_s \gamma_{r,s} C_{se3} \\ & + D_e^u \beta_e \gamma_{z,e} \left(C_{ne2} - C_{se3} \right) \end{aligned} \tag{4.66}$$

$$\begin{aligned} a_{\mathrm{W}}^{u,u} = & -(0.5 + \alpha_w)\, \dot{m}_w - \frac{D_w^u \beta_w}{\hat{n}_w \cdot \hat{s}_w} - D_n^u \beta_n \gamma_{r,n} C_{nw1} + D_s^u \beta_s \gamma_{r,s} C_{sw4} \\ & - D_w^u \beta_w \gamma_{z,w} \left(C_{nw1} - C_{sw4} \right) \end{aligned} \tag{4.67}$$

$$\begin{aligned} a_{\mathrm{N}}^{u,u} = & (0.5 - \alpha_n)\, \dot{m}_n - \frac{D_n^u \beta_n}{\hat{n}_n \cdot \hat{s}_n} + D_e^u \beta_e \gamma_{z,e} C_{ne4} - D_w^u \beta_w \gamma_{z,w} C_{nw3} \\ & + D_n^u \beta_n \gamma_{r,n} \left(C_{ne4} - C_{nw3} \right) \end{aligned} \tag{4.68}$$

$$a_{\mathrm{S}}^{u,u} = -\left(0.5+\alpha_s\right)\dot{m}_s - \frac{D_s^u\beta_s}{\hat{n}_s\cdot\hat{s}_s} - D_e^u\beta_e\gamma_{z,e}C_{se1} + D_w^u\beta_w\gamma_{z,w}C_{sw2} - D_s^u\beta_s\gamma_{r,s}\left(C_{se1}-C_{sw2}\right) \quad (4.69)$$

$$a_{\mathrm{NE}}^{u,u} = \left(D_e^u\beta_e\gamma_{z,e} + D_w^u\beta_w\gamma_{r,n}\right)C_{ne3} \quad (4.70)$$

$$a_{\mathrm{NW}}^{u,u} = -\left(D_w^u\beta_w\gamma_{z,w} + D_n^u\beta_n\gamma_{r,n}\right)C_{nw4} \quad (4.71)$$

$$a_{\mathrm{SE}}^{u,u} = -\left(D_e^u\beta_e\gamma_{z,e} + D_n^u\beta_n\gamma_{r,s}\right)C_{se2} \quad (4.72)$$

$$a_{\mathrm{SW}}^{u,u} = \left(D_w^u\beta_w\gamma_{z,w} + D_s^u\beta_s\gamma_{r,s}\right)C_{sw1} \quad (4.73)$$

where,

$$D_e^u = \frac{\mu_e A_e}{(ds)_e} \qquad D_w^u = \frac{\mu_w A_w}{(ds)_w} \qquad D_n^u = \frac{\mu_n A_n}{(ds)_n} \qquad D_s^u = \frac{\mu_s A_s}{(ds)_s} \quad (4.74)$$

$$\gamma_{z,f} = \frac{(ds)_f}{(dt)_f}\frac{\hat{t}_f\cdot\hat{s}_f}{\hat{n}_f\cdot\hat{s}_f} \qquad \gamma_{r,f} = \frac{(dt)_f}{(ds)_f}\frac{\hat{t}_f\cdot\hat{s}_f}{\hat{n}_f\cdot\hat{t}_f} \quad (4.75)$$

The pressure terms in the momentum equations are implicitly discretised and simultaneously solved in a fully coupled manner. For this reason, the approximations of cylindrical derivatives on main control volume faces (*i.e.* Eqs. (4.39) and (4.40)), are written for the centre node P. Using geometric interpolation for the face pressures, the pressure coefficients of main node ($a_{\mathrm{P}}^{u,p}$) and its four neighbours ($a_{\mathrm{NB4}}^{u,p}$) in Eq. (4.25) are derived as follows:

$$a_{\mathrm{P}}^{u,p} = \forall_{\mathrm{P}}\frac{\mathcal{R}_{t,P}}{(ds)_p}\left(\mathcal{W}_e-\mathcal{W}_w\right) - \forall_{\mathrm{P}}\frac{\mathcal{R}_{s,P}}{(dt)_p}\left(\mathcal{W}_n-\mathcal{W}_s\right) \quad (4.76)$$

$$a_{\mathrm{E}}^{u,p} = \forall_{\mathrm{P}}\frac{\mathcal{R}_{t,P}}{(ds)_p}\left(1-\mathcal{W}_e\right) \quad (4.77)$$

$$a_{\mathrm{W}}^{u,p} = -\forall_{\mathrm{P}}\frac{\mathcal{R}_{t,P}}{(ds)_p}\left(1-\mathcal{W}_w\right) \quad (4.78)$$

$$a_{\mathrm{N}}^{u,p} = -\forall_{\mathrm{P}}\frac{\mathcal{R}_{s,P}}{(dt)_p}\left(1-\mathcal{W}_n\right) \quad (4.79)$$

$$a_{\mathrm{S}}^{u,p} = \forall_{\mathrm{P}}\frac{\mathcal{R}_{s,P}}{(dt)_p}\left(1-\mathcal{W}_s\right) \quad (4.80)$$

The right hand side of Eq. (4.25) is:

$$b_{\mathrm{P}}^{u} = \left(\frac{\rho_{\mathrm{P}} \forbar{V}_{\mathrm{P}}}{\Delta t}\right) U_{\mathrm{P}}^{o} + \rho_{\mathrm{P}} g \forbar{V}_{\mathrm{P}} \tag{4.81}$$

4.2.3 r-Momentum

Each term in the r-momentum equation is derived in the same manner as was used for the z-momentum equation. The corresponding coefficients for Eq. (4.26) are expressed as:

$$a_{\mathrm{P}}^{v,v} = a_{\mathrm{P}}^{u,u} \qquad a_{\mathrm{NB}}^{v,v} = a_{\mathrm{NB}}^{u,u} \tag{4.82}$$

The diffusion coefficient for v as the same as those for u:

$$D_e^v = \frac{\mu_e A_e}{(ds)_e} \qquad D_w^v = \frac{\mu_w A_w}{(ds)_w} \qquad D_n^v = \frac{\mu_n A_n}{(ds)_n} \qquad D_s^v = \frac{\mu_s A_s}{(ds)_s} \tag{4.83}$$

$$a_{\mathrm{P}}^{v,p} = \forbar{V}_{\mathrm{P}} \frac{\mathcal{Z}_{s,P}}{(dt)_p} (\mathcal{W}_n - \mathcal{W}_s) - \forbar{V}_{\mathrm{P}} \frac{\mathcal{Z}_{t,P}}{(ds)_p} (\mathcal{W}_e - \mathcal{W}_w) \tag{4.84}$$

$$a_{\mathrm{E}}^{v,p} = -\forbar{V}_{\mathrm{P}} \frac{\mathcal{Z}_{t,P}}{(ds)_p} (1 - \mathcal{W}_e) \tag{4.85}$$

$$a_{\mathrm{W}}^{v,p} = \forbar{V}_{\mathrm{P}} \frac{\mathcal{Z}_{t,P}}{(ds)_p} (1 - \mathcal{W}_w) \tag{4.86}$$

$$a_{\mathrm{N}}^{v,p} = \forbar{V}_{\mathrm{P}} \frac{\mathcal{Z}_{s,P}}{(dt)_p} (1 - \mathcal{W}_n) \tag{4.87}$$

$$a_{\mathrm{S}}^{v,p} = -\forbar{V}_{\mathrm{P}} \frac{\mathcal{Z}_{s,P}}{(dt)_p} (1 - \mathcal{W}_s) \tag{4.88}$$

$$b_{\mathrm{P}}^{v} = \left(\frac{\rho_{\mathrm{P}} \forbar{V}_{\mathrm{P}}}{\Delta t}\right) V_{\mathrm{P}}^{o} \tag{4.89}$$

4.2.4 Energy

The derivation of $a_{\mathrm{P}}^{t,t}$ and $a_{\mathrm{NB}}^{t,t}$ is analogous to that for the U velocity coefficient in z-momentum equation using k instead of μ in D_f coefficients and $\dot{m}C_p$ instead of $\dot{m}$. The coefficients for the last four terms ($\tilde{D}_e^t$, $\tilde{D}_w^t$, $\tilde{D}_s^t$, $\tilde{D}_n^t$) are as follows:

$$\tilde{D}_e^t = A_e\rho_e D_e^{12}(C_{p,g} - C_{p,v})_e \left(\left.\frac{\partial W}{\partial z}\right|_e\right)^o \qquad \tilde{D}_w^t = A_w\rho_w D_w^{12}(C_{p,g} - C_{p,v})_w \left(\left.\frac{\partial W}{\partial z}\right|_w\right)^o$$
$$\tilde{D}_n^t = A_n\rho_n D_n^{12}(C_{p,g} - C_{p,v})_n \left(\left.\frac{\partial W}{\partial r}\right|_n\right)^o \qquad \tilde{D}_s^t = A_s\rho_s D_s^{12}(C_{p,g} - C_{p,v})_s \left(\left.\frac{\partial W}{\partial r}\right|_s\right)^o \tag{4.90}$$

where all the gradients are calculated using the equations in Section 4.1.3.

4.2.5 Gas Mass Fraction

The derivations of $a_{\mathrm{P}}^{w,w}$ and $a_{\mathrm{NB}}^{w,w}$ are analogous to that for the U velocity coefficient in z-momentum equation using ρD^{12} instead of μ in D_f coefficients.

4.3 Algebraic Interface Equations

The nodes on both liquid and mixture sides of the interface along with the adjacent nodes in the mixture and liquid regions are involved in the discretisation process of the interface equations. Figure 4.2 shows the indexing notation of the interface nodes and their neighbouring control volumes. This naming system is applied for all the algebraic form of the interface equations.

4.3.1 Normal Force Balance

The left hand side of Eq. (2.10) can be written in terms of the normal and shear stresses at the interface. Because the curvature of the interface is expected to be small, the surface

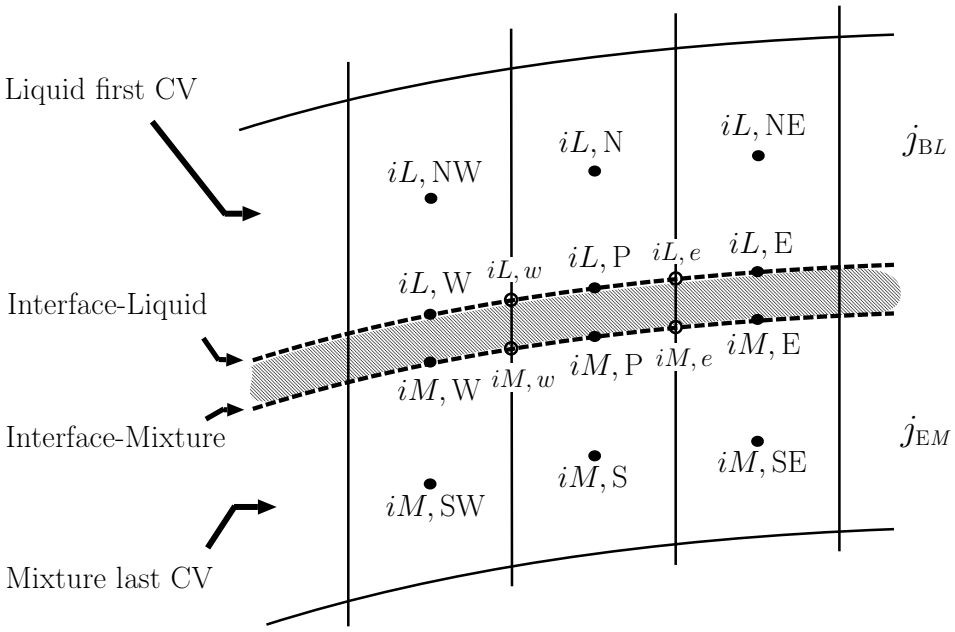

Figure 4.2: Indexing notation for interface and neighbouring control volumes; the spacing between the nodes at the interface is exaggerated for illustration purposes.

tension is neglected, leaving the following equation for the left hand side of Eq. (2.10):

$$\left(\hat{n}\cdot\boldsymbol{\tau}\right)_{iL}\cdot\hat{n}_{iL} = \left(\tau_{zz}\ n_z^2 + 2\ \tau_{zr}\ n_z\ n_r + \tau_{rr}\ n_r^2\right)_{iL} \tag{4.91}$$

Substitution of all stresses into Eq. (4.91) results in:

$$\left(\hat{n}\cdot\boldsymbol{\tau}\right)_{iL}\cdot\hat{n}_{iL} = \left(-P + 2\ \mu\ \left(\frac{\partial U}{\partial z}\right)\ n_z^2 + 2\ \mu\left(\frac{\partial U}{\partial r}+\frac{\partial V}{\partial z}\right)\ n_z\ n_r + 2\ \mu\ \left(\frac{\partial V}{\partial r}\right)\ n_r^2\right)_{iL} \tag{4.92}$$

Following the same procedure, the right hand side term of Eq. (2.10) is given by Eq. (4.93):

$$\left(\hat{n}\cdot\boldsymbol{\tau}\right)_{iM}\cdot\hat{n}_{iM} = \left(-P + 2\ \mu\ \left(\frac{\partial U}{\partial z}\right)\ n_z^2 + 2\ \mu\left(\frac{\partial U}{\partial r}+\frac{\partial V}{\partial z}\right)\ n_z\ n_r + 2\ \mu\ \left(\frac{\partial V}{\partial r}\right)\ n_r^2\right)_{iM} \tag{4.93}$$

The velocity derivatives are evaluated based on central differencing scheme. One-dimensional interpolation is employed to determine the corner values ($U_{iM,e}$ and $U_{iM,w}$) for

the mixture side of the interface and ($U_{iL,e}$ and $U_{iL,w}$) for the liquid side of the interface from its interfacial two neighbours. For example, $U_{iM,e}$ at the mixture side of the interface is determined by ($U_{iM,e} = f_{ne}\ U_{iM\mathrm{P}} + (1 - f_{ne})\ U_{iM,\mathrm{E}}$) where f_{ne} is a linear interpolation factor based on the grid spacing. The derivatives at the interface for any transport variable can be given in general forms by the following expressions:

$$\left.\frac{\partial \Phi}{\partial z}\right|_{iM} = \left(\left.\frac{\partial \Phi}{\partial z}\right|_{n}\right)_{iM,S} = A_{z1}\ \Phi_{iM,\mathrm{S}} + A_{z2}\ \Phi_{iM,\mathrm{P}} + A_{z3}\ \Phi_{iM,\mathrm{E}} + A_{z4}\ \Phi_{iM,\mathrm{W}} \tag{4.94}$$

$$\left.\frac{\partial \Phi}{\partial r}\right|_{iM} = \left(\left.\frac{\partial \Phi}{\partial r}\right|_{n}\right)_{iM,S} = A_{r1}\ \Phi_{iM,\mathrm{S}} + A_{r2}\ \Phi_{iM,\mathrm{P}} + A_{r3}\ \Phi_{iM,\mathrm{E}} + A_{r4}\ \Phi_{iM,\mathrm{W}} \tag{4.95}$$

$$\left.\frac{\partial \Phi}{\partial z}\right|_{iL} = \left(\left.\frac{\partial \Phi}{\partial z}\right|_{s}\right)_{iL,N} = B_{z1}\ \Phi_{iL,\mathrm{N}} + B_{z2}\ \Phi_{iL,\mathrm{P}} + B_{z3}\ \Phi_{iL,\mathrm{E}} + B_{z4}\ \Phi_{iL,\mathrm{W}} \tag{4.96}$$

$$\left.\frac{\partial \Phi}{\partial r}\right|_{iL} = \left(\left.\frac{\partial \Phi}{\partial r}\right|_{s}\right)_{iL,N} = B_{r1}\ \Phi_{iL,\mathrm{N}} + B_{r2}\ \Phi_{iL,\mathrm{P}} + B_{r3}\ \Phi_{iL,\mathrm{E}} + B_{r4}\ \Phi_{iL,\mathrm{W}} \tag{4.97}$$

where Φ stands for U or V or P or T or W and subscript iM,S refers to the control volume centred at iM,S. The subscript iL,N refers to the control volume centred at iL,N. These are the last control volume in the mixture and the first control volume in the liquid, respectively. The coefficients in the Eqs. (4.94) to (4.97) are:

$$\begin{aligned} A_{z1} &= \frac{1}{\Psi_1}\left[\frac{s_{rn}}{(dt)_n}\right]_{iM,\mathrm{S}} & A_{z2} &= \frac{1}{\Psi_1}\left[\frac{t_{rn}}{(ds)_n}\left(f_{ne} - (1 - f_{nw})\right) - \frac{s_{rn}}{(dt)_n}\right]_{iM,\mathrm{S}} \\ A_{z3} &= \frac{1}{\Psi_1}\left[\frac{t_{rn}}{(ds)_n}\ (1 - f_{ne})\right]_{iM,\mathrm{S}} & A_{z4} &= -\frac{1}{\Psi_1}\left[\frac{t_{rn}}{(ds)_n} f_{nw}\right]_{iM,\mathrm{S}} \end{aligned} \tag{4.98}$$

$$\begin{aligned} A_{r1} &= -\frac{1}{\Psi_1}\left[\frac{s_{zn}}{(dt)_n}\right]_{iM,\mathrm{S}} & A_{r2} &= \frac{1}{\Psi_1}\left[\frac{s_{zn}}{(dt)_n} - \frac{t_{zn}}{(ds)_n}\left(f_{ne} - (1 - f_{nw})\right)\right]_{iM,\mathrm{S}} \\ A_{r3} &= -\frac{1}{\Psi_1}\left[\frac{t_{zn}}{(ds)_n}(1 - f_{ne})\right]_{iM,\mathrm{S}} & A_{r4} &= \frac{1}{\Psi_1}\left[\frac{t_{zn}}{(ds)_n} f_{nw}\right]_{iM,\mathrm{S}} \end{aligned} \tag{4.99}$$

$$\begin{aligned} B_{z1} &= -\frac{1}{\Psi_2}\left[\frac{s_{rs}}{(dt)_s}\right]_{iL,\mathrm{N}} & B_{z2} &= \frac{1}{\Psi_2}\left[\frac{t_{rs}}{(ds)_s}\left(f_{se} - (1 - f_{sw})\right) + \frac{s_{rs}}{(dt)_s}\right]_{iL,\mathrm{N}} \\ B_{z3} &= \frac{1}{\Psi_2}\left[\frac{t_{rs}}{(ds)_s}(1 - f_{ne})\right]_{iL,\mathrm{N}} & B_{z4} &= -\frac{1}{\Psi_2}\left[\frac{t_{rs}}{(ds)_s} f_{sw}\right]_{iL,\mathrm{N}} \end{aligned} \tag{4.100}$$

$$B_{r1} = \frac{1}{\Psi_2}\left[\frac{s_{zs}}{(dt)_s}\right]_{iL,\mathrm{N}} \qquad B_{r2} = \frac{1}{\Psi_2}\left[\frac{-s_{zs}}{(dt)_s} - \frac{t_{zs}}{(ds)_s}\left(f_{se} - (1 - f_{sw})\right)\right]_{iL,\mathrm{N}}$$
$$B_{r3} = -\frac{1}{\Psi_2}\left[\frac{t_{zs}}{(ds)_s}\left(1 - f_{se}\right)\right]_{iL,\mathrm{N}} \qquad B_{r4} = \frac{1}{\Psi_2}\left[\frac{t_{zs}}{(ds)_s} f_{nw}\right]_{iL,\mathrm{N}} \tag{4.101}$$

The geometrical terms , Ψ_1 and Ψ_2, are given by:

$$\begin{aligned} \Psi_1 &= \left(s_{zn}\ t_{rn} - t_{zn}\ s_{rn}\right)_{iM,\mathrm{S}} \\ \Psi_2 &= \left(s_{zs}\ t_{rs} - t_{zs}\ s_{rs}\right)_{iL,\mathrm{N}} \end{aligned} \tag{4.102}$$

Applying the mentioned relations, Eqs. (4.92) and (4.93) can be simplified as:

$$\begin{aligned} \left(\hat{n}\cdot\boldsymbol{\tau}\right)_{iL}\cdot\hat{n}_{iL} = -P_{iL} &+ 2\ \left(\mu\ n_z^2\right)_{iL,\mathrm{P}}\left(B_{z1}\ U_{iL,\mathrm{N}} + B_{z2}\ U_{iL,\mathrm{P}} + B_{z3}\ U_{iL,\mathrm{E}} + B_{z4}\ U_{iL,\mathrm{W}}\right) \\ &+2\ \left(\mu\ n_z n_r\right)_{iL,\mathrm{P}}\left(B_{r1}\ U_{iL,\mathrm{N}} + B_{r2}\ U_{iL,\mathrm{P}} + B_{r3}\ U_{iL,\mathrm{E}} + B_{r4}\ U_{iL,\mathrm{W}}\right) \\ &+2\ \left(\mu\ n_z n_r\right)_{iL,\mathrm{P}}\left(B_{z1}\ V_{iL,\mathrm{N}} + B_{z2}\ V_{iL,\mathrm{P}} + B_{z3}\ V_{iL,\mathrm{E}} + B_{z4}\ V_{iL,\mathrm{W}}\right) \\ &+2\ \left(\mu\ n_r^2\right)_{iL,\mathrm{P}}\left(B_{r1}\ V_{iL,\mathrm{N}} + B_{r2}\ V_{iL,\mathrm{P}} + B_{r3}\ V_{iL,\mathrm{E}} + B_{r4}\ V_{iL,\mathrm{W}}\right) \end{aligned} \tag{4.103}$$

$$\begin{aligned} \left(\hat{n}_{iM}\cdot\boldsymbol{\tau}\right)_{iM}\cdot\hat{n}_{iM} = -P_{iM} &+ 2\ \left(\mu\ n_z^2\right)_{iM,P}\left(A_{z1}\ U_{iM,\mathrm{S}} + A_{z2}\ U_{iM,\mathrm{P}} + A_{z3}\ U_{iM,\mathrm{E}} + A_{z4}\ U_{iM,\mathrm{W}}\right) \\ &+2\ \left(\mu\ n_z n_r\right)_{iM,P}\left(A_{r1}\ U_{iM,\mathrm{S}} + A_{r2}\ U_{iM,\mathrm{P}} + A_{r3}\ U_{iM,\mathrm{E}} + A_{r4}\ U_{iM,\mathrm{W}}\right) \\ &+2\ \left(\mu\ n_z n_r\right)_{iM,P}\left(A_{z1}\ V_{iM,\mathrm{S}} + A_{z2}\ V_{iM,\mathrm{P}} + A_{z3}\ V_{iM,\mathrm{E}} + A_{z4}\ V_{iM,\mathrm{W}}\right) \\ &+2\ \left(\mu\ n_r^2\right)_{iM,P}\left(A_{r1}\ V_{iM,\mathrm{S}} + A_{r2}\ V_{iM,\mathrm{P}} + A_{r3}\ V_{iM,\mathrm{E}} + A_{r4}\ V_{iM,\mathrm{W}}\right) \end{aligned} \tag{4.104}$$

Equality of the simplified form of left-hand-side and right-hand-side of the normal force balance equation results in the algebraic form that governs the pressure on the liquid side of the interface.

$$\begin{aligned} &a^{c,p}_{iL,\mathrm{P}}P_{iL,\mathrm{P}} + a^{c,p}_{iL,\mathrm{S}}P_{iM,\mathrm{P}} + a^{c,u}_{iL,\mathrm{P}}U_{iL,\mathrm{P}} + a^{c,u}_{iL,\mathrm{E}}U_{iL,\mathrm{E}} + a^{c,u}_{iL,\mathrm{W}}U_{iL,\mathrm{W}} + a^{c,u}_{iL,\mathrm{N}}U_{iL,\mathrm{N}} + \\ &a^{c,v}_{iL,\mathrm{P}}V_{iL,\mathrm{P}} + a^{c,v}_{iL,\mathrm{E}}V_{iL,\mathrm{E}} + a^{c,v}_{iL,\mathrm{W}}V_{iL,\mathrm{W}} + a^{c,v}_{iL,\mathrm{N}}V_{iL,\mathrm{N}} + a^{c,u}_{iL,\mathrm{S}}U_{iM,\mathrm{P}} + a^{c,u}_{iL,\mathrm{SE}}U_{iM,\mathrm{E}} + \\ &a^{c,u}_{iL,\mathrm{SW}}U_{iM,\mathrm{W}} + a^{c,v}_{iL,\mathrm{S}}V_{iM,\mathrm{P}} + a^{c,v}_{iL,\mathrm{SE}}V_{iM,\mathrm{E}} + a^{c,v}_{iL,\mathrm{SW}}V_{iM,\mathrm{W}} = b^{c}_{iL,\mathrm{P}} \end{aligned} \tag{4.105}$$

The coefficients of Eq. (4.105) are given in Appendix C, Section C.1.

4.3.2 Zero Pressure Gradient on the Mixture Side

This condition is employed on the mixture side of the interface to govern the pressure at iM, P. Discretisation of Eq. (2.20) leads to the algebraic form as follows:

$$\left.\frac{\partial P}{\partial n}\right|_{iM,\mathrm{P}} = \left(A_{z2}P_{iM,\mathrm{P}} + A_{z3}P_{iM,\mathrm{E}} + A_{z4}P_{iM,\mathrm{W}} + A_{z1}P_{iM,\mathrm{S}}\right) n_{zn}|_{iM,\mathrm{S}} + \left(A_{r2}P_{iM,\mathrm{P}} + A_{r3}P_{iM,\mathrm{E}} + A_{r4}P_{iM,\mathrm{W}} + A_{r1}P_{iM,\mathrm{S}}\right) n_{rn}|_{iM,\mathrm{S}} = 0 \quad (4.106)$$

which leads to:

$$a^{c,p}_{iM,\mathrm{P}}P_{iM,\mathrm{P}} + a^{c,p}_{iM,\mathrm{S}}P_{iM,\mathrm{S}} + a^{c,p}_{iM,\mathrm{W}}P_{iM,\mathrm{W}} + a^{c,p}_{iM,\mathrm{E}}P_{iM,\mathrm{E}} = 0 \quad (4.107)$$

The coefficients of Eq. (4.107) are given in Appendix C, Section C.3.

4.3.3 Tangential Force Balance

The algebraic tangential force balance condition is used for the calculation of $U_{iM,\mathrm{P}}$. The left hand side of the Eq. (2.11) with the assumption of negligible surface tension can be written in terms of the normal and shear stresses at the interface as follows:

$$\left(\hat{n}\cdot\boldsymbol{\tau}\right)_{iL}\cdot\hat{s}_{iL} = \left(\tau_{zz}\ n_z s_z + \ \tau_{zr}\left(n_r s_z + n_z s_r\right) + \tau_{rr}\ n_r s_r\right)_{iL} \quad (4.108)$$

which can be further expressed in terms of velocity gradients by applying relations of stress tensor:

$$\left(\hat{n}\cdot\boldsymbol{\tau}\right)_{iL}\cdot\hat{s}_{iL} = \left(2\ \mu\ \left(\frac{\partial U}{\partial z}\right)\ n_z s_z + \ \mu\left(\frac{\partial U}{\partial r} + \frac{\partial V}{\partial z}\right)\left(n_r s_z + n_z s_r\right) + 2\ \mu\ \left(\frac{\partial V}{\partial r}\right)\ n_r s_r\right)_{iL} \quad (4.109)$$

Applying the same procedure for the right hand side of the tangential force balance equation gives:

$$(\hat{n}\cdot\boldsymbol{\tau})_{iM}\cdot\hat{s}_{iM} = \left(2\ \mu\ \left(\frac{\partial U}{\partial z}\right)\ n_z s_z + \ \mu\left(\frac{\partial U}{\partial r}+\frac{\partial V}{\partial z}\right)(n_r s_z + n_z s_r) + 2\ \mu\ \left(\frac{\partial V}{\partial r}\right)\ n_r s_r\right)_{iM} \quad (4.110)$$

The previously mentioned methods of gradients evaluations, simplified the right-hand-side and left-hand-side of the tangential force balance equation as Eq. (4.111) and Eq. (4.112), respectively.

$$\begin{aligned}(\hat{n}\cdot\boldsymbol{\tau})_{iL}\cdot\hat{s}_{iL} = 2\ &(\mu\ n_z s_z)_{iL,\mathrm{P}}\,(B_{z1}\ U_{iL,\mathrm{N}} + B_{z2}\ U_{iL,\mathrm{P}} + B_{z3}\ U_{iL,\mathrm{E}} + B_{z4}\ U_{iL,\mathrm{W}})\\ &+ [\mu\,(n_r s_z + n_z s_r)]_{iL,\mathrm{P}}\,(B_{r1}\ U_{iL,\mathrm{N}} + B_{r2}\ U_{iL,\mathrm{P}} + B_{r3}\ U_{iL,\mathrm{E}} + B_{r4}\ U_{iL,\mathrm{W}})\\ &+ [\mu\,(n_r s_z + n_z s_r)]_{iL,\mathrm{P}}\,(B_{z1}\ V_{iL,\mathrm{N}} + B_{z2}\ V_{iL,\mathrm{P}} + B_{z3}\ V_{iL,\mathrm{E}} + B_{z4}\ V_{iL,\mathrm{W}})\\ &+ 2\,(\mu\ n_r s_r)_{iL,\mathrm{P}}\,(B_{r1}\ V_{iL,\mathrm{N}} + B_{r2}\ V_{iL,\mathrm{P}} + B_{r3}\ V_{iL,\mathrm{E}} + B_{r4}\ V_{iL,\mathrm{W}}) \quad (4.111)\end{aligned}$$

$$\begin{aligned}(\hat{n}_{iM}\cdot\boldsymbol{\tau})_{iM}\cdot\hat{s}_{iM} = &\,2\,(\mu\ n_z s_z)_{iM,\mathrm{P}}\,(A_{z1}\ U_{iM,\mathrm{S}} + A_{z2}\ U_{iM,\mathrm{P}} + A_{z3}\ U_{iM,\mathrm{E}} + A_{z4}\ U_{iM,\mathrm{W}})\\ &+ [\mu\,(n_r s_z + n_z s_r)]_{iM,\mathrm{P}}\,(A_{r1}\ U_{iM,\mathrm{S}} + A_{r2}\ U_{iM,\mathrm{P}} + A_{r3}\ U_{iM,\mathrm{E}} + A_{r4}\ U_{iM,\mathrm{W}})\\ &+ [\mu\,(n_r s_z + n_z s_r)]_{iM,\mathrm{P}}\,(A_{z1}\ V_{iM,\mathrm{S}} + A_{z2}\ V_{iM,\mathrm{P}} + A_{z3}\ V_{iM,\mathrm{E}} + A_{z4}\ V_{iM,\mathrm{W}})\\ &+ 2\,(\mu n_r s_r)_{iM,\mathrm{P}}\,(A_{r1}\ V_{iM,\mathrm{S}} + A_{r2}\ V_{iM,\mathrm{P}} + A_{r3}\ V_{iM,\mathrm{E}} + A_{r4}\ V_{iM,\mathrm{W}})\end{aligned} \quad (4.112)$$

The algebraic form of the equation that governs the U-velocity on the mixture side of the interface can be written as:

$$\begin{aligned}&a^{u,u}_{iM,\mathrm{P}}U_{iM,\mathrm{P}} + a^{u,u}_{iM,\mathrm{E}}U_{iM,\mathrm{E}} + a^{u,u}_{iM,\mathrm{W}}U_{iM,\mathrm{W}} + a^{u,u}_{iM,\mathrm{S}}U_{iM,\mathrm{S}} +\\ &\quad a^{u,v}_{iM,\mathrm{P}}V_{iM,\mathrm{P}} + a^{u,v}_{iM,\mathrm{E}}V_{iM,\mathrm{E}} + a^{u,v}_{iM,\mathrm{W}}V_{iM,\mathrm{W}} + a^{u,v}_{iM,\mathrm{S}}V_{iM,\mathrm{S}} + a^{u,u}_{iM,\mathrm{N}}U_{iL,\mathrm{P}} + a^{u,u}_{iL,\mathrm{NE}}U_{iL,\mathrm{E}} +\\ &\quad\quad a^{u,u}_{iM,\mathrm{NW}}U_{iL,\mathrm{W}} + a^{u,v}_{iM,\mathrm{N}}V_{iL,\mathrm{P}} + a^{u,v}_{iM,\mathrm{NE}}V_{iL,\mathrm{E}} + a^{u,v}_{iM,\mathrm{NW}}V_{iL,\mathrm{W}} = b^{u}_{iM,\mathrm{P}} \quad (4.113)\end{aligned}$$

The coefficients of Eq. (4.113) are given in Appendix C, Section C.2.

4.3.4 Tangential Velocity Equality

The condition of continuous tangential velocity is given by Eq. (2.16). Based on the velocity and tangent vectors the equation can be written as:

$$(U\ \hat{\imath} + V\ \hat{\jmath})_{iM} \cdot (s_z\ \hat{\imath} + s_r\ \hat{\jmath})_{iM} = (U\ \hat{\imath} + V\ \hat{\jmath})_{iL} \cdot (s_z\ \hat{\imath} + s_r\ \hat{\jmath})_{iL} \tag{4.114}$$

This equation is the governing equation for the U velocity on the liquid side of the interface (at iL, P). Therefore, the algebraic form of the equation is:

$$a^{u,u}_{iM,\mathrm{P}} U_{iL,\mathrm{P}} + a^{u,u}_{iM,\mathrm{S}} U_{iM,\mathrm{P}} + a^{u,v}_{iM,\mathrm{P}} V_{iL,\mathrm{P}} + a^{u,v}_{iM,\mathrm{S}} V_{iM,\mathrm{P}} = 0 \tag{4.115}$$

The coefficients of Eq. (4.115) are given in Appendix C, Section C.4.

4.3.5 Mass Balance on the Interface

Equation (2.13) governs the V velocity at the mixture side of the interface (iM, P). This equation can be written in terms of velocity and normal unit vectors as:

$$\left(\rho\, A\ \overrightarrow{V} \cdot \hat{n}\right)_{iL,\mathrm{P}} = \left(\rho\, A\ \overrightarrow{V} \cdot \hat{n}\right)_{iM,\mathrm{P}} \tag{4.116}$$

Simple calculation of the dot product results in:

$$a^{v,u}_{iM,\mathrm{P}} U_{iM,\mathrm{P}} + a^{v,u}_{iM,\mathrm{N}} U_{iL,\mathrm{P}} + a^{v,v}_{iM,\mathrm{P}} V_{iM,\mathrm{P}} + a^{v,v}_{iM,\mathrm{N}} V_{iL,\mathrm{P}} = 0 \tag{4.117}$$

The coefficients of Eq. (4.117) are given in Appendix C, Section C.6.1.

On the other hand, Eq. (2.14) governs the V velocity at the liquid side of the interface (iL, P). This equation can be written in terms of velocity and normal unit vectors as:

$$\left(\rho\, A\ \overrightarrow{V} \cdot \hat{n}\right)_{iL,\mathrm{P}} = \dot{m}_{\mathrm{cond}} = \frac{A_{iL,\mathrm{P}}}{h_{fg}} \left(-k_{iL,\mathrm{P}} \left.\frac{\partial T}{\partial n}\right|_{iL,\mathrm{P}} + k_{iM,\mathrm{P}} \left.\frac{\partial T}{\partial n}\right|_{iM,\mathrm{P}} \right) \tag{4.118}$$

Applying the same approaches for the evaluation of the gradients and calculation of dot product of vectors gives the algebraic form of Eq. (4.118) as:

$$a^{v,u}_{iL,\mathrm{P}}U_{iL,\mathrm{P}} + a^{v,v}_{iL,\mathrm{P}}V_{iL,\mathrm{P}} + a^{v,t}_{iL,\mathrm{P}}T_{iL,\mathrm{P}} + a^{v,t}_{iL,\mathrm{N}}T_{iL,\mathrm{N}} + a^{v,t}_{iL,\mathrm{E}}T_{iL,\mathrm{E}} + a^{v,t}_{iL,\mathrm{W}}T_{iL,\mathrm{W}} + a^{v,t}_{iL,\mathrm{S}}T_{iM,\mathrm{P}} + a^{v,t}_{iL,\mathrm{SE}}T_{iM,\mathrm{E}} + a^{v,t}_{iL,\mathrm{SW}}T_{iM,\mathrm{W}} = b^{v}_{iL,\mathrm{P}} \quad (4.119)$$

The coefficients of Eq. (4.119) are given in Appendix C, Section C.6.2.

4.3.6 Temperature Conditions at the Interface

Since the phase change occurs at the interface, the temperature should be equal to the saturation temperature. This temperature should be calculated based on the pressure and gas mass fraction at that location. Equation (4.120) is used to find the temperature of the mixture side of the interface.

$$T_{iM} = T_{\mathrm{sat}} = A + \frac{B}{\ln\left(P_v \times 10^{-6}\right) + C} \quad (4.120)$$

$A = 0.426776 \times 10^2$, $B = -0.389270 \times 10^4$, and $C = -0.948654 \times 10^1$ [Appendix B]

Substituting of Eq. (2.18) into Eq. (4.120) results in:

$$T_{iM} = T_{\mathrm{sat}} = A + \frac{B}{\ln\left(\frac{P_{iM}(1-W_{iM})M_g \times 10^{-6}}{M_g + W_{iM}(M_v - M_g)}\right) + C} \quad (4.121)$$

The right hand side of Eq. (4.121) is the function of gas mass fraction and pressure at the interface ($T_{iM} = G(W_{iM}, P_{iM})$). Since these two are unknowns, therefore, Newton-Raphson linearisation is applied to linearise the equation. The linearisation forms the equation as follows:

$$T_{iM} = T^o_{iM} + \left.\frac{\partial G}{\partial P_{iM}}\right|_{P^o_{iM}} (P_{iM} - P^o_{iM}) + \left.\frac{\partial G}{\partial W_{iM}}\right|_{W^o_{iM}} (W_{iM} - W^o_{iM}) \quad (4.122)$$

Approximation of the gradients leads to the algebraic form as:

$$a^{t,t}_{iM,\mathrm{P}} T_{iM,\mathrm{P}} + a^{t,p}_{iM,\mathrm{P}} P_{iM,\mathrm{P}} + a^{t,w}_{iM,\mathrm{P}} W_{iM,\mathrm{P}} = b^{t}_{iM,\mathrm{P}} \tag{4.123}$$

The coefficients of Eq. (4.123) are given in Appendix C, Section C.5.1.

For the liquid side, the equation is just the equality of T_{iL} and T_{iM}. Thus the governing equation for the temperature at (iL, P) can be formed as:

$$a^{t,t}_{iL,\mathrm{P}} T_{iL,\mathrm{P}} + a^{t,t}_{iL,\mathrm{S}} T_{iM,\mathrm{P}} = 0 \tag{4.124}$$

The coefficients of Eq. (4.124) are given in Appendix C, Section C.5.2.

4.3.7 Impermeability Equation

Equation (2.19) has an inter-equation coupling term ($\dot{m}_{iM} W_{iM}$). This term includes the velocity components and gas mass fraction on the interface. Therefore, it needs to be linearised using the Newton-Raphson method:

$$\dot{m}_{iM} W_{iM} = \left[\rho n_r V W^o + \rho n_z U W^o + \rho n_r V^o W + \rho n_z U^o W - \rho n_r V^o W^o + \rho n_z U^o W^o\right]_{iM} \tag{4.125}$$

Applying the same approach for the approximation of the gradient term in Eq. (2.19) and use of Eq. (4.125) result in the algebraic form of the impermeability equation:

$$a^{w,w}_{iM,\mathrm{P}} W_{iM,\mathrm{P}} + a^{w,w}_{iM,\mathrm{S}} W_{iM,\mathrm{S}} + a^{w,w}_{iM,\mathrm{E}} W_{iM,\mathrm{E}} + a^{w,w}_{iM,\mathrm{W}} W_{iM,\mathrm{W}} + a^{w,u}_{iM,\mathrm{P}} U_{iM,\mathrm{P}} + a^{w,v}_{iM,\mathrm{P}} V_{iM,\mathrm{P}} = b^{w}_{iM,\mathrm{P}} \tag{4.126}$$

The coefficients of Eq. (4.126) are given in Appendix C, Section C.7.

4.4 Implementation of the Boundary Condition Equations

Boundary conditions are imposed by means of utilizing zero-width boundary control volumes. These control volumes contain a node located at the integration point of each control volume face on the boundary of the solution domain. Each boundary nodal values is defined using a linear algebraic equation and as a function of its nearest interior nodal value of the same dependent variable. The coefficients of the algebraic equation describing each boundary node are determined so that they prescribe the required boundary condition. Then, the boundary condition equations are substituted into the algebraic equations of the control volumes next to the boundaries. Consequently, the boundary conditions are made implicit in all the coupled algebraic equations.The pressure at the boundary nodes is calculated by performing linear extrapolation of the pressure of interior nodes. The extrapolation relations for pressures on the boundaries are subsequently used in all algebraic equations with implicit pressure terms.

4.4.1 Nomenclature for the Boundary Conditions

For the purpose of boundary conditions discussion, any transport variable is referred to as Φ. The code implements two categories of boundary conditions. The first category applies a prescribed value to the boundary, $\Phi_{\mathrm{P}} = \Phi_{bc}$ and is called Dirichlet. The second one is called Neumann in which the gradient is prescribed ($\frac{\partial \Phi}{\partial z}$ or $\frac{\partial \Phi}{\partial r} = \Gamma^{\phi}_{bc}$).

In this section, the west boundary is used as an example to illustrate the way the boundary conditions are being applied. As seen in Fig. 4.3 (a), the boundary conditions are first introduced by taking into account the nine-point equation for the zero width boundary control volume at $(i_{\mathrm{B}} - 1, j)$.

The next inner node, E, is connected to the boundary node P through the boundary

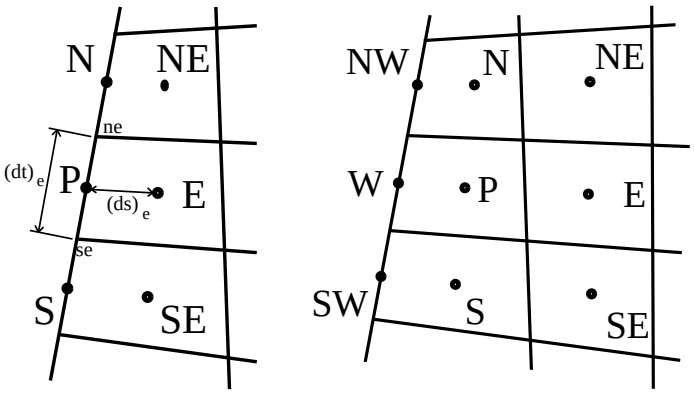

(a) P node at i=i_{B}-1 (b) P node at i=i_{B}

Figure 4.3: West Boundary Computational Molecule

condition. Subsequently, the algebraic equation for the boundary node only uses a^{ϕ}_{P}, a^{ϕ}_{E} and b^{ϕ} coefficients.

Equation (4.29) can be simplified as follows for the fictitious boundary node, $(i_{\mathrm{B}}-1, j)$.

$$a^{\phi,\phi}_{\mathrm{P}(i_{\mathrm{B}}-1,j)}\Phi_{\mathrm{P}(i_{\mathrm{B}}-1,j)} = a^{\phi,\phi}_{\mathrm{E}(i_{\mathrm{B}}-1,j)}\Phi_{\mathrm{E}(i_{\mathrm{B}}-1,j)} + b^{\phi}_{(i_{\mathrm{B}}-1,j)} \tag{4.127}$$

where $\Phi_{E(i_{\mathrm{B}}-1,j)}$ is the first inner node near the boundary.

4.4.2 Dirichlet

In order to implement west Dirichlet boundary condition, $a^{\phi}_{P(i_{\mathrm{B}}-1,j)}$ is set to 1, $(a^{\phi}_{P(i_{\mathrm{B}}-1,j)} = 1)$; $a^{\phi}_{E(i_{\mathrm{B}}-1,j)}$ is set to zero, $(a^{\phi}_{E(i_{\mathrm{B}}-1,j)} = 0)$; and $b^{\phi}_{(i_{\mathrm{B}}-1,j)}$ is set to Φ_{bc}, $(b^{\phi}_{(IB-1,j)} = \Phi_{bc})$. Additionally, all other neighbouring coefficients are set to zero. In this way, it is guaranteed that the boundary transport variable will be the prescribed value, $\Phi_{P(i_{\mathrm{B}}-1,j)} = \Phi_{bc}$.

4.4.3 Neumann

Comparing to the Dirichlet boundary condition, the Neumann boundary condition is less straight forward to implement because of the non-orthogonal grid. In the case of a non-orthogonal grid, $\frac{\partial \Phi}{\partial z}$ should be specified in terms of the gradient along the unit vector directions, $\hat{s}$ and $\hat{t}$. The change in Φ along the west to east direction, $\hat{s}$, and the south to north direction, $\hat{t}$, can be expanded out in a chain rule as shown in Eqs. (4.128) and (4.129), respectively.

$$\frac{\partial \Phi}{\partial s} = \frac{\partial \Phi}{\partial z}\frac{\partial z}{\partial s} + \frac{\partial \Phi}{\partial r}\frac{\partial r}{\partial s} \tag{4.128}$$

$$\frac{\partial \Phi}{\partial t} = \frac{\partial \Phi}{\partial z}\frac{\partial z}{\partial t} + \frac{\partial \Phi}{\partial r}\frac{\partial r}{\partial t} \tag{4.129}$$

The change in Φ in the cylindrical z direction can be calculated as in Eq. (4.130) based on Cramer's rule.

$$\frac{\partial \Phi}{\partial z} = \frac{\begin{vmatrix} \frac{\partial \Phi}{\partial s} & \frac{\partial r}{\partial s} \\ \frac{\partial \Phi}{\partial t} & \frac{\partial r}{\partial t} \end{vmatrix}}{\begin{vmatrix} \frac{\partial z}{\partial s} & \frac{\partial r}{\partial s} \\ \frac{\partial z}{\partial t} & \frac{\partial r}{\partial t} \end{vmatrix}} = \frac{\frac{\partial \Phi}{\partial s}\frac{\partial r}{\partial t} - \frac{\partial \Phi}{\partial t}\frac{\partial r}{\partial s}}{\frac{\partial z}{\partial s}\frac{\partial r}{\partial t} - \frac{\partial r}{\partial s}\frac{\partial z}{\partial t}} \tag{4.130}$$

Employing Eq. (4.130) for the east face of a control volume results in:

$$\left.\frac{\partial \Phi}{\partial z}\right|_e = \frac{\left.\frac{\partial \Phi}{\partial s}\right|_e \left.\frac{\partial r}{\partial t}\right|_e - \left.\frac{\partial \Phi}{\partial t}\right|_e \left.\frac{\partial r}{\partial s}\right|_e}{\left.\frac{\partial z}{\partial s}\right|_e \left.\frac{\partial r}{\partial t}\right|_e - \left.\frac{\partial r}{\partial s}\right|_e \left.\frac{\partial z}{\partial t}\right|_e} = \frac{\left.\frac{\partial \Phi}{\partial s}\right|_e t_{re} - \left.\frac{\partial \Phi}{\partial t}\right|_e s_{re}}{s_{ze}t_{re} - t_{ze}s_{re}} \tag{4.131}$$

Similarly, Eq. (4.130) can be applied to the north face of a control volume as presented in Eq. (4.132).

$$\left.\frac{\partial \Phi}{\partial z}\right|_n = \frac{\left.\frac{\partial \Phi}{\partial s}\right|_n \left.\frac{\partial r}{\partial t}\right|_n - \left.\frac{\partial \Phi}{\partial t}\right|_n \left.\frac{\partial r}{\partial s}\right|_n}{\left.\frac{\partial z}{\partial s}\right|_n \left.\frac{\partial r}{\partial t}\right|_n - \left.\frac{\partial r}{\partial s}\right|_n \left.\frac{\partial z}{\partial t}\right|_n} = \frac{\left.\frac{\partial \Phi}{\partial s}\right|_n t_{rn} - \left.\frac{\partial \Phi}{\partial t}\right|_n s_{rn}}{s_{zn}t_{rn} - t_{zn}s_{rn}} \tag{4.132}$$

Equation (4.131) is used to implement Neumann boundary conditions on the east and west face of a control volume. The change in Φ in the r direction is defined as follows:

$$\frac{\partial \Phi}{\partial r} = \frac{\begin{vmatrix} \frac{\partial z}{\partial s} & \frac{\partial \Phi}{\partial s} \\ \frac{\partial z}{\partial t} & \frac{\partial \Phi}{\partial t} \end{vmatrix}}{\begin{vmatrix} \frac{\partial z}{\partial s} & \frac{\partial r}{\partial s} \\ \frac{\partial z}{\partial t} & \frac{\partial r}{\partial t} \end{vmatrix}} = \frac{\frac{\partial \Phi}{\partial t}\frac{\partial z}{\partial s} - \frac{\partial \Phi}{\partial s}\frac{\partial z}{\partial t}}{\frac{\partial z}{\partial s}\frac{\partial r}{\partial t} - \frac{\partial r}{\partial s}\frac{\partial z}{\partial t}} \tag{4.133}$$

The change in Φ in the r direction for the north face of a control volume can be derived as follows:

$$\left.\frac{\partial \Phi}{\partial r}\right|_n == \frac{\left.\frac{\partial \Phi}{\partial t}\right|_n \left.\frac{\partial z}{\partial s}\right|_n - \left.\frac{\partial \Phi}{\partial s}\right|_n \left.\frac{\partial z}{\partial t}\right|_n}{\left.\frac{\partial z}{\partial s}\right|_n \left.\frac{\partial r}{\partial t}\right|_n - \left.\frac{\partial r}{\partial s}\right|_n \left.\frac{\partial z}{\partial t}\right|_n} = \frac{\left.\frac{\partial \Phi}{\partial t}\right|_n s_{zn} - \left.\frac{\partial \Phi}{\partial s}\right|_n t_{zn}}{s_{zn}t_{rn} - t_{zn}s_{rn}} \tag{4.134}$$

Equation (4.133) can also be revised in the same fashion for the east face of a control volume.

$$\left.\frac{\partial \Phi}{\partial r}\right|_e == \frac{\left.\frac{\partial \Phi}{\partial t}\right|_e \left.\frac{\partial z}{\partial s}\right|_e - \left.\frac{\partial \Phi}{\partial s}\right|_e \left.\frac{\partial z}{\partial t}\right|_e}{\left.\frac{\partial z}{\partial s}\right|_e \left.\frac{\partial r}{\partial t}\right|_e - \left.\frac{\partial r}{\partial s}\right|_e \left.\frac{\partial z}{\partial t}\right|_e} = \frac{\left.\frac{\partial \Phi}{\partial t}\right|_e s_{ze} - \left.\frac{\partial \Phi}{\partial s}\right|_e t_{ze}}{s_{ze}t_{re} - t_{ze}s_{re}} \tag{4.135}$$

Equation (4.134) is used to implement Neumann boundary conditions on the north and south face of a control volume.

In order to implement the Neumann boundary condition on the west boundary, $\frac{\partial \Phi}{\partial z}$ must be set at the west boundary. The desired value for $\frac{\partial \Phi}{\partial z}$ is considered to be Γ^{ϕ}_{bc}. Equation (4.131) is applied to the east face of the west boundary control volume, (at $i = i_{\mathrm{B}} - 1$), and approximation is used for the derivatives. This results in:

$$\left.\frac{\partial \Phi}{\partial z}\right|_{e_{(i_{\mathrm{B}}-1,j)}} = \Gamma^{\phi}_{bc} = \frac{\frac{\Phi_{\mathrm{E}} - \Phi_{\mathrm{P}}}{(ds)_e} t_{re} - \frac{\Phi_{ne} - \Phi_{se}}{(dt)_e} s_{re}}{s_{ze}t_{re} - t_{ze}s_{re}} \tag{4.136}$$

Equation (4.136) can then be rearranged into the form of the boundary algebraic equation, Equation (4.127), as shown below:

$$\Phi_{\mathrm{P}} = \Phi_{\mathrm{E}} - (\Phi_{ne} - \Phi_{se}) \frac{(ds)_e}{(dt)_e} \frac{s_{re}}{t_{re}} - \Gamma^{\phi}_{bc} (ds)_e \frac{s_{ze} t_{re} - t_{ze} s_{re}}{t_{re}} \tag{4.137}$$

The coefficients of the boundary control volume are then assigned as specified in Eq. (4.138). Moreover, all of the neighbour coefficients are set to zero.

$$\left.\begin{aligned} a^{\phi,\phi}_{\mathrm{P}_{(i_{\mathrm{B}}-1,j)}} &= 1, \quad a^{\phi,\phi}_{\mathrm{E}_{(i_{\mathrm{B}}-1,j)}} = 1 \\ b^{\phi}_{(i_{\mathrm{B}}-1,j)} &= -(\Phi_{ne} - \Phi_{se}) \frac{(ds)_e}{(dt)_e} \frac{s_{re}}{t_{re}} - \Gamma^{\phi}_{bc} (ds)_e \frac{s_{ze} t_{re} - t_{ze} s_{re}}{t_{re}} \end{aligned}\right\} \tag{4.138}$$

The control volume velocities at the corners (Φ_{ne} and Φ_{se}) are determined by performing linear interpolation between the nearest nodal values that are also on the boundary. For instance, under the circumstance where the control volume is in a corner of the domain, i.e. $(i_{\mathrm{B}}, j_{\mathrm{B}})$, and both boundaries have Neumann conditions, then $\Phi_{se} = \Phi_{(i_{\mathrm{B}},j_{\mathrm{B}})}$. However, if one of the two boundaries has a Dirichlet condition then Φ_{se} is set to be equal to Φ_{bc} ($\Phi_{se} = \Phi_{bc}$).

4.4.4 Absorbing the Boundary Conditions

As it can be seen from Fig. 4.3 (b), the information from the nodes located on the boundary are necessary to perform calculations for the first inner neighbor node to the west boundary.

Rewriting the Eq. (4.25) for the closest inner node to the west boundary, ($\Phi_{P_{(i_{\mathrm{B}},j)}}$ in Figure 4.3 (b)), results in the following equation:

$$\begin{aligned} a^{\phi,\phi}_{\mathrm{P}_{(i_{\mathrm{B}},j)}} \Phi_{\mathrm{P}_{(i_{\mathrm{B}},j)}} &= a^{\phi,\phi}_{\mathrm{E}_{(i_{\mathrm{B}},j)}} \Phi_{\mathrm{E}_{(i_{\mathrm{B}},j)}} + a^{\phi,\phi}_{\mathrm{W}_{(i_{\mathrm{B}},j)}} \Phi_{\mathrm{W}_{(i_{\mathrm{B}},j)}} + a^{\phi,\phi}_{\mathrm{N}_{(i_{\mathrm{B}},j)}} \Phi_{\mathrm{N}_{(i_{\mathrm{B}},j)}} + a^{\phi,\phi}_{\mathrm{S}_{(i_{\mathrm{B}},j)}} \Phi_{\mathrm{S}_{(i_{\mathrm{B}},j)}} \\ &+ a^{\phi,\phi}_{\mathrm{NE}_{(i_{\mathrm{B}},j)}} \Phi_{\mathrm{NE}_{(i_{\mathrm{B}},j)}} + a^{\phi,\phi}_{\mathrm{SW}_{(i_{\mathrm{B}},j)}} \Phi_{\mathrm{SW}_{(i_{\mathrm{B}},j)}} + a^{\phi,\phi}_{\mathrm{NW}_{(i_{\mathrm{B}},j)}} \Phi_{\mathrm{NW}_{(i_{\mathrm{B}},j)}} + a^{\phi,\phi}_{\mathrm{SE}_{(i_{\mathrm{B}},j)}} \Phi_{\mathrm{SE}_{(i_{\mathrm{B}},j)}} + b^{\phi}_{(i_{\mathrm{B}},j)} \end{aligned} \tag{4.139}$$

This equation is a function of boundary nodal values, specifically Φ_{W}, Φ_{NW}, and Φ_{SW}, which are controlled by the boundary conditions. In order to make the computational domain independent of the boundary nodal values, the boundary nodes should be defined as a function of inner nodes. By rewriting the Eq. (4.127) at $\Phi_{\mathrm{W}(i_{\mathrm{B}},j)}$, the algebraic boundary condition equation for the node at $\Phi_{\mathrm{W}(i_{\mathrm{B}})}$ can be expressed as given in Eq. (4.140). Similar steps are repeated to derive corresponding equations for Φ_{NW} and Φ_{SW}, as provided in Eqs. (4.141) and (4.142), respectively.

$$a^{\phi}_{\mathrm{P}_{(i_{\mathrm{B}}-1,j)}}\Phi_{\mathrm{W}_{(i_{\mathrm{B}},j)}} = a^{\phi}_{\mathrm{E}_{(i_{\mathrm{B}}-1,j)}}\Phi_{\mathrm{P}_{(i_{\mathrm{B}},j)}} + b^{\phi}_{(i_{\mathrm{B}}-1,j)} \tag{4.140}$$

$$a^{\phi}_{\mathrm{P}_{(i_{\mathrm{B}}-1,j+1)}}\Phi_{\mathrm{NW}_{(i_{\mathrm{B}},j)}} = a^{\phi}_{\mathrm{E}_{(i_{\mathrm{B}}-1,j+1)}}\Phi_{\mathrm{N}_{(i_{\mathrm{B}},j)}} + b^{\phi}_{(i_{\mathrm{B}}-1,j+1)} \tag{4.141}$$

$$a^{\phi}_{\mathrm{P}_{(i_{\mathrm{B}}-1,j-1)}}\Phi_{\mathrm{SW}_{(i_{\mathrm{B}},j)}} = a^{\phi}_{\mathrm{E}_{(i_{\mathrm{B}}-1,j-1)}}\Phi_{\mathrm{S}_{(i_{\mathrm{B}},j)}} + b^{\phi}_{(i_{\mathrm{B}}-1,j-1)} \tag{4.142}$$

Now the boundary nodes Φ_{W}, Φ_{NW}, and Φ_{SW} in Eq. (4.139) are replaced with Eqs. (4.140) through (4.142) in order to eliminate the boundary nodes. This substitution results in:

$$\begin{aligned}
a^{\phi,\phi}_{\mathrm{P}_{(i_{\mathrm{B}},j)}}\Phi_{\mathrm{P}_{(i_{\mathrm{B}},j)}} = {} & a^{\phi,\phi}_{\mathrm{E}_{(i_{\mathrm{B}},j)}}\Phi_{\mathrm{E}_{(i_{\mathrm{B}},j)}} + a^{\phi,\phi}_{\mathrm{N}_{(i_{\mathrm{B}},j)}}\Phi_{\mathrm{N}_{(i_{\mathrm{B}},j)}} + a^{\phi,\phi}_{\mathrm{S}_{(i_{\mathrm{B}},j)}}\Phi_{\mathrm{S}_{(i_{\mathrm{B}},j)}} \\
& + a^{\phi,\phi}_{\mathrm{NE}_{(i_{\mathrm{B}},j)}}\Phi_{\mathrm{NE}_{(i_{\mathrm{B}},j)}} + a^{\phi,\phi}_{\mathrm{SE}_{(i_{\mathrm{B}},j)}}\Phi_{\mathrm{SE}_{(i_{\mathrm{B}},j)}} \\
& + a^{\phi,\phi}_{\mathrm{W}_{(i_{\mathrm{B}},j)}}\left[\frac{a^{\phi,\phi}_{\mathrm{E}_{(i_{\mathrm{B}}-1,j)}}}{a^{\phi,\phi}_{\mathrm{P}_{(i_{\mathrm{B}}-1,j)}}}\Phi_{\mathrm{P}_{(i_{\mathrm{B}},j)}} + \frac{b^{\phi}_{(i_{\mathrm{B}}-1)}}{a^{\phi,\phi}_{\mathrm{P}_{(i_{\mathrm{B}}-1)}}}\right] \\
& + a^{\phi,\phi}_{\mathrm{SW}_{(i_{\mathrm{B}},j)}}\left[\frac{a^{\phi,\phi}_{\mathrm{E}_{(i_{\mathrm{B}}-1,j-1)}}}{a^{\phi,\phi}_{\mathrm{P}_{(i_{\mathrm{B}}-1,j-1)}}}\Phi_{\mathrm{S}_{(i_{\mathrm{B}},j)}} + \frac{b^{\phi}_{(i_{\mathrm{B}}-1,j-1)}}{a^{\phi,\phi}_{\mathrm{P}_{(i_{\mathrm{B}}-1,j-1)}}}\right] \\
& + a^{\phi,\phi}_{\mathrm{NW}_{(i_{\mathrm{B}},j)}}\left[\frac{a^{\phi,\phi}_{\mathrm{E}_{(i_{\mathrm{B}}-1,j+1)}}}{a^{\phi,\phi}_{\mathrm{P}_{(i_{\mathrm{B}}-1,j+1)}}}\Phi_{\mathrm{N}_{(i_{\mathrm{B}},j)}} + \frac{b^{\phi}_{(i_{\mathrm{B}}-1,j+1)}}{a^{\phi,\phi}_{\mathrm{P}_{(i_{\mathrm{B}}-1,j+1)}}}\right] + b^{\phi}_{(i_{\mathrm{B}},j)}
\end{aligned} \tag{4.143}$$

The coefficients in Eq. (4.143) are further rearranged and simplified to form Eq. (4.144)

which is the basis for boundary condition absorption.

$$\left(a^{\phi,\phi}_{\mathrm{P}_{(i_\mathrm{B},j)}} - a^{\phi,\phi}_{\mathrm{W}_{(i_\mathrm{B},j)}} \frac{a^{\phi,\phi}_{\mathrm{E}_{(i_\mathrm{B}-1,j)}}}{a^{\phi,\phi}_{\mathrm{P}_{(i_\mathrm{B}-1,j)}}}\right) \Phi_{\mathrm{P}_{(i_\mathrm{B},j)}} =$$

$$a^{\phi,\phi}_{\mathrm{E}_{(i_\mathrm{B},j)}} \Phi_{\mathrm{E}_{(i_\mathrm{B},j)}} + \left(a^{\phi,\phi}_{\mathrm{N}_{(i_\mathrm{B},j)}} + a^{\phi,\phi}_{\mathrm{NW}_{(i_\mathrm{B},j)}} \frac{a^{\phi,\phi}_{\mathrm{E}_{(i_\mathrm{B}-1,j+1)}}}{a^{\phi,\phi}_{\mathrm{P}_{(i_\mathrm{B}-1,j+1)}}}\right) \Phi_{\mathrm{N}_{(i_\mathrm{B},j)}}$$

$$+ \left(a^{\phi,\phi}_{\mathrm{S}_{(i_\mathrm{B},j)}} + a^{\phi,\phi}_{\mathrm{SW}_{(i_\mathrm{B},j)}} \frac{a^{\phi,\phi}_{\mathrm{E}_{(i_\mathrm{B}-1,j-1)}}}{a^{\phi,\phi}_{\mathrm{P}_{(i_\mathrm{B}-1,j-1)}}}\right) \Phi_{\mathrm{S}_{(i_\mathrm{B},j)}} + a^{\phi,\phi}_{\mathrm{NE}_{(i_\mathrm{B},j)}} \Phi_{\mathrm{NE}_{(i_\mathrm{B},j)}} + a^{\phi,\phi}_{\mathrm{SE}_{(i_\mathrm{B},j)}} \Phi_{\mathrm{SE}_{(i_\mathrm{B},j)}}$$

$$+ \left(b^{\phi}_{(i_\mathrm{B},j)} + a^{\phi,\phi}_{\mathrm{W}_{(i_\mathrm{B},j)}} \frac{b^{\phi}_{(i_\mathrm{B}-1,j)}}{a^{\phi,\phi}_{\mathrm{P}_{(i_\mathrm{B}-1,j)}}} + a^{\phi,\phi}_{\mathrm{SW}_{(i_\mathrm{B},j)}} \frac{b^{\phi}_{(i_\mathrm{B}-1,j-1)}}{a^{\phi,\phi}_{\mathrm{P}_{(i_\mathrm{B}-1,j-1)}}} + a^{\phi,\phi}_{NW_{(i_\mathrm{B},j)}} \frac{b^{\phi}_{(i_\mathrm{B}-1,j+1)}}{a^{\phi,\phi}_{\mathrm{P}_{(i_\mathrm{B}-1,j+1)}}}\right) \quad (4.144)$$

The coefficients of the equation for $\Phi_{\mathrm{P}_{(i_\mathrm{B},j)}}$ have been adjusted as below in order to absorb the boundary conditions.

$$\left.\begin{aligned}
a^{\phi,\phi}_{\mathrm{P}(i_\mathrm{B},j)} &= a^{\phi,\phi}_{\mathrm{P}(i_\mathrm{B},j)} - a^{\phi,\phi}_{\mathrm{W}(i_\mathrm{B},j)} \frac{a^{\phi,\phi}_{\mathrm{E}(i_\mathrm{B}-1,j)}}{a^{\phi,\phi}_{\mathrm{P}(i_\mathrm{B}-1,j)}} \\
a^{\phi,\phi}_{\mathrm{N}(i_\mathrm{B},j)} &= a^{\phi,\phi}_{\mathrm{N}(i_\mathrm{B},j)} + a^{\phi,\phi}_{\mathrm{NW}(i_\mathrm{B},j)} \frac{a^{\phi,\phi}_{\mathrm{E}(i_\mathrm{B}-1,j+1)}}{a^{\phi,\phi}_{\mathrm{P}(i_\mathrm{B}-1,j+1)}} \\
a^{\phi,\phi}_{\mathrm{S}(i_\mathrm{B},j)} &= a^{\phi,\phi}_{\mathrm{S}(i_\mathrm{B},j)} + a^{\phi,\phi}_{\mathrm{SW}(i_\mathrm{B},j)} \frac{a^{\phi,\phi}_{\mathrm{E}(i_\mathrm{B}-1,j-1)}}{a^{\phi,\phi}_{\mathrm{P}(i_\mathrm{B}-1,j-1)}} \\
b^{\phi}_{(i_\mathrm{B},j)} &= b^{\phi}_{(i_\mathrm{B},j)} + a^{\phi,\phi}_{\mathrm{W}(i_\mathrm{B},j)} \frac{b^{\phi}_{(i_\mathrm{B}-1,j)}}{a^{\phi,\phi}_{\mathrm{P}(i_\mathrm{B}-1,j)}} \\
&\quad + a^{\phi,\phi}_{\mathrm{SW}(i_\mathrm{B},j)} \frac{b^{\phi}_{(i_\mathrm{B}-1,j-1)}}{a^{\phi,\phi}_{\mathrm{P}(i_\mathrm{B}-1,j-1)}} + a^{\phi,\phi}_{\mathrm{NW}(i_\mathrm{B},j)} \frac{b^{\phi}_{(i_\mathrm{B}-1,j+1)}}{a^{\phi,\phi}_{\mathrm{P}(i_\mathrm{B}-1,j+1)}}
\end{aligned}\right\} \quad (4.145)$$

After the modifications of the interior node coefficients to implement the boundary conditions, the $a_{\mathrm{W}(i_\mathrm{B},j)}$, $a_{\mathrm{SW}(i_\mathrm{B},j)}$, and $a_{\mathrm{NW}(i_\mathrm{B},j)}$ are set to zero.

4.4.5 Face Velocity Boundary Conditions

The face velocity boundary conditions are implemented using the coefficients of the continuity equation at the boundary node control volumes. Again, the west boundary is used as an example to illustrate the face velocity boundary conditions. The remaining boundaries, i.e. east, south, and north are analogous to the west boundary.

The first step is to write the continuity equation for the control volume adjacent to the west boundary, (i_{B}) as in Figure 4.3 (b).

$$\left(a^{c,u}_{e(i_{\mathrm{B}}-1)}U_e + a^{c,v}_{e(i_{\mathrm{B}}-1)}V_e\right) + \left(a^{c,u}_{w(i_{\mathrm{B}}-1)}U_w + a^{c,v}_{w(i_{\mathrm{B}}-1)}V_w\right) + \left(a^{c,u}_{n(i_{\mathrm{B}}-1)}U_n + a^{c,v}_{n(i_{\mathrm{B}}-1)}V_n\right) + \left(a^{c,u}_{s(i_{\mathrm{B}}-1)}U_s + a^{c,v}_{s(i_{\mathrm{B}}-1)}V_s\right) + b^{c}_{\mathrm{P}} = 0 \quad (4.146)$$

In the above continuity equation, all coefficients are for the j index control volumes, so that subscript is omitted for clarity. One can use Eq. (4.146) to produce separate equations for U_w and V_w as follows:

$$U_w = \frac{-1}{a^{c,u}_{w(i_{\mathrm{B}}-1)}}\left\{\left(a^{c,u}_{e(i_{\mathrm{B}}-1)}U_e + a^{c,v}_{e(i_{\mathrm{B}}-1)}V_e\right) + a^{c,v}_{w(i_{\mathrm{B}}-1)}V_w + \left(a^{c,u}_{n(i_{\mathrm{B}}-1)}U_n + a^{c,v}_{n(i_{\mathrm{B}}-1)}V_n\right) + \left(a^{c,u}_{s(i_{\mathrm{B}}-1)}U_s + a^{c,v}_{s(i_{\mathrm{B}}-1)}V_s\right) + b^{c}_{\mathrm{P}}\right\} \quad (4.147)$$

$$V_w = \frac{-1}{a^{c,v}_{v_w(i_{\mathrm{B}}-1)}}\left\{\left(a^{c,u}_{u_e(i_{\mathrm{B}}-1)}U_e + a^{c,v}_{v_e(i_{\mathrm{B}}-1)}V_e\right) + a^{c,u}_{u_w(i_{\mathrm{B}}-1)}U_w + \left(a^{c,u}_{u_n(i_{\mathrm{B}}-1)}U_n + a^{c,v}_{v_n(i_{\mathrm{B}}-1)}V_n\right) + \left(a^{c,u}_{u_s(i_{\mathrm{B}}-1)}U_s + a^{c,v}_{v_s(i_{\mathrm{B}}-1)}V_s\right) + b^{c}_{\mathrm{P}}\right\} \quad (4.148)$$

The coefficient, $a^{c,u}_{w(i_{\mathrm{B}}-1)}$, in the denominator of Eq. (4.147) is not needed so it is replaced by -1 and moved to act as source term as follows:

$$U_w = \left(a^{c,u}_{e(i_{\mathrm{B}}-1)}U_e + a^{c,v}_{e(i_{\mathrm{B}}-1)}V_e\right) + a^{c,v}_{w(i_{\mathrm{B}}-1)}V_w \left(+a^{c,u}_{n(i_{\mathrm{B}}-1)}U_n + a^{c,v}_{n(i_{\mathrm{B}}-1)}V_n\right)\left(+a^{c,u}_{s(i_{\mathrm{B}}-1)}U_s + a^{c,v}_{s(i_{\mathrm{B}}-1)}V_s\right) + a^{c,u}_{w(i_{\mathrm{B}}-1)} \quad (4.149)$$

The V_w equation is rearranged in a similar way to obtain:

$$V_w = \left(a^{c,u}_{e(i_B-1)}U_e + a^{c,v}_{e(i_B-1)}V_e\right) + a^{c,u}_{w(i_B-1)}U_w \\ \left(+a^{c,u}_{n(i_B-1)}U_n + a^{c,v}_{n(i_B-1)}V_n\right)\left(+a^{c,u}_{s(i_B-1)}U_s + a^{c,v}_{s(i_B-1)}V_s\right) + a^{c,v}_{w(i_B-1)} \quad (4.150)$$

The U and V velocity boundary conditions are set independently, and the north and south face velocities are not used to set the west boundary conditions, so Eqs. (4.149) and (4.150) can be simplified to:

$$U_w = a^{c,u}_{e(i_B-1)}U_e + a^{c,u}_{w(i_B-1)} \quad (4.151)$$

and,

$$V_w = a^{c,v}_{e(i_B-1)}V_e + a^{c,v}_{w(i_B-1)} \quad (4.152)$$

respectively.

In order to apply the Dirichlet west face boundary condition $A^c_{u_w(i_B-1)}$ is considered to be equal to U_{bc} for the U velocity ($A^c_{u_w(i_B-1)} = U_{bc}$), and $A^c_{v_w(i_B-1)}$ is set to V_{bc} ($A^c_{v_w(i_B-1)} = V_{bc}$) for the V velocity. All the remaining continuity coefficients are set to zero.

Similar to what has been explained in Section 4.4.4 for nodal boundary conditions, the Neumann boundary condition for face velocity on the west face is implemented by employing, for the U velocity for example, $\frac{\partial U}{\partial z} = \Gamma^u_{bc}$ at the west boundary across the first control volume, from west face to east face, instead of between nodes.

$$\left.\frac{\partial U}{\partial z}\right|_{(i_B,j)} = \Gamma^u_{bc} = \frac{\dfrac{U_e - U_w}{(ds)_p}t_{rw} - \dfrac{U_{nw} - U_{sw}}{(dt)_w}s_{rp}}{s_{zp}t_{rw} - t_{zw}s_{rp}} \quad (4.153)$$

Rearranging Eq. (4.153) in the form of Eq. (4.151) and Eq. (4.152) produces:

$$U_w = U_e - (U_{nw} - U_{sw})\frac{(ds)_p}{(dt)_w}\frac{s_{rp}}{t_{rw}} - \Gamma^u_{bc}(ds)_p\frac{s_{zp}t_{rw} - t_{zw}s_{rp}}{t_{rw}} \quad (4.154)$$

which leads to the following specification for the continuity coefficients on the boundary:

$$\left.\begin{array}{rclrcl}
a^{c,u}_{e(i_{\mathrm{B}}-1)} &=& 1 & a^{c,v}_{e(i_{\mathrm{B}}-1)} &=& 0 \\
a^{c,u}_{n(i_{\mathrm{B}}-1)} &=& 0 & a^{c,v}_{n(i_{\mathrm{B}}-1)} &=& 0 \\
a^{c,u}_{s(i_{\mathrm{B}}-1)} &=& 0 & a^{c,v}_{s(i_{\mathrm{B}}-1)} &=& 0 \\
a^{c,v}_{w(i_{\mathrm{B}}-1)} &=& 0 & & & \\
a^{c,u}_{w(i_{\mathrm{B}}-1)} &=& -\left(U_{nw}-U_{sw}\right)\dfrac{(ds)_p}{(dt)_w}\dfrac{s_{rp}}{t_{rw}} - \Gamma^u_{bc}(ds)_p\dfrac{s_{zp}t_{rw}-t_{zw}s_{rp}}{t_{rw}} & & &
\end{array}\right\} \quad (4.155)$$

The V face velocity Neumann boundary condition is implemented in an analogous way.

$$\left.\begin{array}{rclrcl}
a^{c,u}_{u_e(i_{\mathrm{B}}-1)} &=& 0 & a^{c,v}_{v_e(i_{\mathrm{B}}-1)} &=& 1 \\
a^{c,u}_{u_n(i_{\mathrm{B}}-1)} &=& 0 & a^{c,v}_{v_n(i_{\mathrm{B}}-1)} &=& 0 \\
a^{c,u}_{u_s(i_{\mathrm{B}}-1)} &=& 0 & a^{c,v}_{v_s(i_{\mathrm{B}}-1)} &=& 0 \\
a^{c,u}_{u_w(i_{\mathrm{B}}-1)} &=& 0 & & & \\
a^{c,v}_{v_w(i_{\mathrm{B}}-1)} &=& -\left(V_{nw}-V_{sw}\right)\dfrac{(ds)_p}{(dt)_w}\dfrac{s_{rp}}{t_{rw}} - \Gamma^v_{bc}(ds)_p\dfrac{s_{zp}t_{rw}-t_{zw}s_{rp}}{t_{rw}} & & &
\end{array}\right\} \quad (4.156)$$

To absorb these boundary conditions into the interior nodal equations, Eqs. (4.151) and (4.152) are substituted into the continuity equation, Eq. (4.146), as follows:

$$\begin{aligned}
&\left(a^{c,u}_{e(i_{\mathrm{B}})}U_e + a^{c,v}_{e(i_{\mathrm{B}})}V_e\right) \\
&\quad + a^{c,u}_{w(i_{\mathrm{B}})}\left(a^{c,u}_{e(i_{\mathrm{B}}-1)}U_e + a^{c,u}_{w(i_{\mathrm{B}}-1)}\right) + a^{c,v}_{w(i_{\mathrm{B}})}\left(a^{c,v}_{e(i_{\mathrm{B}}-1)}V_e + a^{c,v}_{w(i_{\mathrm{B}}-1)}\right) \\
&\quad + \left(a^{c,u}_{n(i_{\mathrm{B}})}U_n + a^{c,v}_{n(i_{\mathrm{B}})}V_n\right) + \left(a^{c,u}_{s(i_{\mathrm{B}})}U_s + a^{c,v}_{s(i_{\mathrm{B}})}V_s\right) + b^c_P = 0
\end{aligned} \quad (4.157)$$

Collecting terms yields:

$$\left(a^{c,u}_{u_e(i_\mathrm{B})} + a^{c,u}_{u_w(i_\mathrm{B})}a^{c,u}_{u_e(i_\mathrm{B}-1)}\right)U_e + \left(a^{c,v}_{v_e(i_\mathrm{B})} + a^{c,v}_{v_w(i_\mathrm{B})}a^{c,v}_{v_e(i_\mathrm{B}-1)}\right)V_e + a^{c,u}_{u_w(i_\mathrm{B})}a^{c,u}_{u_w(i_\mathrm{B}-1)} + a^{c,v}_{v_w(i_\mathrm{B})}a^{c,v}_{v_w(i_\mathrm{B}-1)} + \left(a^{c,u}_{u_n(i_\mathrm{B})}U_n + a^{c,v}_{v_n(i_\mathrm{B})}V_n\right) + \left(a^{c,u}_{u_s(i_\mathrm{B})}U_s + a^{c,v}_{v_s(i_\mathrm{B})}V_s\right) + b^c_{P(i_\mathrm{B})} = 0 \quad (4.158)$$

The east face velocities are replaced by the PWIM face velocities definition (see Eqs. (4.7) and (4.8)) which gives:

$$\begin{aligned}
&\left[a^{c,u}_{\mathrm{E}(i_\mathrm{B})} + \left(a^{c,u}_{\mathrm{E}(i_\mathrm{B})}\right)^{\oplus}\right]U_\mathrm{E} + \left[a^{c,u}_{\mathrm{P}(i_\mathrm{B})} + \left(a^{c,u}_{\mathrm{P}(i_\mathrm{B})}\right)^{\oplus}\right]U_\mathrm{P} + \left[a^{c,v}_{\mathrm{E}(i_\mathrm{B})} + \left(a^{c,v}_{\mathrm{E}(i_\mathrm{B})}\right)^{\oplus}\right]V_\mathrm{E} \\
&+ \left[a^{c,v}_{\mathrm{P}(i_\mathrm{B})} + \left(a^{c,v}_{\mathrm{P}(i_\mathrm{B})}\right)^{\oplus}\right]V_\mathrm{P} + \left[a^{c,p}_{\mathrm{P}(i_\mathrm{B})} - \left(a^{c,P}_{\mathrm{P}(i_\mathrm{B})}\right)^{\oplus}\right]P_\mathrm{P} + \left[a^{c,p}_{\mathrm{E}(i_\mathrm{B})} - \left(a^{c,P}_{\mathrm{E}(i_\mathrm{B})}\right)^{\oplus}\right]P_\mathrm{E} \\
&+ \left[a^{c,p}_{\mathrm{N}(i_\mathrm{B})} - \left(a^{c,P}_{\mathrm{N}(i_\mathrm{B})}\right)^{\oplus}\right]P_\mathrm{N} + \left[a^{c,p}_{\mathrm{S}(i_\mathrm{B})} - \left(a^{c,P}_{\mathrm{S}(i_\mathrm{B})}\right)^{\oplus}\right]P_\mathrm{S} + \left[a^{c,p}_{\mathrm{NE}(i_\mathrm{B})} - \left(a^{c,P}_{\mathrm{N}(i_\mathrm{B})}\right)^{\oplus}\right]P_\mathrm{NE} \\
&+ \left[a^{c,p}_{\mathrm{SE}(i_\mathrm{B})} - \left(a^{c,P}_{\mathrm{S}(i_\mathrm{B})}\right)^{\oplus}\right]P_\mathrm{SE} + a^{c,u}_{u_w(i_\mathrm{B})}a^{c,u}_{u_w(i_\mathrm{B}-1)} + a^{c,v}_{v_w(i_\mathrm{B})}a^{c,v}_{v_w(i_\mathrm{B}-1)} \\
&+ \left(a^{c,u}_{u_n(i_\mathrm{B})}U_n + a^{c,v}_{v_n(i_\mathrm{B})}V_n\right) + \left(a^{c,u}_{u_s(i_\mathrm{B})}U_s + a^{c,v}_{v_s(i_\mathrm{B})}V_s\right) + \left(b^c_{P(i_\mathrm{B})} + \left(b^c_{P(i_\mathrm{B})}\right)^{\oplus}\right) = 0 \quad (4.159)
\end{aligned}$$

where the superscript "$\oplus$" refers to modifications to the continuity coefficients in Eq. (4.146). The east U and V continuity coefficients are then modified for the west boundary and the source term has additional terms as follows:

$$\left.\begin{aligned}
\left(a^{c,u}_{\mathrm{E}(i_\mathrm{B})}\right)^{\oplus} &= (1-\mathcal{W}_e)a^{c,u}_{u_w(i_\mathrm{B})}a^{c,u}_{u_e(i_\mathrm{B}-1)} \\
\left(a^{c,u}_{\mathrm{P}(i_\mathrm{B})}\right)^{\oplus} &= \mathcal{W}_e a^{c,u}_{u_w(i_\mathrm{B})}a^{c,u}_{u_e(i_\mathrm{B}-1)} \\
\left(a^{c,v}_{\mathrm{E}(i_\mathrm{B})}\right)^{\oplus} &= (1-\mathcal{W}_e)a^{c,v}_{v_w(i_\mathrm{B})}a^{c,v}_{v_e(i_\mathrm{B}-1)} \\
\left(a^{c,v}_{\mathrm{P}(i_\mathrm{B})}\right)^{\oplus} &= \mathcal{W}_e a^{c,v}_{v_w(i_\mathrm{B})}a^{c,v}_{v_e(i_\mathrm{B}-1)} \\
\left(a^{c,p}_{\mathrm{P}(i_\mathrm{B})}\right)^{\oplus} &= a^{c,u}_{u_w(i_\mathrm{B})}a^{c,u}_{u_e(i_\mathrm{B}-1)}\hat{d}^u_e\left[\frac{-\mathcal{R}_{t,e}}{(ds)_e} + \frac{\mathcal{R}_{s,e}}{(dt)_e}\left(C_{se4} - C_{ne1}\right)\right] \\
&+ a^{c,v}_{v_w(i_\mathrm{B})}a^{c,v}_{v_e(i_\mathrm{B}-1)}\hat{d}^v_e\left[\frac{\mathcal{Z}_{t,e}}{(ds)_e} + \frac{\mathcal{Z}_{s,e}}{(dt)_e}\left(C_{ne1} - C_{se4}\right)\right]
\end{aligned}\right\} \quad (4.160a)$$

$$
\left.
\begin{aligned}
\left(a^{c,p}_{\mathrm{E}(i_\mathrm{B})}\right)^{\oplus} &= a^{c,u}_{u_w(i_\mathrm{B})} a^{c,u}_{u_e(i_\mathrm{B}-1)} \hat{d}^u_e \left[\frac{\mathcal{R}_{t,e}}{(ds)_e} - \frac{\mathcal{R}_{s,e}}{(dt)_e}\left(C_{ne2} - C_{se3}\right)\right] \\
&+ a^{c,v}_{v_w(i_\mathrm{B})} a^{c,v}_{v_e(i_\mathrm{B}-1)} \hat{d}^v_e \left[\frac{-\mathcal{Z}_{t,e}}{(ds)_e} + \frac{\mathcal{Z}_{s,e}}{(dt)_e}\left(C_{ne2} - C_{se3}\right)\right] \\
\left(a^{c,p}_{\mathrm{N}(i_\mathrm{B})}\right)^{\oplus} &= C_{ne4}\left[a^{c,u}_{u_w(i_\mathrm{B})} a^{c,u}_{u_e(i_\mathrm{B}-1)} \hat{d}^u_e \frac{-\mathcal{R}_{s,e}}{(dt)_e} + a^{c,v}_{v_w(i_\mathrm{B})} a^{c,v}_{v_e(i_\mathrm{B}-1)} \hat{d}^v_e \frac{\mathcal{Z}_{s,e}}{(dt)_e}\right] \\
\left(a^{c,p}_{\mathrm{S}(i_\mathrm{B})}\right)^{\oplus} &= C_{se1}\left[a^{c,u}_{u_w(i_\mathrm{B})} a^{c,u}_{u_e(i_\mathrm{B}-1)} \hat{d}^u_e \frac{\mathcal{R}_{s,e}}{(dt)_e} - a^{c,v}_{v_w(i_\mathrm{B})} a^{c,v}_{v_e(i_\mathrm{B}-1)} \hat{d}^v_e \frac{\mathcal{Z}_{s,e}}{(dt)_e}\right] \\
\left(a^{c,p}_{\mathrm{NE}(i_\mathrm{B})}\right)^{\oplus} &= C_{ne3}\left[-a^{c,u}_{u_w(i_\mathrm{B})} a^{c,u}_{u_e(i_\mathrm{B}-1)} \hat{d}^u_e \frac{\mathcal{R}_{s,e}}{(dt)_e} + a^{c,v}_{v_w(i_\mathrm{B})} a^{c,v}_{v_e(i_\mathrm{B}-1)} \hat{d}^v_e \frac{\mathcal{Z}_{s,e}}{(dt)_e}\right] \\
\left(a^{c,p}_{\mathrm{SE}(i_\mathrm{B})}\right)^{\oplus} &= C_{se2}\left[a^{c,u}_{u_w(i_\mathrm{B})} a^{c,u}_{u_e(i_\mathrm{B}-1)} \hat{d}^u_e \frac{\mathcal{R}_{s,e}}{(dt)_e} - a^{c,v}_{v_w(i_\mathrm{B})} a^{c,v}_{v_e(i_\mathrm{B}-1)} \hat{d}^v_e \frac{\mathcal{Z}_{s,e}}{(dt)_e}\right] \\
\left(b^{c}_{P(i_\mathrm{B})}\right)^{\oplus} &= a^{c,u}_{u_w(i_\mathrm{B})} a^{c,u}_{u_w(i_\mathrm{B}-1)} + a^{c,v}_{v_w(i_\mathrm{B})} a^{c,v}_{v_w(i_\mathrm{B}-1)}
\end{aligned}
\right\} \tag{4.160b}
$$

4.5 E-Factor

This work is focused only on the steady-state solution to the governing equations, so transient terms are used in the equations only as relaxation in the solution of the coupled non-linear set of equations.

Van Doormaal and Raithby [61] and Raithby and Schneider [62] replaced the transient term with a distorted transient term and defined a so-called E-factor, E. To use the distorted transient, part of the original transient term is redefined as:

$$
\frac{\rho_\mathrm{P} \forbidden{\mathcal{V}}_\mathrm{P}}{\Delta t} = \frac{\left(a^{u,u}_\mathrm{P}\right)^*}{E^u} \tag{4.161}
$$

where,

$$
\begin{aligned}
\left(a^{u,u}_\mathrm{P}\right)^* = &-\left(0.5 - \alpha_e\right)\dot{m}_e + \left(0.5 + \alpha_w\right)\dot{m}_w - \left(0.5 - \alpha_n\right)\dot{m}_n + \left(0.5 + \alpha_s\right)\dot{m}_s \\
&+ \frac{D^u_e \beta_e}{\hat{n}_e \cdot \hat{s}_e} + \frac{D^u_w \beta_w}{\hat{n}_w \cdot \hat{s}_w} + \frac{D^u_n \beta_n}{\hat{n}_n \cdot \hat{s}_n} + \frac{D^u_s \beta_s}{\hat{n}_s \cdot \hat{s}_s} + D^u_e \beta_e \gamma_{z,e}\left(C_{ne1} - C_{se1}\right) \\
&- D^u_w \beta_w \gamma_{z,w}\left(C_{nw1} - C_{sw1}\right) + D^u_n \beta_n \gamma_{r,n}\left(C_{ne1} - C_{nw1}\right) - D^u_s \beta_s \gamma_{r,s}\left(C_{se1} - C_{sw1}\right)
\end{aligned} \tag{4.162}
$$

Substituting Eq. (4.161) into Eq. (4.65) and Eq. (4.81) produces the following new definition of the $a_{\mathrm{P}}^{u,u}$ and b_{P}^{u} coefficients:

$$a_{\mathrm{P}}^{u,u} = (a_{\mathrm{P}}^{u,u})^* + \frac{(a_{\mathrm{P}}^{u,u})^*}{E^u} \tag{4.163}$$

and,

$$b_{\mathrm{P}}^{u} = \frac{(a_{\mathrm{P}}^{u,u})^*}{E^u} U_{\mathrm{P}}^{o} + \rho_{\mathrm{P}} g \forbidden{V}_{\mathrm{P}} \tag{4.164}$$

accordingly. A similar definition is used for the V, T, and W equations.

The E-factor formulation allows taking a different Δt in each control volume (if the control volumes have different sizes), which can lead to faster convergence. In the computer code implementation of the coefficient calculations, both the E-factor and true transient formulations are available and are selected through the specification of E and Δt values. When the E-factor formulation is used, the coefficients of the P equation that come from the PWIM are modified appropriately.

4.6 Interface Movement Procedure

Equation (2.23) leads to a connection between δ_e and δ_w and can be applied, starting at the inlet, to determine the film thickness all along the domain. At the inlet, the film thickness is zero. In practice, however, because a structured grid is used, a zero height of liquid at the interface is not used. Instead, the position of the node on the interface at the inlet is fixed at a r distance of 1×10^{-9} m to 1×10^{-7} m from the wall. This allows generating the grid in the liquid region at the inlet but has negligible effect on the results. There is a significant film thickness variation at the top for the cases with high condensation rate. This leads to an extreme skewness of the control volumes in that region. For these cases, height of liquid at the inlet should be assigned to 1×10^{-7}, while this value could be decreased toward 1×10^{-9} as the condensation rate decreases. To implement the interface movement algorithm, special

treatment of the row of control volumes in the liquid adjacent to the interface was necessary. Mass conservation equations were not solved on that row to enable the ILMB method to correct the interface location. If this step was not taken, strongly enforced mass conservation at the end of the fixed-mesh solution step would prevent mesh movement.

Numerical integration of the Eq. (2.23) from r_1 (location of the interface) to R is done using face velocities and, by applying a forward marching scheme, yields the value of δ_e for all the nodal locations along the z direction. Thus, the integrals are converted to summations as follows:

$$\left[\sum_{j=j_{\mathrm{B}L}}^{j_{\mathrm{E}L}} \rho_{L,j} U_{L,j} \left(r_1 + (j-0.5)(\Delta r)^2\right)_j\right]_w + \left.\frac{\dot{m}_{\mathrm{cond}}}{2\pi}\right|_{we} = \left[\sum_{j=j_{\mathrm{B}L}}^{j_{\mathrm{E}L}} \rho_{L,j} U_{L,j} \left(r_1 + (j-0.5)(\Delta r)^2\right)_j\right]_e \tag{4.165}$$

Assuming uniform grid spacing along r direction: $\Delta r = \dfrac{\delta}{\mathtt{N}_{r,L}}$ and $r_1 = R - \delta$, Eq. (4.165) is written in a simpler form.

$$\begin{aligned}\left[\frac{-1}{\mathtt{N}_{r,L}} \sum_{j=j_{\mathrm{B}L}}^{j_{\mathrm{E}L}} \rho_{L,j} U_{L,j} + \frac{1}{2\mathtt{N}_{r,L}^2} \sum_{j=j_{\mathrm{B}L}}^{j_{\mathrm{E}L}} \rho_{L,j} U_{L,j} (2j-1)\right]_w \delta_w^2 \\ + \left[\frac{1}{\mathtt{N}_{r,L}} R \sum_{j=j_{\mathrm{B}L}}^{j_{\mathrm{E}L}} \rho_{L,j} U_{L,j}\right]_w \delta_w + \left.\frac{\dot{m}_{\mathrm{cond}}}{2\pi}\right|_{we} = \\ \left[\frac{-1}{\mathtt{N}_{r,L}} \sum_{j=j_{\mathrm{B}L}}^{j_{\mathrm{E}L}} \rho_{L,j} U_{L,j} + \frac{1}{2\mathtt{N}_{r,L}^2} \sum_{j=j_{\mathrm{B}L}}^{j_{\mathrm{E}L}} \rho_{L,j} U_{L,j} (2j-1)\right]_e \delta_e^2 + \left[\frac{1}{\mathtt{N}_{r,L}} R \sum_{j=j_{\mathrm{B}L}}^{j_{\mathrm{E}L}} \rho_{L,j} U_{L,j}\right]_e \delta_e\end{aligned} \tag{4.166}$$

This yields to a quadratic equation for the liquid film thickness as follows:

$$C_{1,e}\delta_e^2 + C_{2,e}\delta_e - (C_{1,w}\delta_w^2 + C_{2,w}\delta_w + \dot{m}_{\mathrm{cond}}) = 0 \tag{4.167}$$

The coefficients of this quadratic equation are:

$$C_1 = \frac{-2\pi}{\mathtt{N}_{r,L}} \sum_{j=j_{\mathrm{B}L}}^{j_{\mathrm{E}L}} \rho_{L,j} U_{L,j} + \frac{\pi}{\mathtt{N}_{r,L}^2} \sum_{j=j_{\mathrm{B}L}}^{j_{\mathrm{E}L}} \rho_{L,j} U_{L,j} (2j-1)$$
$$C_2 = \frac{2\pi}{\mathtt{N}_{r,L}} R \sum_{j=j_{\mathrm{B}L}}^{j_{\mathrm{E}L}} \rho_{L,j} U_{L,j} \tag{4.168}$$

The coefficients of Eq. 4.167 should be calculated on the west and east faces of each control volume. This can be done with the application of face velocities and densities for the calculation of each coefficient in Eq. 4.168.

The position of the first node on the interface ($i = i_{\mathrm{B}} - 1$) is fixed which is assumed as δ_w. Therefore, applying forward marching gives the position of the interface for the other stations along z direction.

4.7 Solution Procedure

Applying a finite volume method with the mentioned techniques results in a linearised fully coupled algebraic form of the equations which govern the field variables (U, V, P, T and W).

At each node, the solution vector is defined as: $[U_{\mathrm{P}},\ V_{\mathrm{P}},\ P_{\mathrm{P}},\ T_{\mathrm{P}},\ W_{\mathrm{P}}]^T$. Therefore, the coefficients for each node are stored in a nine-banded 5-block matrix. Then all the coefficients are assembled in a sparse matrix. Extra coefficients for the interface that fall outside the nine nodal equations are added to the sparse matrix. This sparse matrix equation can be solved by either a direct or an iterative solver.

The following iterative solvers were tested:

- ILUT[1] preconditioned GMRES[2] [63]

[1] Incomplete Lower-Upper factorisation with Threshold
[2] Generalized Minimal Residual Method

- ASM[3] and LU preconditioned BCGS[4] package [64–66]

In the present work, most cases resulted in a sparse matrix equation with a very large condition number and high range of eigenvalues. For example, the set of equations for the cases with high condensation rate from a gas-vapour mixture with the presence of reverse flow is difficult to solve. Although, iterative solvers are generally preferred because they are less computationally expensive, a direct solver works better for these cases. Thus, SuperLU-DIST [67] and MUMPS [68] direct solvers were adopted. These solvers are external packages for PETSc[5] [65]. PETSc is a suite of data structures and routines for the scalable (parallel) solution of scientific applications modeled by partial differential equations [64].

4.7.1 Steady State Convergence

The final solution of the set of algebraic equations is obtained by iterating the calculations and moving the interface. At each iteration the matrix equation is solved on a fixed mesh and after moving the interface and based on the new field variables, the matrix of coefficients is updated. This process continues until the interface stops moving (*e.g.*, the maximum nodal interface movement becomes less than 1×10^{-12}) and the non-linear algebraic equations are satisfied.

In addition to the interface movement criterion, a steady-state convergence criterion, Δ^{ϕ}_{spec}, is set separately for each solution variable, Φ being one of (U, V, P, T, or W). At each time step, at each control volume, the Φ value is compared with its value at the previous time step and normalized by the range of values of that variable to calculate:

$$\Delta^{\phi} = \max(\Delta^{\phi}_{all(i,j)}) = \frac{|\Phi_{(i,j)} - \Phi^{o}_{(i,j)}|}{(\max(\Phi_{all(i,j)}) - \min(\Phi_{all(i,j)}))} \tag{4.169}$$

[3] Additive Schwarz Method

[4] Bi-Conjugate Gradient Squared

[5] The Portable, Extensible Toolkit for Scientific Computation

The largest value of $\Delta^{\phi}_{(i,j)}$ is used as the measure of convergence for that variable field and that step. Steady-state convergence is declared when,

$$\Delta^{\phi} \leq \Delta^{\phi}_{\text{spec}} \tag{4.170}$$

for the U, V, P, and T fields.

The values of $\Delta^{\phi}_{\text{spec}}$ for each variable for a typical reflux condensation case were: $\Delta^{u}_{\text{spec}} \leq 5.0\times10^{-7}$, $\Delta^{v}_{\text{spec}} \leq 1.0\times10^{-6}$, $\Delta^{p}_{\text{spec}} \leq 5.0\times10^{-7}$, $\Delta^{t}_{\text{spec}} \leq 5.0\times10^{-7}$, and $\Delta^{w}_{\text{spec}} \leq 5.0\times10^{-7}$.

These criteria ensured tightly converged solutions.

4.8 Code Development Process

An in-house computer code implements the numerical solution approach discussed in this chapter. The code development started based on a single phase code and during the development, it was tested by solving several non-condensing two-phase laminar flow cases. For example, a horizontal stratified gas-liquid flow in a channel and falling film on a vertical plate were solved and the results compared well with the literature. In addition, results that match the Nusselt solution for pure vapour condensation.

The following chapters present the validation results and new results for the co-current and counter-current condensation from gas-vapour mixtures in vertical parallel-plate channels and tubes.

Chapter 5

Parallel-Plate Channels: Co-Current Flow

5.1 Introduction

Earlier studies of laminar film condensation in parallel plate channels started by considering pure vapour (e.g., [69,70]). To the best of author's knowledge, a detailed numerical simulation of laminar film condensation from a gas-vapour mixture in a vertical parallel-plate channels has only been made by Siow *et al.* [6] and Dharma Rao *et al.* [71].

Comparisons of the present work with the previous work by Siow *et al.* and Dharma Rao *et al.* [71] are used for the purpose of validation and also to reveal the capabilities of each approach (elliptic versus parabolic). These comparisons, which are the focus of this chapter, will start to help to understand when to select the parabolic and elliptic approaches for detailed numerical analysis of film condensation from gas-vapour mixtures in channels. Hereafter, the approach used by Siow *et al.* will be referred as the Siow model.

The geometry of the vertical parallel-plate channel is shown in Fig. 5.1. A mixture of saturated vapour and a non-condensable gas flows in a vertical, parallel plate channel. The space between two plates is $2H$ and the temperatures of both plates are constant at T_{wall}. The flow is two-dimensional and symmetrical about the centre-line of the channel. The mixture has uniform profiles of velocity, temperature and gas mass fraction ($U_{M,\text{in}}$, $V_{M,\text{in}}$, $T_{M,\text{in}}$ and W_{in}) at the inlet. Due to the temperature difference between the wall and the flow, the vapour condenses and starts building a liquid film with the thickness of δ. The same assumptions as given in Section 2.1 are applied to form the mathematical model. The governing equations and interface conditions are the same as those presented in Appendix A. The numerical simulation was done based on the same approach that was discussed in Chapter 4.

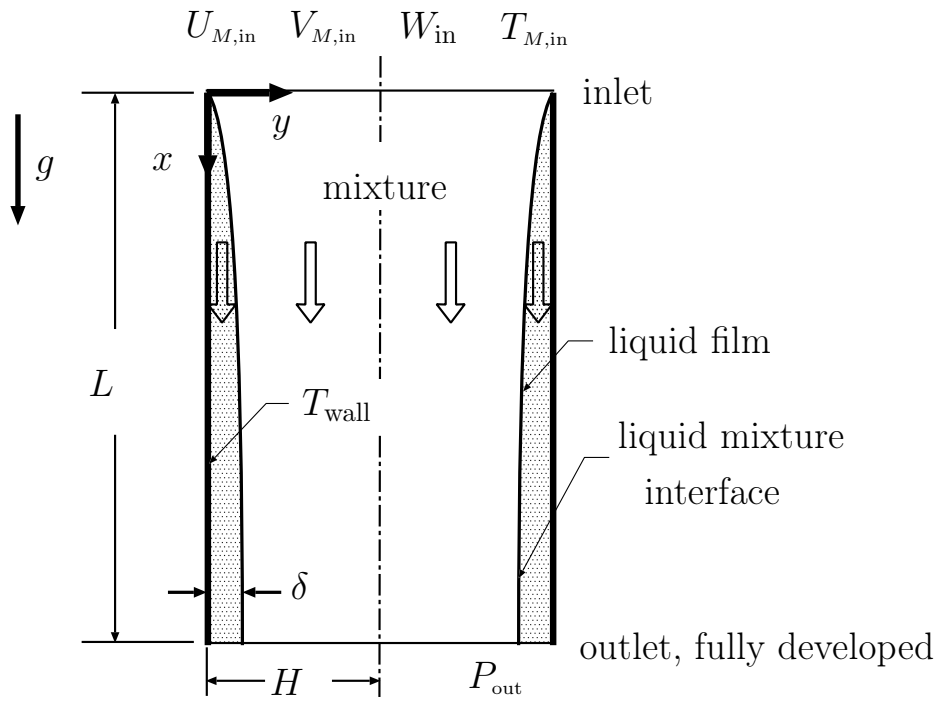

Figure 5.1: Model domain

5.2 Boundary Conditions

At the inlet, uniform profiles of $U_{M,\text{in}}$, $T_{M,\text{in}}$, and W_{in} are specified and $V_{M,\text{in}}$ is set to zero. Saturation conditions are assumed. For the reasons described in Section 4.6, a film thickness of 1×10^{-9} m is specified at the inlet. A uniform liquid inlet velocity equal to the mixture inlet velocity is prescribed.

At the cooled, isothermal plate ($y = 0$), no slip and constant temperature are imposed as shown in Eqs. (5.1).

$$U_L = 0 \quad , \quad V_L = 0 \quad , \quad T_L = T_{\text{wall}} \tag{5.1}$$

At the centre-line ($y = H$), symmetry is prescribed using Eqs. (5.2).

$$V_M = 0 \quad , \quad \frac{\partial U_M}{\partial y} = \frac{\partial T_M}{\partial y} = \frac{\partial W}{\partial y} = 0 \tag{5.2}$$

At the outlet, fully developed boundary conditions (zero gradient of U, V, T, and W in the axial direction) are applied, similar to Eqs. (2.21) and (2.22), and a solution pressure of zero is specified at one node. For the calculations of the properties, the pressure field is shifted to obtain the absolute pressure of P_{ref} at the inlet.

5.3 Comparison with Previous Work

Results from the present numerical model were compared with Siow *et al.* [6] and Dharma Rao *et al.* [71].

5.3.1 Siow Model, Cases 1 to 4

To compare against Siow *et al.*, results were obtained for a steam-air mixture at $P_{\text{in}} = 1$ bar for $\text{Re}_{\text{in}} = 500$. Other tests were performed for Reynolds numbers of 1000 and 2000 and the trends were similar to those discussed here. The half height of the channel was specified to be $H = 2.5$ mm and the plate length was $L = 250$ mm. The computer codes for the present model and the Siow model were run for a variety of cases in the range $0.001 \leq W_{\text{in}} \leq 0.5$ for six inlet-to-wall temperature differences ($\Delta T = 1, 5, 10, 20, 30, 40$ K).

Four representative cases were chosen for discussion here. The definitions of the cases are as follows:

- Case 1: $\Delta T = 20$ K, $W_{\text{in}} = 0.1$, $T_{\text{in}} = 371.01$ K
- Case 2: $\Delta T = 20$ K, $W_{\text{in}} = 0.5$, $T_{\text{in}} = 359.86$ K
- Case 3: $\Delta T = 30$ K, $W_{\text{in}} = 0.1$, $T_{\text{in}} = 371.01$ K
- Case 4: $\Delta T = 10$ K, $W_{\text{in}} = 0.5$, $T_{\text{in}} = 359.86$ K

Grid independence tests were carried out for Cases 1 to 4. The range of values considered was as follows: $40 \leq \mathtt{N}_x \leq 200$ with $1.0 \leq S_x \leq 1.1$, $20 \leq \mathtt{N}_{y,L} \leq 40$, and $20 \leq \mathtt{N}_{y,M} \leq 100$ with $1.0 \leq S_{y,M} \leq 1.1$. A grid with $\mathtt{N}_x$= 130 with S_x= 1.02, $\mathtt{N}_{y,L}$= 20, $\mathtt{N}_{y,M}$= 80 with $S_{y,M}$= 1.1 had maximum difference of the film thickness of less than 0.67% compared to the next finer mesh. Therefore, this grid was used for the results presented in this study. Grids in the Siow model were based on previous grid independence study [8]. The grid used in the Siow code was as follows: $\mathtt{N}_x$= 500, $\mathtt{N}_{y,L}$= 40, $\mathtt{N}_{y,M}$= 80 with $S_{y,M}$= 1.0.

The comparisons of the code results are based primarily on axial variation of film thickness, local Nusselt number and, pressure profiles. Due to the build up of the film and significant variations near the inlet, axial variations are studied in the range $0 \leq x^\star \leq 30$.

Figure 5.2 shows the increase of the liquid film thickness along $x^\star$ for all four cases. The

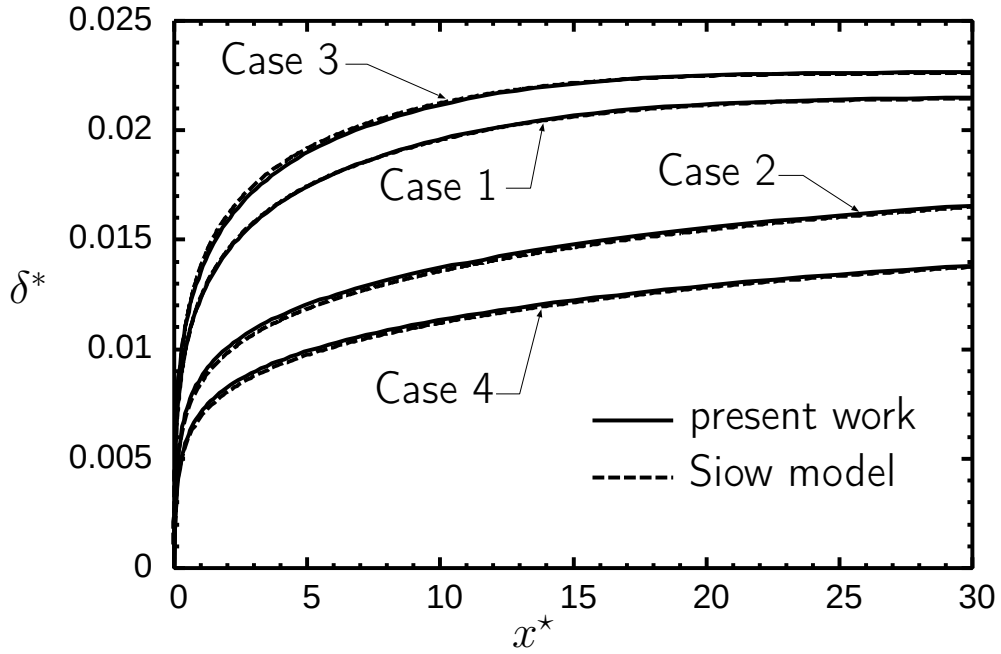

Figure 5.2: Film thickness

rate of growth of the film slows along the channel due to the increased film thickness and a build-up of gas at the interface. The film thickness increases as the gas mass fraction at

the inlet decreases. For almost all four cases, the film thickness compares well between the present work and the Siow model. For Case 3, which has higher condensation rate compared to others, the maximum difference of interface height between the present work and Siow model is 0.37%.

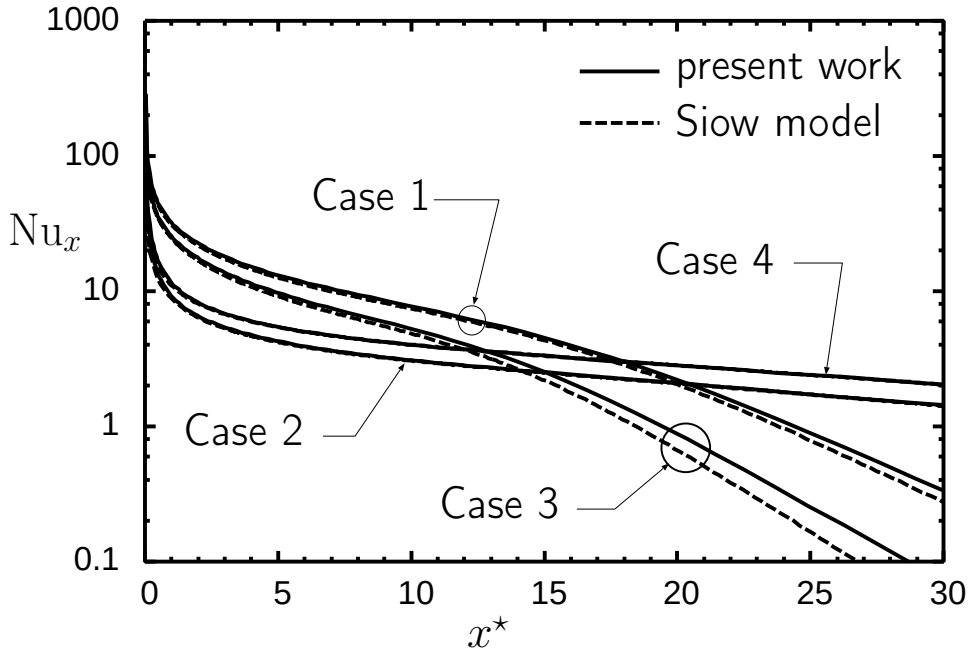

Figure 5.3: Local Nusselt number

Figure 5.3 shows the local Nusselt number for all three cases. The Nusselt number definition is written as Eq. (5.3).

$$\mathrm{Nu}_x = \frac{H \frac{\partial T_L}{\partial y}|_{y=0}}{T_{\mathrm{in}} - T_{\mathrm{wall}}} \tag{5.3}$$

As expected, there is a good agreement between the present work and the Siow model for Cases 2 and 4. The decrease in the amount of non-condensable gas from Case 2 to Case 1 causes an increase in the local heat transfer rate in the region near the inlet. As W_{in} decreases, there is more rapid decrease of Nusselt number towards the outlet of the tube. This trend is due to a higher condensation rate for lower W_{in}. A higher condensation rate

corresponds to a thicker film (as seen in Fig. 5.2).

One of the major differences between the present work and Siow model is the method of pressure calculation. In the Siow model, it was assumed that the pressure is constant in the y direction and the overall mass conservation equation was used to determine the local axial pressure gradient. In the present work, the pressure is calculated based on the continuity equation. The pressure profiles for Case 1 are given in Fig. 5.4 using the dimensionless coordinate η defined by Eqs. (5.4).

$$\begin{aligned} \eta &= y/\delta && \text{for} \quad 0 \le y \le \delta \\ \eta &= (y-\delta)/(H-\delta)+1 && \text{for} \quad \delta \le y \le H \end{aligned} \tag{5.4}$$

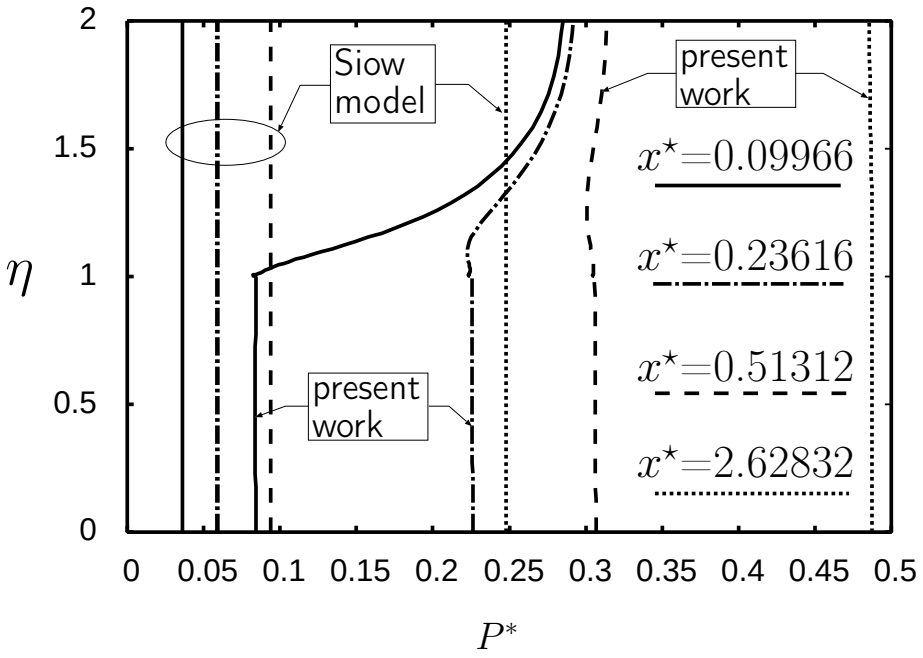

Figure 5.4: Pressure profiles for Case 1

The profiles of the pressure show that the assumption of constant pressure in y direction may not be realistic at the inlet region of the channel. For the present work, the maximum

pressure difference in the y direction is about 0.90 Pa at the very first column of control volumes at the inlet. Also, there is a small jump in the pressure between the phases for the few stations close to the inlet. Comparing the total pressure rise along the full length of the channel also shows a difference between the present work and the Siow model. The value of P^* at the outlet is 7.572 from the present model and 6.417 from the Siow model. These differences in pressure profile and overall pressure drop are not causing noticeable differences in the overall results for the two models, as seen from previous figures.

5.3.2 Dharma Rao *et al.*

The second comparison was made with the results of Dharma Rao *et al.* [71]. These cases are also for a steam-air mixture, but with inlet pressure and Reynolds number of 1 bar and 4000, respectively. The Reynolds number in [71] was calculated with the assumption of the channel full width as the characteristic length. In the present work, however, half width of the channel was applied for the Reynolds number calculation. Therefore, $\mathrm{Re}_{\mathrm{in}} = 4000$ in the present work will provide the same inlet condition as $\mathrm{Re}_{\mathrm{in}} = 2000$ in [71]. Furthermore, The half height of the channel was specified to be $H = 12.5$ mm and the channel length was $L = 1$ m. The wall temperature was constant and equal to 5°C. Dharma Rao *et al.* presented all the results based on two relative humidities (ϕ =100% and 80%) and two inlet temperatures ($T_{\mathrm{in}} = 25$°C and 40°C). The relation between these parameters and inlet gas mass fraction is given in [9].

Comparison of the axial variations of the liquid Reynolds number are presented in Fig. 5.5. This comparison is for inlet temperatures of 25°C and 40°C. As shown, although there is a qualitative agreement between results of the present work and Dharma Rao *et al.*, there are significant quantitative differences. These differences are expected to be due to different modelling approaches (elliptic versus parabolic), plus Dharma Rao *et al.* [71] did not solve the complete set of equations for the liquid, approximated the mixture density variation

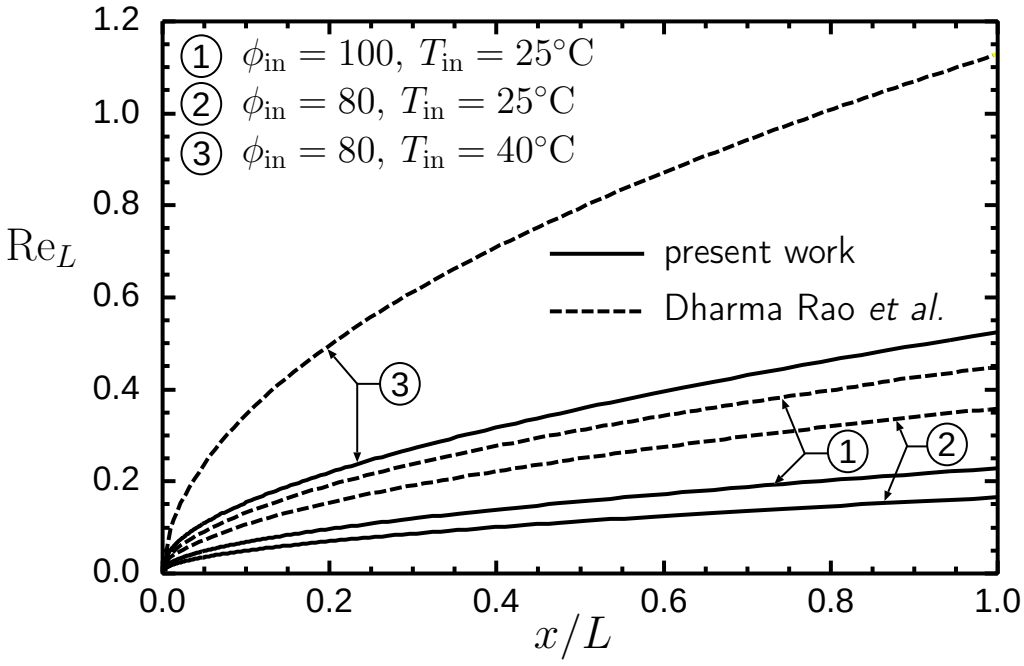

Figure 5.5: Liquid film Reynolds number

in y direction as constant, and used different interface mass balance and pressure gradient calculations. Furthermore, it is possible that using different equations for the calculation of thermophysical properties could affect the results. For the present work, all the properties were calculated using the equations in Appendix B. Dharma Rao *et al.* had a slightly different set of equations for property calculation [72].

Dharma Rao *et al.* showed that interface temperature increases along the channel and the highest value of the interface temperature occurrs at the outlet. Physically, the interface temperature should decrease along the channel due to the gas build up at the interface. At the end of condensation (toward the channel outlet) the interface temperature would be equal to the wall temperature. For the shown cases, the inlet gas mass fraction is high. Therefore, there is a relatively small amount of vapour to condense and end of condensation is achieved before the end of the channel. As can be seen in Table 5.1, in the present work the interface temperature at the outlet became equal to the wall temperature for all three

cases. Moreover, the outlet gas mass fraction at the interface corresponds to the relation with local temperature and pressure.

Table 5.1: Comparison of interface temperature at the outlet

	W_{in}	T_{in}(°C)	$W_{\text{int,out}}$ (present work)	$T_{\text{int,out}}$(°C) (present work)	$T_{\text{int,out}}$(°C) (Dharma Rao *et al.*)
1	0.9800	25	0.9946	5	5.08
2	0.9841	25	0.9946	5	5.06
3	0.9624	40	0.9946	5	5.18

Based on the comparisons made, there are higher deviations from the present work in the predictions of Dharma Rao *et al.* [71] than those of Siow *et al.* [6]. Furthermore, it was shown that for higher condensation rates (lower inlet gas mass fraction and/or higher inlet-to-wall temperature difference) the deviations are higher. It has also been found that there were cases that parabolic approach could not solve. These cases are discussed in the next section.

5.3.3 Siow Model, Cases 5 and 6

For some cases with lower values of W_{in}, the Siow model code produced results that predicted the onset of a negative mixture velocity near the centre line at an axial location before the prescribed channel length, at which point it terminated the computations. The present model, however, produced converged solutions for the entire channel in all cases. The difference between the two models can be illustrated by examining, near the inlet of the channel, how the models predict the development of the complicated balance of condensation rate, film thickness, gas mass fraction, and axial velocity. Two representative cases were chosen for that purpose. Both cases are for a steam-air mixture with $P_{\text{in}} = 1$ bar and $\text{Re}_{\text{in}} = 500$:

Case 5: $\Delta T = 20$ K, $W_{\text{in}} = 0.01$, $T_{\text{in}} = 372.70$ K

Case 6: $\Delta T = 40$ K, $W_{\text{in}} = 0.01$, $T_{\text{in}} = 372.70$ K

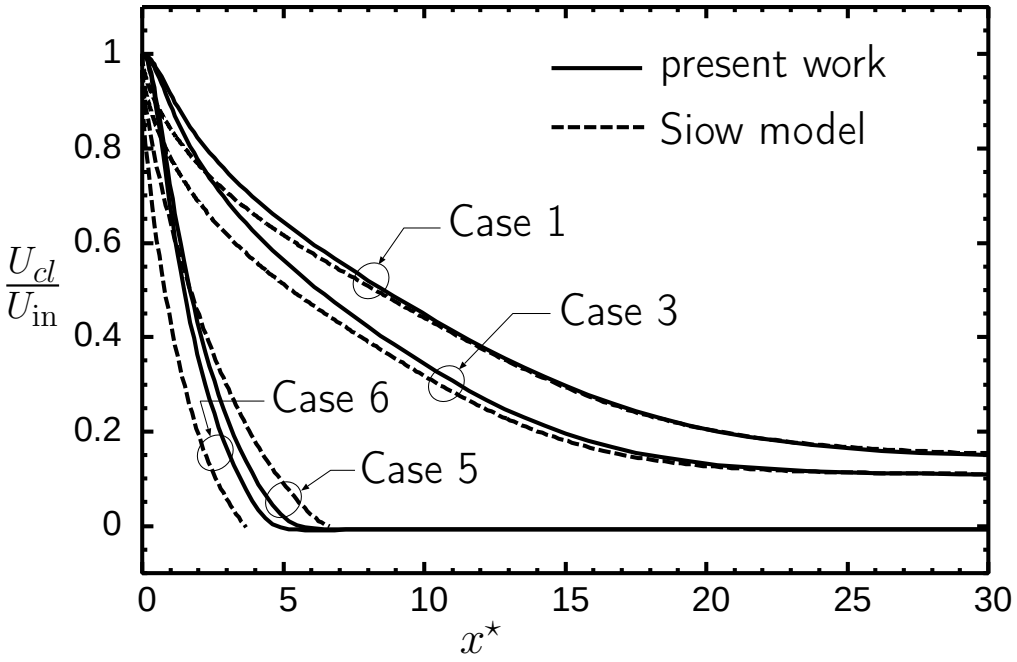

Figure 5.6: Centre-line velocity for different cases

Figure 5.6 shows the dimensionless centre-line axial velocity profiles for Cases 5 and 6, plus Cases 1 and 3 for reference purposes. The results for Cases 1 and 3 show deviations between the Siow model and the present model near the inlet, but excellent agreement after $x^\star = 20$. The deviation close to the inlet are expected to be related to the differences in the pressure profiles and the development of the velocity fields. For Case 5 and Case 6, there is a similarity in the trends of the two models up to the stopping points of the Siow model. For those cases, the Siow model predicted a strong condensation rate and the rapid removal of vapour from the mixture. After most of the vapour had been condensed, the continuing condensation caused a deficit in vapour mass which resulted in the onset of negative U velocity in the region near the centre line. The Siow model is not valid after a negative U velocity is detected, so it could not proceed after $x^\star = 6.658$ and $x^\star = 3.687$, for Cases 5 and 6, respectively. The present model also predicted rapid removal of vapour from the mixture.

Figure 5.6 also shows that the present model predicts a small negative velocity that extends to the outlet.

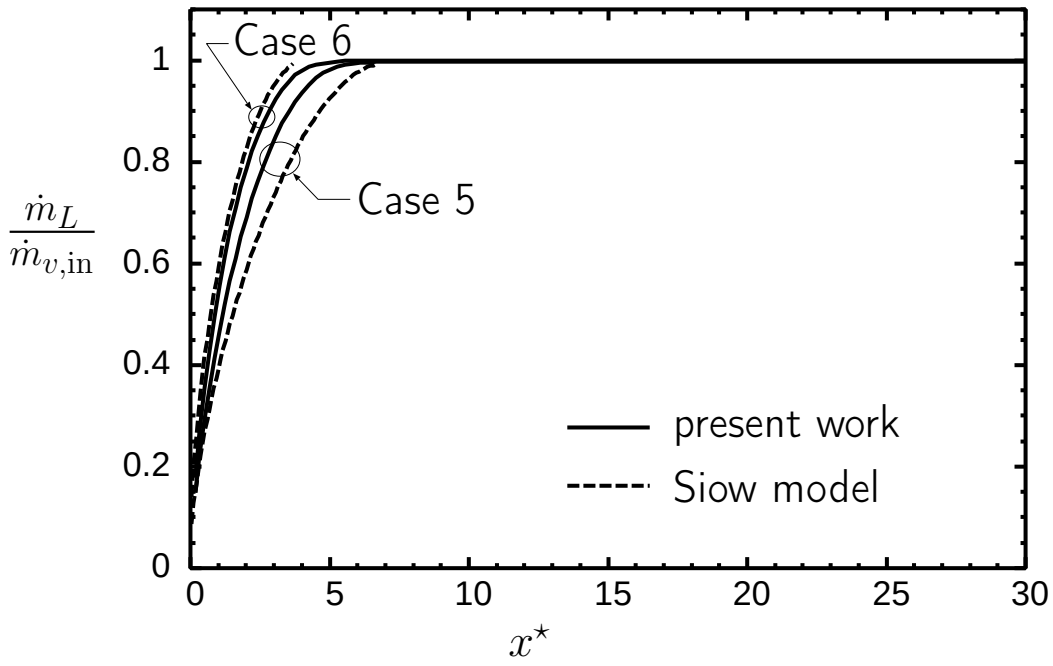

Figure 5.7: Normalised liquid mass flow rate

Figure 5.7 shows the axial variation of the liquid mass flow rate relative to the amount of vapour entering the channel: $(\dot{m}_L/\dot{m}_{v,\text{in}})$. A value near 1 indicates that nearly all of the incoming vapour has been condensed. As inlet-to-wall temperature difference increases (Case 6 compared to Case 5), both models predict that higher proportions of the inlet vapour condensed more quickly. The Siow model stopped when almost all of the inlet vapour was condensed. In both cases, the present model predicts most of the vapour being condensed by about $x^\star = 6$. As will be seen shortly, the present model finds an equilibrium with a large W_{int} and a practically zero condensation rate after nearly all of the inlet vapour has been condensed, leaving only saturated vapour in the mixture at the wall temperature.

Figure 5.8 shows the development of the film thickness for Cases 5 and 6. The Siow model values of the film thickness at the stopping points are very similar to those of the

present model. The film thickness develops at a somewhat slower rate compared to the present model, however, for Case 5. This difference will be discussed below with respect to the development of the velocity and gas mass fraction fields.

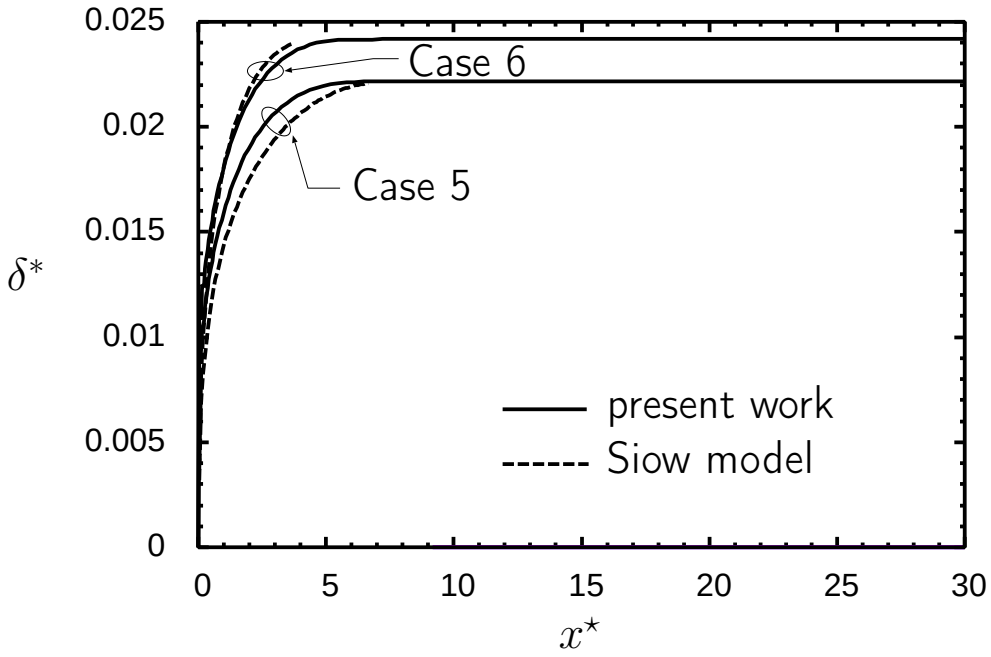

Figure 5.8: Film thickness for Case 5 and Case 6

The axial variation of the interface gas mass fraction is shown in Fig. 5.9 for these two cases. For both cases, both models predict a rapid rise in W_{int} due to the initial strong condensation rates. The Siow model predicts a slower build-up of gas at the interface than the present model. This slower build-up of gas is related to the development of the velocity and will be discussed shortly. The development of the flow in Case 5 is now examined by looking at the local velocity and gas mass fraction profiles before the stopping point of the Siow code.

Figure 5.10 shows the local U velocity profiles from both models at three axial stations for Case 5 before the Siow model stopping point ($x^\star = 6.658$). The velocity profiles of both models show the loss of mass as $x^\star$ increases, but they have very different shapes. At a given

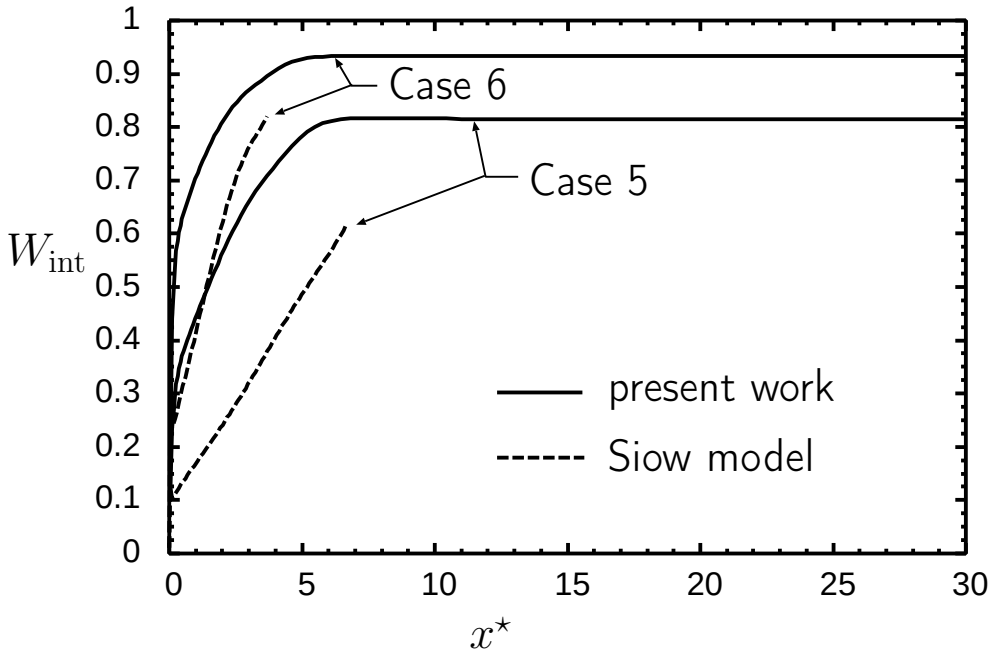

Figure 5.9: Interface gas mass fraction

axial station, the profiles show that the Siow model has more mass in the mixture region. This is consistent with Fig. 5.7 which shows that there is much more liquid condensed in the present model than the Siow model at a given axial location in the range considered in Fig. 5.10. In the Siow model, the larger magnitude of the U velocity and its higher gradient near the interface, resulted in greater interfacial shear and a thinner film. The film is also thinner because of a lower amount of liquid condensed. This is consistent with Fig. 5.8.

Figure 5.11 shows the local W profiles from both models for Case 5 at the same three axial stations as in Fig. 5.10. The Siow model predicts much lower W values in the entire mixture region compared to the present model. This difference is expected to be mainly due to the higher U velocity near the interface in the Siow model, which would help to flush air away from the interface. The lower gas mass fraction near the interface in the Siow model will also be due to a lower condensation rate which would lead to smaller V velocity advecting air towards the interface.

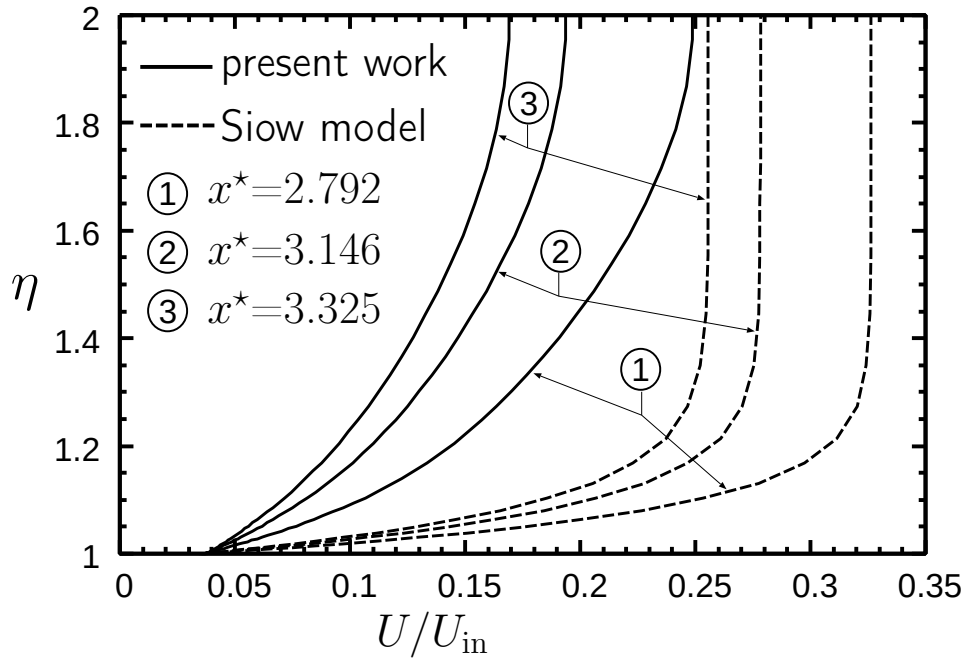

Figure 5.10: Velocity profiles between the inlet and the Siow model stopping point for Case 5

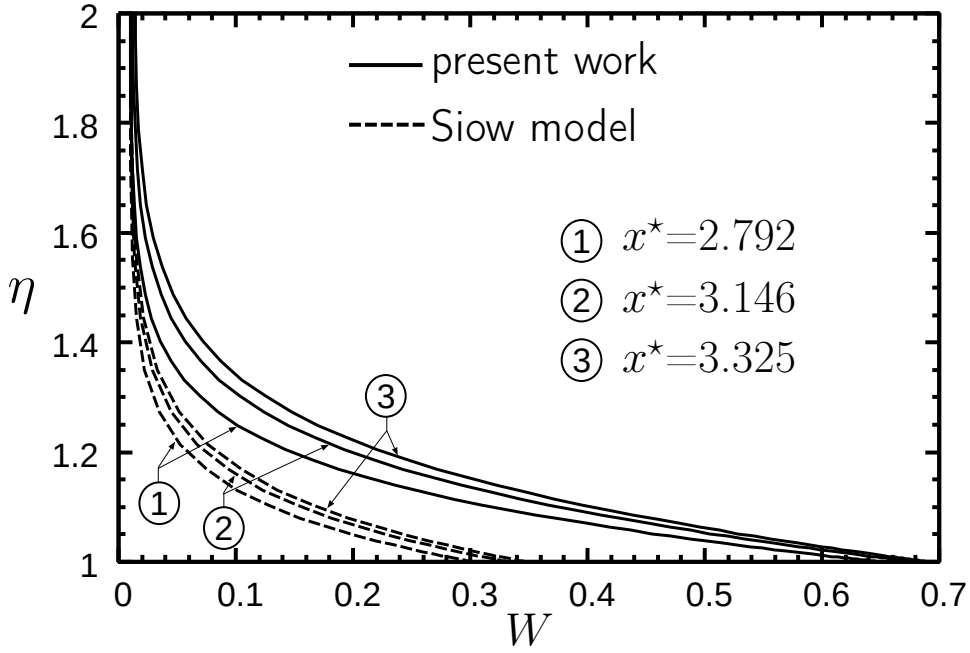

Figure 5.11: Gas mass fraction profiles near the inlet for Case 5

To examine the details of the flow near where the Siow model stops in Case 5, profiles of axial velocity are plotted in Fig. 5.12 for both models at that specific location. The profiles for the Siow model just before stopping and the present model for the outlet are also shown. The velocity profiles for the Siow model in Fig. 5.12 show that the high condensation rate

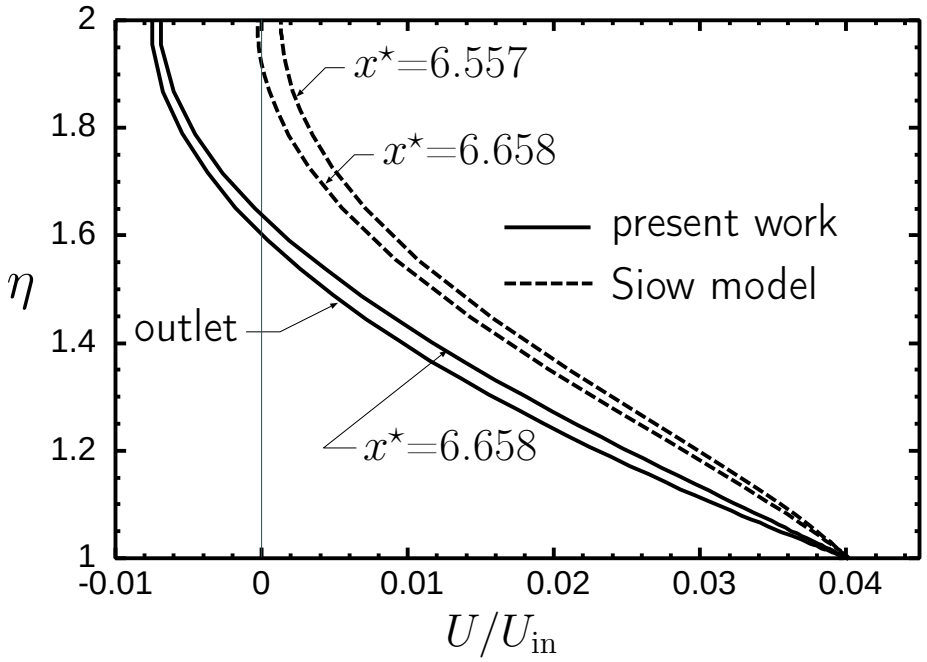

Figure 5.12: Velocity profiles for Case 5

has removed so much vapour that the centre-line velocity approaches zero; this was seen in Fig. 5.6. The profile at $x^\star = 6.557$ in Fig. 5.12 is the last station before negative velocity was detected in the Siow model for this case. The present model predicted a region of small negative velocity near the centre line. For Case 5, this region starts at $x^\star = 5.42$ and continues to the outlet. There is a region for η from approximately 1.6 to 2.0 where there is a reverse flow of mixture at the outlet. The flow coming in the inlet has the same conditions as the flow leaving at the outlet. In this case, the outlet conditions have a gas mass fraction of 0.814 and a temperature of 79.55°C. The total reverse mass flow rate is only 0.27% of the total inlet mass flow rate.

Chapter 6

Parallel Plate Channels: Counter-Current Flow

6.1 Introduction

To the best of author's knowledge, there are no previous work on the computational modelling of reflux condensation in a vertical channel. Furthermore, the available open source and commercial software programs have limited capabilities in modelling this phenomenon.

This chapter focuses on reflux condensation in vertical parallel plate channels. The sample results of the present work will start to help to understand appropriate set of equations, boundary conditions and computational scheme for the simulation of reflux condensation from gas-vapour mixtures in vertical channels.

The same numerical solution approach that described in Chapter 5 was used for the analysis. The only difference in the model is in the boundary conditions. There are, however, significant differences in the convergence behaviour of the solution.

6.2 Boundary Conditions

The geometry of the vertical channel is shown in Fig. 6.1. The cooled section is the section with length of L_2 and constant wall temperature. Above and below the cooling section, boundary conditions must be specified for the mixture flow. The conditions of the mixture flow entering the channel from below are dependent on the geometry and thermal conditions in the piping that supplies the mixture. Taking this into account would extend the solution domain to include a three-dimensional region that is application-specific. Therefore, it was decided that an excellent first analysis could be performed using a two-dimensional model. In order to keep the model domain two-dimensional and reasonable in size, an inlet section

with an adiabatic wall with length of L_3 is added at the mixture inlet side of the cooled section. This additional length permits the development of the mixture flow before the cooled section and section of film flow with no mass flow change. Likewise, a section with an adiabatic wall of length L_1 is added at the mixture outlet side of the cooled section. This additional section permits the application of an appropriate outflow condition on the mixture as it flows without mass removal.

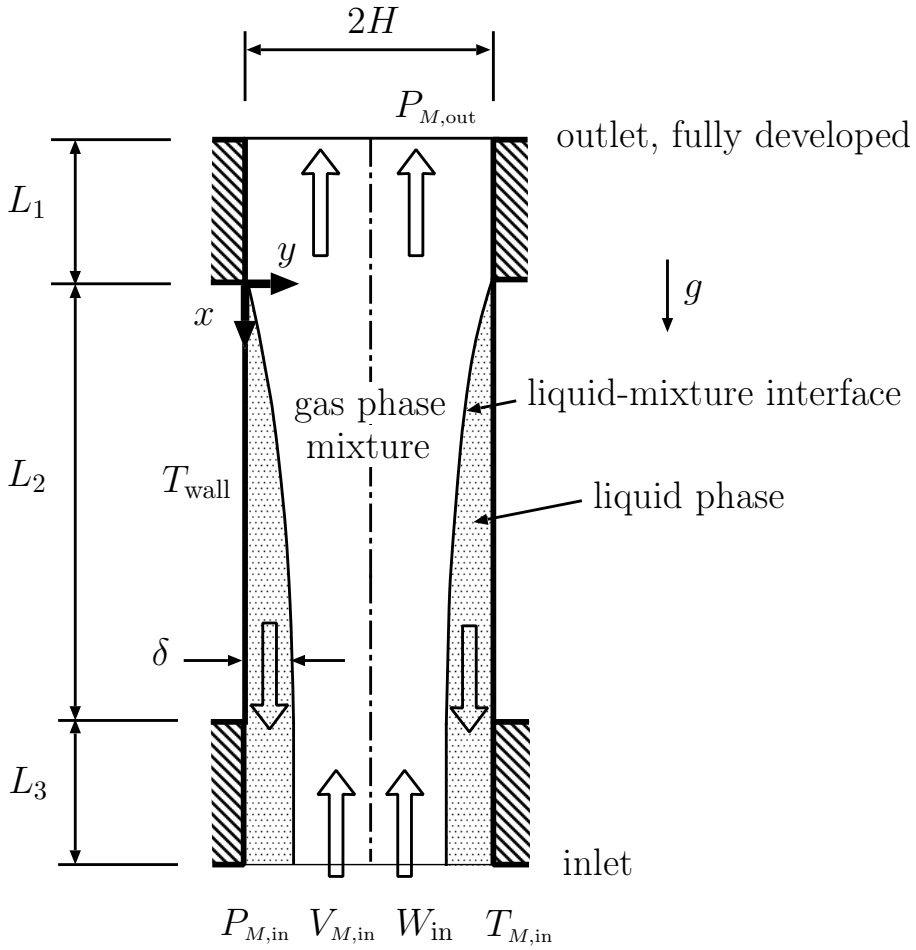

Figure 6.1: Reflux condensation model domain

A mixture of saturated vapour and air (as a non-condensable gas) flows in a vertical, parallel plate channel. The space between two plates is $2H$. The flow is two-dimensional

and symmetrical about the centre-line of the channel.

At the inlet (bottom) for the flow going in, uniform profiles of $T_{M,\text{in}}$, $P_{M,\text{in}}$, and W_{in} are specified and $V_{M,\text{in}}$ is set to zero. Saturation conditions are assumed. For the downward flow of liquid and mixture at the bottom, fully developed boundary conditions are applied, similar to Eqs. (2.21) and (2.22).

At the outlet (top), fully developed boundary conditions are prescribed, similar to Eq. (2.21). A film thickness of 1×10^{-7} m is specified at the top. A uniform liquid inlet velocity of 1×10^{-7} m/s is prescribed for the liquid inlet velocity at the top. A solution pressure of zero relative to P_{in} is specified at one node at the outlet in order to obtain a given $\Delta P = P_{\text{in}}$. For the calculations of the properties, the pressure field is shifted to obtain absolute pressure of P_{ref} at the inlet.

At the wall ($y = 0$), no slip boundary conditions are imposed as shown in Eqs. (6.1).

$$U_{L} = 0 \quad , \quad V_{L} = 0 \tag{6.1}$$

The wall temperature is constant and uniform along the cooled section (L_2). For the two bottom and top sections (L_1 and L_3), an adiabatic wall is assumed as shown in Eqs. (6.2).

$$\begin{aligned} T_{L} &= T_{\text{wall}} \qquad \text{for} \quad 0 \leq x \leq L_2 \\ \tfrac{\partial T}{\partial y} &= 0 \quad \text{for} \quad -L_1 \leq x < 0 \text{ and } L_2 < x \leq L_3 \end{aligned} \tag{6.2}$$

At the centre-line ($y = H$), symmetry is prescribed using Eqs. (6.3).

$$V_{M} = 0 \quad , \quad \frac{\partial U_{M}}{\partial y} = \frac{\partial T_{M}}{\partial y} = \frac{\partial W}{\partial y} = 0 \tag{6.3}$$

6.3 Results and Discussion

Results were obtained for a steam-air mixture at relative inlet pressures of $\Delta P = 4$ Pa and $\Delta P = 7$ Pa for two channels with different lengths: short and long. Other pressures and

lengths in the laminar regime are possible. Trends discussed here will be similar under other conditions.

The half height of the channel was specified to be $H = 2.5$ mm and the plate lengths were $L = 250$ mm (short channel) and $L = 600$ mm (long channel). For the short channel L_1 and L_3 were set to 100 mm and 120 mm and for the long channel, they were set to 250 mm and 100 mm, respectively. The present model was run for cases with $W_{\text{in}} = 0.0$ and 0.001 and the inlet-to-wall temperature difference of $\Delta T = 1$ K.

Grid independence tests were carried out based on the film thickness for all cases that are presented in this study. The range of values considered was as follows: $75 \leq \mathtt{N}_x \leq 250$ with $1.0 \leq S_x \leq 1.02$, $20 \leq \mathtt{N}_{y,L} \leq 40$, and $20 \leq \mathtt{N}_{y,M} \leq 100$ with $1.0 \leq S_{y,M} \leq 1.1$. A grid with $\mathtt{N}_x$= 175 with S_x= 1.00, $\mathtt{N}_{y,L}$= 20, $\mathtt{N}_{y,M}$= 80 with $S_{y,M}$= 1.1 had normalized maximum difference of film thickness of less than 1.07 % compared to a finer mesh. Therefore, this grid was used for the results presented in this section.

The sample results presented in this section include the profiles of velocity and gas mass fraction as well as the film thickness for the mentioned cases. Due to the build up of the film and significant variations near the beginning of the cooled section, transverse profiles of axial velocity and gas mass fraction are presented far from this region. Important details are found by plotting transverse profiles of axial velocity in the liquid and mixture close to the interface. Additional insights are drawn from examining the inlet pressure variation for a specific length of the channel.

Figure 6.2 shows the axial variation of the liquid film thickness for all cases with $\Delta P = 4$ Pa and $\Delta P = 7$ Pa for the short and long channel, respectively. The film thickness did not change noticeably as the gas mass fraction at the inlet increased from 0 to 0.001. In addition, this figure shows that the non-dimensional value of film thickness with respect to $x^\star$ is the same for both channel lengths. As discussed before, there is a small oscillation in the film thickness at $x^\star = 0.16$ and $x^\star = 0.67$ for the short and long channels, respectively. This

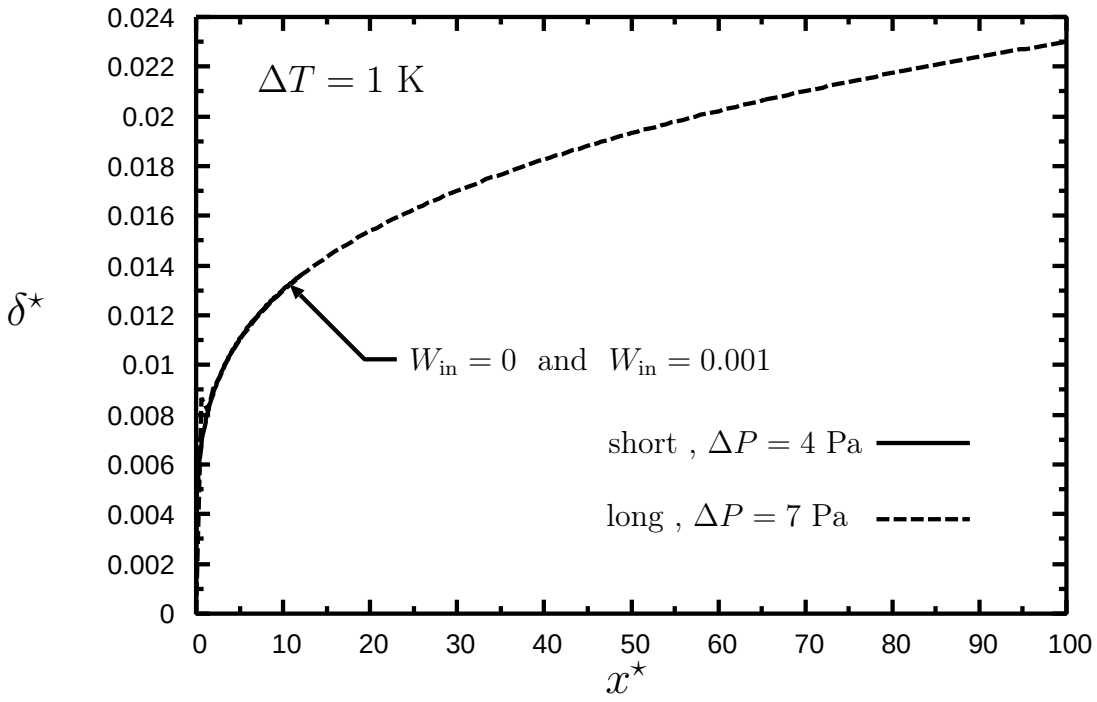

Figure 6.2: Film thickness

is due to the skewness of the grid because of the sudden change of film thickness. Applying a finer grid at the beginning of cooled section may resolve this issue. However, this leads to prohibitive computational cost. Also, the small oscillation does not have an impact on the interface height along the channel.

The axial velocity profiles in three different stations are given in Fig. 6.3 for $W_{\text{in}} = 0.001$ using the dimensionless coordinate η defined by Eqs. (6.4). The relative inlet pressure was set to 4 Pa and 7 Pa for the short and long channel, respectively. Note that vertical axis of Fig. 6.3 has been arranged to show the negative velocity (upflow) directed in the positive vertical axis direction.

$$\begin{aligned} \eta &= y/\delta && \text{for} \quad 0 \le y \le \delta \\ \eta &= (y-\delta)/(H-\delta) + 1 && \text{for} \quad \delta \le y \le H \end{aligned} \tag{6.4}$$

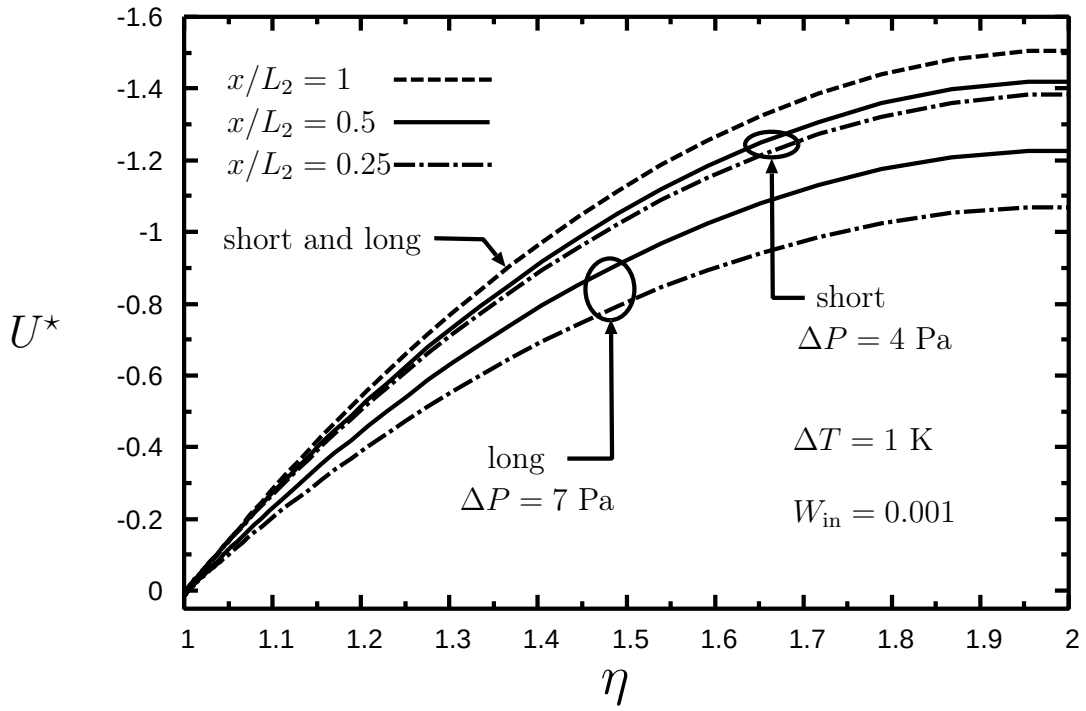

Figure 6.3: Velocity profiles

At the inlet, the velocity profiles are similar to the fully-developed channel velocity profiles for both lengths. The cooled section inlet Reynolds numbers based on average gas phase velocity and channel half height are $\text{Re}_{\text{in,c}} = 1228.6$ and $\text{Re}_{\text{in,c}} = 1375.3$ for the short and long channel, respectively. Due to the condensation, vapour has been removed from the gas-vapour mixture in the cooling section. Therefore, the velocities decrease and the higher length of cooled section for the long channel leads to higher reduction of the velocity values. Negative velocity corresponds to upward flow in the mixture region. All velocities in the liquid are positive, and some U values close to the interface in the mixture region are also positive, as discussed next.

Figure 6.4 shows the velocity profiles in the liquid region and close to the interface in the mixture region for the same stations and cases as in Fig. 6.3.

The profiles are plotted versus y/H instead of η in order to clearly show the velocity

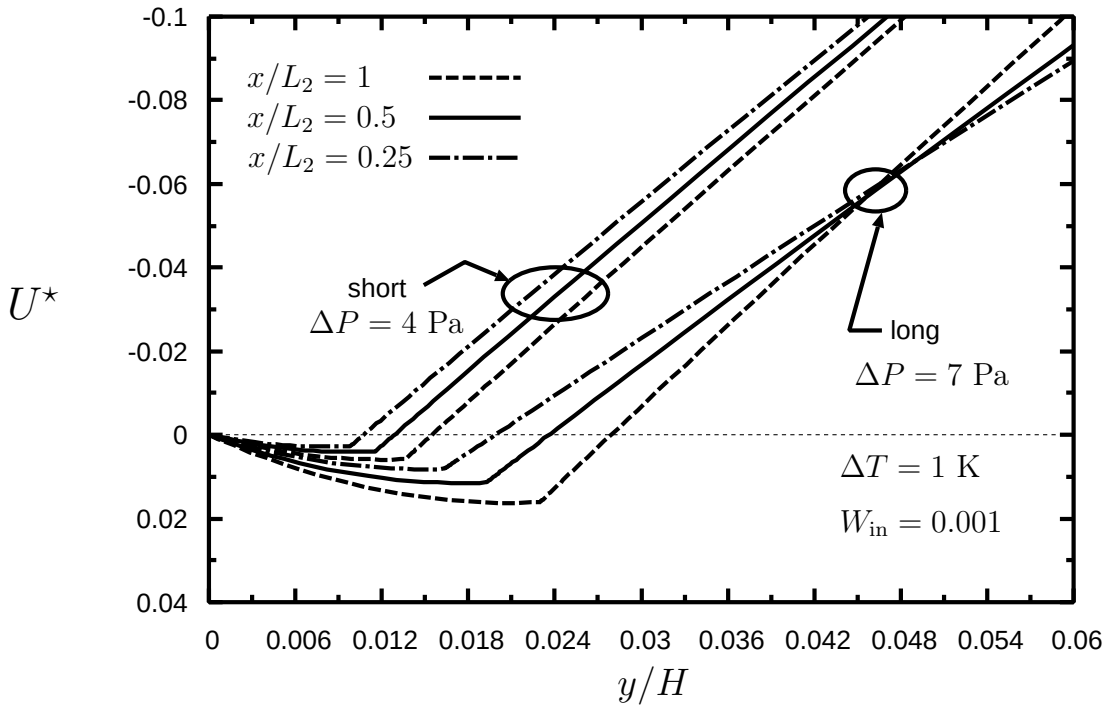

Figure 6.4: Velocity profiles close to the interface

profiles in the liquid and mixture near the interface for different film thicknesses. The liquid mixture interface coincides with the sudden change in slope of the velocity profiles. These profiles indicate that there is a sudden small decrease in the magnitude of the liquid velocity at the interface (*i.e.*, $\frac{\partial U_L}{\partial y} < 0$ at the interface). Note the region of positive mixture velocity and the change of sign in the mixture velocity profiles. The sign change point will be referred to as the break point between the downflow and upflow. Positive velocities in the mixture region correspond to the flow going out at the bottom of the domain. Shear force at the interface pulls the mixture down and causes downward flow in the mixture. This positive velocity region in the mixture becomes smaller toward the outlet (top of the domain) and finally at the outlet there is no positive velocity. Basically, inlet-to-wall temperature difference, inlet pressure and inlet gas mass fraction are the key parameters that determine the place of the break-point. The point could move closer to the liquid region for small film thickness and high mixture inlet velocity. In the limit of these conditions, the gravity force

is no longer larger than shear force at the interface and liquid starts flowing upward. This phenomenon is beyond the scope of this analysis.

Gas mass fraction profiles are presented in Fig. 6.5 for the cases with $W_{\text{in}} = 0.001$ and $\Delta P = 7$ Pa. As expected, longer length of condensation results in higher gas mass fraction

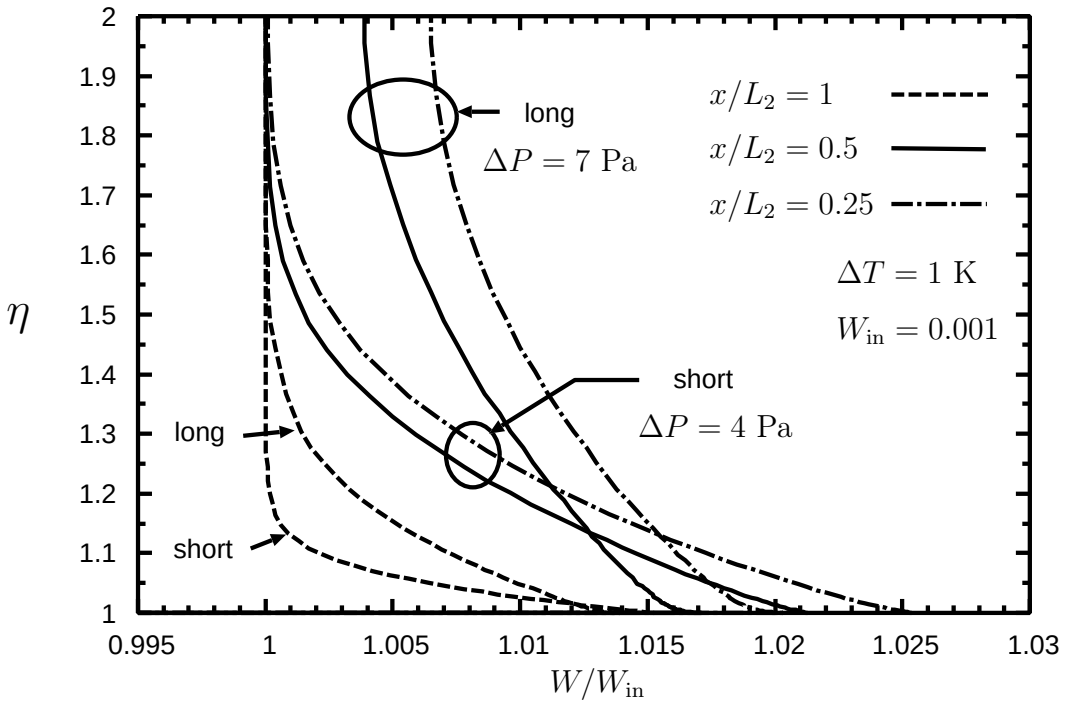

Figure 6.5: Gas mass fraction profiles

because of the greater vapour removal from the mixture. The highest gas mass fraction values occur at the interface for all cases. The gas mass fraction does not change significantly along the cooled section. Low condensation rate due to the small inlet-wall-temperature difference and the downward flow in the mixture region near the interface could be the possible reasons for the small gas mass fraction variation.

Pressure drop, ΔP, is a key parameter to control the amount of mass flow rate going in the channel. A small ΔP may not bring enough mass to match the amount of vapour condensing. In this case, the condensation driving force will draw the required mass from

the outlet (top) of the channel. In that case, the condensation rate is mainly governed by the length of the cooled section, inlet gas mass fraction and inlet-to-wall temperature difference. Figure 6.6 shows the case where the inlet relative pressure was not high enough to force the mass to exit the channel from the top. Compared to the previous cases, the

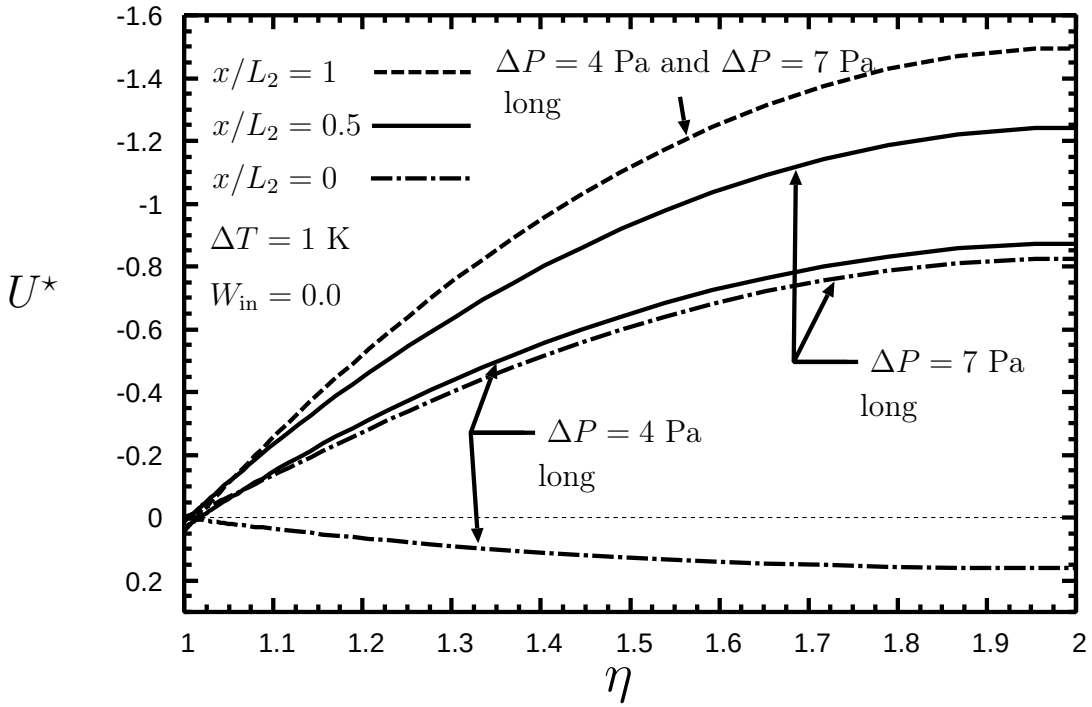

Figure 6.6: Velocity profiles for different inlet pressures for the long channel

inlet relative pressure was reduced to $\Delta P = 4$ Pa for the long channel. As can be seen, condensation driving force starts pulling vapour from the top. Thus, the mixture velocity near the beginning of the cooled section ($x/L_2 = 0$) is positive. This means that vapour is coming from both top and bottom of the channel. The outflow is at the bottom which contains liquid and a small amount of vapour. The vapour downflow is caused by the shear force at the interface.

Chapter 7

Tubes: Co-Current Flow

7.1 Introduction

Results of analysis of film condensation in vertical pipes with co-current flow of mixture and liquid are presented here as a demonstration of the capability of the present model. First, the present model is validated through comparison with the previous work by Groff *et al.* [10]. Hereafter, the approach used by Groff *et al.* will be referred as the Groff model. After comparison with the Groff model, some sample additional results are presented.

The geometry of the vertical tube is shown in Fig. 7.1. A mixture of saturated vapour and air (as a non-condensable gas) flows in a vertical tube with a radius of R and the constant wall temperature of T_{wall}. The flow is symmetrical about the centre-line of the tube. The mixture has uniform profiles of velocity, temperature and gas mass fraction ($U_{M,\text{in}}$, $V_{M,\text{in}}$, $T_{M,\text{in}}$ and W_{in}) at the inlet. Due to the temperature difference between the wall and the flow, the vapour condenses and starts building a liquid film with the thickness of δ. The same assumptions and equations as given in Chapter 2 are applied to form the mathematical model. The only difference here is the boundary conditions. The numerical simulation was done based on the same approach that was discussed in Chapter 4.

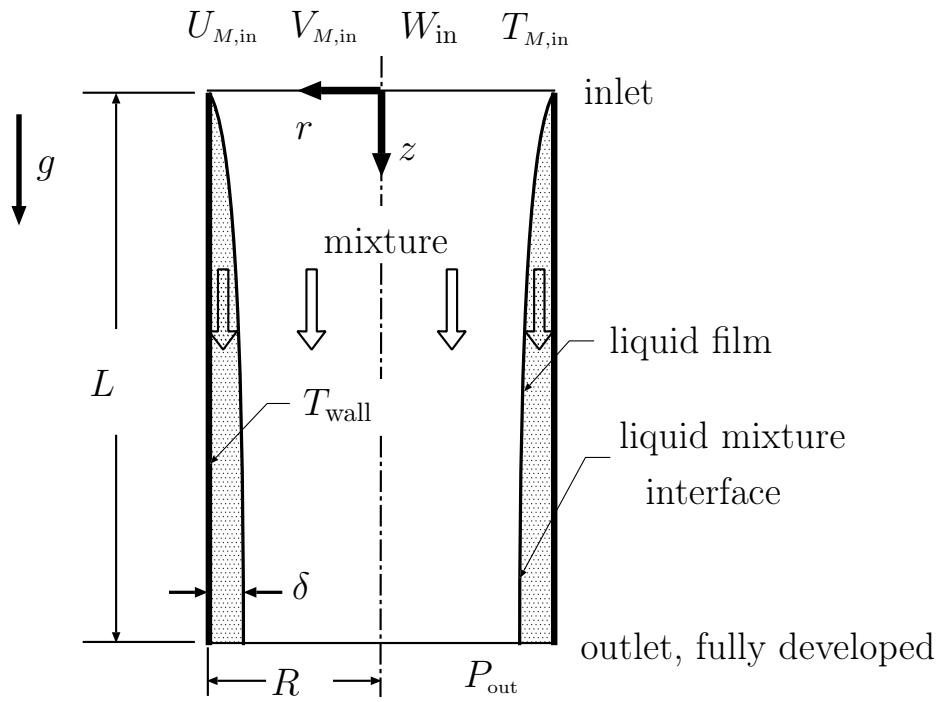

Figure 7.1: Model domain

7.2 Boundary Conditions

At the inlet, uniform profiles of $U_{M,\text{in}}$, $T_{M,\text{in}}$, and W_{in} are specified and $V_{M,\text{in}}$ is set to zero. Saturation conditions are assumed. A film thickness of 1×10^{-8} m is specified at the inlet. A uniform liquid inlet velocity equal to the mixture inlet velocity is prescribed. This specification of an extremely small film thickness has negligible impact on the final results.

At the cooled, isothermal plate ($r = R$), no slip and constant temperature are imposed as shown in Eqs. (7.1).

$$U_L = 0 \quad , \quad V_L = 0 \quad , \quad T_L = T_{\text{wall}} \tag{7.1}$$

At the centre-line ($r = 0$), symmetry is prescribed using Eqs. (7.2).

$$V_M = 0 \quad , \quad \frac{\partial U_M}{\partial r} = \frac{\partial T_M}{\partial r} = \frac{\partial W}{\partial r} = 0 \tag{7.2}$$

At the outlet, fully developed boundary conditions are applied, similar to

Eqs. (2.21) and (2.22), and a solution pressure of zero is specified at one node. For the calculations of the properties, the pressure field is shifted to obtain absolute pressure of P_{ref} at the inlet.

7.3 Comparison with Groff Model

To compare against the Groff model, results were obtained for a steam-air mixture at $P_{\text{in}} = 1$ bar for $\text{Re}_{\text{in}} = 1000$. Other pressures and Reynolds numbers in the laminar regime are possible. Trends discussed here will be similar under other conditions. The radius of the tube was specified to be $R = 5.0$ mm and the tube length was $L = 400$ mm. The codes for the present model and the Groff model were run for a variety of cases in the range $0.1 \leq W_{\text{in}} \leq 0.5$ for three inlet-to-wall temperature differences ($\Delta T = 5, 10, 20$ K).

Grid independence tests were carried out based on the film thickness for the case with the lowest inlet gas mass fraction and the highest inlet-to-wall temperature difference. The range of values considered was as follows: $40 \leq \mathtt{N}_z \leq 200$ with $1.0 \leq S_z \leq 1.1$, $15 \leq \mathtt{N}_{r,L} \leq 40$, and $20 \leq \mathtt{N}_{r,M} \leq 100$ with $0.9 \leq S_{r,M} \leq 1.0$. A grid with $\mathtt{N}_z$= 150 with S_z= 1.04, $\mathtt{N}_{r,L}$= 20, $\mathtt{N}_{r,M}$= 80 with $S_{r,M}$= 0.95 had normalized maximum difference of film thickness of less than 0.045% compared to the next finer mesh. Therefore, this grid was used for the results presented in this study.

The results presented in this section are for the inlet gas mass fraction of 0.1 and 0.5 with the inlet-to-wall temperature of 5 K and 10 K. The comparisons of the code results are based primarily on axial variation of film thickness, local Nusselt number and, interface gas mass fraction.

Figure 7.2 shows the increase of the liquid film thickness along $z^\star$ for all four cases. The rate of growth of the film slows along the tube due to the increased film thickness and a build-up of gas at the interface. The film thickness increases as the gas mass fraction at

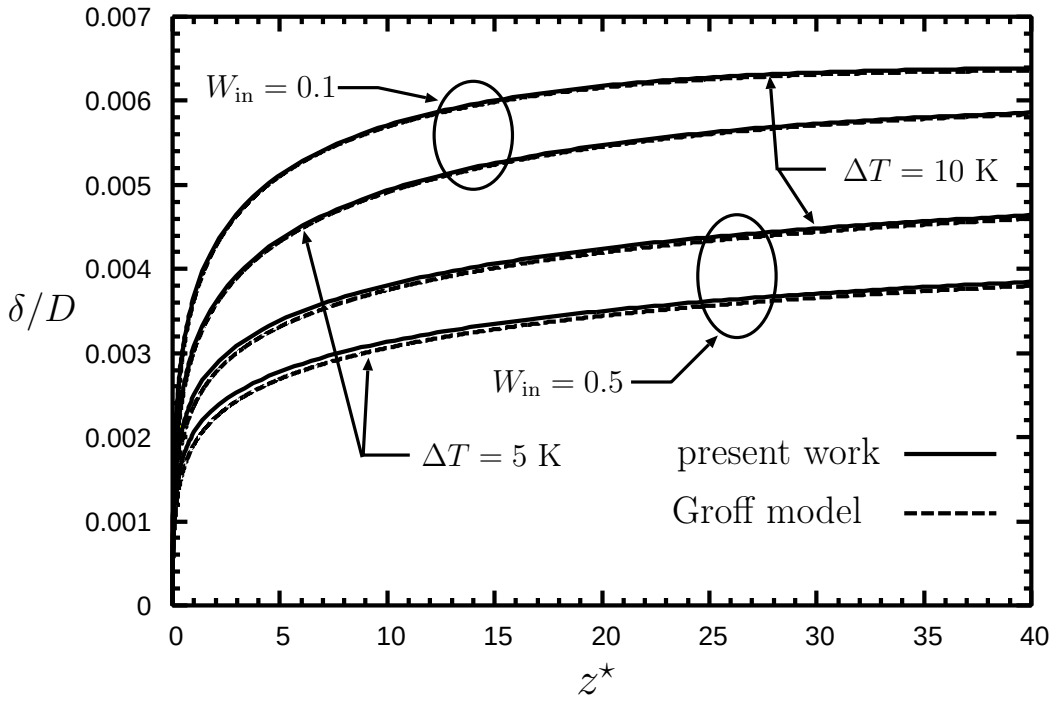

Figure 7.2: Film thickness comparison with Groff model

the inlet decreases or the inlet-to-wall temperature difference increases. For all four cases, the film thickness compares well between the present work and the Groff model. There is slightly greater deviation for the $W_{\text{in}} = 0.5$ cases.

Figure 7.3 shows the local Nusselt number for all the same cases as in Fig. 7.2. The Nusselt number definition is written as Eq. (7.3).

$$\text{Nu}_z = \frac{(2R)\frac{\partial T_L}{\partial r}|_{r=R}}{T_{\text{in}} - T_{\text{wall}}} \tag{7.3}$$

As expected, there is a good agreement between the present work and the Groff model for all cases. The decrease in the amount of non-condensable gas from 0.5 to 0.1 causes an increase in the local heat transfer rate in the region near the inlet. As W_{in} decreases, there is more rapid decrease of Nusselt number towards the outlet of the tube. This trend is due to a higher condensation rate for lower W_{in}. Although there is a thicker film for the higher

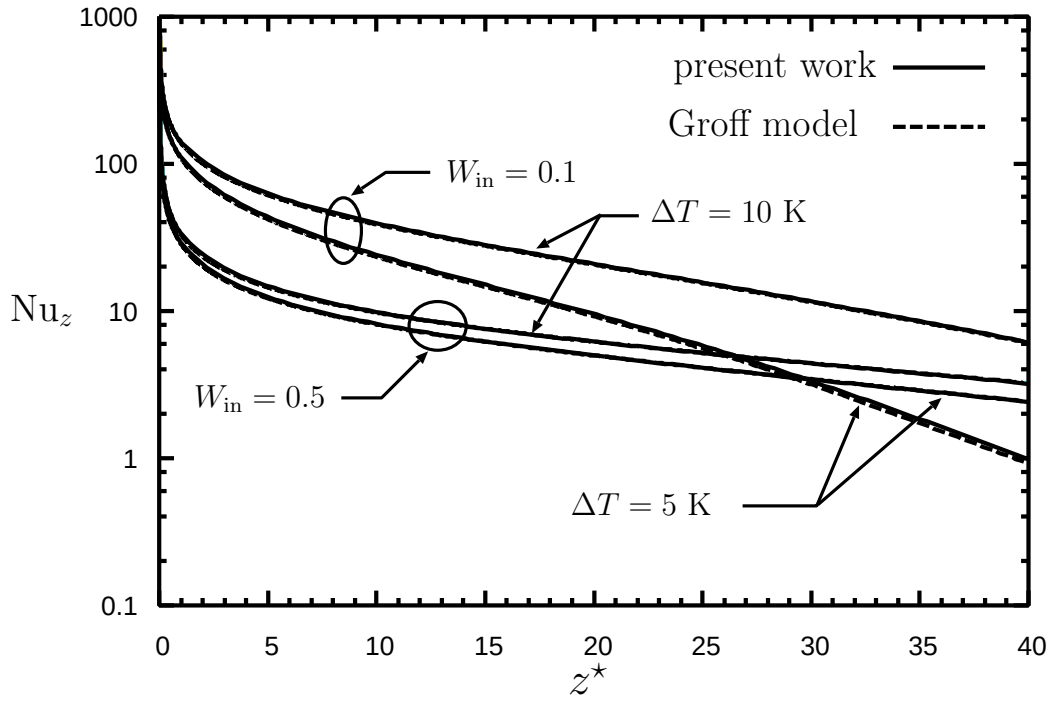

Figure 7.3: Local Nusselt number comparison with Groff model

condensation rate, but the lower inlet gas mass fraction leads to lower interface gas mass fraction and more condensation.

The axial variation of the interface gas mass fraction, shown in Fig. 7.4, also shows good agreement between the two models. It is noted that the interface air mass fraction increases axially in all cases due to the loss of vapour. The axial increase of W_{int} is smaller for higher inlet gas mass fraction because the air mass fraction is already quite close to the maximum possible (the air mass fraction value corresponding to the partial pressure of the steam at the wall temperature).

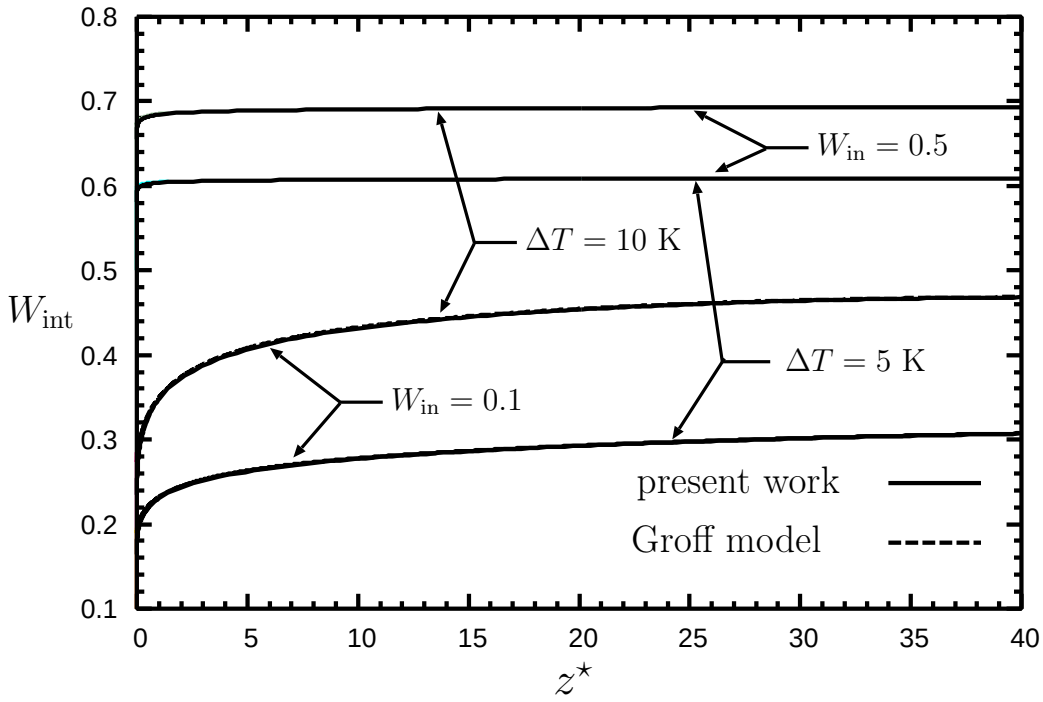

Figure 7.4: Interface gas mass fraction comparison with Groff model

7.4 Additional Results

As shown in the previous section, there is a very good agreement between the present work and the Groff model which used a parabolic modelling approach. In this section, the effects of Reynolds number, gas mass fraction, and inlet-to-wall temperature difference are investigated briefly. More detailed discussion about the physical phenomena and the role of the above-mentioned parameters can be found in [9]. All the results in this section are presented for the same tube as the previous section.

Figure 7.5 shows the Nusselt number for two inlet Reynolds numbers and three different inlet gas mass fractions with a constant inlet-to-wall temperature difference. The same definition as Eq. 7.3 was applied for the calculation of the Nusselt number. Higher Re_{in} causes more shear at the interface and make the film thinner. Therefore, the Nusselt number increases as the inlet Reynolds number increases. As expected, lowest inlet gas mass fraction

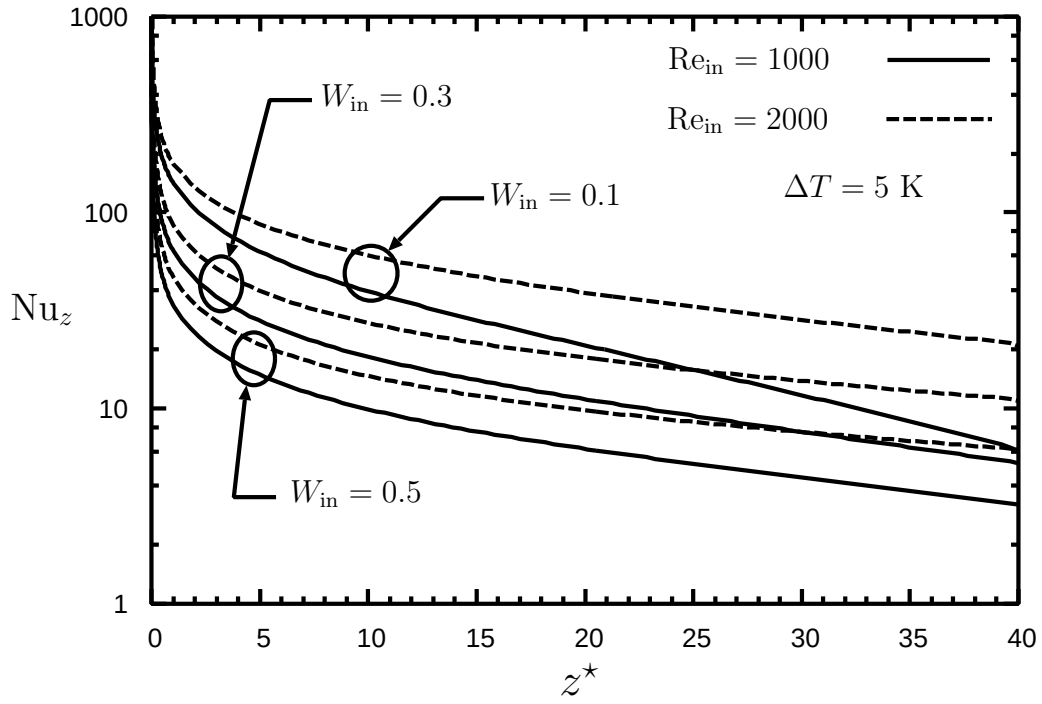

Figure 7.5: Axial variation of local Nusselt number

has the highest Nusselt number for the both inlet Reynolds numbers. This is due to the existence of more vapour and higher condensation rate.

Figure 7.6 shows the axial variation of the amount of the liquid condensed relative to the amount of vapour entering the tube: $(\frac{\dot{m}_L}{\dot{m}_{v,\text{in}}})$. The value of 1 indicates that most of the incoming vapour has been condensed. As W_{in} decreases, the present model predicts much higher proportions of the inlet vapour condensed. As well, the rate of condensation is higher for the cases with lower W_{in}. A higher condensation rate corresponds to a thicker film (as seen in Fig. 7.2). For the case of $W_{\text{in}} = 0.1$ and $\Delta T = 20$ °C, for example, over 92% of the inlet vapour has been condensed.

As mentioned in Section 5.3, one of the major differences between the elliptic approach and parabolic approach is the method of pressure calculation. In the Groff model, it was assumed that the pressure is constant in the r direction and the overall mass conservation

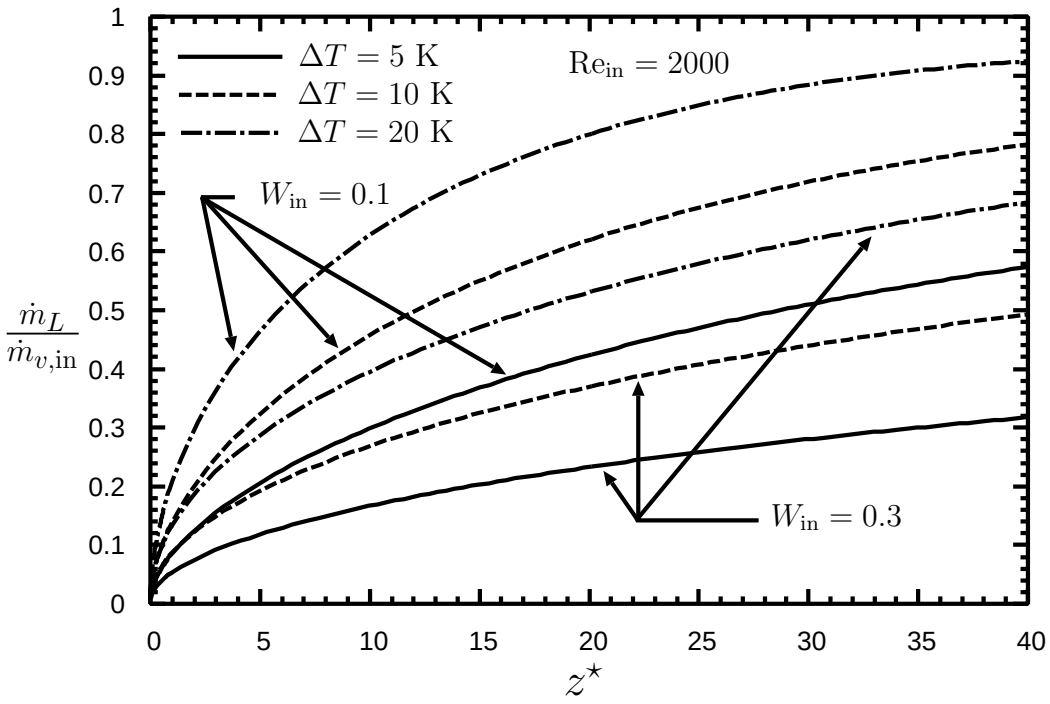

Figure 7.6: Axial variation of normalised liquid mass flow rate

equation was used to determine the local axial pressure gradient. In the present work, the pressure is connected to the two momentum equations and is calculated based on the continuity equation. The pressure profiles for two different inlet Reynolds numbers are given in Figs. 7.7 and 7.8 using the dimensionless coordinate η defined by Eqs. (7.4).

$$\begin{aligned} \eta &= r/(R-\delta) && \text{for} \quad 0 \le r \le R-\delta \\ \eta &= (r+\delta-R)/\delta + 1 && \text{for} \quad R-\delta \le r \le R \end{aligned} \tag{7.4}$$

The locations of the shown profiles are given in Table 7.1.

Table 7.1: Axial locations of the pressure profiles

$z_1^\star$	$z_2^\star$	$z_3^\star$	$z_4^\star$	$z_5^\star$	$z_6^\star$	$z_7^\star$	$z_8^\star$	$z_9^\star$
0.0241	0.0648	0.1491	0.5777	0.9337	2.365	4.1315	8.2150	12.115

For the demonstration of the pressure profiles, the inlet gas mass fraction was set to 0.1 and the inlet-to-wall temperature difference was set to 10 K. The profiles for the pressure in Figs. 7.7 and 7.8 show that the assumption of constant pressure in r direction may not be realistic in the inlet region of the tube. The maximum pressure difference in the r direction is about 0.9 Pa and 1.8 Pa for $\mathrm{Re_{in}} = 1000$ and $\mathrm{Re_{in}} = 2000$, respectively. This maximum difference happens at the very first column of control volumes at the inlet. Also, there is a small jump in the pressure between the phases for the few stations close to the inlet. The total pressure rise along the full length of the tube is 3.07 Pa and 4.94 Pa for $\mathrm{Re_{in}} = 1000$ and $\mathrm{Re_{in}} = 2000$, respectively. For both cases, after $z^\star \approx 0.5$ the pressure profiles become uniform along the r direction.

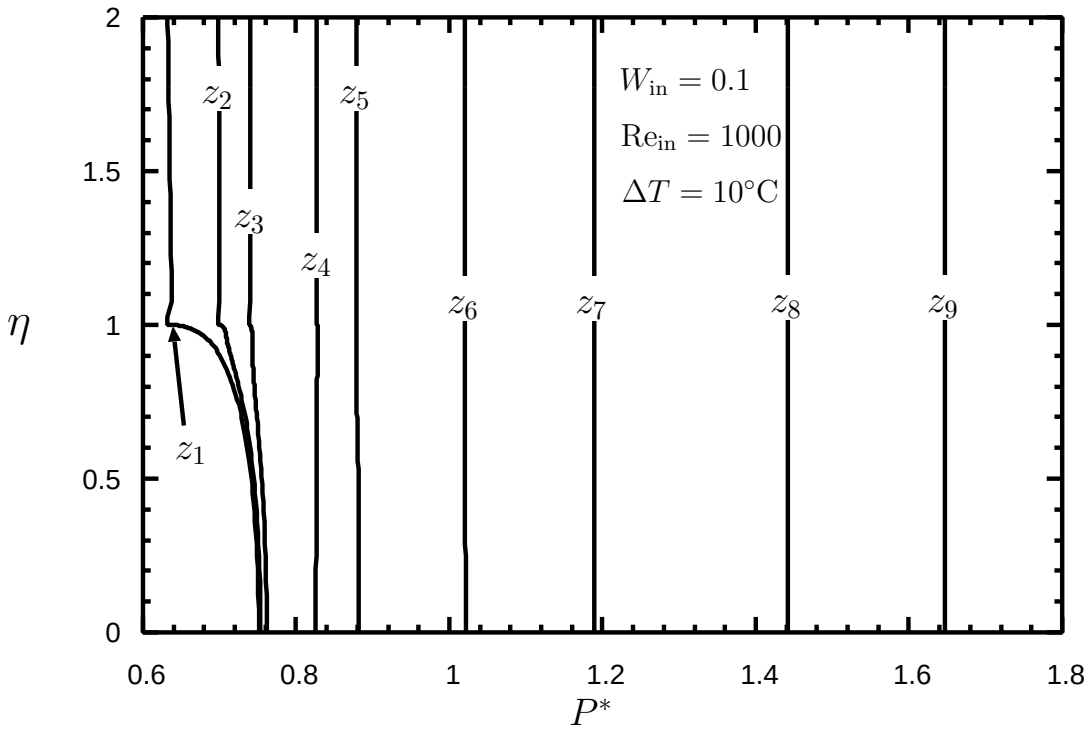

Figure 7.7: Pressure profiles for $\mathrm{Re_{in}} = 1000$

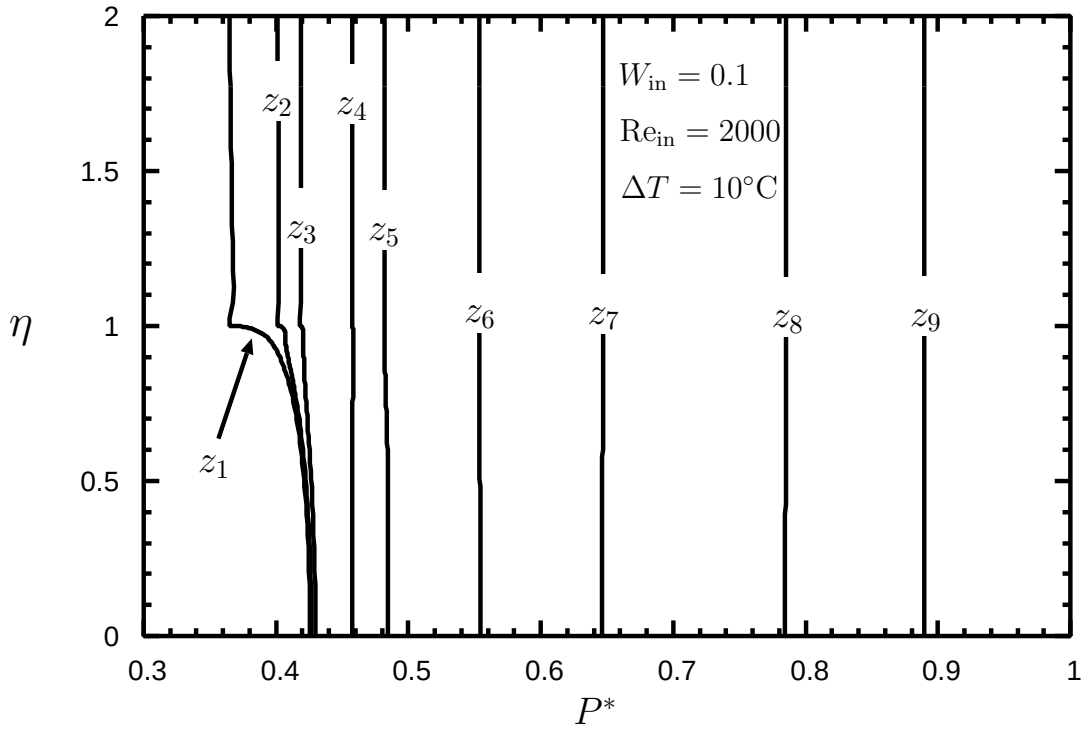

Figure 7.8: Pressure profiles for $\text{Re}_{\text{in}} = 2000$

Chapter 8

Tubes: Counter-Current Flow

8.1 Introduction

This chapter focuses on reflux condensation in vertical tubes. In Section 1.4 the model domain and all the boundary conditions were explained. As shown in Fig. 1.4, the domain has three sections. The results in this chapter are presented with the focus on the cooled section.

Figure 8.1 illustrates schematically the key regions of downward flow of liquid and gas phases and upward flow of the gas phase. The gas-vapour mixture flows upward into the tube from the bottom. Liquid condensate starts forming at the top of the cooled section and flows down the wall. The main difference between this form of condensation and the co-current condensation is the direction of the flow in the mixture. As shown in Fig. 8.1, the flow in the mixture is divided into two parts. Shear at the phase interface causes the mixture near the interface to flow downward with the liquid. The remaining mixture flows upward. As mentioned before, the point that the direction of the mixture velocity changes is referred to here as the "break-point". This is the point where the mixture velocity becomes zero. At each axial station, the break-point is located at r_b. The location of the break point is affected by the condensation rate and the velocity of the flow core. The dashed lines in Fig. 8.1 are a schematic illustration of the connection of all break-points. The shape of the break-point line is a function of all the parameters that control the condensation rate such as the mixture velocity, the length of the cooled section, the inlet mass flow rate, the inlet gas mass fraction, and the inlet-to-wall temperature difference.

The highest condensation rate occurs close to the inlet of the cooled section. Further up the domain, the condensation rate decreases due to the gas build-up at the interface and the

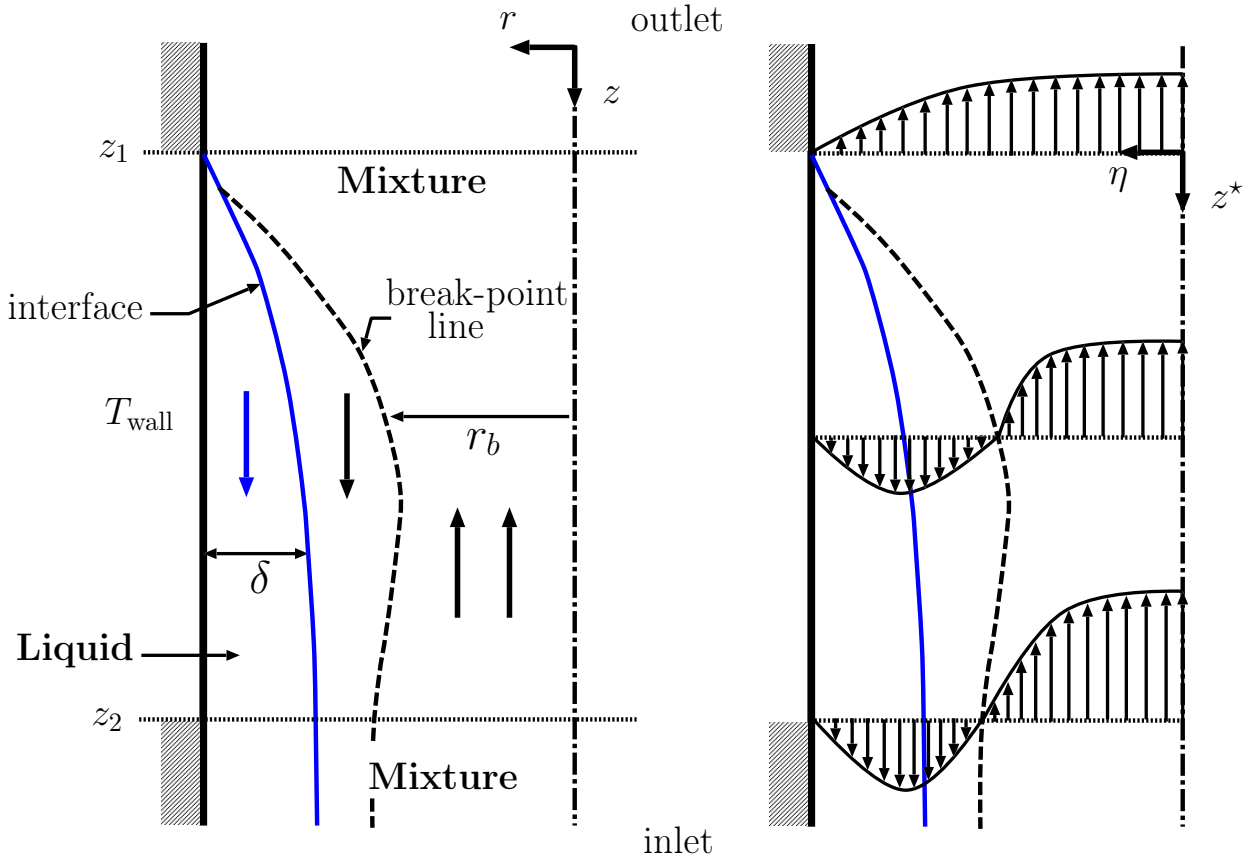

Figure 8.1: Axial variation of the film thickness and the break-point location; the film thickness and location of the break-points are exaggerated for illustration purposes.

reduction of the interface-to-wall temperature difference. Therefore, the interface gas mass fraction increases from the inlet to the outlet while the interface temperature decreases.

As the gas-vapour mixture flows inside the tube, condensation removes mass from the flow core and this slows down the flow. Thus, the mixture velocity decreases along the domain from inlet to outlet. On the other hand, the liquid average velocity increases from top to bottom. The interface velocity may decrease from top to bottom, however, for the cases with high mixture velocity. A very high mixture velocity can lead to liquid hold-up which is the situation where the liquid interface velocity becomes negative and liquid tends to flow upward in the same direction as the mixture. This situation often leads to flooding. In

addition to the mixture flow velocity, the downward liquid film acceleration is also a function of the weight of the condensate flow. More condensation results in heavier film that tends to avoid liquid hold-up.

As mentioned in the literature review (in Section 1.5), the research that was done by Vierow *et al.* [31,38] are the best available experimental data that could be used as a reference for the comparison and validation of laminar reflux condensation in tubes. The comparison of the present numerical model results with the data given by Vierow *et al.* is presented in the next section. After that comparison, additional results are provided for different geometries and boundary conditions.

8.2 Comparison with Previous Work

As mentioned in the literature review, the detailed information and results provided by Nagae *et al.* [33] and Vierow *et al.* [31] were not sufficient for the purpose of comparison and validation.The case that was used for the comparison was defined based on the information in the two unpublished technical reports obtained from Dr.Vierow [38]. Vierow *et al.* designed and constructed an experimental facility at Purdue University in 2003. The main objectives of their research were to provide local heat transfer data for development of methods to analyze reflux condensation in pressurized water reactor steam generator U-tubes and to investigate the potential of flooding. They ran tests over a specified test matrix and measured steady-state wall temperatures and centre-line temperatures in order to calculate the local heat transfer coefficients. The experiments were performed for the following ranges: pressure from 0.1 to 0.4 MPa; steam flow rate from 1 to 3 g/s; and air mass flow rate of 0.02 to 0.18 g/s. Vierow *et al.* did not report pure vapour results because steady-state conditions were not possible for pure steam. They managed to get steady-state data for 21 different cases. Reynolds numbers for the mentioned cases are in the range of 2692 to 11366, which they called laminar. Due to the high inlet-to-wall temperature difference, much of the vapour

condenses close to the inlet. This mass loss reduces the velocity of the mixture and thus reduces the Reynolds number quickly. Therefore, the assumption of laminar flow may be valid in some portions of the tube, but possibly not at the inlet. The present study applies only to laminar reflux condensation, so the case with the lowest Reynolds number (Test 1, $\mathrm{Re}_{\mathrm{in}} = 2692.02$ [38]) was chosen for validation purposes.

8.2.1 Geometry and Boundary Conditions

The experiment was conducted for a tube with a diameter of 19.3 mm and cooled section length of 1.78 m. Other given data for Test 1 are: $\dot{m}_{g,in} = 0.12$ g/s; $\dot{m}_{v,in} = 0.42$ g/s; and $P_{\mathrm{in}} = 100$ kPa. Vierow *et al.* assumed that all vapour of the mixture condenses in the tube and pure air exits the tube at the top. The energy balance calculation shows that this assumption led to negligible errors for their tests, however, this could not be used as a general boundary condition for the numerical model. For their experiment, a more reasonable assumption would have been saturated air leaving the tube at the top. In reality, there may be cases that not necessarily all vapour condenses.

The wall temperature was measured by Vierow *et al.* and therefore, variable wall temperature should be imposed as boundary condition in the numerical model. Based on the provided data, a sixth order polynomial as a function of z was used to apply the same wall temperature as the experiment.

The wall temperature function used was:

$$T_{\mathrm{wall}}(z) = -4.8416z^6 + 13649z^5 - 13.275z^3 + 15.593z^2 - 1.3742z + 294.05 \tag{8.1}$$

8.2.2 Challenges in the Modelling

As mentioned earlier, Vierow *et al.* assumed that all the vapour condenses in the tube. They also measured the inlet gas mass flow rate. Therefore, the inlet vapour mass flow rate

and consequently the inlet gas mass fraction could be calculated based on the inlet gas and condensate mass flow rates. The experimentally measured mass flow rates were taken to be net mass flow rates. The inlet temperature, however, was not reported by Vierow *et al.*, so it was necessary to assume the inlet temperature as the saturation temperature at the inlet gas mass fraction and pressure. This may be different than what happened in the experiment and the inlet temperature could be the temperature of superheated vapour. Thermophysical properties and the inlet Reynolds number were calculated based on this temperature.

The conditions that could be prescribed in the numerical model as the boundary conditions are inlet gas mass fraction and inlet temperature. The inlet velocity profile is unknown and as explained before; instead, the relative pressure is prescribed at the inlet of the tube. The pressure difference over the length of the tube, and the condensation rate control the inlet mass flow rate. Thus, to reach the exact same inlet mass flow rate as the experiment, the pressure difference in the tube should be adjusted.

As mentioned in Section 2.3, liquid hold-up and instabilities, inlet Reynolds number, and condensation rate should be monitored for any reflux condensation simulation case. In addition to all these constraints, a new constraint exists for this comparison case: the net inlet mass flow rate should match the experiment. As discussed before, at the inlet of the tube, mixture has two regions of inflow and outflow. The summation of inflow and outflow mass flow rates produces the net mass flow rate at the inlet which should match the reported experimental inlet mass flow rate.

Another particularly important challenge is related to the geometry. The length of the cooled section and the diameter were defined by the experiment. However, the lengths of two additional sections in the domain (top and bottom sections) must be selected carefully. These sections must be long enough to ensure proper boundary conditions are prescribed but not too long so that they affect the flow significantly.

Experience showed that it was very difficult to provide initial guesses for the velocity,

gas mass fraction, temperature, and pressure fields that were consistent with the steady-state solution. Prescribing an appropriate pressure difference in the tube was difficult as well. During the first few thousands of iterations, it was necessary to define the pressure difference high enough to help the flow to develop through the domain and not allow any mass to enter the tube from the top. After this stage, the pressure difference could be reduced to keep the inlet flow in the laminar region.

The lengths of the bottom and top sections must be defined based on the approximate Reynolds numbers at the outlet and inlet of the cooled section, together with the temperature and gas mass fraction profiles at the outlet of the cooled section. These lengths could not be determined until the pressure range that satisfied the previously mentioned constraints had been determined. Furthermore, after changing the lengths, the model behaved differently and it was necessary to define a new pressure difference for the new length to satisfy the other constraints. Moreover, the grid size should be modified based on the new lengths.

This time-consuming and computationally expensive monitoring procedure was carried out until the inlet mass flow rate matched the experiment data and all other constraints were satisfied.

In preliminary runs of counter-current flows in tubes with the model described in Chapter 4, convergence problems were encountered due to temperature boundary condition jump in the liquid region at the boundary of the cooled and bottom section. Note that the inlet-to-wall temperature differences were very high for all the attempted cases. It was found that solving the energy equation in the liquid in that specific region is almost impossible. This problem was severe and prevented converged solutions from being obtained. A simple solution, that had negligible effect on the results for the cooled section, was to not solve the energy equation in the liquid region in the bottom section. Thus, with the assumption of no heat transfer at the interface and the insulated wall for the bottom section, the liquid temperature was set to be equal to the mixture temperature only in this section. In reality,

the liquid leaving the cooled section flows into a tank or reservoir which means that the mentioned assumption is reasonable. This modified condition was then used for all cases of counter-current flow in tubes presented in this thesis.

8.2.3 Grid Independence Test

Three sets of grids were used for the grid independence test. All the previously mentioned challenges were faced during this process and it was difficult to achieve the specified inlet mass flow rate for these cases. The specifications of the tested grids are given in Table 8.1. All the grid expansion factors were set to 1.

Table 8.1: Grid parameters for the grid independence tests

	$\mathtt{N}_{L_1}$	$\mathtt{N}_{L_2}$	$\mathtt{N}_{L_3}$	$\mathtt{N}_{r,M}$	$\mathtt{N}_{r,L}$
Grid #1	30	150	50	140	20
Grid #2	30	250	50	160	20
Grid #3	30	250	50	200	20

$\mathtt{N}_{L_1}$, $\mathtt{N}_{L_2}$, and $\mathtt{N}_{L_3}$ are the axial number of nodes in the top, cooled and bottom sections, respectively. In the r direction, $\mathtt{N}_{r,M}$ is the number of nodes in the mixture and $\mathtt{N}_{r,L}$ is the number of nodes in the liquid. Because the film thickness is so small and no strong gradients in the fields occur within the falling film, relatively few nodes are required in the liquid region. As discussed for the co-current cases, in the range of $15 \leq \mathtt{N}_{r,L} \leq 40$, the results may differ by less than 0.1% (maximum percentage difference). Therefore, $\mathtt{N}_{r,L}$ was set to 20 for all grids. From Grid #1 to Grid #2, 50 and 20 nodes were added to the cooled section axially and mixture region radially, respectively. From Grid #2 to Grid #3 just the number of nodes in the mixture in r direction was increased by 40. Values of centre-line temperature and film thickness were used to assess the effect of changing the grid. The centre-line temperature is

the parameter that was used for the comparison with the experimental data. For the grid independence tests, convergence criteria were the same as those explained in Section 4.7.1.

As shown in Table 8.2, the maximum relative differences of the results with respect to their range among all these three grids are sufficiently small for both parameters. These tests show that even Grid #1 is suitable for the study of this geometry, Grid #3 was selected, however, to ensure good quality results. To be conservative, the results presented in the next section were obtained using Grid #3.

Table 8.2: Grid independence test results

	Grid #1 to #2	**Grid #2 to #3**
Maximum percentage difference for T_{cl} with respect to the range	1.453%	0.189%
Maximum percentage difference for δ with respect to the range	1.625%	0.063%

8.2.4 Comparison with the Experiment

As mentioned before, Vierow *et al.* measured and reported centre-line temperature at nine axial locations. Figure 8.2 shows the comparison of the results from the present work and the reported experimental data. Also, the wall temperature profile is shown in the same figure. The numerical results match the experimental data qualitatively. The numerical model, however, predicts higher core flow temperature than the experiment. The difference may originate from the different inlet temperature conditions.

To achieve the exact net inlet mass flow rate as the experiment the pressure difference was set to 15.6 Pa. Table 8.3 is a summary of the available and calculated data of the experiment.

As presented in Table 8.3, the net inlet mixture, vapour, and gas mass flow rates match

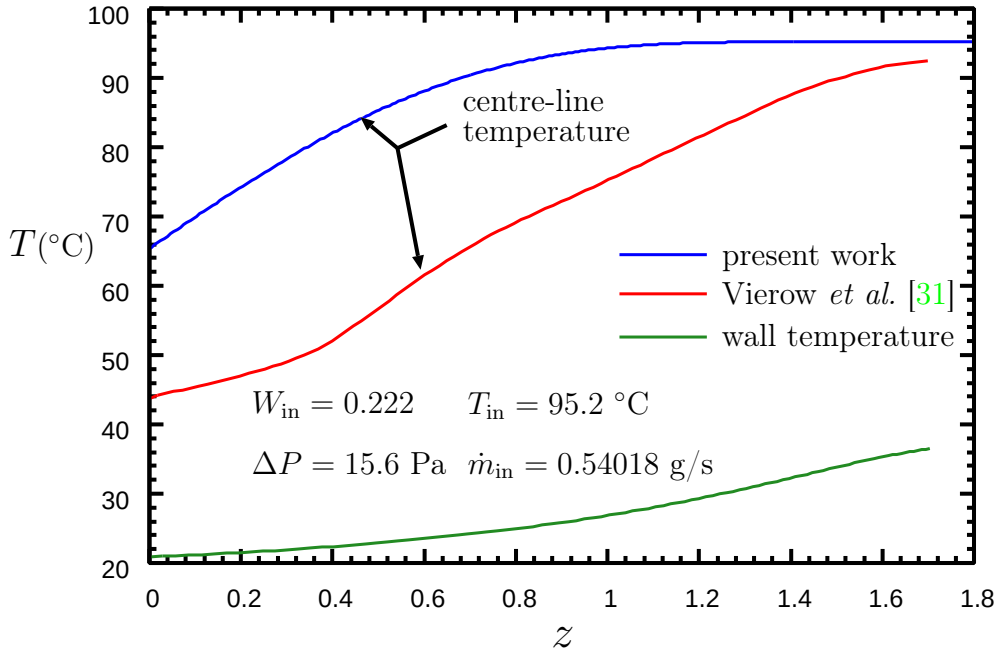

Figure 8.2: Comparison of centre-line temperature with Vierow *et al.* [31]

Table 8.3: Comparison of all conditions and results between the present work and the work by Vierow *et al.*

	Re_{in}	$\dot{m}_{\text{in}}{}^{\#}$ [g/s]	$\dot{m}_{g,\text{in}}{}^{\#}$ [g/s]	W_{in}	$\dot{m}_{v,\text{in}}{}^{\#}$ [g/s]	$\dot{m}_L$ [g/s]	T_{in} [K]
Vierow	2692.02*	0.54*	0.12	0.222*	0.42*	0.42	-
present work	2690.9	0.54018	0.1199	0.222+	0.42026	0.40105	368.354+

net value

* Calculated based on the available data

+ Prescribed boundary conditions

the experimental data. The numerical model predicts 0.40105 g/s of condensate leaving the tube while this was reported as 0.42 g/s for the experiment. The difference is 4.512% which is reasonable.

8.3 Test Case Definitions

The new results were obtained for three different tube geometries and different boundary conditions. The three geometries were: (1) short length with small diameter (G1), (2) longer length with small diameter (G2), and (3) long length with large diameter (G3). The dimensions of those tubes are given in Table 8.4. A wide range of W_{in} and ΔT was considered to generate the test matrix of a parametric study. The focus of the presentation of results will be mainly on the cooled section.

Table 8.4: Geometrical information of the defined cases

Geometry	L_1 [m]	L_2 [m]	L_3 [m]	R [mm]	Description
G1	0.4	0.5	0.4	6.35	shorter tube, smaller diameter
G2	0.5	1.0	0.5	6.35	longer tube, smaller diameter
G3	0.5	1.78	0.22	9.65	long tube, larger diameter

8.4 Grid Selection

As explained in Section 8.2.3, a grid independence test was done for the large-diameter tube with the boundary conditions same as the experimental case. The two other cases (G1 and G2) have smaller diameters (12.7 mm compared to 19.3 mm) and shorter cooled sections (1.0 m and 0.5 m compared to 1.78 m). Therefore, it is expected that any of the grids in Table 8.1 could be suitable for studying the G1 and G2 cases. In order to be conservative and following the experience gained in the preliminary tests, a grid with the following specifications was chosen for the analysis of cases for G1 and G2: $\mathtt{N}_{L_1} = 50$, $\mathtt{N}_{L_2} = 250$, $\mathtt{N}_{L_3} = 50$, $\mathtt{N}_{r,M} = 180$, $\mathtt{N}_{r,L} = 20$ (all the grid expansion factors were set to 1.0). Grid #3, described in Section 8.2.3, was used for G3.

8.5 Detailed Examination of the Predictions for G1

For G1, the model was run for a variety of cases in the range $0.01 \leq W_{\text{in}} \leq 0.7$ for seven inlet-to-wall temperature differences ($\Delta T = 3, 5, 10, 20, 30, 40, 60$ K). As shown in Table 8.5, there are 20 cases that have a converged solution. There are also 14 cases that are possible

Table 8.5: Cases for G1*

		W_{in}					
		0.01	0.1	0.2	0.3	0.5	0.7
ΔT [K]	3	C	P	P	P	P	P
	5	C	C	C	C	C	P
	10	X	P	C	P	C	P
	20	X	C	C	C	C	C
	30	X	P	P	C	C	P
	40	X	X	C	C	C	C
	60	X	X	X	C	P	P

* C: Converged; P: Possible; X: Violate Constraints

which were attempted and showed potential to converge but were not completed due to the limitations of the computational resources. It is estimated that the completion of these "Possible" runs would take a year with the currently available resources. There are also cases for which the conditions would lead to results that do not meet the solutions constraints; that is, the inlet flow is turbulent or mass is drawn from the top or there are oscillations due to liquid hold-up. These cases are marked with an X in Table 8.5 are referred to as "Violate Constraints". For example, for the case with $W_{\text{in}} = 0.01$, it was possible to obtain a valid, converged solution for ΔT of 3 K and 5 K. Once, the inlet-to-wall temperature difference was increased to 10 K, however, the condensation rate was high enough to pull in mass from the outlet. Therefore, the pressure difference had to be increased which resulted in more mass flowing in from the inlet and higher inlet Reynolds number that was in the turbulent

region.

For the examination of the details of the model predictions, one of the cases was selected and the results are presented for this specific case in this section. In this case, the gas-vapour mixture flows in the tube from the bottom with $W_{\text{in}} = 0.1$, $T_{\text{in}} = 371.01$ K ($\Delta T = 5$ K), and $\text{Re}_{\text{in}} = 1572.9$. A pressure difference of 10 Pa was specified to obtain the mentioned inlet Reynolds number.

As discussed in Section 8.1, the gas-vapour mixture has regions of upflow and downflow. Figure 8.3 shows the film thickness and the location of the break-point line. In this figure, r_b

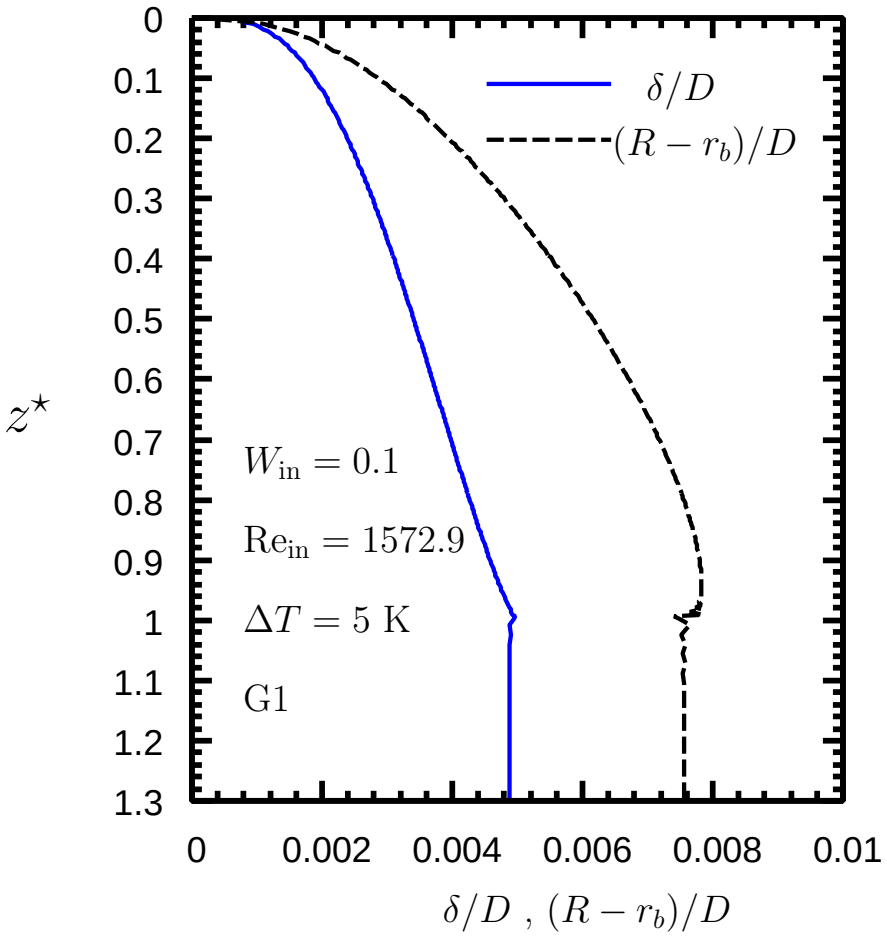

Figure 8.3: Axial variation of the film thickness and the break-point location

corresponds to the location of break-point at any axial station, and R and D are the radius and diameter of the tube, respectively. Also, $z^\star$ is defined by Eq. (8.2)

$$z^\star = \frac{z - z_1}{z_2 - z_1} \tag{8.2}$$

where, $0 \leq z^\star \leq 1$ represents the cooled section and $z^\star < 0$, and $z^\star > 1$ correspond to the top and bottom sections, respectively.

As seen in Fig. 8.3, the film thickness is nearly constant in the bottom section. As the upward flow reaches the cooled section ($z^\star = 1$), there is a small bump due to the abrupt change of the boundary conditions at the wall and sudden start of condensation. As expected, the film is thicker close to the inlet (bottom) because of the lowest interface gas mass fraction and highest interface-to-wall temperature difference at that location. The film thickness goes to zero at the top which is the end of the cooled section ($z^\star = 0$).

The maximum width of the mixture downward flow region for this specific case is 4.18×10^{-5} m which occurred at $z^\star = 0.838$. At the same location, the film thickness is 5.565×10^{-5} m, and the width of the downward flow region is about 75.1% of the film thickness. The maximum width of the downward flow region relative to the film thickness is 81.7% which occurred at $z^\star = 0.626$. At this location the film thickness and the downward flow region thickness are 4.785×10^{-5} m and 3.91×10^{-5} m, respectively. In order to understand the flow behaviour better, velocity profiles at various axial locations are presented next.

The U-velocity profiles in the mixture are presented in Fig. 8.4. The profiles are plotted at different axial locations which are defined in Table 8.6.

Table 8.6: Axial locations of the profiles for G1

$z_1^\star$	$z_2^\star$	$z_3^\star$	$z_4^\star$	$z_5^\star$	$z_6^\star$	$z_7^\star$
-0.216	0.018	0.198	0.598	0.798	0.898	1.584

Locations $z_2^\star$ to $z_6^\star$ are in the cooled section, while $z_1^\star$ and $z_7^\star$ belong to the top and bottom

sections, respectively. The spatial variable η is defined by Eq. (7.4); it is equal to zero at the centre-line, one at the interface, and two at the wall. The velocity profiles are normalised by the magnitude of the average inlet velocity, as in $U^\star = U/|\,\overline{U}_{M,\text{in}}\,|$. The average inlet velocity, $\overline{U}_{M,\text{in}}$, is based on the net mass flow and the density of mixture at the inlet.

As seen in Fig. 8.4, the mixture velocity profile at the bottom of the cooled section, $z_7^\star$, is close to the fully-developed velocity profile in a tube. This profile was not prescribed

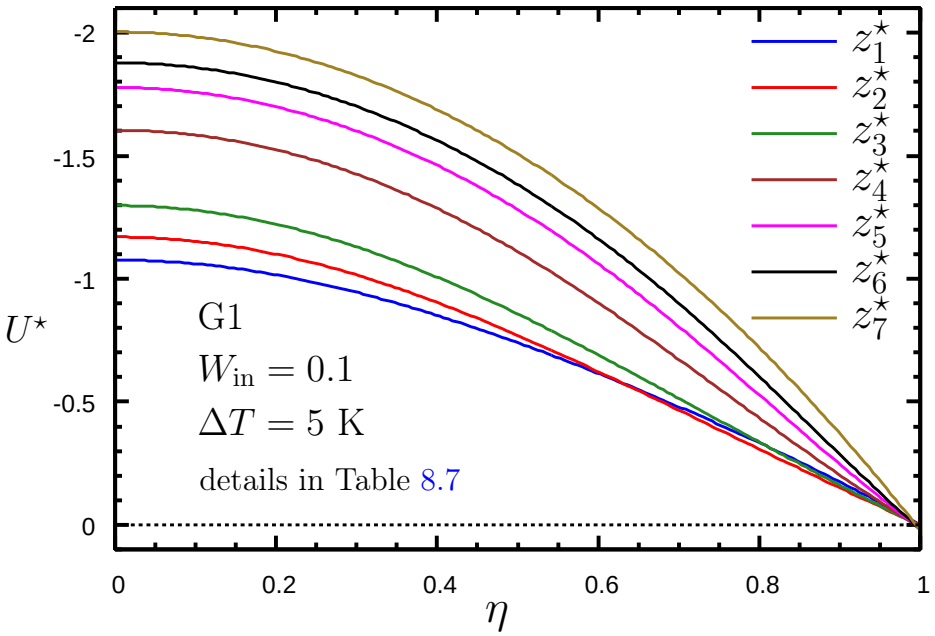

Figure 8.4: U-velocity profiles in the mixture for G1, $W_{\text{in}} = 0.1$, $\Delta T = 5$ K

at the inlet and was part of the solution. The velocity is negative at the centre-line which corresponds to the upward flow in the core flow. From the inlet to the outlet, the mixture velocity decreases because of the mass loss due to the condensation. This is confirmed by a close look at the centre-line velocity (at $\eta = 0$) as $z^\star$ decreases ($z_6^\star$ to $z_2^\star$). The interface velocity is always positive because of the shear force caused by the downward flow of the liquid. Near the interface, the mixture flows in the same direction as the liquid (downward). The details of that region are seen in Fig. 8.5. The break-points are at locations where

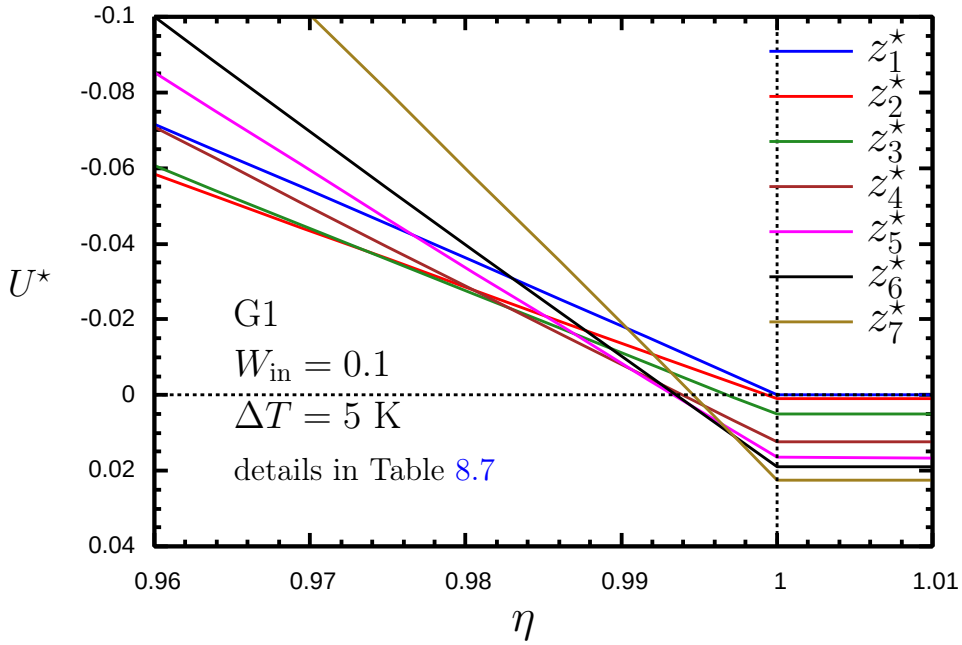

Figure 8.5: U-velocity profiles close to the interface for G1, $W_{\text{in}} = 0.1$, $\Delta T = 5$ K

$U^\star = 0$. The largest extent of downward flow is approximately 0.6% of the whole mixture region ($0.994 \leq \eta \leq 1$) at $z^\star = 0.898$ in this case.

The elliptic nature of the present model provides the benefit of the calculation of the V velocity based on the r-direction momentum equation. The V-velocity profiles in the mixture are shown in Fig. 8.6 for the same stations as used for the U velocity. The velocity profiles are normalised by the magnitude of the average inlet velocity, as in $V^\star = V/\mid \overline{U}_{M,\text{in}} \mid$. The V velocity at the bottom section is zero, so the V-velocity profile at $z_7^\star$ is not plotted in the figure. The highest radial velocity is at the beginning of the cooled section ($z_6^\star$) due to the high condensation rate. As the gas builds up at the interface and the rate of condensation decreases along the tube (from $z_5^\star$ to $z_2^\star$), the V velocity also decreases. Finally, at the top section ($z_1^\star$), the radial velocity is approaching to zero because of the fully developed boundary conditions that were applied at the exit of the top section. The maximum value of the V velocity does not occur at the interface because of the downward flow close to the interface. It is noticed that as the downward flow becomes weaker, the maximum point of

the V velocity gets closer to the interface.

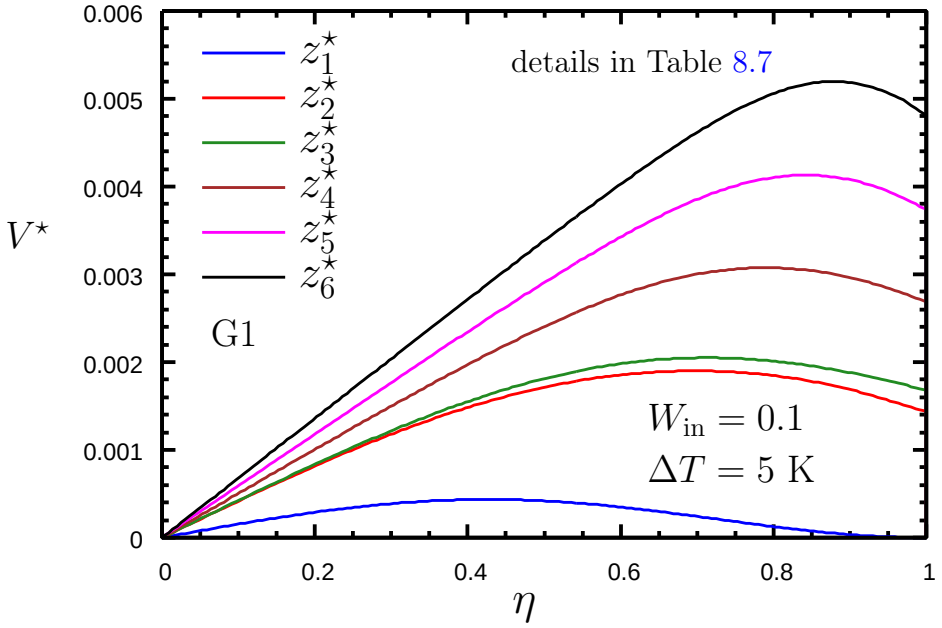

Figure 8.6: V-velocity profiles in the mixture for G1, $W_{\text{in}} = 0.1$, $\Delta T = 5$ K

Figure 8.7 presents the temperature profiles in the mixture. The non-dimensional form the of temperature, $T^\star$, is defined as $(T - T_{\text{wall}})/(T_{\text{in}} - T_{\text{wall}})$. In the bottom section, and before the cooled section ($z_7^\star$) there is no change in the temperature field because of no condensation and heat transfer. Beginning at the inlet of the cooled section ($z_6^\star$), the temperature starts dropping rapidly at the interface ($\eta = 1$) due to gas build-up. The centre-line temperature drops as well but with a lower rate compared to the temperature at the interface. In the top section, the temperature field is becoming more uniform because there is no energy transfer at the wall.

The gas mass fraction profiles have trends that are opposite to those for the temperature, as seen in Fig. 8.8. As condensation occurs, the gas mass fraction at the interface increases because gas is drawn toward the interface with the condensing vapour and the interface is impermeable to gas. There is a sudden jump at the interface from $z_7^\star$ to $z_6^\star$ because of the

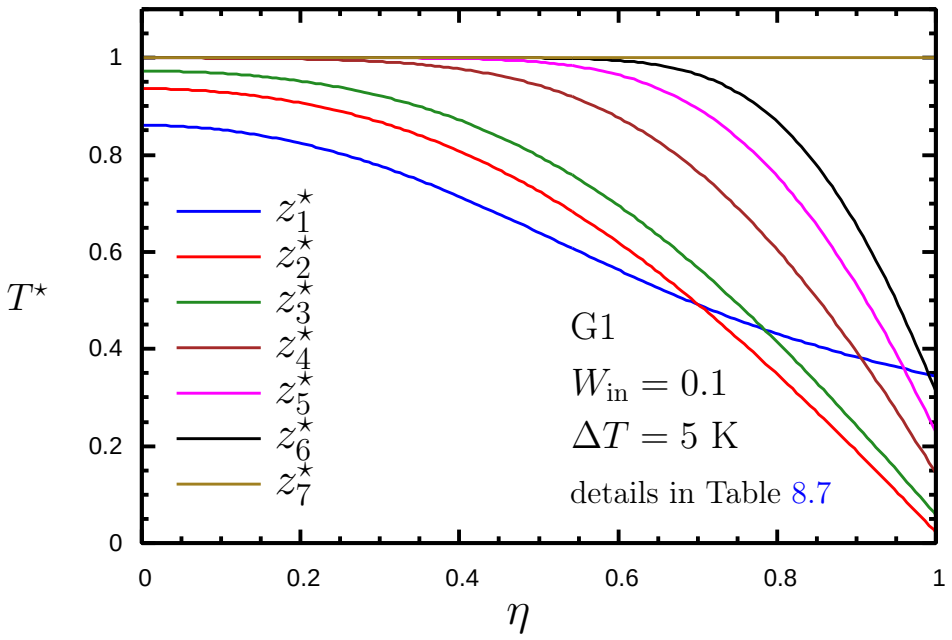

Figure 8.7: Temperature profiles in the mixture for G1, $W_{\text{in}} = 0.1$, $\Delta T = 5$ K

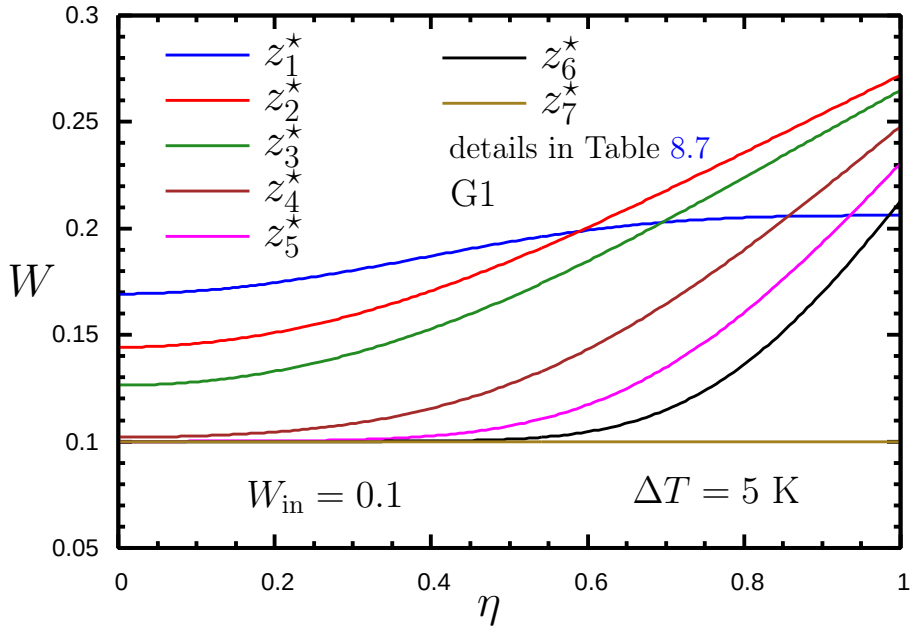

Figure 8.8: Gas mass fraction profiles in the mixture for G1, $W_{\text{in}} = 0.1$, $\Delta T = 5$ K

downward flow of the mixture that brings flow with higher gas mass fraction from the top of the tube to the bottom. The centre-line gas mass fraction increases as well but at a lower

rate than the gas mass fraction at the interface. Similar to the temperature, in the top section, the gas mass fraction becomes more uniform towards the outlet ($z_1^\star$).

Figures 8.9 and 8.10 show velocity and temperature profiles in the liquid region. The profiles at the top and bottom sections are not plotted in these figures. In the bottom section, the U velocity profiles are almost fully developed in the liquid region. In the top section, the film thickness is almost zero (specified to be 1×10^{-7} m) as discussed in Section 4.6. As seen in Fig. 8.9, the liquid accelerates in the z direction. Due to the condensation, the film gets thicker and heavier toward the inlet. At the wall ($\eta = 2$), the velocity is zero and at the interface ($\eta = 1$) it has the maximum value. The temperature profiles are almost linear in the liquid region because of the small film thickness.

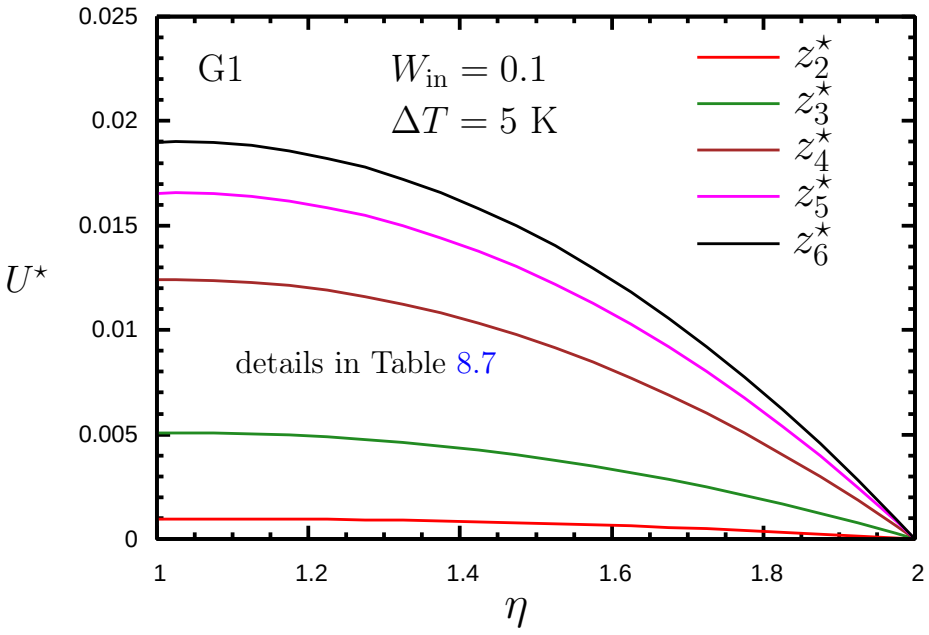

Figure 8.9: U-velocity profiles in the liquid for G1, $W_{\text{in}} = 0.1$, $\Delta T = 5$ K

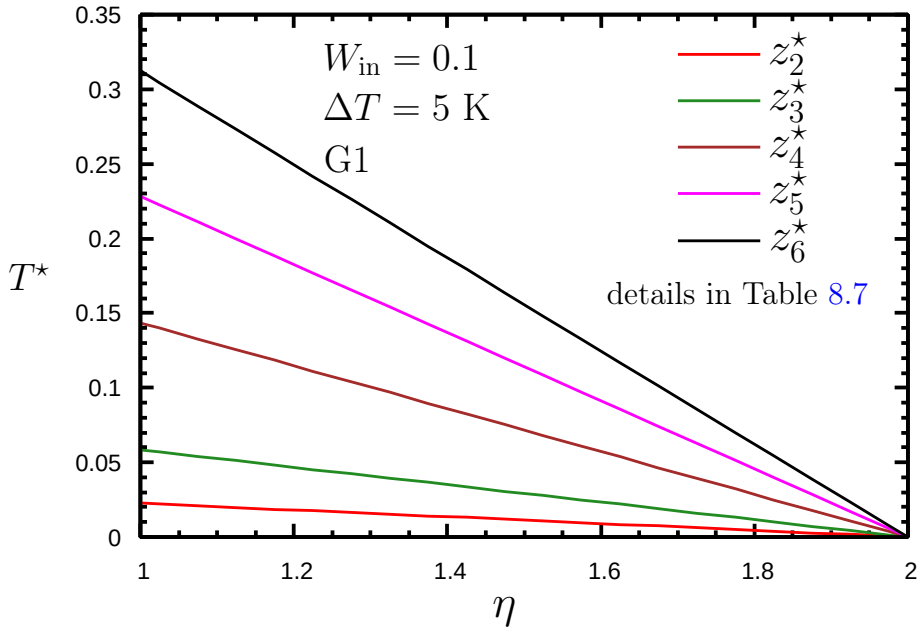

Figure 8.10: Temperature profiles in the liquid for G1, $W_{\text{in}} = 0.1$, $\Delta T = 5$ K

8.6 Parametric Study Results for G1

8.6.1 Overview of Cases

Because the inlet mass flow rate is part of the solution and there is no obvious relation between the pressure difference and the inlet mass flow rate, it is very difficult to fix the inlet mass flow rate for different conditions. For example, reduction of inlet gas mass fraction from 0.5 to 0.3 at a fixed ΔT results in higher condensation rate. The change of condensation rate changes the effect of pressure difference and the amount of net inlet mass flow rate. Thus, to reach the same net mass flow rate, the pressure difference must be changed. Obtaining a particular net inlet mass flow could only be done by a trial-and-error process. Each trial takes at least a week of computational effort. Also, the solutions were very sensitive to changes of ΔP, so many trials would be needed for each case. It was impractical to do this for any other cases besides the validation comparison.

For the following presented results, the net inlet mass flow rates may not be constant across a series of cases, but they all correspond to laminar inlet flow. The detailed information of boundary conditions for the G1 cases are given in Table 8.7. As described in Section 2.4,

Table 8.7: Total pressure difference [Pa], inlet temperature [K], and inlet Reynolds number for G1 cases

		W_{in}					
		0.01	0.1	0.2	0.3	0.5	0.7
$\Delta T = 3$ K	ΔP	6.3					
	T_{in}	372.69					
	Re_{in}	1683.1					
$\Delta T = 5$ K	ΔP	2	10	12	13	16	
	T_{in}	372.69	371.01	368.87	366.38	359.86	
	Re_{in}	2125.5	1572.9	1247.3	1244.1	1286.1	
$\Delta T = 10$ K	ΔP			10		14	
	T_{in}			368.87		359.86	
	Re_{in}			1638		1078.4	
$\Delta T = 20$ K	ΔP		5.5	8	11	15	17
	T_{in}		371.01	368.87	366.38	359.86	349.54
	Re_{in}		1879.7	1857.2	1560.2	1436.2	1206.2
$\Delta T = 30$ K	ΔP				10	14	
	T_{in}				366.38	359.86	
	Re_{in}				1652.9	1384.3	
$\Delta T = 40$ K	ΔP			5	9	14	17
	T_{in}			368.87	366.38	359.86	349.54
	Re_{in}			2206.4	1751.9	1614.1	1389.1
$\Delta T = 60$ K	ΔP				10		
	T_{in}				366.38		
	Re_{in}				1532.7		

ΔP, ΔT, and T_{in} are the independent parameters that were prescribed, whereas the Re_{in} was obtained from the net inlet mass flow rate that was part of the solution. As shown, the highest inlet Reynolds numbers belong to the cases with the highest condensation rates. Those cases are either cases with the lowest W_{in} or highest ΔT.

8.6.2 Effect of Changing W_{in}

For the investigation of the effect of changing W_{in}, five cases with $\Delta T = 5$ K are selected. Details of these cases are given in Table 8.7. Figure 8.11 shows the film thickness for the cases with inlet gas mass fraction values of 0.01 to 0.5. The highest W_{in} value leads to the lowest amount of condensation and the thinnest film. This behaviour is the same as in co-current condensation. As more vapour flows into the tube, the condensation rate is higher because there is less gas build-up at the interface.

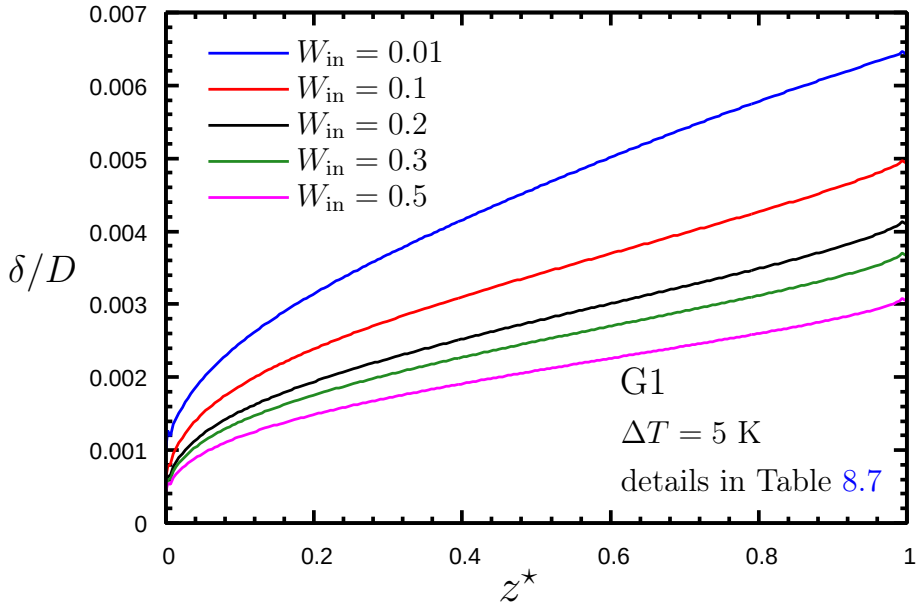

Figure 8.11: Axial variation of film thickness for G1: effect of changing W_{in} for $\Delta T = 5$ K

The axial variation of the local Nusselt number is shown in Fig. 8.12. The local Nusselt

number is defined in Eq. (7.3). Because of the small film thickness, conduction plays the

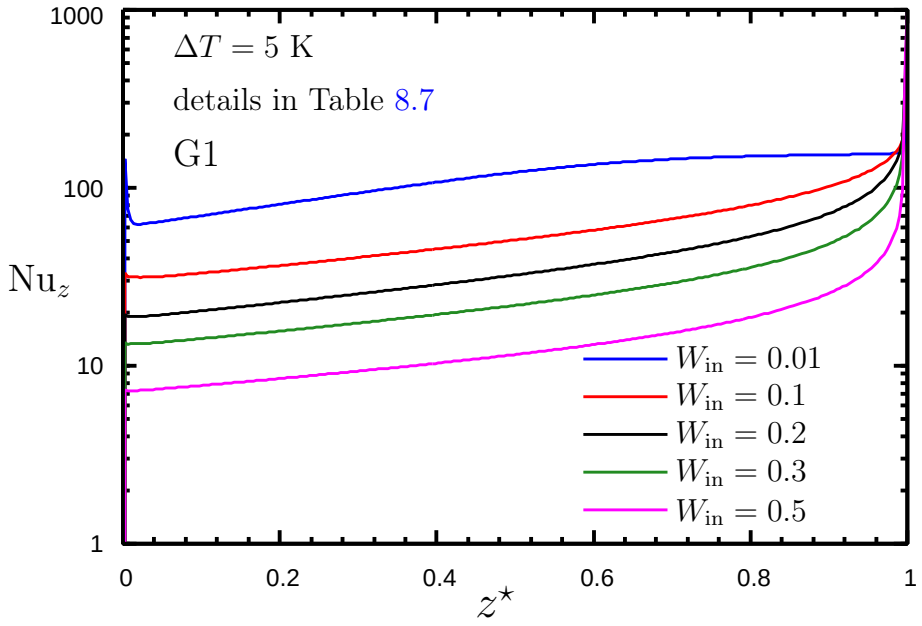

Figure 8.12: Axial variation of local Nusselt number for G1: effect of changing W_{in} for $\Delta T = 5$ K

main role in heat transfer in the liquid region. Thus, the wall heat flux is the function of film thickness and interface-to-wall temperature difference. Despite the thick film at the inlet of the cooled section ($z^\star = 1$), the maximum Nusselt number occurs there due to the high interface-to-wall temperature difference at that location. This shows that interface-to-wall temperature difference is the dominant parameter that determines the amount of wall heat transfer. Along the tube toward the outlet, the Nusselt number decreases because of the gas build-up at the interface and the decrease of interface temperature. As can be seen, the case with the lowest W_{in} has the highest heat transfer rate. Although the film is thicker for this case, the interface-to-wall temperature difference is high enough to keep the heat transfer higher compared to the cases with higher W_{in}. This trend is confirmed by examining the interface temperature and gas mass fraction.

Figures 8.13 and 8.14 are plots of the axial variation of the interface temperature and gas mass fraction, respectively. The interface gas mass fraction increases rapidly at the inlet

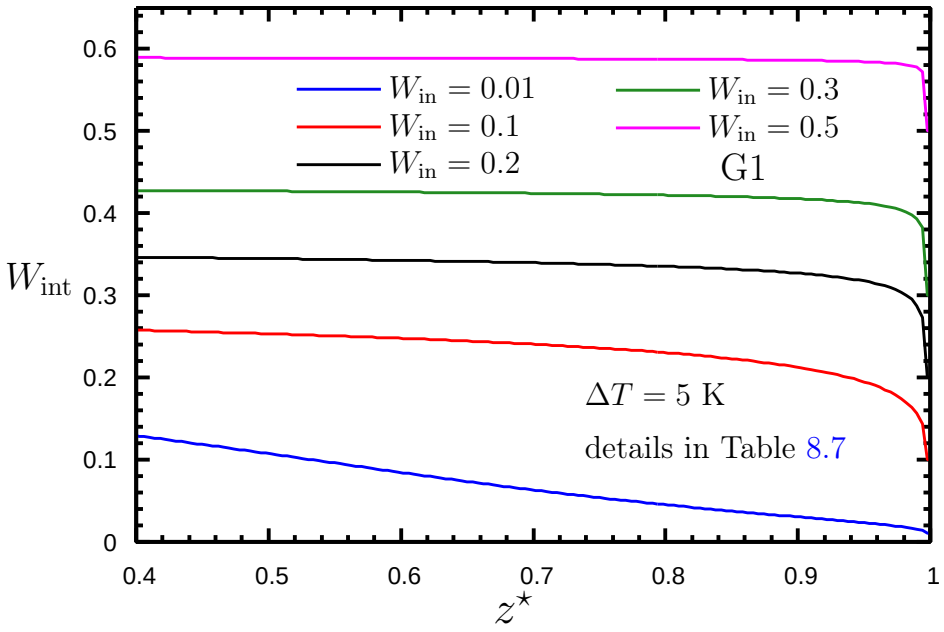

Figure 8.13: Axial variation of interface gas mass fraction for G1: effect of changing W_{in} for $\Delta T = 5$ K

of the cooled section. This happens because of the downward flow of mixture close to the interface. This downward flow has high W and therefore brings gas from the top of the tube to the bottom. Therefore, in addition to gas build up at the interface because of the condensation, the downward flow acts against the condensation by increasing W_{int} more. For most of the domain, W_{int} remains relatively constant. The expected matching trend is seen for the interface temperature. There is a sudden drop of interface temperature at the inlet of the cooled section and a decrease at a lower rate along the domain.

As expected, the lowest interface gas mass fraction occurs for the case with the lowest W_{in}. As the gas mass fraction decreases, the interface temperature increases which leads to higher interface-to-wall temperature difference, higher heat transfer rate, and more condensation.

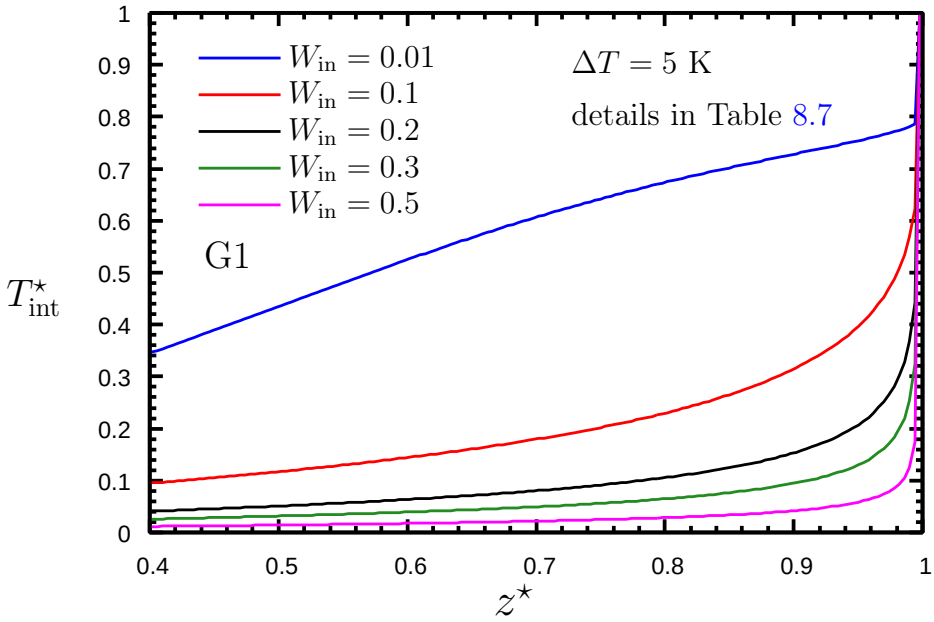

Figure 8.14: Axial variation of interface temperature for G1: effect of changing W_{in} for $\Delta T = 5$ K

Figure 8.15 shows the amount of liquid condensed relative to the amount of vapour entering the tube. This figure is consistent with the film thickness trends that were discussed before. As shown, about 85% of the vapour is condensed for the case of $W_{in} = 0.01$. As W_{in} increases, less vapour is condensed because of greater gas build-up at the interface. For the case with $W_{in} = 0.5$, only 20% of the vapour is condensed. Of the cases being compared here, the case with $W_{in} = 0.5$ has the lowest interface-to-wall temperature difference, as seen in Fig. 8.14.

The centre-line temperature axial variation is shown in Fig. 8.16. From the inlet of the cooled section ($z^{\star} = 1$) to the top of the cooled section ($z^{\star} = 0$), the centre-line temperature decreases because condensation removes mass and energy from the gas core flow. As W_{in} decreases, the centre-line temperature decreases with a lower rate along the cooled section. This means that, for the cases with lower W_{in}, condensation affects mostly the interface region. Because there is less vapour for the cases with higher W_{in}, the influence of the

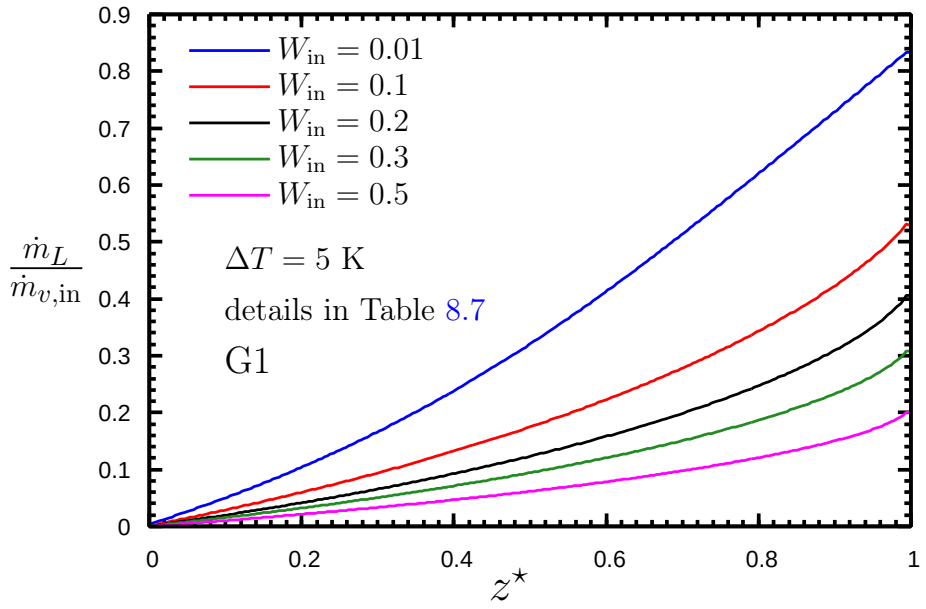

Figure 8.15: Axial variation of normalised liquid mass flow rate for G1: effect of changing W_{in} for $\Delta T = 5$ K

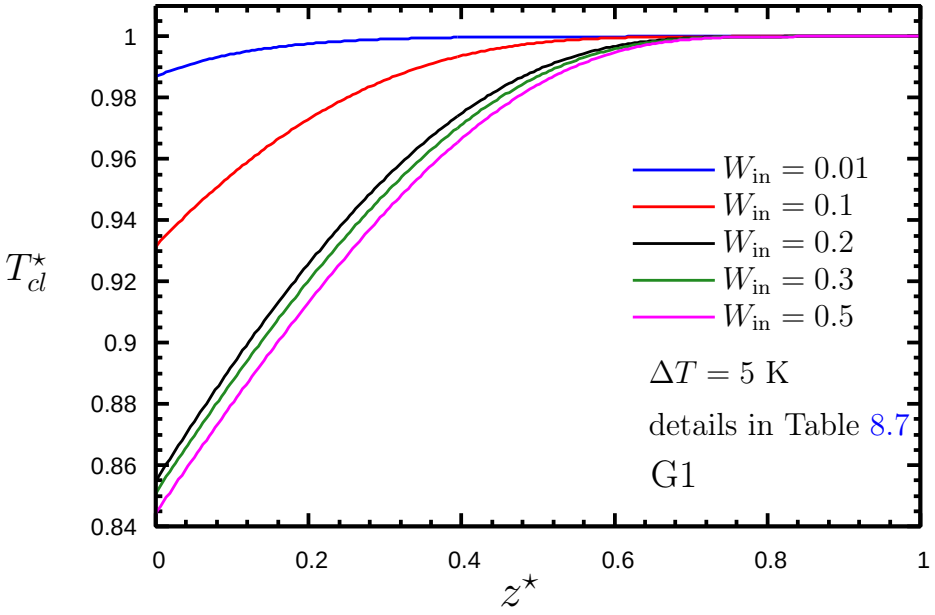

Figure 8.16: Axial variation of centre-line temperature for G1: effect of changing W_{in} for $\Delta T = 5$ K

condensation spreads to the centre-line as well. Therefore, the centre-line temperature drop is greater for cases with higher W_{in}. Even so, the drop in centre-line temperature is not significant, with the lowest value being approximately 0.84 in these cases.

8.6.3 Effect of Changing ΔT

For the investigation of the effect of ΔT, five cases with $W_{\text{in}} = 0.3$ and ΔT in the range of 5 K to 60 K were selected. Details of these cases are given in Table 8.7.

Figure 8.17 shows the film thickness for the above-mentioned cases. The highest ΔT leads to the highest amount of condensation and the thickest film. This behaviour is the same as in co-current condensation. It is observed that the film thickness does not increase proportionally with ΔT.

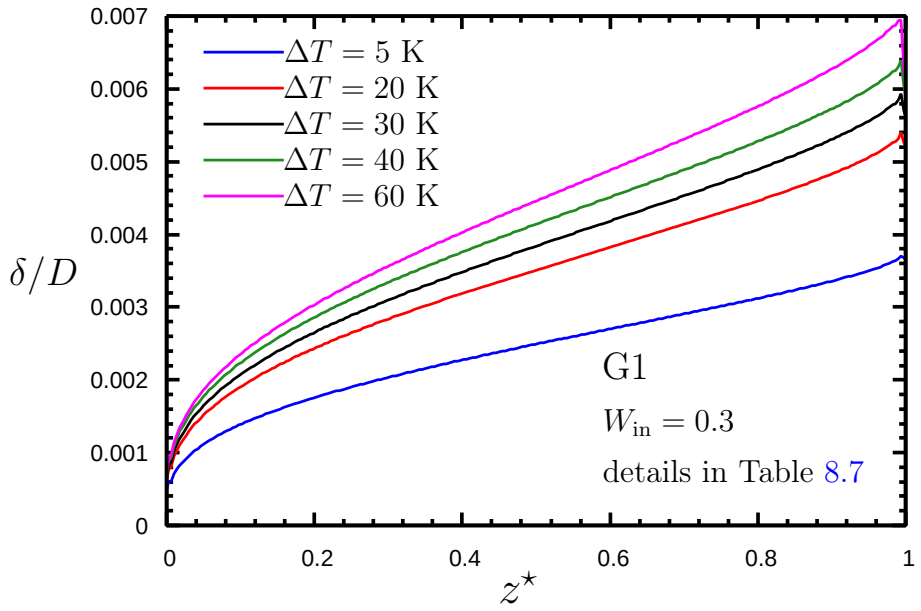

Figure 8.17: Axial variation of film thickness for G1: effect of changing ΔT for $W_{\text{in}} = 0.3$

The same behaviour as the film thickness is expected in the Nusselt number axial variation. Figure 8.18 shows the Nusselt number axial variation along the cooled section. Al-

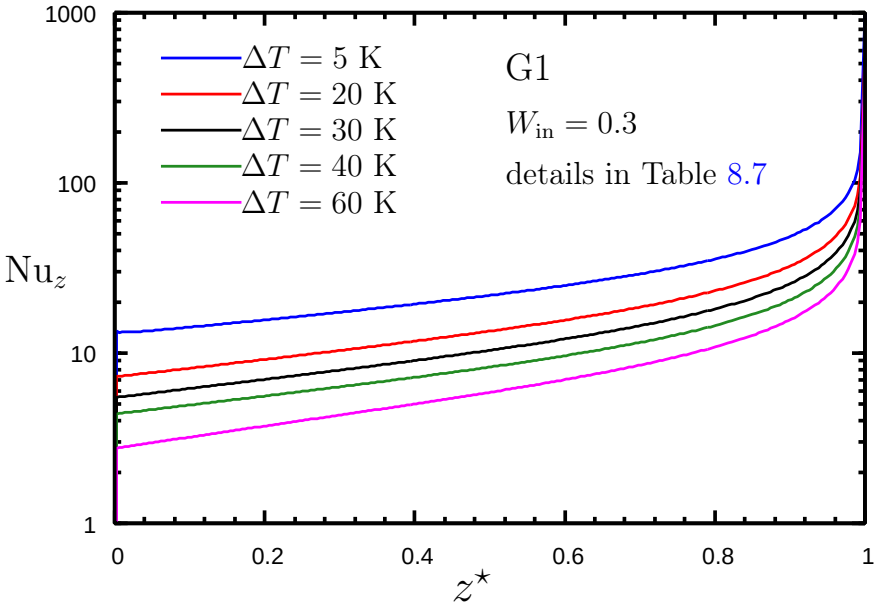

Figure 8.18: Axial variation of local Nusselt number for G1: effect of changing ΔT for $W_{\text{in}} = 0.3$

though there is higher heat transfer rate for the cases with higher ΔT, the Nusselt number decreases as the inlet-to-wall temperature difference increases. This trend occurs because of the definition of the Nusselt number in Eq. (7.3). As ΔT increases, the heat transfer increases with the lower rate relative to the rate of increase of ΔT.

Figures 8.19 and 8.20 show the axial variation of the interface gas mass fraction and temperature, respectively. For all cases, a sudden increase of W_{int} occurs at the beginning of the cooled section. The interface gas mass fraction is higher for cases with higher ΔT. This was expected because the condensation rate is much higher for those cases. For the highest ΔT, the interface gas mass fraction is approximately 0.97. This means that there is a large gas build-up for this case that reduces the interface temperature drastically as seen in Fig. 8.20). The axial variation of the interface temperature for all cases is as expected considering the trends in W_{int}. The lowest interface temperature corresponds to the highest ΔT. For $\Delta T = 60$ K, the interface temperature approaches closely to the wall temperature

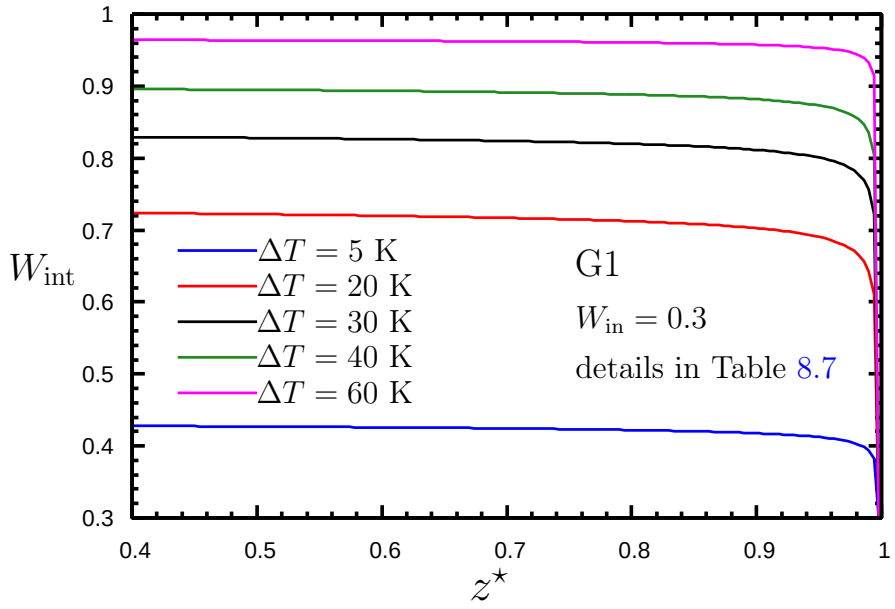

Figure 8.19: Axial variation of interface gas mass fraction for G1: effect of changing ΔT for $W_{\text{in}} = 0.3$

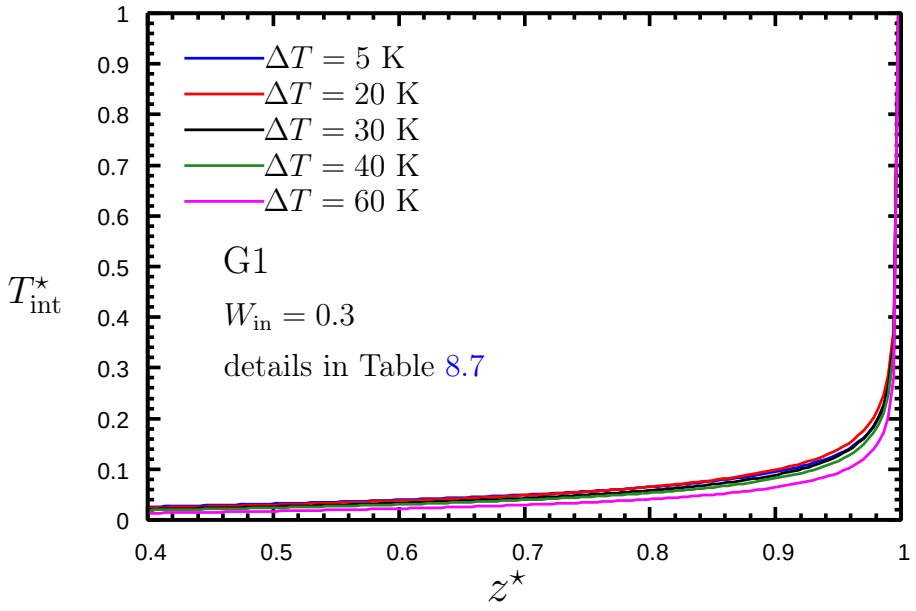

Figure 8.20: Axial variation of interface temperature for G1: effect of changing ΔT for $W_{\text{in}} = 0.3$

towards the top of the cooled section.

For these same cases, the relative amount of liquid condensed is shown in Fig. 8.21. For the case with $\Delta T = 60$ K almost 85% of the inlet vapour is condensed, whereas for $\Delta T = 5$ K only about 30% was condensed. The trends in this figure are consistent with what was observed in previous figures.

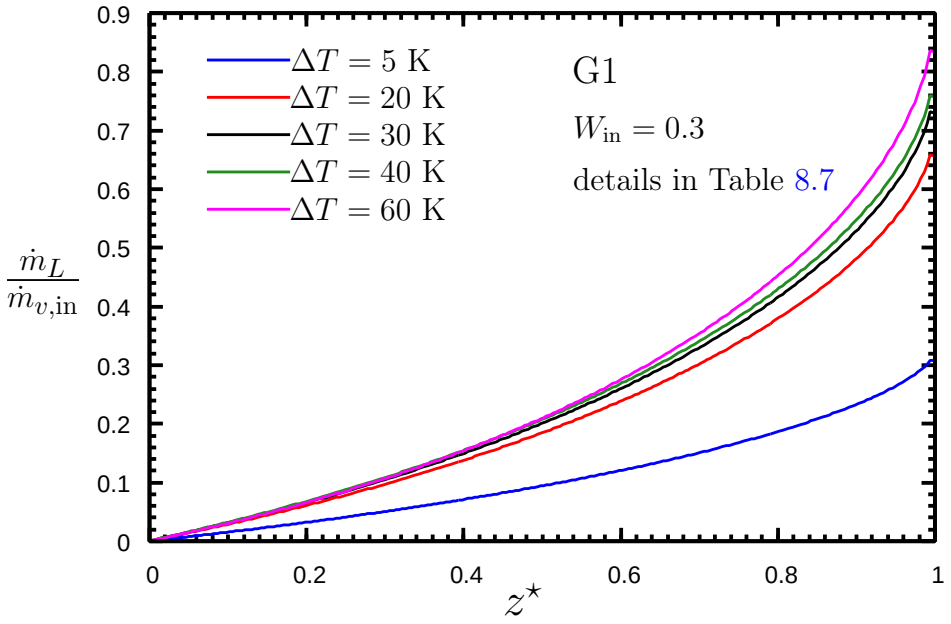

Figure 8.21: Axial variation of normalised liquid mass flow rate for G1: effect of changing ΔT for $W_{\text{in}} = 0.3$

To complete the examination of the detailed results of the parametric study for G1, mass flow rate and Reynolds number of the liquid film leaving the tube, are presented in Table 8.8 for all cases. Reynolds number of liquid was calculated as $(4\dot{m}_L)/(2\pi R\mu_L)$. As seen, the values are consistent with previous discussions. As the gas mass fraction decreases or the inlet-to-wall temperature increases, there is more condensation and the Reynolds number of the liquid film is higher. For some cases, for example cases of $\Delta T = 40$ K and $\Delta T = 60$ K with $W_{\text{in}} = 0.3$, the exact same trend can not be seen. Different net inlet mass flow rates

and consequently different amount of inlet vapour mass are responsible for this deviation from the expected trend (see Table 8.7).

Table 8.8: Liquid film mass flow rate [g/s] and Reynolds number at the bottom of the tube for G1 cases

		W_{in}					
		0.01	0.1	0.2	0.3	0.5	0.7
$\Delta T = 3$ K	$\dot{m}_L$	0.1459					
	Re_L	52.168					
$\Delta T = 5$ K	$\dot{m}_L$	0.2109	0.08998	0.05302	0.03687	0.01950	
	Re_L	75.404	32.983	18.15	12.267	6.025	
$\Delta T = 10$ K	$\dot{m}_L$			0.0969		0.032281	
	Re_L			33.174		9.972	
$\Delta T = 20$ K	$\dot{m}_L$		0.1789	0.1384	0.09866	0.05836	0.2882
	Re_L		62.744	47.39	32.827	18.028	7.869
$\Delta T = 30$ K	$\dot{m}_L$				0.1163	0.06749	
	Re_L				38.706	20.849	
$\Delta T = 40$ K	$\dot{m}_L$			0.1800	0.1283	0.08082	0.04224
	Re_L			61.621	42.677	24.967	11.533
$\Delta T = 60$ K	$\dot{m}_L$				0.1238		
	Re_L				41.208		

8.7 Parametric Study Results for G2

8.7.1 Overview of Cases

For G2, cases were defined in the range of $0.1 \leq W_{\text{in}} \leq 0.7$ for six inlet-to-wall temperature differences between 20 K and 70 K. As shown in Table 8.9, there are 16 cases that

have converged solutions, nine cases that are possible but not completed due to the lack of computational resources, and 14 cases that could not produce results within the problem constraints. There were also seven cases that were not attempted and left blank in the table.

Table 8.9: Cases for G2*

		W_{in}					
		0.01	0.1	0.2	0.3	0.5	0.7
ΔT [K]	5	X	X	X	X		
	10	X	X	X	X		
	20	X	X	C	C	C	C
	30	X	X	C	C	P	P
	40	X	X	C	C	C	C
	50		C	C	C	P	P
	60		C	C	C	P	C
	70		C	P	P	P	P

* C: Converged; P: Possible; X: Violates Constraints

For a given set of W_{in} and ΔT, values there is generally more condensation flow rate for G2 compared to G1 because of the greater cooled section surface area in G2. This greater condensation rate increased the net inlet mass flow and created relatively more cases for G2 that would have a turbulent inlet velocity and violate the problem constraints. For G2, there are cases (such as the case with $W_{\text{in}} = 0.2$ and ΔT of 10 K) where the condensation is not high enough to avoid liquid hold-up. For these cases, increasing the ΔT led to more condensation, thicker film and heavier liquid which could avoid liquid hold-up. This is the reason that cases with small values of ΔT such as 3 K or 5 K were not possible to converge for G2. Detailed information about all the cases in the test matrix is given in Table 8.10. Note that Re_{in} values are calculated based on the net inlet mass flow rate that was part of the solution. As explained before, inlet U-velocity profile, inlet mass flow rate and Reynolds

number are dependent parameters and unknown.

Table 8.10: Total pressure difference [Pa], inlet temperature [K], and inlet Reynolds number for G2 cases

		W_{in}				
		0.1	0.2	0.3	0.5	0.7
$\Delta T = 20$ K	ΔP		16	18	22	28
	T_{in}		368.87	366.38	359.86	349.54
	Re_{in}		1479.7	1344.5	1052.7	1410
$\Delta T = 30$ K	ΔP		16	18		
	T_{in}		368.87	366.38		
	Re_{in}		1619.1	1574.1		
$\Delta T = 40$ K	ΔP		15	19	23	27
	T_{in}		368.87	366.38	359.86	349.54
	Re_{in}		1647.9	1121.5	1326.4	1337.9
$\Delta T = 50$ K	ΔP	13	15	18		
	T_{in}	371.01	368.87	366.38		
	Re_{in}	1933.4	1751.3	1640.9		
$\Delta T = 60$ K	ΔP	15	22	18		27
	T_{in}	371.01	368.87	366.38		349.54
	Re_{in}	1713.5	1332.3	1812.6		1224.6
$\Delta T = 70$ K	ΔP	15				
	T_{in}	371.01				
	Re_{in}	1730.4				

8.7.2 Effects of Changing W_{in} and ΔT Separately

For the investigation of the effect of changing W_{in}, four cases with $\Delta T = 20$ K were selected. Details of these cases are given in Table 8.10. On the other hand, for the investigation of the effect of changing ΔT, five cases with $W_{\text{in}} = 0.2$ were selected. Details of these cases are also given in Table 8.10.

For the above mentioned cases, the trends of δ, Nu, W_{int}, T_{int}, and $\frac{\dot{m}_L}{\dot{m}_{v,\text{in}}}$ are the same as for G1. Therefore, all the plots for the mentioned parameters are presented in Appendix D for reference. The only different behaviour seen for G2 compared to G1 is the centre-line temperature during the investigation of the effect of changing W_{in}. Figure 8.22 is a plot of the axial variation of the centre-line temperature for various values of W_{in}. In the case of G2, the influence of the condensation on temperature extends to the centre-line even for the case with the lowest W_{in}. This will be discussed more detail in Section 8.8.2.

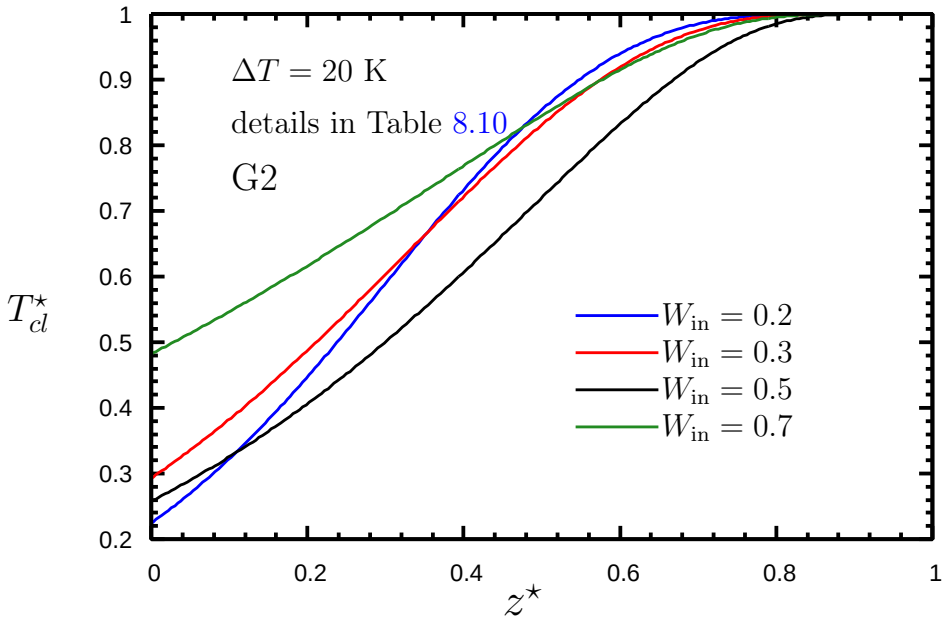

Figure 8.22: Axial variation of centre-line temperature for G2: effect of changing W_{in} for $\Delta T = 20$ K

To complete the examination of the detailed results of the parametric study for G2, mass flow rate and Reynolds number of the liquid film leaving the tube, are presented in Table 8.11 for all cases. The Reynolds number of liquid was calculated as $(4\dot{m}_L)/(2\pi R\mu_L)$. As seen, the values are consistent with previous discussions. As the gas mass fraction decreases or the inlet-to-wall temperature increases, there is more condensation and the Reynolds number of

the liquid film is higher.

Table 8.11: Liquid film mass flow rate [g/s] and Reynolds number at the bottom of the tube for G2 cases

		W_{in}				
		0.1	0.2	0.3	0.5	0.7
$\Delta T = 20$ K	$\dot{m}_L$		0.1362	0.09362	0.05746	0.04139
	Re_L		46.643	35.211	17.750	11.301
$\Delta T = 30$ K	$\dot{m}_L$		0.1581	0.1340		
	Re_L		54.115	44.602		
$\Delta T = 40$ K	$\dot{m}_L$		0.1666	0.1020	0.08721	0.05320
	Re_L		57.054	33.948	26.941	14.526
$\Delta T = 50$ K	$\dot{m}_L$	0.2159	0.1794	0.1497		
	Re_L	75.742	61.409	49.828		
$\Delta T = 60$ K	$\dot{m}_L$	0.1923	0.09362	0.1658		0.05371
	Re_L	67.447	32.053	55.176		14.663
$\Delta T = 70$ K	$\dot{m}_L$	0.1951				
	Re_L	68.429				

8.8 Comparison of G1 and G2 Results

8.8.1 Overview of Cases

In this section, comparisons are made between the G1 and G2 results. For this purpose, cases with the same W_{in} and ΔT were selected. It should be recalled that the Re_{in} may be different for these cases. It is expected, however, that a modest variation in Reynolds number is acceptable in terms of assessing the trends in the result. The details of discussed cases in this section are given in Tables 8.7 and 8.10.

8.8.2 Effect of Changing W_{in}

The cases discussed in this section have a $\Delta T = 40$ K and three different inlet gas mass fractions: 0.2, 0.5, and 0.7.

Figure 8.23 shows the axial variation of the local Nusselt number. In all instances, the G2 cases have a higher Nusselt number than their G1 counter parts in the most part of the domain. The cases with $W_{\text{in}} = 0.7$ have similar values of Re_{in} (1337.9 and 1389.1 for G1 and G2, respectively). In this situation, the Nusselt number is higher for G2 close to the

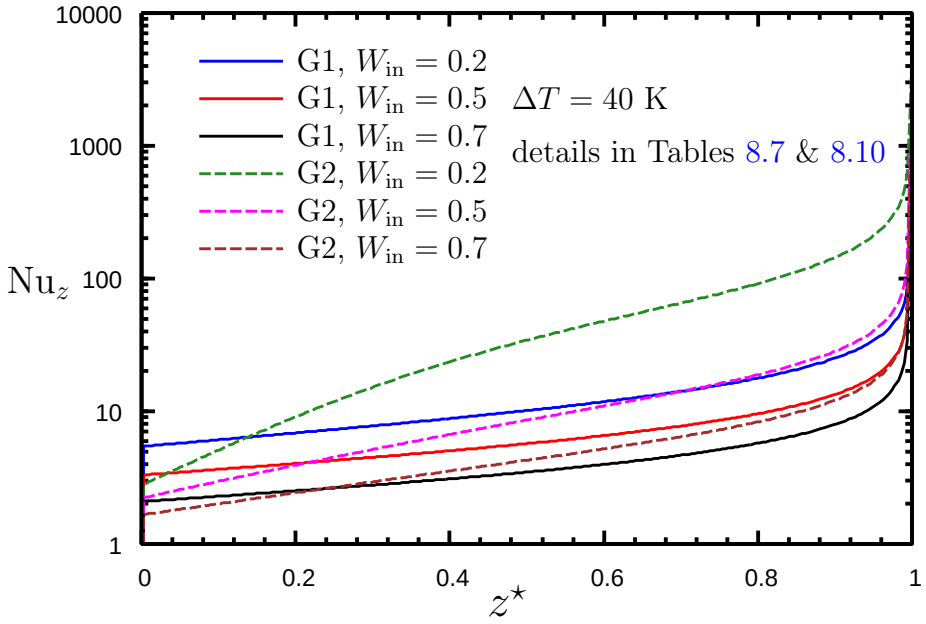

Figure 8.23: Axial variation of local Nusselt number for G1 and G2: effect of changing W_{in} for $\Delta T = 40$ K

inlet of the cooled section ($z^\star = 1$), while it is lower close to the outlet. The film thickness is almost the same for G1 and G2 in the outlet region, however, there are differences along the domain which caused the differences in Nusselt number. Figure 8.24 demonstrates the axial variation of film thickness for the same cases as shown in Fig. 8.23. A closer look at the case with $W_{\text{in}} = 0.2$ reveals the reason of higher Nusselt number for G2. The film thickness

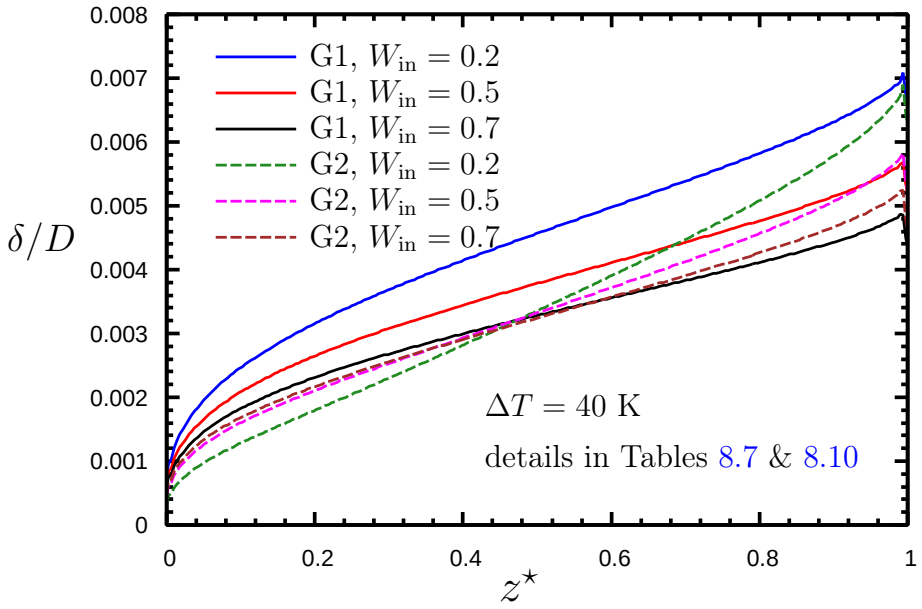

Figure 8.24: Axial variation of film thickness for G1 and G2: effect of changing W_{in} for $\Delta T = 40$ K

is smaller for G2 compared to G1 and this caused higher Nusselt number. The interface temperature will also be examined later to support this theory. The lower value of Nusselt number for the G2 cases compared to G1 at the top of the cooled section originates from a lower interface temperature due to a higher value of interface gas mass fraction at that location.

The axial variation of W_{int} and T_{int} for the cases with equal W_{in} are quite similar for G1 and G2, especially for the cases with higher W_{in}, as seen in Figs. 8.25 and 8.26. There is not much difference in T_{int} between G1 and G2 cases except the case with $W_{in} = 0.2$. For this specific case, the interface gas mass fraction is noticeably higher and the interface temperature is lower for G2 because of more condensation. The relatively small difference in T_{int} between G1 and G2 cases indicates that the film thickness causes the Nusselt number difference among these cases. The difference is more distinct for the case with the lower inlet gas mass fraction ($W_{in} = 0.2$).

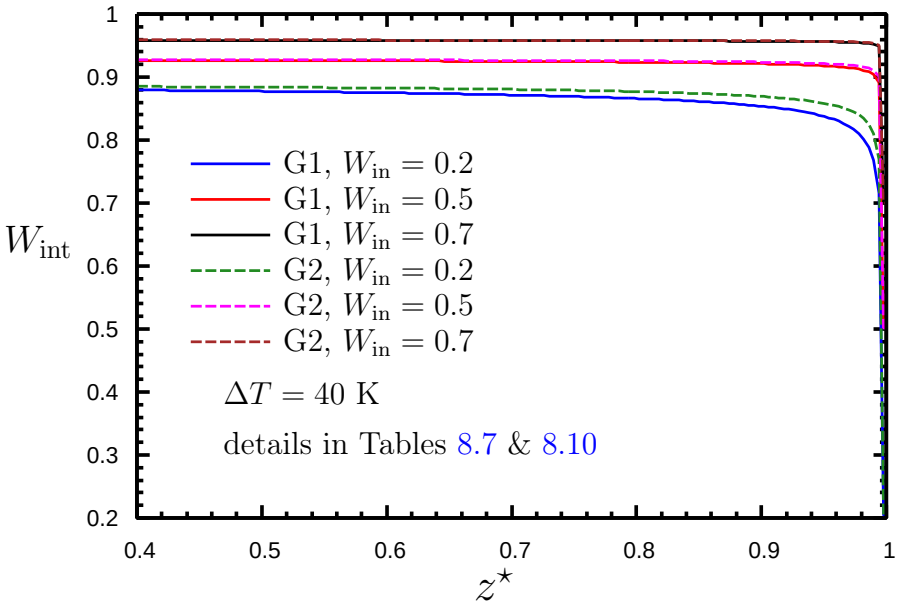

Figure 8.25: Axial variation of interface gas mass fraction for G1 and G2: effect of changing W_{in} for $\Delta T = 40$ K

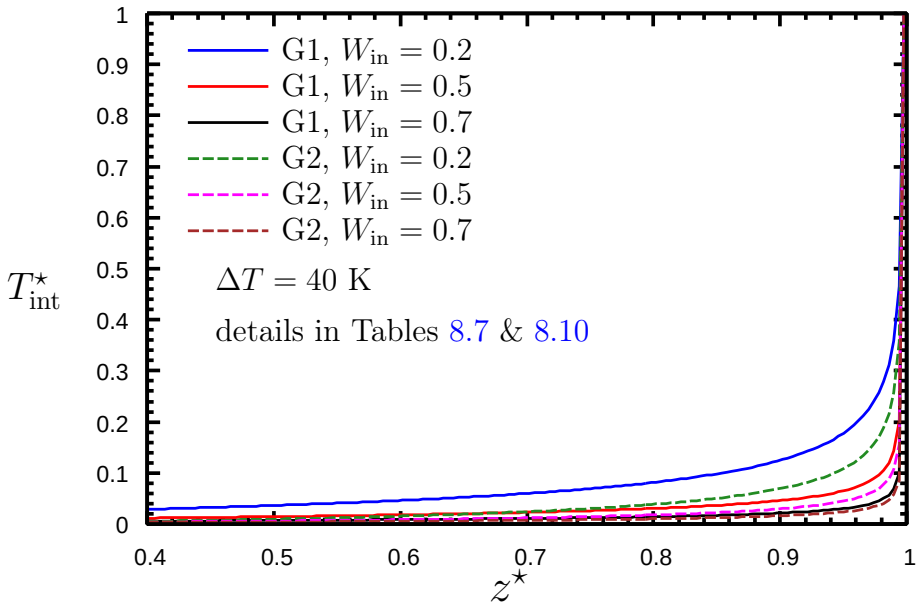

Figure 8.26: Axial variation of interface temperature for G1 and G2: effect of changing W_{in} for $\Delta T = 40$ K

Figure 8.27 shows that over 97% of the inlet vapour is condensed for the case with the lowest W_{in} for G2, whereas only 80% of the inlet vapour is condensed for the same conditions for G1. The trends in this figure are consistent with those that were discussed earlier. The availability of a larger cooled surface leads to higher condensation for the G2 cases.

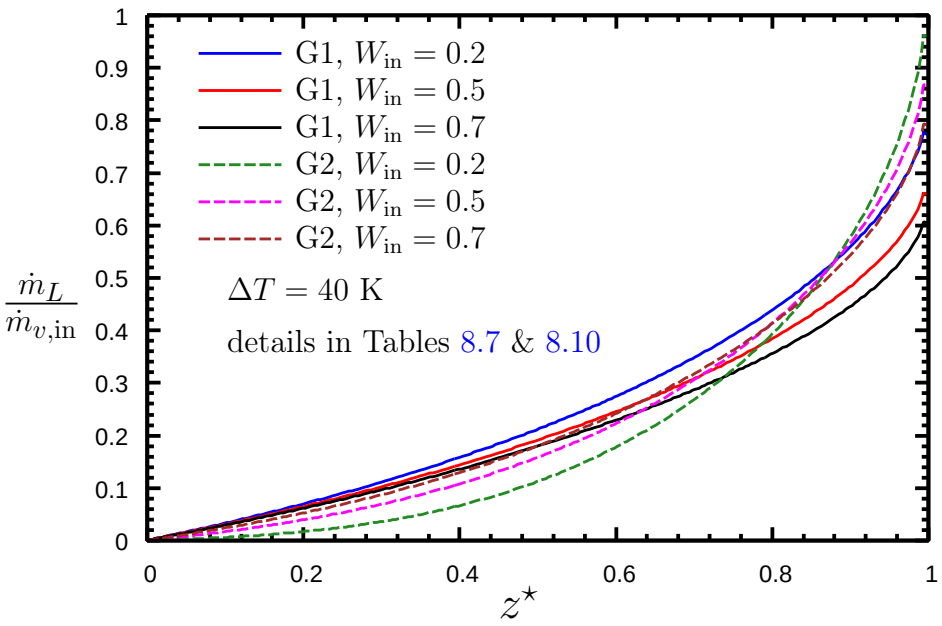

Figure 8.27: Axial variation of normalised liquid mass flow rate for G1 and G2: effect of changing W_{in} for $\Delta T = 40$ K

The axial variation of the centre-line temperature is shown in Fig. 8.28. As mentioned before with respect to Fig. 8.22, the behaviour of this parameter is completely different between G1 and G2. For G1, due to the shorter length of the cooled section, the centre-line conditions are not affected too much by the condensation. For G2, however, there is a large drop of centre-line temperature along the cooled section. In addition, for G2 with lower W_{in} and higher condensation rate, the centre-line temperature drop is larger than the cases with higher W_{in} and lower condensation rate. This trend is reversed for G1 as explained before (Section 8.6.2).

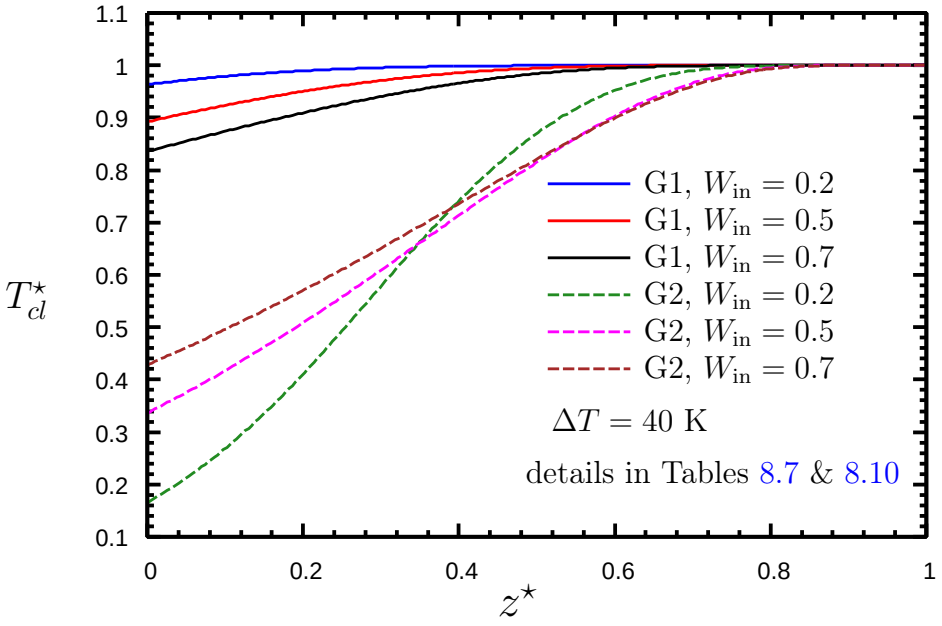

Figure 8.28: Axial variation of centre-line temperature for G1 and G2: effect of changing W_{in} for $\Delta T = 40$ K

8.8.3 Effect of Changing ΔT

The selected cases which are discussed in this section have two different inlet-to-wall temperature differences (20 K and 40 K) with W_{in} equal to 0.2.

Figure 8.29 presents the axial variation of the Nusselt number for G1 and G2 for the conditions mentioned above. The Nusselt number is higher for G2 due to the longer cooled section and smaller film thickness. In both G1 and G2, the heat transfer rate is higher for the case with higher ΔT, but the Nusselt number is lower because the heat transfer increases more slowly than does ΔT (see Eq. (7.3)).

As shown in Fig. 8.30, the interface gas mass fraction is slightly higher for G2 due to the greater condensation rate. There is a rapid increase in W_{int} close to the inlet of the cooled section and W_{int} remains almost constant along the cooled section for both G1 and G2 for both values of ΔT.

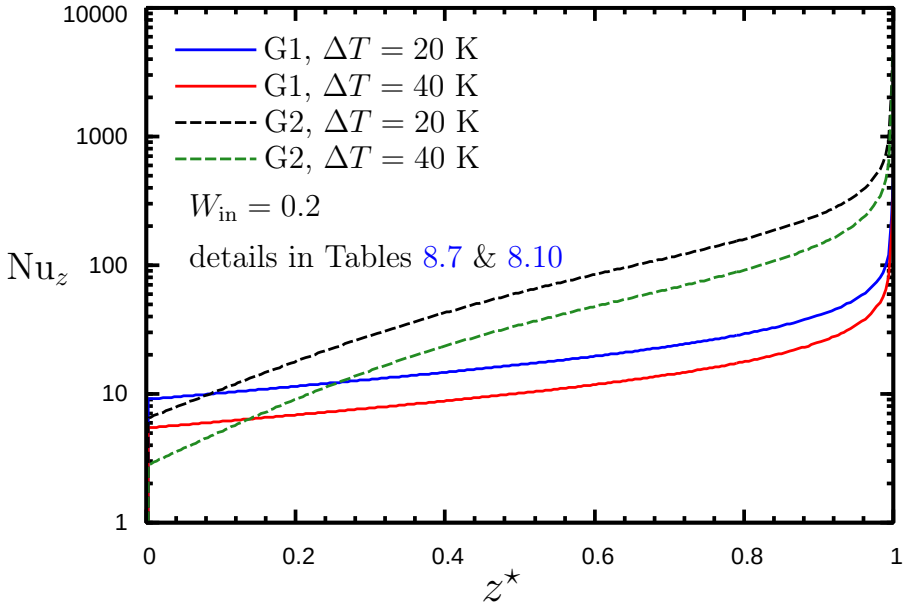

Figure 8.29: Axial variation of Nusselt number for G1 and G2: effect of changing ΔT for $W_{\mathrm{in}} = 0.2$

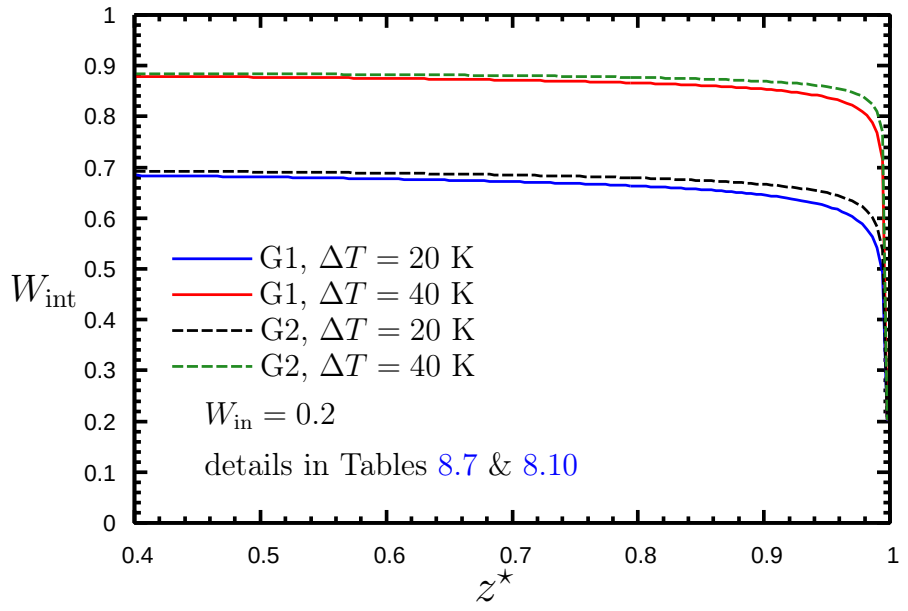

Figure 8.30: Axial variation of interface gas mass fraction for G1 and G2: effect of changing ΔT for $W_{\mathrm{in}} = 0.2$

Figure 8.31 is plot of the axial variation of the interface temperature. There is a complete consistency between the values of $T^{\star}_{\text{int}}$ and W_{int}. As explained before, these parameters are connected via Eq. (2.18).

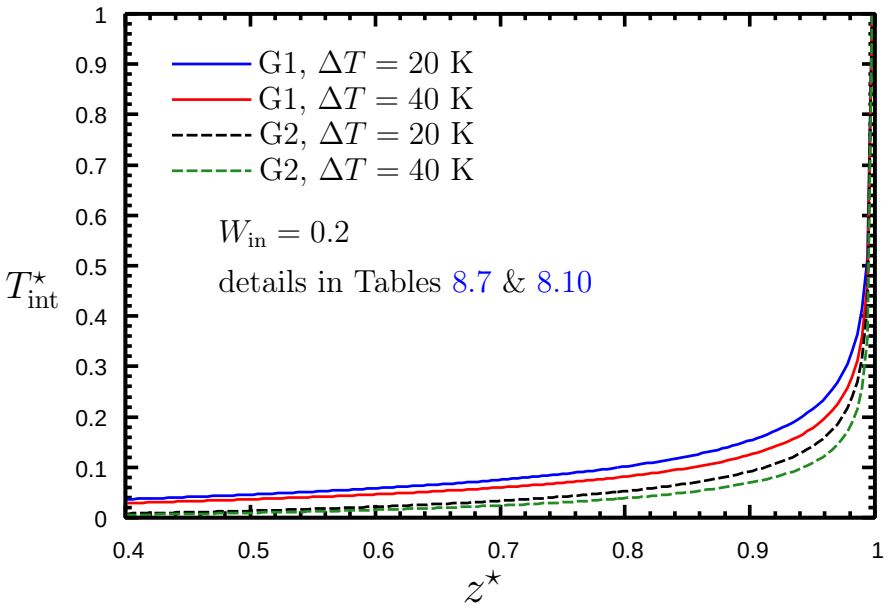

Figure 8.31: Axial variation of interface temperature for G1 and G2: effect of changing ΔT for $W_{\text{in}} = 0.2$

The normalised liquid mass flow rate is plotted in Fig. 8.32. The longer cooled section in G2 results in more condensation. Thus, at the end of the cooled section there is more liquid flowing out for the G2 cases. It is seen that most of the condensation happens close to the inlet of the cooled section in the G2 cases, whereas the rate changes less along the cooled section for the G1 cases.

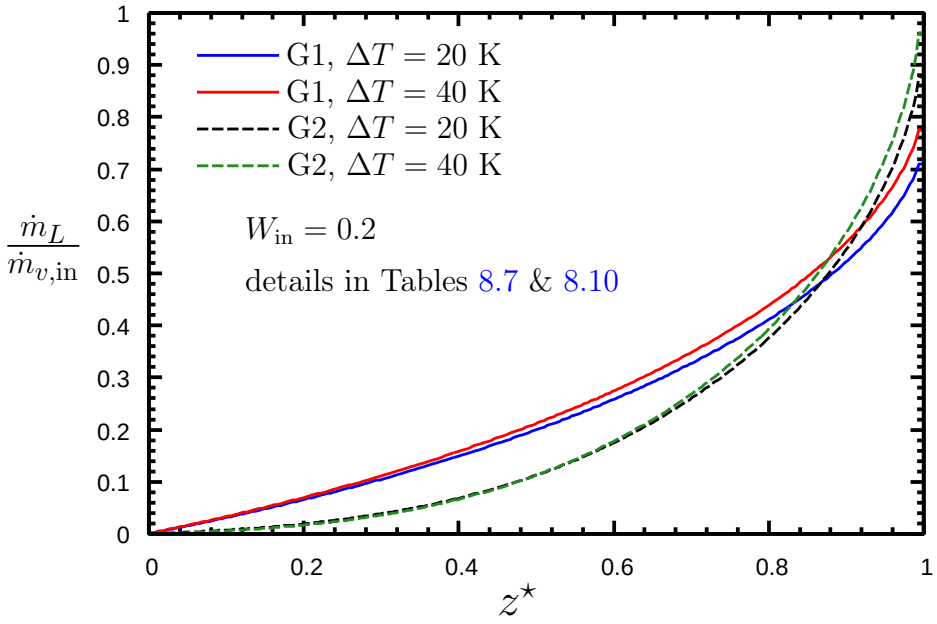

Figure 8.32: Axial variation of Normalised liquid mass flow rate for G1 and G2: effect of changing ΔT for $W_{\text{in}} = 0.2$

8.9 Parametric Study Results for G3

8.9.1 Overview of Cases

In order to see the effect of large diameter and cooling section length, G3 (the geometry that used for the validation) was selected. The wall temperature was a function of the axial location for the validation case. For the new cases defined here, however, the wall temperature is uniform. Four inlet gas mass fractions (0.1, 0.222 (same as the validation case), 0.4, and 0.7) and four inlet-to-wall temperature differences (65, 75, 85 and 95 K) were chosen to form the test matrix shown in Table 8.12. Because of the much longer cooled section (1.78 m), the cases with small W_{in} lead to turbulent inlet flow because of the high condensation rate. There are seven converged cases, four possible cases, two cases that violate the constraints, and three cases not attempted. Table 8.13 presents all the detailed information of converged cases for G3.

Table 8.12: Cases for G3*

		W_{in}			
		0.1	0.222	0.4	0.7
ΔT [K]	65		C	C	P
	75	X	C	C	C
	85	X	P	C	P
	95		C	P	

* C: Converged; P: Possible; X: Impossible

Table 8.13: Total pressure difference [Pa], inlet temperature [K], and inlet Reynolds number for G3 cases

		W_{in}			
		0.222	0.3	0.4	0.7
$\Delta T = 65$ K	ΔP			20	
	T_{in}			363.43	
	Re_{in}			2325.9	
$\Delta T = 75$ K	ΔP	15.63	17	20	27
	T_{in}	368.35	366.38	363.43	349.54
	Re_{in}	2675.4	2522.6	2424	1949.4
$\Delta T = 85$ K	ΔP		18.5	20	
	T_{in}		366.38	363.43	
	Re_{in}		2352.3	2422.3	
$\Delta T = 95$ K	ΔP	16			
	T_{in}	368.35			
	Re_{in}	2705.4			
$\Delta T = T_{\text{in}} - T_{\text{wall}}(z)$, Eq.(8.1)	ΔP	15.6			
	T_{in}	368.35			
	Re_{in}	2690.9			

8.9.2 Effects of Changing W_{in} and ΔT Separately

For the investigation of the effect of changing W_{in}, four cases with $\Delta T = 75$ K were selected. Details of these cases are given in Table 8.13. For the investigation of the effect of changing ΔT, three cases with $W_{\text{in}} = 0.222$ were selected. One of these cases has the same wall temperature profile as the validation case (Eq.(8.1)). For the two other cases, ΔT was set to 75 K and 95 K. Details of these cases are also given in Table 8.13.

During the study of the effect of inlet gas mass fraction, it was seen that the variation of the parameters such as δ, Nu, W_{int}, T_{int}, and $\frac{\dot{m}_L}{\dot{m}_{v,\text{in}}}$ are very similar to those seen for G1 and G2. Therefore, all the plots for those parameters are presented in Appendix E for reference.

Figure 8.33 shows the axial variation of the Nusselt number for the cases with $W_{\text{in}} = 0.222$.

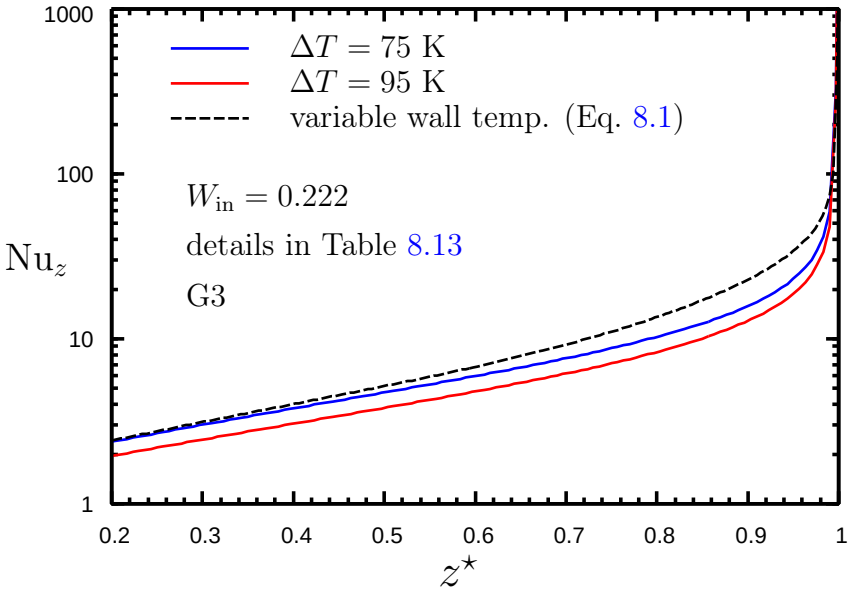

Figure 8.33: Axial variation of local Nusselt number for G3: effect of changing ΔT for $W_{\text{in}} = 0.222$

There is not much difference between the Nusselt values for these cases. The average value of ΔT for the case with variable wall temperature (black dashed-line) is about 66.86 K.

Because of the Nusselt number definition, the variable wall temperature (lowest ΔT, on average) case has the highest Nusselt number and the case with ΔT of 95 K has the lowest Nusselt number.

The axial variation of the interface gas mass fraction and temperature are shown in Figs. 8.34 and 8.35. Because most of the change occurs close to the inlet of the cooled

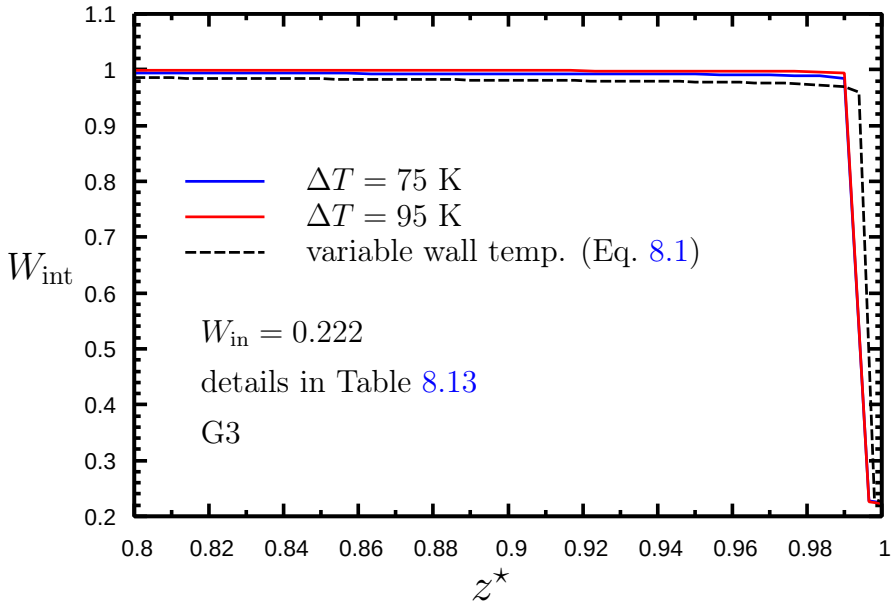

Figure 8.34: Axial variation of interface gas mass fraction for G3: effect of changing ΔT for $W_{\text{in}} = 0.222$

section, the values are plotted in that region ($0.8 \leq z^\star \leq 1.0$). As in previously discussed cases, there is a rapid increase of W_{int} and rapid decrease of T_{int} at the inlet of the cooled section. Over a distance of only about 1% of the cooled section length W_{int} reaches maximum possible value. Consequently, T_{int} rapidly approaches the wall temperature and then reduces at a much lower rate over the rest of the cooled section.

Figure 8.36 presents the normalised liquid mass flow rate along the cooled section. Based on the discussion in Section 8.8.3, it was anticipated that higher inlet-to-wall temperature difference would result in a higher condensation rate. Figure 8.36 shows that, for these cases

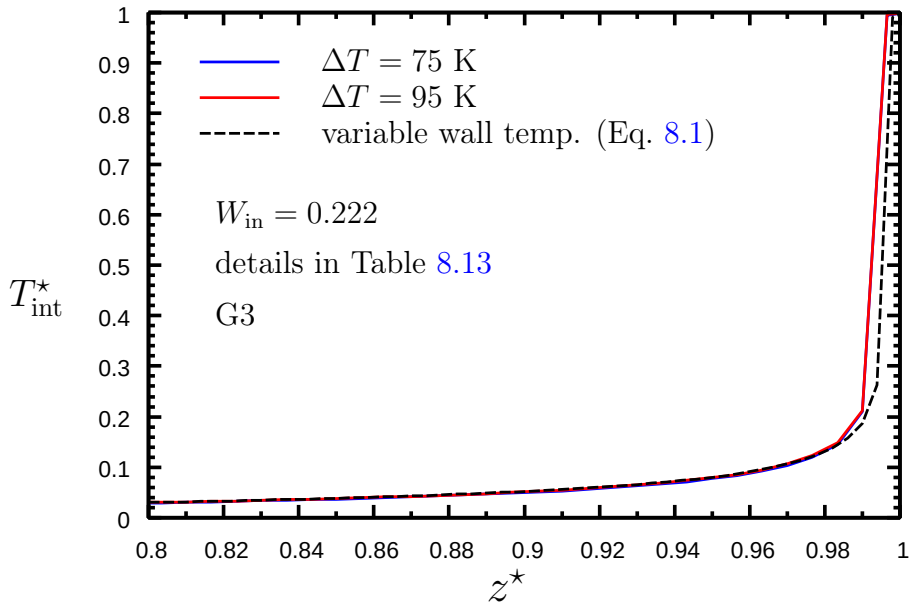

Figure 8.35: Axial variation of interface temperature for G3: effect of changing ΔT for $W_{\text{in}} = 0.222$

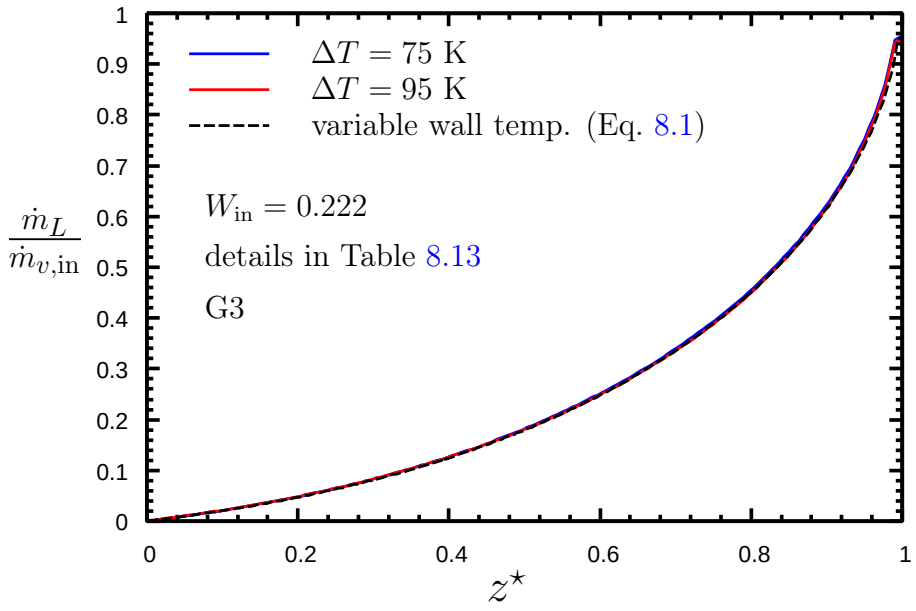

Figure 8.36: Axial variation of normalised liquid mass flow rate for G3: effect of changing ΔT for $W_{\text{in}} = 0.222$

with a much longer cooled section, when the ΔT is relatively high, the condensation rate does not change strongly as ΔT is changed. In these cases, almost all the vapour condenses (more than 97%), and it appears that the interface gas mass fraction and temperature profiles adjust themselves to distribute the same condensation rates along the long domain. This trend was seen somewhat in Fig. 8.32 as the difference between condensate mass flow rates for two different values of ΔT was smaller for the longer tube.

As shown in Table 8.13, the Reynolds numbers for the three cases in Fig. 8.32 are quite close to each other ($\mathrm{Re}_{\mathrm{in}} = 2675.4$ for $\Delta T = 75$ K, $\mathrm{Re}_{\mathrm{in}} = 2705.4$ for $\Delta T = 95$ K, and $\mathrm{Re}_{\mathrm{in}} = 2690.9$ for the case with variable wall temp.). Thus, the amount of mass flowing in the tube in form of vapour and gas is almost equal for all these cases. As mentioned earlier, nearly all the vapour condenses in the cooled section for all three cases and the condensation rates are almost the same. To examine this phenomenon in more detail, the film thickness and interface U velocity are plotted in Figs. 8.37 and 8.38, respectively. These figures show that as ΔT increases the film thickness increases while the interface velocity decreases. Because nearly all the inlet vapour is condensed in the tube, the film thickness adjusts itself based on the interface-to-wall temperature to distribute the same total condensation rate along the cooled section. Also, the case with the highest film thickness has less shear at the interface and therefore the lowest interface U velocity, as shown in Fig. 8.38. Based on this limited analysis, it appears that, for a very long tube, increasing ΔT beyond a specific value has a negligible effect on the condensation rate, even though differences exist in the film thickness and interface parameters.

To complete the detailed results of the parametric study for G3, mass flow rate and Reynolds number of the liquid film leaving the tube, are presented in Table 8.14 for all cases. The Reynolds number of liquid was calculated as $(4\dot{m}_{_L})/(2\pi R\mu_L)$. As seen, the values are consistent with previous discussions. For the cases with low W_{in}, almost all the vapour condenses and saturated air at the wall temperature leaves the tube from the outlet (top). This is the reason that the total mass of liquid for these cases are close (for example the

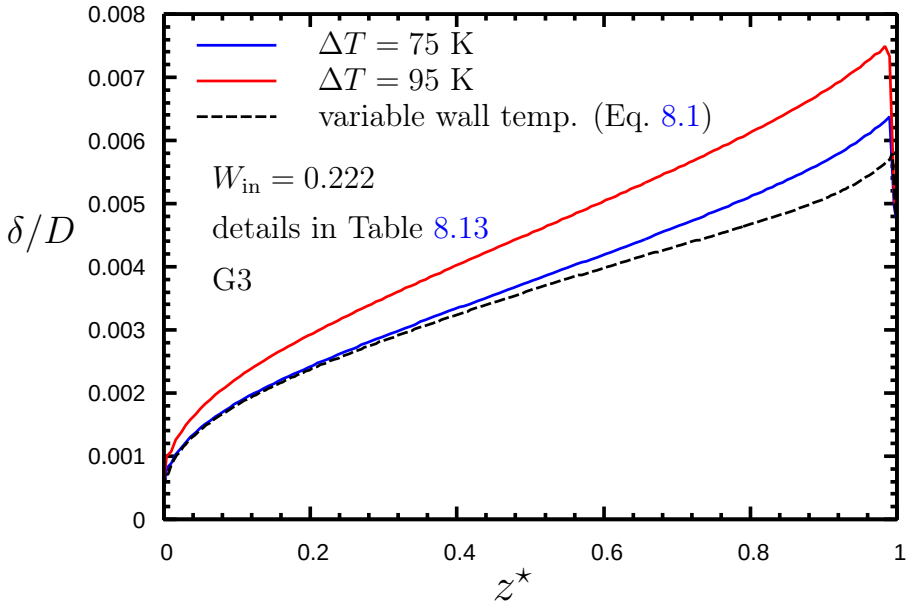

Figure 8.37: Axial variation of film thickness for G3: effect of changing ΔT for $W_{\text{in}} = 0.222$

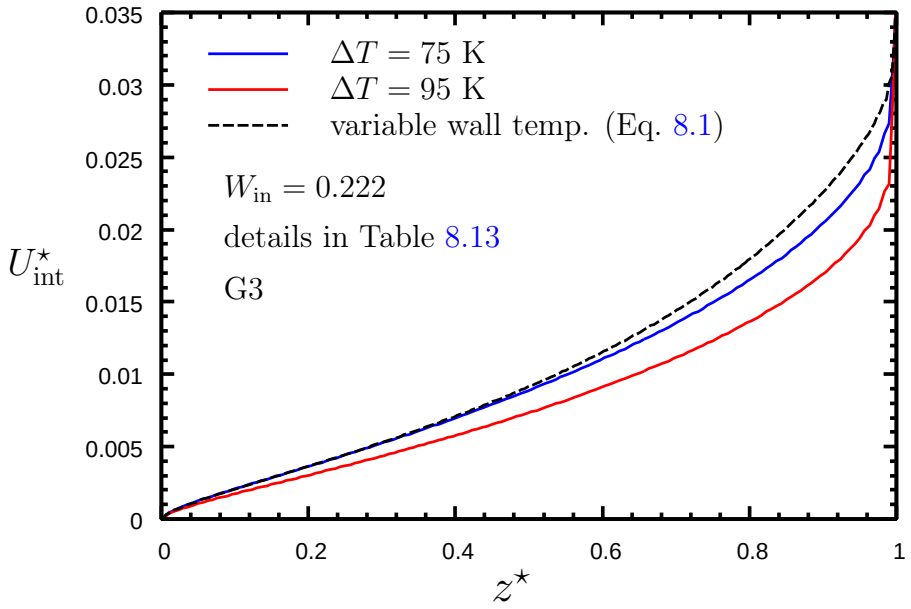

Figure 8.38: Axial variation of interface U Velocity for G3: effect of changing ΔT for $W_{\text{in}} = 0.222$

cases with $W_{\text{in}} = 0.222$ and different ΔT values). Note that for the case with $W_{\text{in}} = 0.3$ the overall condensation decreases as ΔT increases. This is due to the less inlet mass flow rate for the case with $\Delta T = 85$ compared to the case with $\Delta T = 75$. As shown in Table 8.10, inlet Reynolds number is 2352.3 for $\Delta T = 85$ K, whereas it is 2522.6 for $\Delta T = 75$ K.

Table 8.14: Liquid film mass flow rate [g/s] and Reynolds number at the bottom of the tube for G3 cases

		W_{in}			
		0.222	0.3	0.4	0.7
$\Delta T = 65$ K	$\dot{m}_L$			0.2741	
	Re_L			58.030	
$\Delta T = 75$ K	$\dot{m}_L$	0.3993	0.34167	0.2833	0.1209
	Re_L	89.419	74.808	59.963	21.721
$\Delta T = 85$ K	$\dot{m}_L$		0.3225	0.2828	
	Re_L		70.619	59.872	
$\Delta T = 95$ K	$\dot{m}_L$	0.4018			
	Re_L	89.978			
$\Delta T = T_{\text{in}} - T_{\text{wall}}(z)$, Eq.(8.1)	$\dot{m}_L$	0.4010			
	Re_L	89.810			

8.10 Computational Resources

The computational resources required to obtain the converged solutions of all cases in Tables 8.5, 8.9 and 8.12 were very significant. For the same grid as reported for these cases, each case needs at least 8640 core-hours. In other words, each case would run with 12 cores continuously for 30 days in order to obtain a converged solution.

Compute Canada High Performance Computing (HPC) clusters were used to run all the jobs. Because the Compute Canada Resource Allocation Committee did not allocate any priority computing resources to this research for 2016, almost all the cases were run using

the default allocation. The default allocation is a low priority, resource limited access to the clusters. Therefore, to avoid jobs sitting in the queues for a long time, each job had to be submitted asking for a short amount of running time (24 to 48 hours) and resubmitted after passing the specified run time. Administrating the jobs on different machines (repeating the mentioned process for all the jobs on different machines) required a huge amount of time and continuous effort. Table 8.15 presents a summary of the computational resource usage for all cases given in Tables 8.5, 8.9 and 8.12. Less than 20% of the computational resources were used for non-converged (Possible and Violate Constraints) cases.

The table shows that during 15 months in 2015 (12 months) and 2016 (3 months) over 5000 jobs were submitted on 8 different HPC clusters across Canada. To finish these jobs, 535 core-years were needed. This means that 535 cores would have to work continuously for one year in order to achieve the results for the mentioned cases. It also means that 15 months of real time was needed to achieve the converged results presented in this thesis. At that rate pursuing the possible cases would have taken at least another year, and was not feasible.

Table 8.15: Summary of the computational resource usage

	2015 and 2016 (15 months)	
HPC Cluster	Core-Years	Number of submitted jobs
MP2	210.9	481
Nestor	47.3	711
Guillimin	66	989
Orcinus	71.6	736
Grex	126.5	1930
Lattice	11.6	191
Parallel	0.47	14
Jasper	0.07	6
Total	534.4	5058

Chapter 9

Summary, Conclusions, and Recommendations for Future Work

9.1 Summary

Reflux condensation is the mode of phase change heat transfer occurring when a gas-vapour mixture and the liquid condensate flow in opposite directions. This phenomenon can be seen in many industrial applications such as pressurized water reactors of the nuclear power plants, compact heat exchangers, and thermosyphons. The main objective of the present work was to develop a detailed numerical model for the simulation of reflux condensation in a vertical tube.

There are many experimental and theoretical works about reflux condensation. Although most of them focused on the flooding and counter-current flow limitations, there are a few works which concentrated on reflux condensation heat transfer.

As mentioned in the literature review, all the previous theoretical models have been developed with specific assumptions. The key points that have not been addressed adequately in previous work for reflux condensation simulation in a vertical tube are:

1. Consideration of the presence of non-condensable gas
2. Solving the complete set of equations in the mixture region
3. Consideration of fundamental force balances at the interface instead of using correlations
4. Definition of appropriate boundary conditions which conform to industrial applications and also experiments

5. Tracking the liquid-mixture interface sharply

6. Including the effect of variations of the thermophysical properties under the influence of temperature, pressure and, gas mass fraction changes

In the present work, a numerical model was presented for steady, laminar film condensation from co-current and counter-current flows of vapour-gas mixtures in vertical channels and tubes. The numerical model is based on the complete elliptic set of governing equations. A full simultaneous solution in the entire two-dimensional solution domain was obtained for the velocities, pressure, and temperature in both phases plus the gas mass fraction and the interface location. Fundamental balances of mass, force, and energy were applied at the phase interface; no approximations or correlation equations for interface shear force or heat and mass transfer were used. A sharp-interface approach was used so that the faces of the control volumes adjacent to the interface matched exactly the interface location. A special algorithm for moving the mesh at each solution time step toward steady state was presented. A finite volume discretisation method was employed with non-staggered storage on a non-orthogonal structured mesh. The linearised equation set was solved using a pressure-based coupled solution approach and a Rhie-Chow style of face velocity calculation. In each step of the model development, the model was validated by comparison with previous works, analytical solutions or experimental results.

The process started from the simulation of co-current flows without condensation in parallel-plate channels (*e.g.*, stratified flow, falling film and etc.). Following that step, co-current pure vapour condensation was modelled in vertical parallel-plate channels. Next, the co-current gas-vapour mixture condensation with the application of variable thermophysical properties was simulated. At this stage, the model was validated using the previous works by Siow *et al.* [6] and Dharma Rao *et al.* [71]. It was shown that for two cases with low inlet gas concentration and higher inlet-to-wall temperature difference, the Siow model terminated calculations before the end of the channel. The elliptic model, however, was able to solve

over the full channel length and predicted a small region of reverse flow in the mixture. This capability of the model is crucial for the reflux condensation numerical simulation. Details of both models' predictions of the development of the flow up to the stopping point of the parabolic model were presented and discussed.

The next step was to impose the new boundary conditions for the reflux condensation in a vertical parallel-plate channel. Obtaining reasonable results in this step established the capability of the numerical model in handling reflux condensation problems.

There are no experimental data to validate the results of reflux condensation simulation in parallel-plate channels. Therefore, the next step was to develop the model equations in cylindrical coordinates. In this step, all the new cylindrical form of the equations were discretised to get the new set of algebraic equations. During the first part of this step, co-current condensation was studied and comparisons were made against the previous work by Groff *et al.* [10]

The proper boundary conditions for the reflux condensation in tubes were then implemented. In this step the model was validated using the data provided by Dr.Vierow [38]. There were many challenges to obtain the same inlet mass flow rate as the experiment for the validation process. The length of the top and bottom sections along with the inlet relative pressure had to be defined properly to match the inlet mass flow rate with the experimental data and avoid turbulent inlet Reynolds number, downward flow at the outlet, and liquid hold-up and instabilities. The numerical model prediction of condensation rate was in very good agreement with the data provided by the experiment.

Finally, a parametric study was conducted using three different geometries. To define the cases in each test matrix, wide range of inlet gas mass fraction and inlet-to-wall temperature difference were considered. Due to all the numerical complexities, each run needed approximately four weeks to reach the converged solution. Thus, the number of cases for the parametric study was limited by available computing resources.

The U-velocity, V-velocity, temperature, and gas mass fraction profiles in the gas-vapour mixture region as well as the U-velocity and temperature profiles in the liquid region were presented. The axial variation of many parameters such as film thickness, local Nusselt number, interface gas mass fraction and temperature, centre-line temperature, normalised liquid mass flow rate, and interface velocity were presented and discussed in detail.

9.2 Conclusions

The fully elliptic coupled numerical model successfully computed flow characteristics for the laminar film condensation from co-current and counter-current flows of vapour-gas mixtures in vertical parallel-plate channels and tubes.

Due to the physical and numerical complexities of co-current and counter-current condensation problems, the coupling of all parameters is essential. This coupling approach along with all fundamental balances at the phase interface makes the system of equations extremely difficult to solve. The available iterative solvers in PETSc package could not solve the nearly singular system of equations of these problems. Direct solvers, however, are successful in obtaining results for such ill-conditioned system of equations.

For the simulation of co-current film condensation from gas-vapour mixtures in channels and tubes, the results are in good agreement with the previous work. It was found that for the cases with high condensation rate, reverse flow could occur. The previous methods (marching methods) are not able to handle these cases, whereas, the model developed and presented in this thesis is able to capture the reverse flow and obtain the solution for the whole domain.

For the simulation of the counter-current film condensation from gas-vapour mixture, the developed model predicts the condensation rate well and produces detailed axial variations of different parameters such as local Nusselt number, interface temperature and gas mass frac-

tion, film thickness, and centre-line temperature and velocity. It was shown that most of the trends are similar to the physical expectations. Based on the studied cases, it was observed that condensation increases as gas mass fraction decreases or inlet-to-wall temperature difference increases. Moreover, larger cooled surface area also leads to more condensation. The behaviour of the centre-line temperature is different for short and long tubes. For the cases that nearly all the inlet vapour is condensed in the tube, the film thickness adjusts itself based on the interface-to-wall temperature to distribute the same total condensation rate along the cooled section.

9.3 Recommendations for Future Work

In order to improve the capabilities of the model and reduce the computational costs, the following future work is recommended:

- **Add a turbulent model for the mixture and liquid regions**

  This would help to remove the limitation on the inlet Reynolds number and enable the model to predict reflux condensation characteristics with a wider range of inlet mass flow rates.

- **Develop a suitable iterative solver**

  The system of equations of the coupled two-phase flow problems is ill-conditioned and extremely hard to solve, and therefore requires the use of a computationally expensive direct solver. A combination of pre-conditioners and an iterative solver should be developed to reduce overall computational cost.

- **Couple the interface and mesh movement into the system of equations**

  The interface location determination could be implicitly coupled to the solution for the field variables. Applying a geometric conservation law as the governing equation

for the interface and mesh movement and coupling it with all other equations could help to achieve faster convergence. This approach, however, may make the system of equations harder to solve.

- **Comparative study of the present model with the simplified models**

  As explained in the literature review, there are simplified models which applied correlations or boundary layer equations to simulate reflux condensation. These models could be studied and compared with the presented results. The comparison may justify the necessity of having a detailed model for such a complicated phenomenon as reflux condensation.

References

[1] F. P. Incropera, D. P. DeWitt, T. L. Bergman and A. S. Lavine, *Fundamentals of Heat and Mass Transfer*, 6th ed., John Wiley and Sons, New York (2006).

[2] J. Palen and Z. Yang, Reflux condensation flooding prediction: Review of current status, *Chemical Engineering Research and Design* **79**(A4) (May 2001), 463–469.

[3] Y. Moon, H. Park, Y. Bang, U. N. R. C. O. of Nuclear Regulatory Research, H. Kisurwŏn, H. Yŏnï¿o¡ijguso and H. Kisurwŏn, *Assessment of RELAP5/MOD3. 2 for Reflux Condensation Experiment*, Office of Nuclear Regulatory Research, US Nuclear Regulatory Commission (2000).

[4] Y. Utanohara and M. Murase, Numerical analysis of steam-air behavior in a pressurizer during reflux cooling, *Nuclear Engineering and Design* **240**(12) (Dec. 2010), 3930–3941.

[5] F. Dobran and R. S. Thorsen, Forced flow laminar filmwise condensation of a pure saturated vapor in a vertical tube, *International Journal of Heat and Mass Transfer* **23**(2) (1980), 161–177.

[6] E. C. Siow, S. J. Ormiston and H. M. Soliman, A two-phase model for laminar film condensation from steam-air mixtures in vertical parallel-plate channels, *Heat and Mass Trasnfer* **40**(5) (2004), 365–375.

[7] V. D. Rao, V. M. Krishna, P. K. Sarma and K. V. Sharma, Convective condensation of vapor in laminar flow in a vertical parallel plate channel in the presence of a high-concentration noncondensable gas, *Journal of Heat Transfer-Transactions of ASME* **131**(011502) (Jan. 2009).

[8] E. C. Siow, Numerical solution of a two-phase model for laminar film condensation of vapour-gas mixtures in channels, M.Sc. thesis, University of Manitoba, Department of Mechanical and Industrial Engineering (July 2001).

[9] F. Hassaninejadfarahani, M. Guyot and S. Ormiston, Numerical analysis of mixed-convection laminar film condensation from high air mass fraction steamâĂŞair mixtures in vertical tubes, *International Journal of Heat and Mass Transfer* **78** (2014), 170 – 180.

[10] M. K. Groff, S. J. Ormiston and H. M. Soliman, Analysis of laminar film condensation from vapor-gas mixtures in vertical tubes, in *Proceedings of the 3rd International Symposium on Two-Phase Flow Modelling and Experimentation*, Pisa, Italy (Sep. 2004).

[11] V. Dharma Rao, V. Murali Krishna, K. V. Sharma and P. V. J. Mohana Rao, Convective condensation of vapor in the presence of a non-condensable gas of high concentration in laminar flow in a vertical pipe, *International Journal of Heat and Mass Transfer* **51**(25-26) (Dec. 2008), 6090–6101.

[12] Y. El Hammami, M. Feddaoui, T. Mediouni and A. Mir, Numerical study of condensing a small concentration of vapour inside a vertical tube, *Heat and Mass Transfer* **48**(9) (Sep. 2012), 1675–1685.

[13] C.-Y. Wang and C.-J. Tu, Effects of non-condensable gas on laminar film condensation in a vertical tube, *International Journal of Heat and Mass Transfer* **31**(11) (1988), 2339–2345.

[14] A. Dehbi and S. Guentay, A model for the performance of a vertical tube condenser in the presence of noncondensable gases, *Nuclear Engineering and Design* **177**(1-3) (Dec. 1997), 41–52.

[15] M. Siddique, M. W. Golay and M. S. Kazimi, Theoretical modeling of forced convection of steam in a vertical tube in the presence of a noncondensable gas, *Nuclear Technology* **106** (May 1994), 202–215.

[16] S. M. Ghiaasiaan, B. K. Kamboj and S. I. Abdel-Khalik, Two-fluid modeling of condensation in the presence of noncondensables in two-phase channel flows, *Nuclear Science and Engineering* **119** (1995), 1–17.

[17] H. A. Hasanein, M. S. Kazimi and M. W. Golay, Forced convection in-tube steam condensation in the presence of noncondensable gases, *International Journal of Heat and Mass Transfer* **39**(13) (1996), 2625–2639.

[18] L. Herranz, J. Munoz-Cobo and G. Verdu, Heat transfer modeling in the vertical tubes of the passive containment cooling system of the simplified boiling water reactor, *Nuclear Engineering and Design* **178**(1) (Dec. 1997), 29–44.

[19] H. C. No and H. S. Park, Non-iterative condensation modeling for steam condensation with non-condensable gas in a vertical tube, *International Journal of Heat and Mass Transfer* **45**(4) (Feb. 2002), 845–854.

[20] R. Yuann, V. Schrock and X. Chen, Numerical modeling of condensation from vapor-gas mixtures for forced down flow inside a tube, in *Proceedings of the NURETH-7 Conference*, pp. 377–401 (1995).

[21] M. K. Groff, S. J. Ormiston and H. M. Soliman, Numerical solution of film condensation from turbulent flow of vapor-gas mixtures in vertical tubes, *International Journal of Heat and Mass Transfer* **50**(19–20) (2007), 3899–3912.

[22] M.-H. Chun and S.-O. Yu, Effect of steam condensation on countercurrent flow limiting in nearly horizontal two-phase flow, *Nuclear Engineering and Design* **196**(2) (2000), 201 – 217.

[23] S. Fiedler, S. Yildiz and H. Auracher, Determination of film thickness and flooding during reflux condensation in a small, inclined tube with an ultrasonic transducer, *International Journal of Energy Research* **27**(4) (2003), 315–325.

[24] S. Fiedler, H. Auracher and D. Winkelmann, Effect of inclination n flooding and heat transfer during reflux condensation in a small diameter tube, *International Communications in Heat and Mass Transfer* **29**(3) (2002), 289 – 302.

[25] I. Choutapalli and K. Vierow, Wall pressure measurements of flooding in vertical countercurrent annular air-water flow, *Nuclear Engineering and Design* **240**(10) (2010), 3221–3230.

[26] I. Choutapalli and K. Vierow, Effect of air inlet geometry on flooding in a large diameter vertical tube, *Nuclear Engineering and Design* **240**(10) (2010), 3677–3681.

[27] Deendarlianto, A. Ousaka, Indarto, A. Kariyasaki, D. Lucas, K. Vierow, C. Vallee and K. Hogan, The effects of surface tension on flooding in counter-current two-phase flow in an inclined tube, *Experimental Thermal and Fluid Science* **34**(7) (Oct. 2010), 813–826.

[28] S. Chen, J. Reed and C. Tien, Reflux condensation in a two-phase closed thermosyphon, *International Journal of Heat and Mass Transfer* **27**(9) (1984), 1587 – 1594.

[29] R. Girard and J. S. Chang, Reflux condensation phenomena in single vertical tubes, *International Journal of Heat and Mass Transfer* **35**(9) (1992), 2203–2218.

[30] Y. M. Moon, H. C. No and Y. S. Bang, Local heat transfer coefficients for reflux condensation experiment in a vertical tube in the presence of noncondensible gas, *Journal of the Korean Nuclear Society* **31**(5) (1999), 486–97.

[31] T. W. K. Vierow, T. Nagae, Experimental investigation of reflux condensation heat transfer in pwr steam generator tubes in the presence of noncondensible gases, in *The 10th International Topical Meeting on Nuclear Reactor Thermal Hydraulics*, Seoul, Korea (Oct. 2003).

[32] S. Fiedler and H. Auracher, Experimental and theoretical investigation of reflux condensation in an inclinded small diameter tube, *International Journal of Heat and Mass Transfer* **47** (2004), 4031–4034.

[33] T. Nagae, M. Murase, T. Wu and K. Vierow, Evaluation of reflux condensation heat transfer of steam-air mixtures under gas-liquid countercurrent flow in a vertical tube, *Journal of Nuclear Science and Technology* **42**(1) (Jan. 2005), 50–57.

[34] T. Nagae, M. Murase, T. Chikusa, K. Vierow and T. Wu, Reflux condensation heat transfer of steam-air mixture under turbulent flow conditions in a vertical tube **44**(2) (Feb. 2007), 171–182.

[35] K. Lee, H. No, I. Chu, Y. Moon and M. Chun, Local heat transfer during reflux condensation mode in a u-tube with and without noncondensible gases, *International Journal of Heat and Mass Transfer* **49**(11-12) (June 2006), 1813–1819.

[36] T. Klahm, H. Auracher and F. Ziegler, Heat transfer during reflux condensation of an R134a/R123 mixture in vertical and inclined narrow tubular and rectangular channels, *International Journal of Refrigeration* **33**(7) (Nov. 2010), 1319–1326.

[37] B. Noel and R. Deruaz, Reflux condenser mode with non-condensable gas - assessment of cathare against bethsy test-7.2c, *Nuclear Engineering and Design* **149**(1-3) (Sep. 1994), 291–298.

[38] K. Vierow, Private Communications (2015).

[39] R. Seban and J. Hodgson, Laminar film condensation in a tube with upward vapor flow, *International Journal of Heat and Mass Transfer* **25**(9) (1982), 1291 – 1300.

[40] D. Bharathan and G. Wallis, Air water countercurrent annular-flow, *International Journal of Multiphase Flow* **9** (1983), 349–366.

[41] G. Chou and J. Chen, Heat transfer characteristics of reflux condensation phenomena in a single vertical tube, *Nuclear Science and Engineering* **127**(2) (Oct. 1997), 220–229.

[42] G. Chou and J. Chen, A general modeling for heat transfer during reflux condensation inside vertical tubes surrounded by isothermal fluid, *International Journal of Heat and Mass Transfer* **42**(12) (June 1999), 2299–2311.

[43] Y. Pan, Condensation characteristics inside a vertical tube considering the presence of mass transfer, vapor velocity and interfacial shear, *International Journal of Heat and Mass Transfer* **44**(23) (2001), 4475 – 4482.

[44] Y. Liao, S. Guentay, D. Suckow and A. Dehbi, Reflux condensation of flowing vapor and non-condensable gases counter-current to laminar liquid film in a vertical tube, *Nuclear Engineering and Design* **239**(11) (Nov. 2009), 2409–2416.

[45] V. K. Liao, Y., A generalized diffusion layer model for condensation of vapor with noncondensable gases, *ASME Journal of Heat Transfer 129, 988-994* (2007).

[46] D. Lakehal, M. Fulgosi and G. Yadigaroglu, Direct numerical simulation of condensing stratified flow, *Journal of Heat Transfer-Transactions of ASME* **130**(2) (Feb. 2008).

[47] Y. Utanohara, I. Kinoshita, M. Murase, N. Minami, T. Nariai and A. Tomiyama, Numerical simulation using cfd software of countercurrent gasŰliquid flow in a pwr hot leg under reflux condensation, *Nuclear Engineering and Design* **241**(5) (2011), 1643 – 1655.

[48] J. M. Floryan and H. Rasmussen, Numerical methods for viscous flows with moving boundaries, *Applied Mechanics Reviews* **42** (1989), 323–341.

[49] F. H. Harlow and J. E. Welch, Numerical study of large-amplitude free-surface motions, *Physics of Fluids* **9**(5) (1966), 842–851.

[50] C. Hirt and B. Nichols, Volume of fluid (vof) method for the dynamics of free boundaries, *Journal of Computational Physics* **39**(1) (1981), 201 – 225.

[51] G. Raithby, W. XU and G. Stubley, Prediction of incompressible free surface flows with an element-based finite volume method, *Journal of Computational Fluid Dynamics* **04**(03) (Oct. 1995), 353–371.

[52] C. W. Hirt, A. A. Amsden and J. L. Cook, An arbitrary lagrangian-eulerian computing method for all flow speeds, *Journal of Computational Physics* **135**(2) (Aug. 1997), 203–216.

[53] J. M. Floryan and H. Rasmussen, Numerical Methods for Viscous Flows With Moving Boundaries, *Applied Mechanics Reviews* **42** (1989), 323.

[54] Y. Q. Wang, L. A. Penner and S. J. Ormiston, Analysis of laminar forced convection of air for crossflow in banks of staggered tubes, *Numerical Heat Transfer, Part A (Applications)* **38**(8) (2000), 819–845.

[55] L. Penner, Two-dimensional flow predictions in a tube bundle using orthogonal and non-orthogonal grids, M.Sc. thesis (1996).

[56] S. V. Patankar, *Numerical Heat Transfer and Fluid Flow*, Hemisphere, Washington (1980).

[57] C. M. Rhie and W. L. Chow, Numerical Study of the Turbulent Flow Past an Airfoil with Trailing Edge Separation, *AIAA Journal* **21**(11) (1983), 1525–1532.

[58] B. Yu, Y. Kawaguchi, W. Tao and H. Ozoe, Checkerboard pressure predictions due to the underrelaxation factor and time step size for a nonstaggered grid with momentum interpolation method, *Numerical Heat Transfer, Part B (Fundamentals)* **41**(1) (2002), 85–94.

[59] S. Vakilipour and S. J. Ormiston, A coupled pressure-based co-located finite-volume solution method for natural-convection flows, *Numerical Heat Transfer, Part B (Fundamentals)* **61** (2012), 91–115.

[60] G. D. Raithby and G. E. Schneider, Elliptic systems: Finite-difference method ii, in *Handbook of Numerical Heat Transfer*, edited by W. J. Minkowycz, E. M. Sparrow, G. E. Schneider and R. H. Pletcher, John Wiley & Sons (1988).

[61] J. van Doormaal and C. Raithby, Enhancements of the SIMPLE method for predicting incompressible fluid flows, *Numerical Heat Transfer* **7** (1984), 147–163.

[62] G. Raithby and G. Schneider, Numerical solution of problems in incompressible fluid flow: Treatment of the velocity-pressure coupling, *Numerical Heat Transfer* **2**(2) (1979), 417–440.

[63] Y. Saad and M. H. Schultz, Gmres: A generalized minimal residual algorithm for solving nonsymmetric linear systems, *SIAM J. Sci. Stat. Comput.* **7**(3) (Jul. 1986), 856–869.

[64] S. Balay, S. Abhyankar, M. F. Adams, J. Brown, P. Brune, K. Buschelman, V. Eijkhout, W. D. Gropp, D. Kaushik, M. G. Knepley, L. C. McInnes, K. Rupp, B. F. Smith and H. Zhang, PETSc Web page, http://www.mcs.anl.gov/petsc (2014).

[65] S. Balay, S. Abhyankar, M. F. Adams, J. Brown, P. Brune, K. Buschelman, V. Eijkhout, W. D. Gropp, D. Kaushik, M. G. Knepley, L. C. McInnes, K. Rupp, B. F. Smith and H. Zhang, PETSc users manual, Tech. Rep. ANL-95/11 - Revision 3.5, Argonne National Laboratory (2014).

[66] S. Balay, W. D. Gropp, L. C. McInnes and B. F. Smith, Efficient management of parallelism in object oriented numerical software libraries, in *Modern Software Tools in Scientific Computing*, edited by E. Arge, A. M. Bruaset and H. P. Langtangen, pp. 163âĂŞ–202, Birkhauser Press, Boston (1997).

[67] X. S. Li and J. W. Demmel, Superlu-dist: A scalable distributed-memory sparse direct solver for unsymmetric linear systems, *ACM Trans. Math. Softw.* **29**(2) (June 2003), 110–140.

[68] P. Amestoy and I. Duff, Multifrontal parallel distributed symmetric and unsymmetric solvers, *Computer Methods in Applied Mechanics and Engineering* **184** (Apr. 2000), 501–520.

[69] P. K. Panday, Two-dimensional turbulent film condensation of vapours flowing inside a vertical tube and between parallel plates: A numerical approach, *International Journal of Refrigeration* **26**(4) (Jun. 2003), 492–503.

[70] A. Narain, G. Yu and Q. Ziu, Interfacial shear models and their required asymptotic form for annular/stratified film condensation flows in inclined channels and vertical pipes, *International Journal of Heat and Mass Transfer* **40**(15) (Oct. 1997), 3559–3575.

[71] V. D. Rao, V. M. Krishna, P. K. Sarma and K. V. Sharma, Convective Condensation of Vapor in Laminar Flow in a Vertical Parallel Plate Channel in the Presence of a High-Concentration Noncondensable Gas, *Journal of Heat Transfer-Transactions of the ASME* **131**(1) (JAN 2009).

[72] V. D. Rao, V. M. Krishna, K. V. Sharma and P. K. Sarma, A theoretical study on convective condensation of water vapor from humid air in turbulent flow in a vertical duct, *Journal of Heat Transfer-Transactions of the ASME* **129**(12) (DEC 2007), 1627–1637.

[73] T. F. Irvine, Jr. and P. E. Liley, *Steam and Gas Tables with Computer Equations*, Academic Press, Orlando, FL (1984).

[74] F. P. Incropera and D. P. DeWitt, *Fundamentals of Heat and Mass Transfer*, 4th ed., John Wiley and Sons, New York, NY (1996).

[75] R. C. Reid, J. M. Prausnitz and T. K. Sherwood, *The Properties of Gases and Liquids*, 3rd ed., McGraw-Hill, Blacklick, OH (1977).

Appendix A

Equations in Cartesian Coordinates

A.1 Liquid Region

Equations (A.1), (A.2), (A.3) and (A.4) are the conservation of mass, x momentum, y momentum, and energy in the liquid region, respectively.

$$\frac{\partial}{\partial t}(\rho_L) + \frac{\partial}{\partial x}(\rho_L\ U_L) + \frac{\partial}{\partial y}(\rho_L\ V_L) = 0 \tag{A.1}$$

$$\begin{aligned}\frac{\partial\,(\rho_L\ U_L)}{\partial t} + \frac{\partial}{\partial x}(\rho_L\ U_L\ U_L) + \frac{\partial}{\partial y}(\rho_L\ V_L\ U_L) = \\ -\frac{\partial P_L}{\partial x} + \frac{\partial}{\partial x}\left(\mu_L\ \frac{\partial U_L}{\partial x}\right) + \frac{\partial}{\partial y}\left(\mu_L \frac{\partial U_L}{\partial y}\right) + \rho_L\ g\end{aligned} \tag{A.2}$$

$$\begin{aligned}\frac{\partial\,(\rho_L\ V_L)}{\partial t} + \frac{\partial}{\partial x}(\rho_L\ U_L\ V_L) + \frac{\partial}{\partial y}(\rho_L\ V_L\ V_L) = \\ -\frac{\partial P_L}{\partial y} + \frac{\partial}{\partial x}\left(\mu_L \frac{\partial V_L}{\partial x}\right) + \frac{\partial}{\partial y}\left(\mu_L \frac{\partial V_L}{\partial y}\right)\end{aligned} \tag{A.3}$$

$$\begin{aligned}\frac{\partial\,(\rho_L C_{p,L}\ T_L\ )}{\partial t} + \frac{\partial\,(\rho_L C_{p,L}\ U_L\ T_L)}{\partial x} + \frac{\partial\,(\rho_L C_{p,L}\ V_L\ T_L)}{\partial y} = \\ \frac{\partial}{\partial x}\left(k_L \frac{\partial T_L}{\partial x}\right) + \frac{\partial}{\partial y}\left(k_L \frac{\partial T_L}{\partial y}\right)\end{aligned} \tag{A.4}$$

A.2 Mixture Region

$$\frac{\partial}{\partial t}(\rho_M) + \frac{\partial}{\partial x}(\rho_M\ U_M) + \frac{\partial}{\partial y}(\rho_M\ V_M\ ) = 0 \tag{A.5}$$

$$\begin{aligned}\frac{\partial\,(\rho_M\ U_M)}{\partial t} + \frac{\partial}{\partial x}(\rho_M\ U_M\ U_M) + \frac{\partial}{\partial y}(\rho_M\ V_M\ U_M) = \\ -\frac{\partial P_M}{\partial x} + \frac{\partial}{\partial x}\left(\mu_M\ \frac{\partial U_M}{\partial x}\right) + \frac{\partial}{\partial y}\left(\mu_M \frac{\partial U_M}{\partial y}\right) + \rho_M\ g\end{aligned} \tag{A.6}$$

$$\frac{\partial\left(\rho_M\ V_M\right)}{\partial t}+\frac{\partial}{\partial x}(\rho_M\ U_M\ V_M)+\frac{\partial}{\partial y}(\rho_M\ V_M\ V_M)= -\frac{\partial P_M}{\partial y}+\frac{\partial}{\partial x}\left(\mu_M\frac{\partial V_M}{\partial x}\right)+\frac{\partial}{\partial y}\left(\mu_M\frac{\partial V_M}{\partial y}\right) \tag{A.7}$$

$$\frac{\partial\left(\rho_M C_{p,M}\ T_M\ \right)}{\partial t}+\frac{\partial\left(\rho_M C_{p,M}\ U_M\ T_M\right)}{\partial x}+\frac{\partial\left(\rho_M C_{p,M}\ V_M\ T_M\right)}{\partial y}= \frac{\partial}{\partial x}\left(k_M\frac{\partial T_M}{\partial x}\right)+\frac{\partial}{\partial y}\left(k_M\frac{\partial T_M}{\partial y}\right)+ \frac{\partial}{\partial x}\left(\rho_M D^{12}(C_{p,v}-C_{p,g})\frac{\partial W}{\partial x}T_M\right)+\frac{\partial}{\partial y}\left(\rho_M D^{12}(C_{p,v}-C_{p,g})\frac{\partial W}{\partial y}T_M\right) \tag{A.8}$$

$$\frac{\partial}{\partial t}(\rho_M\ W)+\frac{\partial}{\partial x}(\rho_M\ U_M\ W)+\frac{\partial}{\partial y}(\rho_M\ V_M\ W)= \frac{\partial}{\partial x}\left(\rho_M\ D^{12}\frac{\partial W}{\partial x}\right)+\frac{\partial}{\partial y}\left(\rho_M\ D^{12}\frac{\partial W}{\partial y}\right) \tag{A.9}$$

Equations (A.5), (A.6), (A.7), and (A.8) are the continuity, x-momentum conservation, y-momentum conservation, and energy conservation equations, respectively. Equation (A.9) represents mass conservation for the gas. The thermophysical and transport properties were calculated as functions of the local temperature, pressure and mixture composition (see Appendix B).

A.3 Conditions Prescribed at the Liquid-Mixture Interface

At the interface, flow fields must be coupled appropriately by applying jump conditions that relate the variables in each side of the interface.

A normal force balance is enforced using:

$$\left[(\hat{n}\cdot\boldsymbol{\tau})\cdot\hat{n}\right]_{iL}=-\left[(\hat{n}\cdot\boldsymbol{\tau})\cdot\hat{n}\right]_{iM} \tag{A.10}$$

where $\boldsymbol{\tau}$ is the stress tensor, $\hat{n}$ is the local normal unit vector to the interface. For the present work, the surface tension effects are neglected.

A tangential force balance is enforced using:

$$[(\hat{n}\cdot\boldsymbol{\tau})\cdot\hat{s}]_{iL} = [(\hat{n}\cdot\boldsymbol{\tau})\cdot\hat{s}]_{iM} \tag{A.11}$$

where $\hat{s}$ is the local tangential unit vector to the interface.

Conservation of mass and interfacial mass flow due to condensation are prescribed using Eq. (A.12).

$$\dot{m}_{iL} = \dot{m}_{iM} = -\dot{m}_{\text{cond}} \tag{A.12}$$

The interface condensation rate is calculated using Eq. (A.13).

$$\dot{m}_{\text{cond}} = \frac{A_{iL}}{h_{fg}}\left(+k_{iL}\frac{\partial T_{L}}{\partial n}\bigg|_{iL} - k_{iM}\frac{\partial T_{M}}{\partial n}\bigg|_{iM}\right) \tag{A.13}$$

It should be noted that, in the Cartesian coordinate system, the assumed direction of $\dot{m}_{\text{cond}}$ is in the negative y direction.

Equations (A.14) and (A.15) are the continuity of tangential velocity and temperature, respectively.

$$\overrightarrow{(V_t)}_{iL} = \overrightarrow{(V_t)}_{iM} \tag{A.14}$$

$$T_{iL} = T_{iM} = T_{sat} \tag{A.15}$$

Impermeability to gas at the interface is prescribed applying Eq. (A.16).

$$\dot{m}_{iM}W_{iM} - (\rho_{M}D^{12})_{iM}A_{iM}\frac{\partial W}{\partial n}\bigg|_{iM} = 0 \tag{A.16}$$

where A_{iM} is the local interfacial area. Equation (A.17) is a final closure condition for pressure in the mixture at the interface.

$$\frac{\partial P}{\partial n}\bigg|_{iM} = 0 \tag{A.17}$$

Appendix B

Thermophysical and Transport Properties Calculations

B.1 Partial Pressure of Gas and Vapour

Using the assumption of an ideal gas mixture:

$$\frac{P_g}{P_{tot}} = 1 - \frac{P_v}{P_{tot}} = \frac{W}{\left[W + (1-W)(\frac{M_g}{M_v})\right]} \tag{B.1}$$

where $M_v = 18.015$ [kg kmol^{-1}] and $M_g = 28.97$ [kg kmol^{-1}].

B.2 Water Properties

B.2.1 Liquid Water: Density

Symbol: ρ_L [kg m^{-3}]; Source: Page 22 of [73]; Temperature Range: 273.16 K $\leq T_L \leq$ 647.3 K

Evaluated using:

$$\rho_L = \left\{ 3.155 \times 10^{-3} \left[A + B\, t_c^{1/3} + C\, t_c^{5/6} + D\, t_c^{7/8} + \sum_{n=1}^{5} E_n t_c^n \right] \right\}^{-1} \tag{B.2}$$

where $t_c = \frac{(647.3 - T_L)}{647.3}$, $A = 1.0$, $B = -1.9153882$, $C = 1.2015186 \times 10^1$, $D = -7.8464025$, $E_1 = -3.888614$, $E_2 = 2.0582238$, $E_3 = -2.0829991$, $E_4 = 8.2180004 \times 10^{-1}$, and $E_5 = 4.7549742 \times 10^{-1}$.

B.2.2 Liquid Water: Specific Heat, Dynamic Viscosity, and Thermal Conductivity

Symbols: $C_{p,L}$ [$\mathrm{J\,kg^{-1}\,K^{-1}}$], μ_L [$\mathrm{kg\,m^{-1}\,s^{-1}}$], and k_L [$\mathrm{W\,m^{-1}\,K^{-1}}$]; Source: Page 846 of [74]; Temperature Range: $273.15\ \mathrm{K} \leq T_L \leq 647.3\ \mathrm{K}$

Evaluated at T_L using linear interpolation of the tabulated data.

B.2.3 Water Vapour: Density

Symbol: ρ_v [$\mathrm{kg\,m^{-3}}$]

Evaluated using:

$$\rho_v = \frac{P_v M_v}{\mathcal{R} T_M} \tag{B.3}$$

where P_v is evaluated using Eq. ((B.1)).

B.2.4 Water Vapour: Specific Heat, Dynamic Viscosity, and Thermal Conductivity

Symbols: $C_{p,v}$ [$\mathrm{J\,kg^{-1}\,K^{-1}}$], μ_v [$\mathrm{kg\,m^{-1}\,s^{-1}}$], and k_v [$\mathrm{W\,m^{-1}\,K^{-1}}$]; Source: Page 846 of [74]; Temperature Range: $273.15\ \mathrm{K} \leq T_L \leq 647.3\ \mathrm{K}$

Evaluated at T_M using linear interpolation of the tabulated data.

B.2.5 Water Vapour: Saturation Temperature

Symbol: T_{sat} [K]; Source: Page 21 of [73]; Pressure Range: $611\ \mathrm{Pa} \leq P_{\mathrm{sat}} < 1.233 \times 10^7\ \mathrm{Pa}$

Evaluated using:

$$T_{\mathrm{sat}} = A + \frac{B}{\left[\ln\left(1 \times 10^{-6} P_{\mathrm{sat}}\right) + C\right]} \tag{B.4}$$

where $A = 4.26776 \times 10^1$, $B = -3.89270 \times 10^3$, and $C = -9.48654$.

B.2.6 Water Vapour: Saturation Pressure

Symbol: P_{sat} [Pa]; Source: Page 21 of [73]; Temperature Range: 273.16 K $\leq T_{\text{sat}} <$ 600.0 K

Evaluated using:

$$P_{\text{sat}} = 1\times10^{6}\left[\exp\left(\frac{B}{(T_{\text{sat}}-A)}-C\right)\right] \tag{B.5}$$

where the coefficients are the same as those used in Eq. (B.4).

B.2.7 Water: Latent Heat of Vaporisation

Symbol: h_{fg} [J kg^{-1}]; Source: Page 23 of [73]; Temperature Range: 273.16 K $\leq T_{\text{int}} \leq$ 647.3 K

Evaluated using:

$$h_{fg} = 2.5009\times10^{3}\left[A + B\,t_c^{1/3} + C\,t_c^{5/6} + D\,t_c^{7/8} + \sum_{n=1}^{5} E_n t_c^{n}\right] \tag{B.6}$$

where $t_c = \frac{647.3-T_{\text{int}}}{647.3}$, $A = 0.0$, $B = 7.79221\times10^{-1}$, $C = 4.62668$, $D = -1.07931$, $E_1 = -3.87446$, $E_2 = 2.94553$, $E_3 = -8.06395$, $E_4 = 1.15633\times10^{1}$, and $E_5 = -6.02884$.

B.3 Air Properties

B.3.1 Air: Density

Symbol: ρ_g [kg m^{-3}]

Evaluated using:

$$\rho_g = \frac{P_g M_g}{\mathcal{R} T_M} \tag{B.7}$$

where P_g is evaluated using Eq. (B.1).

B.3.2 Air: Specific Heat

Symbol: $C_{p,g}$ [$\mathrm{J\,kg^{-1}\,K^{-1}}$]; Source: Page 97 of [73];
Temperature Range: 250 K $\leq T_M \leq$ 2000 K

Evaluated using:

$$C_{p,g} = 1.0\times10^{3}\left[\sum_{n=1}^{5} A_n T_M^{n-1}\right] \tag{B.8}$$

where $A_1 = 1.03409$, $A_2 = -2.848870\times10^{-4}$, $A_3 = 7.816818\times10^{-7}$, $A_4 = -4.970786\times10^{-10}$, and $A_5 = 1.077024\times10^{-13}$.

B.3.3 Air: Dynamic Viscosity

Symbol: μ_g [$\mathrm{kg\,m^{-1}\,s^{-1}}$]; Source: Page 113 of [73]; Temperature Range: 250 K $\leq T_M \leq$ 1050 K

Evaluated using:

$$\mu_g = 1.0\times10^{-6}\left[\sum_{n=1}^{5} B_n T_M^{n-1}\right] \tag{B.9}$$

where

- For the temperature range: 250 K $\leq T_M \leq$ 600 K
  $B_1 = -9.8601\times10^{-1}$, $B_2 = 9.080125\times10^{-2}$, $B_3 = -1.17635575\times10^{-4}$,
  $B_4 = 1.2349703\times10^{-7}$, and $B_5 = -5.7971299\times10^{-11}$.
- For the temperature range: 600 K $< T_M \leq$ 1050 K
  $B_1 = 4.8856745$, $B_2 = 5.43232\times10^{-2}$, $B_3 = -2.4261775\times10^{-5}$,
  $B_4 = 7.9306\times10^{-9}$, and $B_5 = -1.10398\times10^{-12}$.

B.3.4 Air: Thermal Conductivity

Symbol: k_g [$\mathrm{W\,m^{-1}\,K^{-1}}$]; Source: Page 114 of [73];
Temperature Range: 250 K $\leq T_M \leq$ 1050 K

Evaluated using:

$$k_g = \sum_{n=1}^{6} C_n T_M^{n-1} \tag{B.10}$$

where $C_1 = -2.276501 \times 10^{-3}$, $C_2 = 1.2598485 \times 10^{-4}$, $C_3 = -1.4815235 \times 10^{-7}$, $C_4 = 1.73550646 \times 10^{-10}$, $C_5 = -1.066657 \times 10^{-13}$, and $C_6 = 2.47663035 \times 10^{-17}$.

B.4 Mixture Property Evaluation

B.4.1 Mixture: Binary Diffusion Coefficient

Symbol: D^{12} [$\mathrm{m^2\,s^{-1}}$]; Source: Eq. (11-4.1) on page 554 of [75]

Evaluated using:

$$D^{12} = 1 \times 10^{-4} \left[\frac{0.001\ T_M^{1.75} \sqrt{\frac{(M_g + M_v)}{M_g M_v}}}{\left(\frac{P_{tot}}{1.0133 \times 10^5} \right) \left(\gamma_g^{1/3} + \gamma_v^{1/3} \right)^2} \right] \tag{B.11}$$

where $\gamma_g = 20.1$ and $\gamma_v = 12.7$ from Table 11-1 of [75].

B.4.2 Mixture: Density

Symbol: ρ_M [$\mathrm{kg\,m^{-3}}$]

Evaluated using:

$$\rho_M = \rho_v + \rho_g \tag{B.12}$$

B.4.3 Mixture: Specific Heat

Symbol: $C_{p,M}$ [$\mathrm{J\,kg^{-1}\,K^{-1}}$]

Evaluated using:

$$C_{p,M} = W C_{p,g} + (1 - W)\, C_{p,v} \tag{B.13}$$

B.4.4 Mixture: Dynamic Viscosity

Symbol: μ_M [$\mathrm{kg\,m^{-1}\,s^{-1}}$]; Source: Eq. (9-5.4) on page 411 of [75]

Evaluated using:

$$\mu_M = \frac{\mathrm{mf}_g\,\mu_g}{\mathrm{mf}_g + \mathrm{mf}_v\,\phi_{gv}} + \frac{\mathrm{mf}_v\,\mu_v}{\mathrm{mf}_v + \mathrm{mf}_g\,\phi_{vg}} \tag{B.14}$$

where the mole fraction of gas and vapour are found using $\mathrm{mf}_g = (P_g/P_{tot})$ and $\mathrm{mf}_v = (P_v/P_{tot})$.

and

$$\phi_{gv} = \frac{\left\{1 + \left(\frac{\mu_g}{\mu_v}\right)^{1/2}\left(\frac{M_v}{M_g}\right)^{1/4}\right\}^2}{\left\{8\left[1 + \left(\frac{M_g}{M_v}\right)\right]\right\}^{1/2}}$$

$$\phi_{vg} = \phi_{gv}\left(\frac{\mu_v}{\mu_g}\right)\left(\frac{M_g}{M_v}\right)$$

B.4.5 Mixture: Thermal Conductivity

Symbol: k_M [$\mathrm{W\,m^{-1}\,K^{-1}}$]; Source: Eq. (10-6.1) on page 508 of [75]

Evaluated using:

$$k_M = \frac{\mathrm{mf}_g\,k_g}{\mathrm{mf}_g + \mathrm{mf}_v\,\phi_{gv}} + \frac{\mathrm{mf}_v\,k_v}{\mathrm{mf}_v + \mathrm{mf}_g\,\phi_{vg}} \tag{B.15}$$

where mf_g, mf_v, ϕ_{gv}, and ϕ_{vg} are calculated as in Section B.4.4.

Appendix C

Coefficients in Interface Algebraic Equations

C.1 Normal Force Balance

$$a^{c,p}_{iL,\mathrm{P}} = 1 \tag{C.1}$$

$$a^{c,p}_{iL,\mathrm{S}} = -1 \tag{C.2}$$

$$a^{c,u}_{iL,\mathrm{P}} = -2\ \mu_{iL,\mathrm{P}} \left(n^2_{zs} B_{z2} + n_{zs} n_{rs} B_{r2}\right)_{iL,\mathrm{N}} \tag{C.3}$$

$$a^{c,u}_{iL,\mathrm{E}} = -2\ \mu_{iL,\mathrm{P}} \left(n^2_{zs} B_{z3} + n_{zs} n_{rs} B_{r3}\right)_{iL,\mathrm{N}} \tag{C.4}$$

$$a^{c,u}_{iL,\mathrm{W}} = -2\ \mu_{iL,\mathrm{P}} \left(n^2_{zs} B_{z4} + n_{zs} n_{rs} B_{r4}\right)_{iL,\mathrm{N}} \tag{C.5}$$

$$a^{c,u}_{iL,\mathrm{N}} = -2\ \mu_{iL,\mathrm{P}} \left(n^2_{zs} B_{z1} + n_{zs} n_{rs} B_{r1}\right)_{iL,\mathrm{N}} \tag{C.6}$$

$$a^{c,v}_{iL,\mathrm{P}} = -2\ \mu_{iL,\mathrm{P}} \left(n_{zs} n_{rs} B_{z2} + n^2_{rs} B_{r2}\right)_{iL,\mathrm{N}} \tag{C.7}$$

$$a^{c,v}_{iL,\mathrm{E}} = -2\ \mu_{iL,\mathrm{P}} \left(n_{zs} n_{rs} B_{z3} + n^2_{rs} B_{r3}\right)_{iL,\mathrm{N}} \tag{C.8}$$

$$a^{c,v}_{iL,\mathrm{W}} = -2\ \mu_{iL,\mathrm{P}} \left(n_{zs} n_{rs} B_{z4} + n^2_{rs} B_{r4}\right)_{iL,\mathrm{N}} \tag{C.9}$$

$$a^{c,v}_{iL,\mathrm{N}} = -2\ \mu_{iL,\mathrm{P}} \left(n_{zs} n_{rs} B_{z1} + n^2_{rs} B_{r1}\right)_{iL,\mathrm{N}} \tag{C.10}$$

$$a^{c,u}_{iL,\mathrm{S}} = 2\ \mu_{iM,\mathrm{P}} \left(n^2_{zn} A_{z2} + n_{zn} n_{rn} A_{r2}\right)_{iM,\mathrm{S}} \tag{C.11}$$

$$a^{c,u}_{iL,\mathrm{SE}} = 2\ \mu_{iM,\mathrm{P}} \left(n^2_{zn} A_{z3} + n_{zn} n_{rn} A_{r3}\right)_{iM,\mathrm{S}} \tag{C.12}$$

$$a^{c,u}_{iL,\mathrm{SW}} = 2\ \mu_{iM,\mathrm{P}} \left(n^2_{zn} A_{z4} + n_{zn} n_{rn} A_{r4}\right)_{iM,\mathrm{S}} \tag{C.13}$$

$$a^{c,v}_{iL,\mathrm{S}} = 2\ \mu_{iM,\mathrm{P}} \left(n_{zn} n_{rn} A_{z2} + n^2_{rn} A_{r2}\right)_{iM,\mathrm{S}} \tag{C.14}$$

$$a^{c,v}_{iL,\mathrm{SE}} = 2\ \mu_{iM,\mathrm{P}} \left(n_{zn} n_{rn} A_{z3} + n^2_{rn} A_{r3}\right)_{iM,\mathrm{S}} \tag{C.15}$$

$$a^{c,v}_{iL,\mathrm{SW}} = 2\ \mu_{iM,\mathrm{P}} \left(n_{zn} n_{rn} A_{z4} + n^2_{rn} A_{r4}\right)_{iM,\mathrm{S}} \tag{C.16}$$

$$b^{c}_{iL,\mathrm{P}} = -2\mu_{iM,\mathrm{P}} \left(n^2_{zn} A_{z1} + n_{zn} n_{rn} A_{r1}\right)_{iM,\mathrm{S}} U_{iM,\mathrm{S}} - 2\mu_{iM,\mathrm{P}} \left(n_{zn} n_{rn} A_{z1} + n^2_{rn} A_{r1}\right)_{iM,\mathrm{S}} V_{iM,\mathrm{S}} \tag{C.17}$$

C.2 Tangential Force Balance

$$a^{u,u}_{iM,\mathrm{P}} = \mu_{iM,\mathrm{P}} \left(2n_{zn}s_{zn}A_{z2} + (n_{rn}s_{zn} + n_{zn}s_{rn})A_{r2}\right)_{iM,\mathrm{S}} \tag{C.18}$$

$$a^{u,u}_{iM,\mathrm{E}} = \mu_{iM,\mathrm{P}} \left(2n_{zn}s_{zn}A_{z3} + (n_{rn}s_{zn} + n_{zn}s_{rn})A_{r3}\right)_{iM,\mathrm{S}} \tag{C.19}$$

$$a^{u,u}_{iM,\mathrm{W}} = \mu_{iM,\mathrm{P}} \left(2n_{zn}s_{zn}A_{z4} + (n_{rn}s_{zn} + n_{zn}s_{rn})A_{r4}\right)_{iM,\mathrm{S}} \tag{C.20}$$

$$a^{u,u}_{iM,\mathrm{S}} = \mu_{iM,\mathrm{P}} \left(2n_{zn}s_{zn}A_{z1} + (n_{rn}s_{zn} + n_{zn}s_{rn})A_{r1}\right)_{iM,\mathrm{S}} \tag{C.21}$$

$$a^{u,v}_{iM,\mathrm{P}} = \mu_{iM,\mathrm{P}} \left(2n_{rn}s_{rn}A_{r2} + (n_{rn}s_{zn} + n_{zn}s_{rn})A_{z2}\right)_{iM,\mathrm{S}} \tag{C.22}$$

$$a^{u,v}_{iM,\mathrm{E}} = \mu_{iM,\mathrm{P}} \left(2n_{rn}s_{rn}A_{r3} + (n_{rn}s_{zn} + n_{zn}s_{rn})A_{z3}\right)_{iM,\mathrm{S}} \tag{C.23}$$

$$a^{u,v}_{iM,\mathrm{W}} = \mu_{iM,\mathrm{P}} \left(2n_{rn}s_{rn}A_{r4} + (n_{rn}s_{zn} + n_{zn}s_{rn})A_{z4}\right)_{iM,\mathrm{S}} \tag{C.24}$$

$$a^{u,v}_{iM,\mathrm{S}} = \mu_{iM,\mathrm{P}} \left(2n_{rn}s_{rn}A_{r1} + (n_{rn}s_{zn} + n_{zn}s_{rn})A_{z1}\right)_{iM,\mathrm{S}} \tag{C.25}$$

$$a^{u,u}_{iM,\mathrm{N}} = -\mu_{iL,\mathrm{P}} \left(2n_{zs}s_{zs}B_{z2} + (n_{rs}s_{zs} + n_{zs}s_{rs})B_{r2}\right)_{iL,\mathrm{N}} \tag{C.26}$$

$$a^{u,u}_{iM,\mathrm{NE}} = -\mu_{iL,\mathrm{P}} \left(2n_{zs}s_{zs}B_{z3} + (n_{rs}s_{zs} + n_{zs}s_{rs})B_{r3}\right)_{iL,\mathrm{N}} \tag{C.27}$$

$$a^{u,u}_{iM,\mathrm{NW}} = -\mu_{iL,\mathrm{P}} \left(2n_{zs}s_{zs}B_{z4} + (n_{rs}s_{zs} + n_{zs}s_{rs})B_{r4}\right)_{iL,\mathrm{N}} \tag{C.28}$$

$$a^{u,v}_{iM,\mathrm{N}} = -\mu_{iL,\mathrm{P}} \left(2n_{rs}s_{rs}B_{r2} + (n_{rs}s_{zs} + n_{zs}s_{rs})B_{z2}\right)_{iL,\mathrm{N}} \tag{C.29}$$

$$a^{u,v}_{iM,\mathrm{NE}} = -\mu_{iL,\mathrm{P}} \left(2n_{rs}s_{rs}B_{r3} + (n_{rs}s_{zs} + n_{zs}s_{rs})B_{z3}\right)_{iL,\mathrm{N}} \tag{C.30}$$

$$a^{u,v}_{iM,\mathrm{NW}} = -\mu_{iL,\mathrm{P}} \left(2n_{rs}s_{rs}B_{r4} + (n_{rs}s_{zs} + n_{zs}s_{rs})B_{z4}\right)_{iL,\mathrm{N}} \tag{C.31}$$

$$\begin{aligned} b^{u}_{iM,\mathrm{P}} = {} & \mu_{iL,\mathrm{P}} \left(2n_{zs}s_{zs}B_{z1} + (n_{rs}s_{zs} + n_{zs}s_{rs})B_{r1}\right)_{iL,\mathrm{N}} U_{iL,\mathrm{N}} \\ & + \mu_{iL,\mathrm{P}} \left(2n_{rs}s_{rs}B_{r1} + (n_{rs}s_{zs} + n_{zs}s_{rs})B_{z1}\right)_{iL,\mathrm{N}} V_{iL,\mathrm{N}} \end{aligned} \tag{C.32}$$

C.3 Zero Pressure Gradient

$$a^{c,p}_{iM,\mathrm{P}} = \left(A_{z2}n_{zn} + A_{r2}n_{rn}\right)_{iM,\mathrm{S}} \tag{C.33}$$

$$a^{c,p}_{iM,\mathrm{S}} = \left(A_{z1}n_{zn} + A_{r1}n_{rn}\right)_{iM,\mathrm{S}} \tag{C.34}$$

$$a^{c,p}_{iM,\mathrm{W}} = \left(A_{z4}n_{zn} + A_{r4}n_{rn}\right)_{iM,\mathrm{S}} \tag{C.35}$$

$$a^{c,p}_{iM,\mathrm{E}} = \left(A_{z3}n_{zn} + A_{r3}n_{rn}\right)_{iM,\mathrm{S}} \tag{C.36}$$

C.4 Tangential Velocity Equality

$$a^{u,u}_{iM,\mathrm{P}} = -s_{zs}\big|_{iL,\mathrm{N}} \tag{C.37}$$

$$a^{u,u}_{iM,\mathrm{S}} = s_{zn}\big|_{iM,\mathrm{S}} \tag{C.38}$$

$$a^{u,v}_{iM,\mathrm{P}} = s_{rs}\big|_{iL,\mathrm{N}} \tag{C.39}$$

$$a^{u,v}_{iM,\mathrm{S}} = -s_{rn}\big|_{iM,\mathrm{S}} \tag{C.40}$$

C.5 Temperature Conditions

C.5.1 Mixture Side

$$\zeta = \ln\left(\frac{P^o_{iM,\mathrm{P}}\left(1 - W^o_{iMm\mathrm{P}}\right) M_g \times 10^{-6}}{M_g + W^o_{iM,\mathrm{P}}\left(M_v - M_g\right)}\right)$$

$$a^{t,t}_{iM,\mathrm{P}} = 1 \tag{C.41}$$

$$a^{t,p}_{iM,\mathrm{P}} = \frac{B}{P^o_{iM,\mathrm{P}}\left(\zeta + C\right)^2} \tag{C.42}$$

$$a^{t,w}_{iM,\mathrm{P}} = \frac{-B}{\left(\zeta + C\right)^2}\left(\frac{1}{1 - W^o_{iM,\mathrm{P}}} + \frac{M_v - M_g}{M_g + W^o_{iM,\mathrm{P}}(M_v - M_g)}\right) \tag{C.43}$$

$$b^t_{iM,\mathrm{P}} = T^o_{iM,\mathrm{P}} + \left[\frac{B}{P^o_{iM,\mathrm{P}}\left(\zeta + C\right)^2}\right] P^o_{iM,\mathrm{P}} - \left[\frac{-B}{\left(\zeta + C\right)^2}\left(\frac{1}{1 - W^o_{iM,\mathrm{P}}} + \frac{M_v - M_g}{M_g + W^o_{iM,\mathrm{P}}(M_v - M_g)}\right)\right] W^o_{iM,\mathrm{P}} \tag{C.44}$$

C.5.2 Liquid Side

$$a^{t,t}_{iL,\mathrm{P}} = 1 \tag{C.45}$$

$$a^{t,t}_{iL,\mathrm{S}} = -1 \tag{C.46}$$

C.6 Mass Balance

C.6.1 Mixture Side

$$a^{v,u}_{iM,\mathrm{P}} = -\rho_{iM,\mathrm{P}}(n_{zn})_{iM,\mathrm{S}} \tag{C.47}$$

$$a^{v,u}_{iM,\mathrm{N}} = \rho_{iL,\mathrm{P}}(n_{rs})_{iL,\mathrm{N}} \tag{C.48}$$

$$a^{v,v}_{iM,\mathrm{P}} = -\rho_{iM,\mathrm{P}}(n_{rn})_{iM,\mathrm{S}} \tag{C.49}$$

$$a^{v,v}_{iM,\mathrm{N}} = \rho_{iL,\mathrm{P}}(n_{rs})_{iL,\mathrm{N}} \tag{C.50}$$

C.6.2 Liquid Side

$$a^{v,u}_{iL,\mathrm{P}} = \rho_{iL,\mathrm{P}}(n_{zs})_{iL,\mathrm{N}} \tag{C.51}$$

$$a^{v,v}_{iL,\mathrm{P}} = \rho_{iL,\mathrm{P}}(n_{rs})_{iL,\mathrm{N}} \tag{C.52}$$

$$a^{v,t}_{iL,\mathrm{P}} = \left.\frac{k}{h_{fg}}\right|_{iL,\mathrm{P}} (B_{z2}n_{zs} + B_{r2}n_{rs})_{iL,\mathrm{N}} \tag{C.53}$$

$$a^{v,t}_{iL,\mathrm{N}} = \left.\frac{k}{h_{fg}}\right|_{iL,\mathrm{P}} (B_{z1}n_{zs} + B_{r1}n_{rs})_{iL,\mathrm{N}} \tag{C.54}$$

$$a^{v,t}_{iL,\mathrm{E}} = \left.\frac{k}{h_{fg}}\right|_{iL,\mathrm{P}} (B_{z3}n_{zs} + B_{r3}n_{rs})_{iL,\mathrm{N}} \tag{C.55}$$

$$a^{v,t}_{iL,\mathrm{W}} = \left.\frac{k}{h_{fg}}\right|_{iL,\mathrm{P}} (B_{z4}n_{zs} + B_{r4}n_{rs})_{iL,\mathrm{N}} \tag{C.56}$$

$$a^{v,t}_{iL,\mathrm{S}} = -\left.\frac{k}{h_{fg}}\right|_{iM,\mathrm{P}} (A_{z2}n_{zn} + A_{r2}n_{rn})_{iM,\mathrm{S}} \tag{C.57}$$

$$a^{v,t}_{iL,\mathrm{SE}} = -\left.\frac{k}{h_{fg}}\right|_{iM,\mathrm{P}} (A_{z3}n_{zn} + A_{r3}n_{rn})_{iM,\mathrm{S}} \tag{C.58}$$

$$a^{v,t}_{iL,\mathrm{SW}} = -\left.\frac{k}{h_{fg}}\right|_{iM,\mathrm{P}} (A_{z4}n_{zn} + A_{r4}n_{rn})_{iM,\mathrm{S}} \tag{C.59}$$

$$b^{v}_{iL,\mathrm{P}} = \left.\frac{k}{h_{fg}}\right|_{iM,\mathrm{P}} (A_{z1}n_{zn} + A_{r1}n_{rn})_{iM,\mathrm{S}}\, T_{iM,S} \tag{C.60}$$

C.7 Impermeability

$$a^{w,w}_{iM,\mathrm{P}} = -(\rho D^{12})_{iM,\mathrm{P}} \left(n_{zn}A_{z2} + n_{rn}A_{r2}\right)_{iM,\mathrm{S}}$$
$$+(\rho V^o)_{iM,\mathrm{P}} n_{rn}|_{iM,\mathrm{S}} + (\rho U^o)_{iM,\mathrm{P}} n_{zn}|_{iM,\mathrm{S}} \tag{C.61}$$

$$a^{w,w}_{iM,\mathrm{S}} = -(\rho D^{12})_{iM,\mathrm{P}} \left(n_{zn}A_{z1} + n_{rn}A_{r1}\right)_{iM,\mathrm{S}} \tag{C.62}$$

$$a^{w,w}_{iM,\mathrm{E}} = -(\rho D^{12})_{iM,\mathrm{P}} \left(n_{zn}A_{z3} + n_{rn}A_{r3}\right)_{iM,\mathrm{S}} \tag{C.63}$$

$$a^{w,w}_{iM,\mathrm{W}} = -(\rho D^{12})_{iM,\mathrm{P}} \left(n_{zn}A_{z4} + n_{rn}A_{r4}\right)_{iM,\mathrm{S}} \tag{C.64}$$

$$a^{w,u}_{iM,\mathrm{P}} = (\rho W^o)_{iM,\mathrm{P}} n_{zn}|_{iM,\mathrm{S}} \tag{C.65}$$

$$a^{w,v}_{iM,\mathrm{P}} = (\rho W^o)_{iM,\mathrm{P}} n_{rn}|_{iM,\mathrm{S}} \tag{C.66}$$

$$b^{w}_{iM,\mathrm{P}} = (\rho U^o W^o)_{iM,\mathrm{P}} n_{zn}|_{iM,\mathrm{S}} + (\rho V^o W^o)_{iM,\mathrm{P}} n_{rn}|_{iM,\mathrm{S}} \tag{C.67}$$

Appendix D

The Effect of Changing W_{in} and ΔT Separately for G2 Cases

D.1 Effect of Changing W_{in}

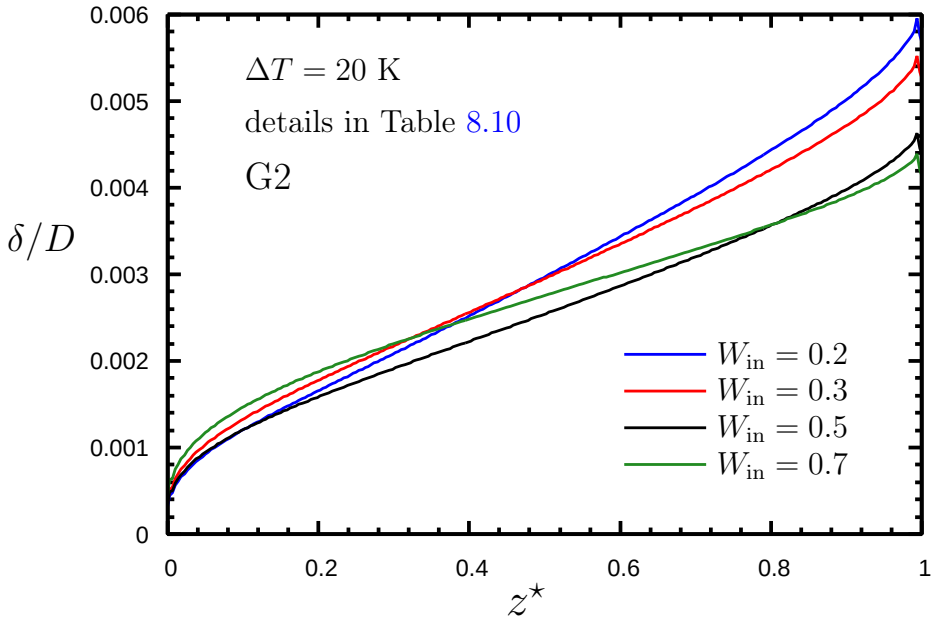

Figure D.1: Axial variation of film thickness for G2: effect of changing W_{in} for $\Delta T = 20$ K

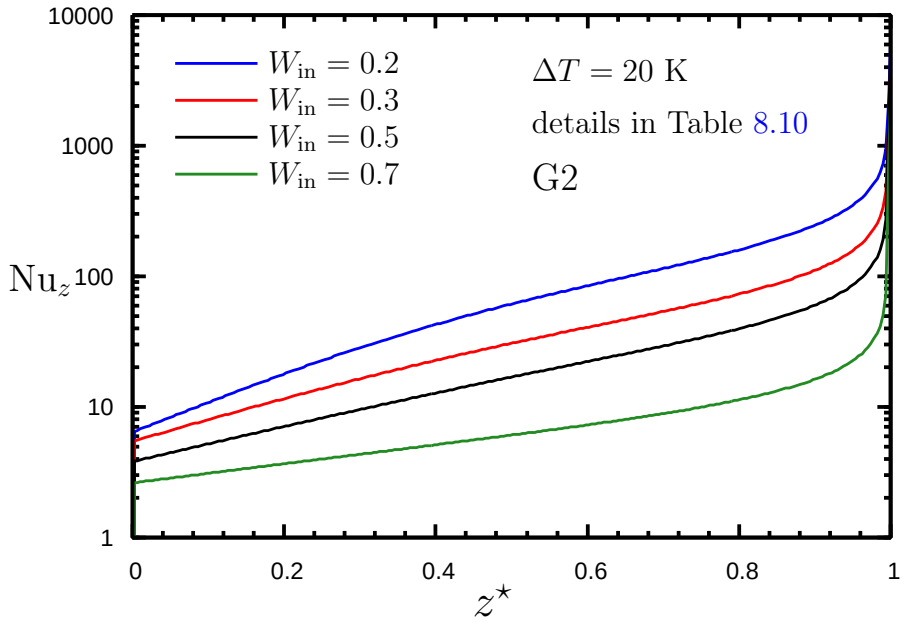

Figure D.2: Axial variation of local Nusselt number for G2: effect of changing W_{in} for $\Delta T = 20$ K

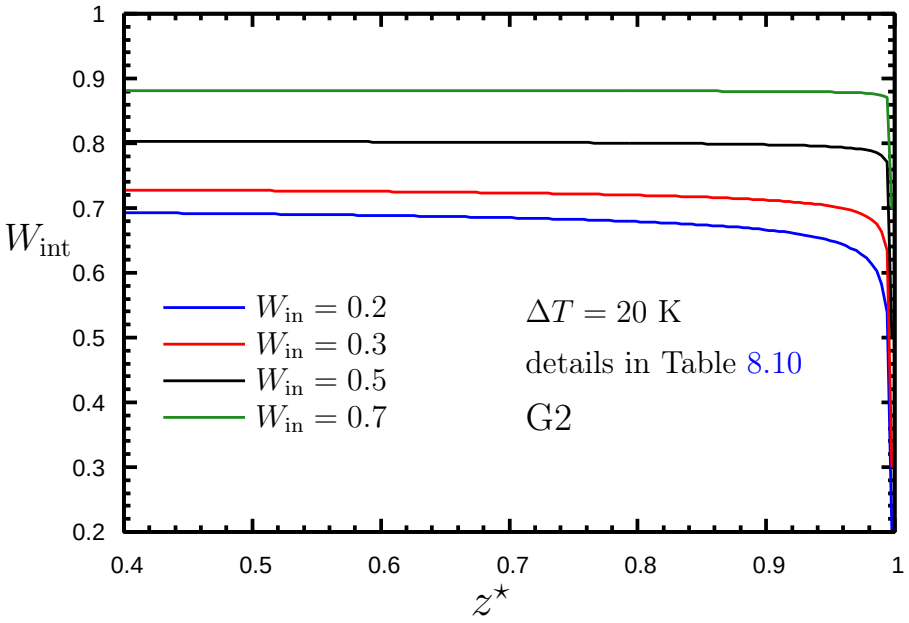

Figure D.3: Axial variation of interface gas mass fraction for G2: effect of changing W_{in} for $\Delta T = 20$ K

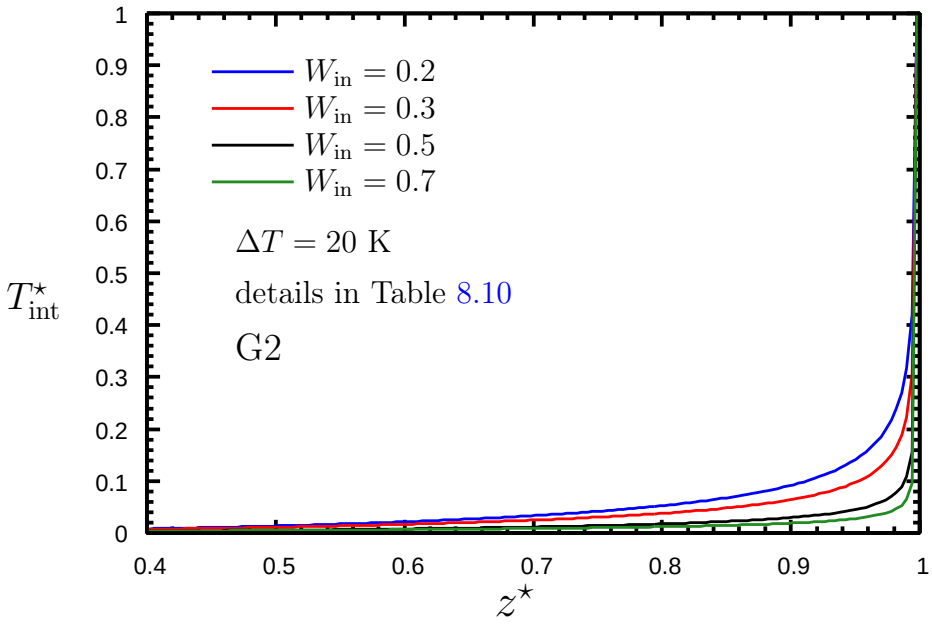

Figure D.4: Axial variation of interface temperature for G2: effect of changing W_{in} for $\Delta T = 20$ K

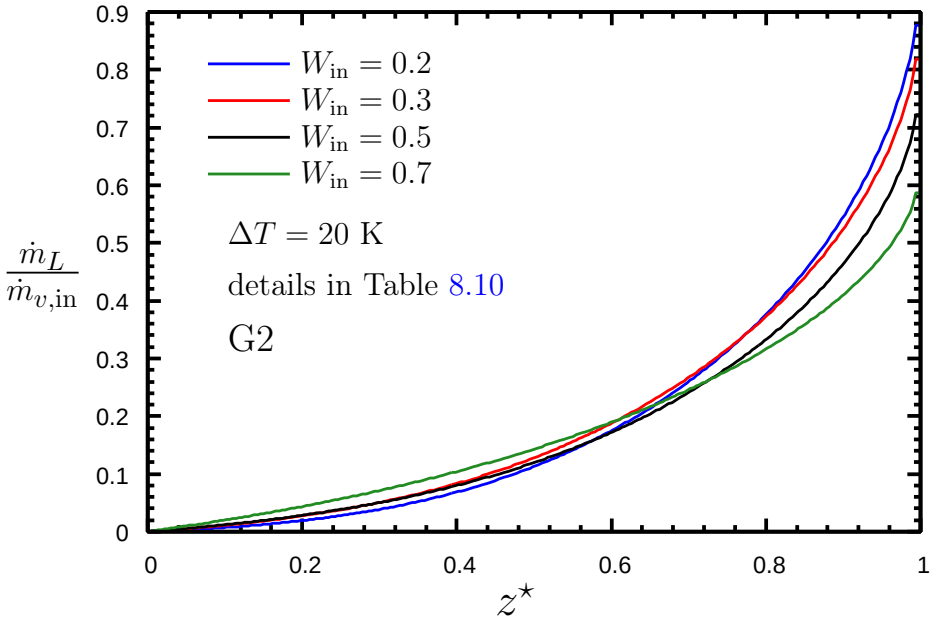

Figure D.5: Axial variation of normalised liquid mass flow rate for G2: effect of changing W_{in} for $\Delta T = 20$ K

D.2 Effect of Changing ΔT

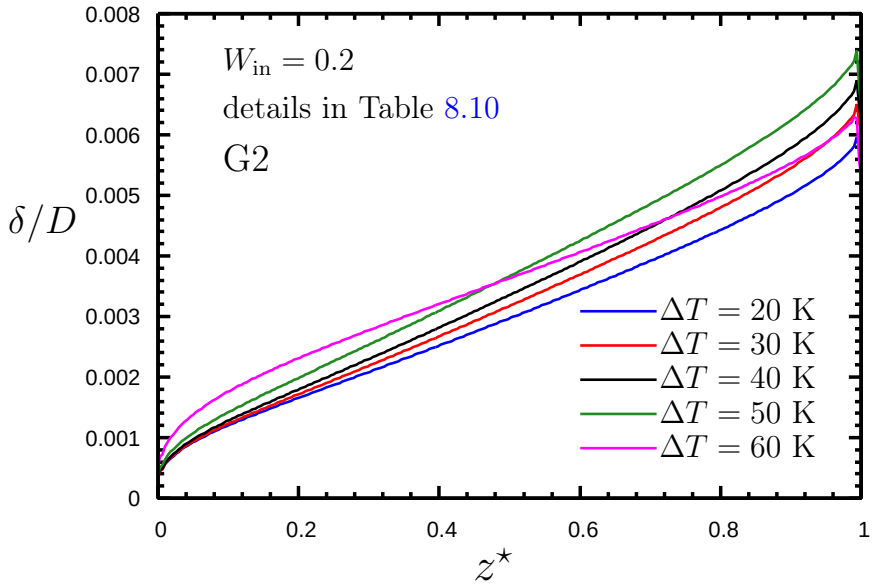

Figure D.6: Axial variation of film thickness for G2: effect of changing ΔT for $W_{\text{in}} = 0.2$

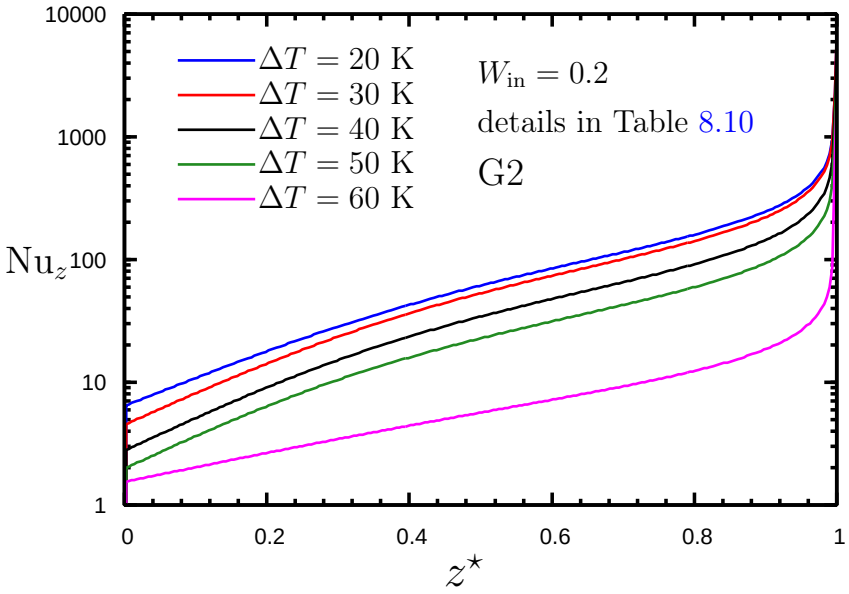

Figure D.7: Axial variation of local Nusselt number for G2: effect of changing ΔT for $W_{\text{in}} = 0.2$

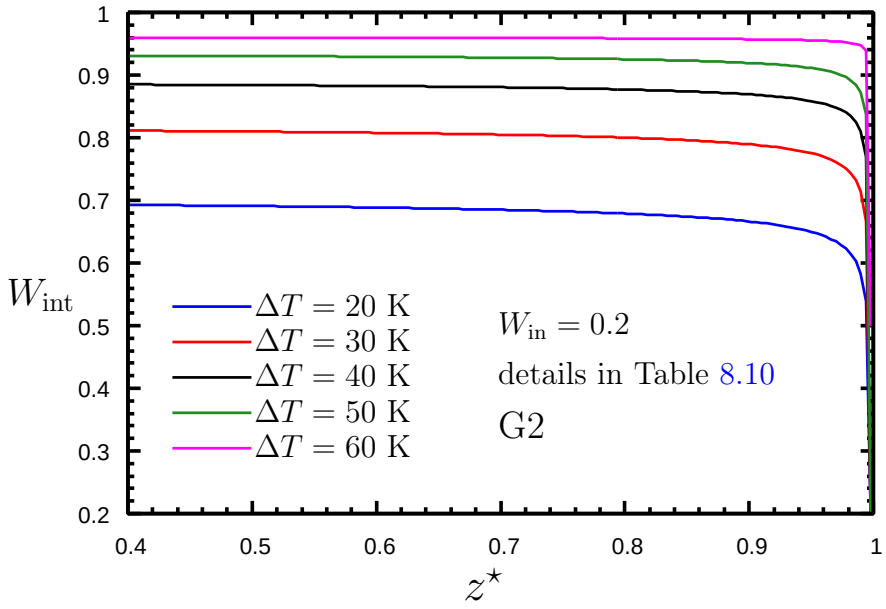

Figure D.8: Axial variation of interface gas mass fraction for G2: effect of changing ΔT for $W_{\text{in}} = 0.2$

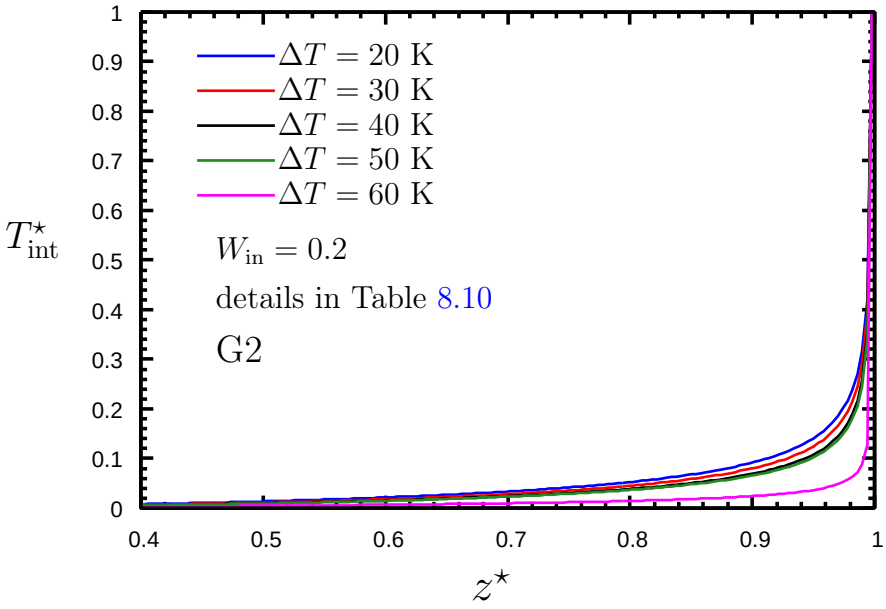

Figure D.9: Axial variation of interface temperature for G2: effect of changing ΔT for $W_{\text{in}} = 0.2$

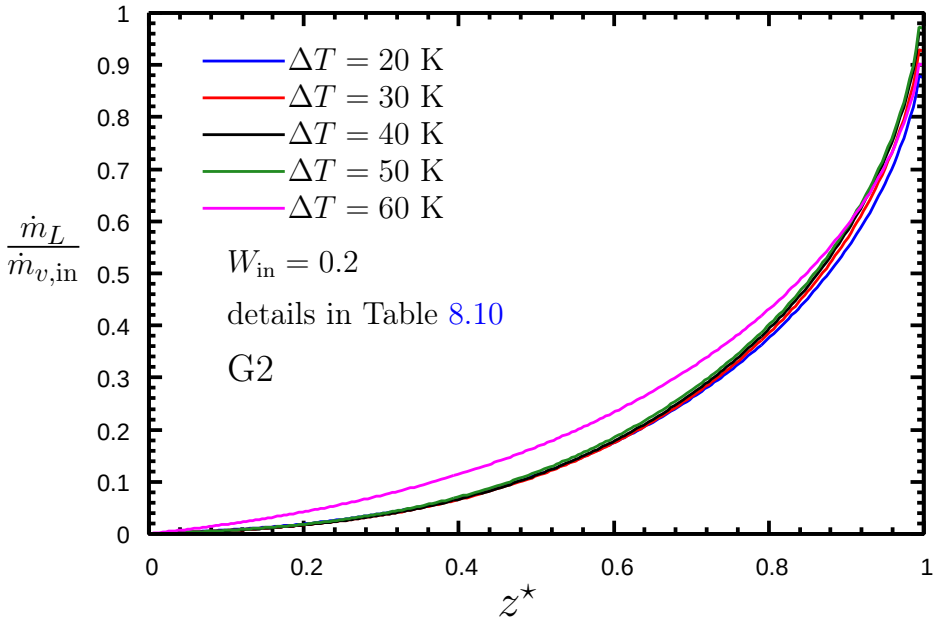

Figure D.10: Axial variation of normalised liquid mass flow rate for G2: effect of changing ΔT for $W_{\text{in}} = 0.2$

Appendix E

The Effect of Changing W_{in} for G3 Cases

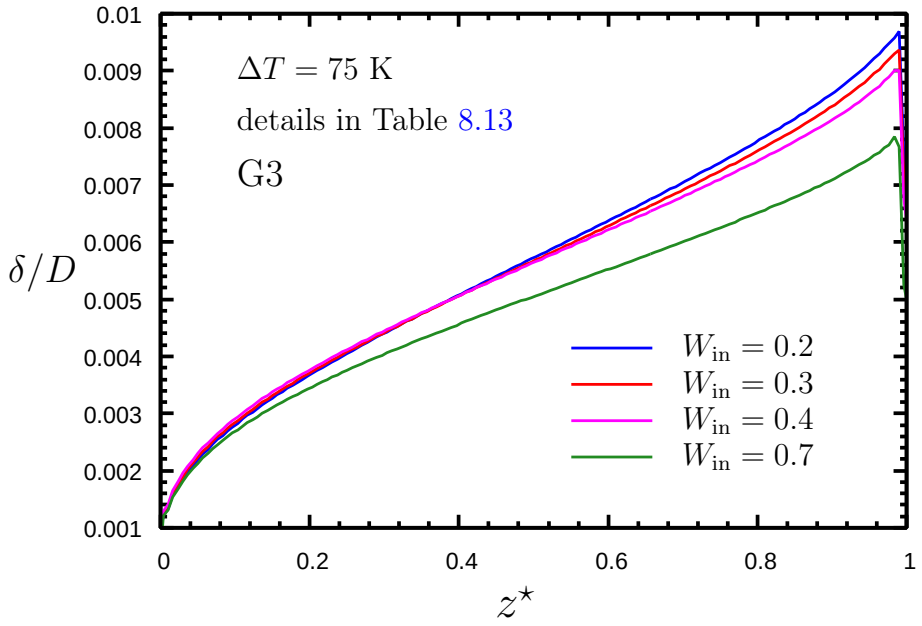

Figure E.1: Axial variation of film thickness for G3: effect of changing W_{in} for $\Delta T = 75$ K

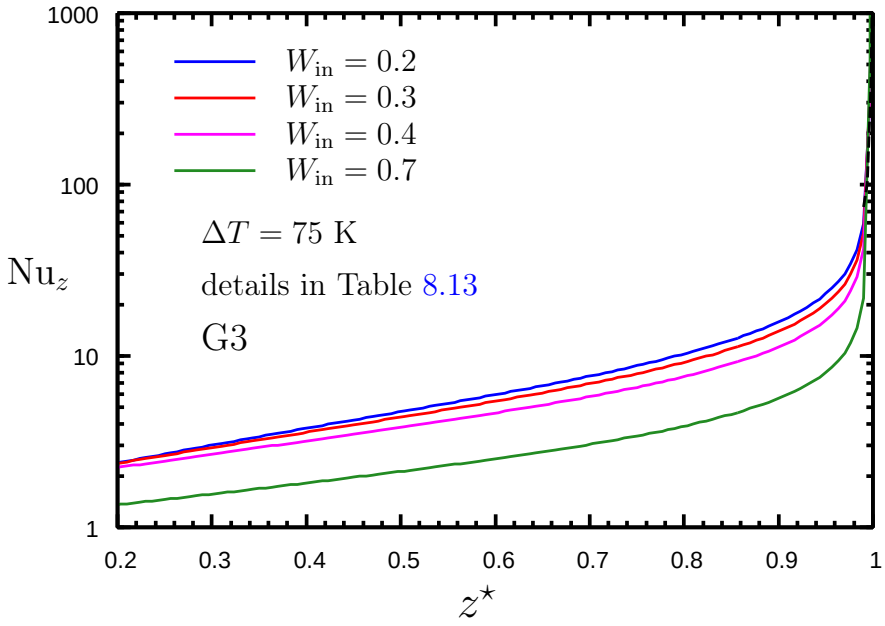

Figure E.2: Axial variation of local Nusselt number for G3: effect of changing W_{in} for $\Delta T = 75$ K

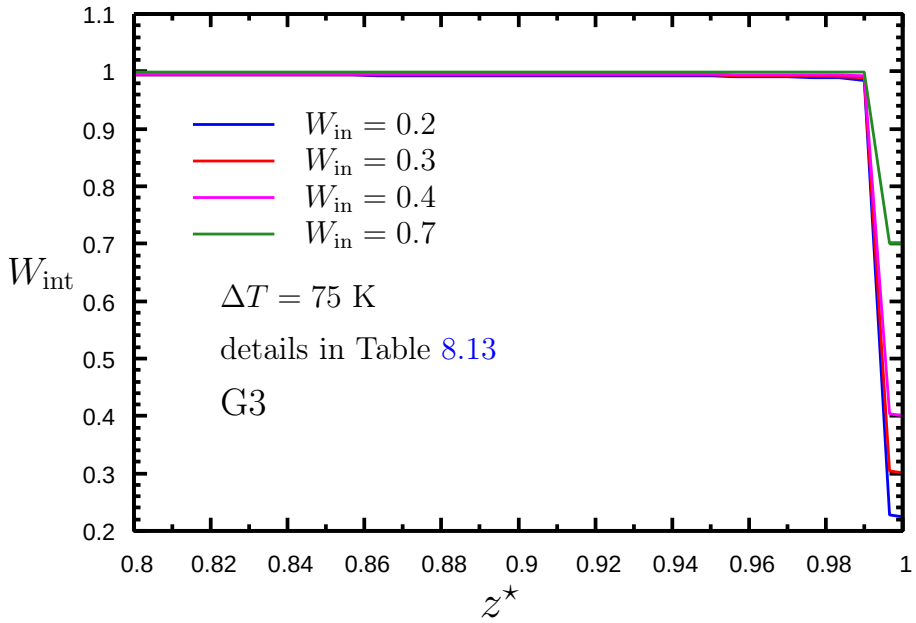

Figure E.3: Axial variation of interface gas mass fraction for G3: effect of changing W_{in} for $\Delta T = 75$ K

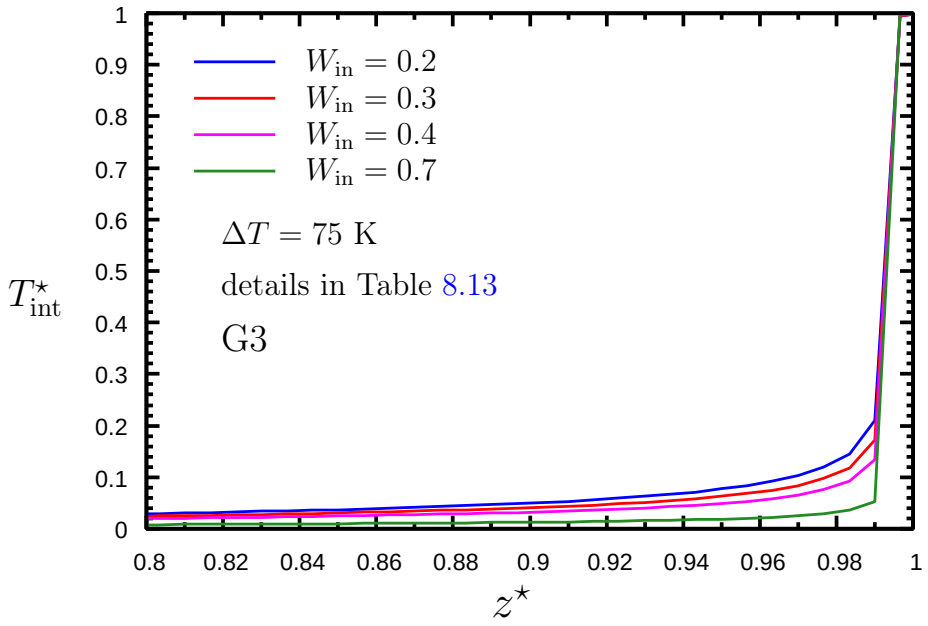

Figure E.4: Axial variation of interface temperature for G3: effect of changing W_{in} for $\Delta T = 75$ K

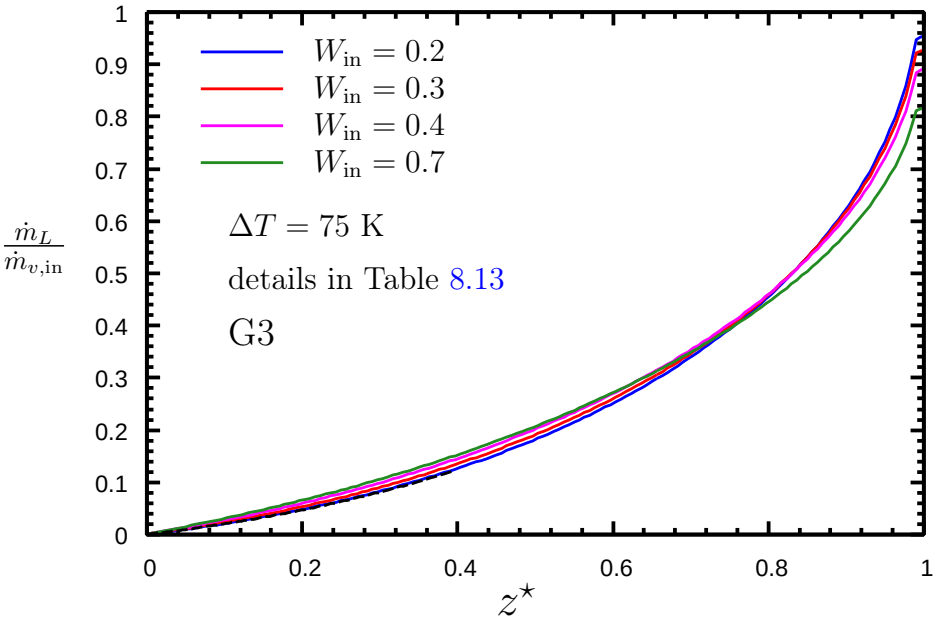

Figure E.5: Axial variation of normalised liquid mass flow rate for G3: effect of changing W_{in} for $\Delta T = 75$ K